

# STAR FORMATION IN INTERACTING DWARF GALAXIES

**Sandra Elizabeth Liss**

Weston, Florida

B.A. Physics, Swarthmore College, 2011  
M.S. Astronomy, University of Virginia, 2014

A Dissertation Presented to the Graduate Faculty of the  
*University of Virginia*  
in Candidacy for the Degree of  
*Doctor of Philosophy*

Department of Astronomy  
University of Virginia  
July 2018

© Copyright by  
Sandra Elizabeth Liss  
All rights reserved  
July 2018

## Committee Members:

Kelsey E. Johnson

Aaron S. Evans

Nitya J. Kallivayalil

Claire R. Cronmiller

# Abstract

Merging galaxies in the nearby universe can provide an ideal local analog of the early universe. Though mergers are less common today, they were prevalent at higher redshift where the increased number density of galaxies led to frequent and prolonged galaxy interactions. However, although the majority of mergers at all redshifts are expected to occur between low mass galaxies, such interactions are poorly understood and largely overlooked in comparison to interactions between massive galaxies. The TiNy Titans (TNT) survey, designed to address this gap in knowledge, is a combined multi-wavelength observational and theoretical campaign aimed at investigating the role that dwarf galaxy interactions play in the larger picture of galaxy evolution.

Stars are one of the fundamental components that make up all galaxies, and their formation is ubiquitous throughout cosmic time. Consequently, some of the most pressing open questions related to dwarf-dwarf interactions concern how stars form in these systems. Understanding how these stars form, especially in the early universe, is a necessary foundation for topics ranging from planet formation to galaxy evolution. In this thesis, we examine the ongoing star formation in the TNT interacting dwarf galaxies in unprecedented detail.

In Chapter 2, we present the ultraviolet through mid-infrared spectral energy distributions (SEDs) of the TNT sample. In addition to allowing us to compare multiwavelength tracers of SFRs, these SEDs are used to quantify the ‘typical’ SED of interacting dwarf-dwarf interactions. We present trends in the SEDs as a function of pair properties, galaxy properties, and tidal index. We then compare the interacting dwarf SEDs to other star-forming galaxies in order to contextualize their role in galaxy formation and evolution.

In Chapter 3, we discuss the total amount, distribution, and packaging (diffuse vs. clumped) of star forming regions within the TNT interacting dwarfs based on narrowband H $\alpha$  imaging from the Gemini North Telescope. We present a quantitative analysis of the star formation morphology and discuss the impact of galaxy properties and environment on the magnitude and clustering of star formation in these low mass dwarf galaxies.

In Chapter 4, we examine an important subset of the TNT interacting dwarf sample – groups of three or more low mass interacting galaxies isolated from massive galaxies. We have identified the first such candidate groups that are both (1) compact in physical and velocity space, and (2) isolated from massive galaxies. We find that the evolution of these low mass groups is markedly different from that of compact groups of massive galaxies. We present these data as well as a discussion of the cosmological context and role of the groups in high redshift galaxy formation.

# Contents

<b>List of Figures</b>	<b>vi</b>
<b>List of Tables</b>	<b>xiv</b>
<b>Acknowledgements</b>	<b>xvi</b>
<b>1 Introduction</b>	<b>1</b>
1.1 Overview of Galaxies . . . . .	1
1.1.1 “The Great Debate” and Our Place in the Universe . . . . .	1
1.1.2 Galaxy Classification . . . . .	4
1.1.3 Galaxy Evolution via Interactions and Mergers . . . . .	5
1.1.3.1 Massive Galaxy Interactions . . . . .	6
1.1.3.2 Low Mass Galaxy Interactions . . . . .	8
1.1.3.3 Comparing Massive Galaxies and Low Mass Galaxies . . . . .	12
1.2 The TiNy Titans Survey Overview . . . . .	15
1.2.1 TNT Theory Program . . . . .	15
1.2.2 TNT Local Volume Program . . . . .	16
1.2.3 TNT Low-z Program . . . . .	16
1.3 Early Results from the TNT Low-z Program . . . . .	19
1.4 Thesis Overview . . . . .	23
<b>2 The Spectral Energy Distributions of Interacting Dwarf Galaxies</b>	<b>25</b>
2.1 Introduction . . . . .	25
2.2 Data and Methods . . . . .	26
2.2.1 Ultraviolet data from GALEX . . . . .	27
2.2.2 Optical data from SDSS . . . . .	28
2.2.3 Infrared data from WISE . . . . .	28
2.2.4 Binning targets by pair and galaxy properties . . . . .	30
2.3 Results . . . . .	30
2.3.1 SEDs as a function of projected radial separation . . . . .	30
2.3.2 SEDs as a function of projected velocity separation . . . . .	33
2.3.3 SEDs as a function of pair mass ratio . . . . .	35
2.3.4 SEDs as a function of galaxy metallicity . . . . .	37
2.3.5 SEDs as a function of galaxy star formation rate . . . . .	40
2.3.6 SEDs as a function of massive host tidal index . . . . .	40

2.3.7	Comparison to other astronomical systems . . . . .	42
2.3.7.1	NGC 0337 - A barred spiral galaxy . . . . .	45
2.3.7.2	UGCA 219 - A blue compact dwarf galaxy . . . . .	46
2.3.7.3	Arp 220 - An ultra-luminous infrared galaxy . . . . .	48
2.4	Discussion and Conclusion . . . . .	48
<b>3</b>	<b>Narrowband H<math>\alpha</math> Imaging with Gemini/GMOS-N</b>	<b>50</b>
3.1	Introduction . . . . .	50
3.2	Observations . . . . .	53
3.2.1	Sample Properties . . . . .	53
3.2.1.1	Optical imaging with Gemini North/GMOS-N . . . . .	54
3.2.2	Comparison Systems . . . . .	54
3.2.2.1	The Magellanic Clouds . . . . .	54
3.2.2.2	Previous work on diffuse H $\alpha$ emission fraction . . . . .	55
3.2.2.3	Previous work on galaxy-wide star formation properties . . . . .	55
3.3	Results . . . . .	56
3.3.1	Star Formation Rates . . . . .	57
3.3.2	H $\alpha$ Region Ratios . . . . .	60
3.3.3	Number of HIIPhot-Identified Regions . . . . .	66
3.3.4	Brightest Region Luminosity . . . . .	68
3.4	Discussion and Conclusion . . . . .	72
<b>4</b>	<b>The Discovery of Compact Groups of Dwarf Galaxies</b>	<b>74</b>
4.1	Introduction . . . . .	74
4.2	Methods . . . . .	76
4.2.1	Group Candidate Selection . . . . .	76
4.2.2	Follow-up observations . . . . .	77
4.2.2.1	Optical imaging with the Maryland-Magellan Tunable Filter . . . . .	77
4.2.2.2	Optical imaging with the Gemini Multi-Object Spectrograph . . . . .	78
4.2.2.3	Optical spectroscopy with the Apache Point Dual Imaging Spectrograph . . . . .	78
4.3	Results . . . . .	79
4.3.1	Redshifts and boundedness . . . . .	79
4.3.2	Narrowband imaging and star formation morphology . . . . .	81
4.4	Discussion . . . . .	82
4.4.1	Possible projection effects and interlopers . . . . .	82
4.4.2	Comparison to other associations of low mass galaxies . . . . .	83
4.4.3	Statistical comparison to theoretical predictions . . . . .	85
4.4.4	Qualitative comparison to massive galaxy groups . . . . .	86
4.5	Conclusion . . . . .	86
<b>5</b>	<b>Summary and Conclusion</b>	<b>88</b>
<b>A</b>	<b>TNT Low-<math>z</math> Sample Properties and Photometry</b>	<b>91</b>

---

<b>B</b>	<b><i>Spitzer</i> Infrared Imaging of Isolated TNT Dwarf Galaxies</b>	<b>117</b>
B.1	Motivation . . . . .	117
B.2	Progress and Future Plans . . . . .	120
<b>C</b>	<b>Dark Skies, Bright Kids! and the Value of Repeated Interactions with Elementary School Students</b>	<b>123</b>
	<b>Bibliography</b>	<b>127</b>

# List of Figures

1.1	The ‘Great Andromeda Nebula’ as observed by Isaac Roberts in 1899. Public domain photo of from A Selection of Photographs of Stars, Star-clusters and Nebulae, Volume II, The Universal Press, London, 1899. . . . .	2
1.2	From Shapley (1919), the observed distribution of globular clusters relative to the plane of the Milky Way. The distance units are 100 pc. The Sun’s position is shown as an <i>X</i> at the origin. . . . .	3
1.3	From left to right: representative examples of the morphologies of an elliptical galaxy, a lenticular galaxy, a spiral galaxy, and an irregular galaxy.	4
1.4	As described in Hubble (1926), the original galaxy classification ‘tuning fork’ diagram. Elliptical galaxies appear on the left, spirals on the right (split in to barred and unbarred), and lenticular (S0) in the center. Note that this schematic does not include irregular or peculiar galaxies, as they were not considered to be part of the sequence. . . . .	5
1.5	A <i>conceptual</i> view of the future Milky Way-Andromeda merger as seen from the point of view of an observer on Earth. <b>a</b> : Present day spirals. Andromeda is the bright extended feature to the top left of the Milky Way Band. <b>b+c</b> : The distance between galaxies decreasing, increasing the angular size of Andromeda. <b>d+e+f</b> : Gas and dust is funneled to center, burst of star formation begins, and the central AGN is fueled. <b>g</b> : The remaining gas used up or expelled and star formation decreases, eventually stopping. <b>h</b> : The end state of the system is a red elliptical galaxy. Image adapted from NASA; ESA; Z. Levay and R. van der Marel, STScI; T. Hallas, and A. Mellinger [Public domain], via Wikimedia Commons. . . . .	7
1.6	The luminosity function (number of galaxies per unit luminosity/stellar mass) of galaxies at a variety of redshifts, broken down by galaxy type (elliptical – red; spiral – blue; irregular – green). The redshift increases from left to right and top to bottom. In each panel, the low luminosity (low mass) galaxies dominate in number. The relative number of these dwarf galaxies increases with redshift. Figure adapted from Ramos et al. (2011). . . . .	9

1.7	<b>Left:</b> A 3-dimensional schematic of the Local Group of galaxies. Black ellipses indicate the location of massive spiral galaxies (the Milky Way, Andromeda, and M33. Red and orange ellipses mark the location of quenched dwarf galaxies. Blue and green ellipses represent star forming dwarf galaxies. The distribution of dwarf galaxies is such that the star forming galaxies tend to be located far from the massive spirals, while those dwarfs that are close to these galaxies have stopped forming stars. From Grebel et al. (1999). <b>Right:</b> The fraction of quenched galaxies as a function of distance from their nearest massive neighbor. The different color bins represent different galaxy stellar masses, decreasing from red to blue. Beyond a distance of 1.5 Mpc from a massive galaxy there are no quenched low mass ( $M_* < 10^9 M_\odot$ ) galaxies. From Geha et al. (2012). . . . .	10
1.8	Wide-field image of the Large and Small Magellanic Clouds from Besla et al. (2016). The black and white background image was taken with an extremely broad Baader Luminance filter designed to detect incredibly faint structures. A deep optical image of the Magellanic Clouds is shown against the Luminance data for reference. . . . .	11
1.9	The observed metallicity of galaxies as a function of their stellar mass. Metallicity increases with increasing stellar mass over several orders of magnitude in mass. Figure from Kirby et al. (2013). . . . .	12
1.10	The ratio of gas mass to total baryonic mass in a galaxy as a function of the galaxy's stellar mass. The gas fraction increases with decreasing stellar mass. Figure from Geha et al. (2006). . . . .	13
1.11	The star formation efficiency of a dwarf galaxy (black), a Milky Way-like galaxy (green), and an elliptical galaxy (orange) as a function of redshift or lookback time. Figure from Madau et al. (2014). . . . .	14
1.12	Visualization of the two isolation criteria ( $d_{\text{host}}$ and $\Theta$ ) applied to the TiNy Titans dwarf galaxies. Square points are considered isolated based on distance from a massive host and circles are nonisolated in $d_{\text{host}}$ scheme. The tidal index parameter, plotted on the x-axis, gives red points as isolated, green as marginally isolated, and blue as nonisolated. Dashed lines show the boundaries between the isolation category for each definition. . . . .	19
1.13	A schematic of the sources of electromagnetic emission during the star formation process. . . . .	20
1.14	The star formation rate enhancement for the isolated (top) and nonisolated (bottom) TNT interacting dwarf galaxies as a function of projected radial separation. The bottom portion of each panel shows the star formation rates for paired (blue) and unpaired (red) dwarf galaxies, the ratios of which is used used to calculate the enhancements for the dwarf pairs in the top panel (blue). A similar analysis of the star formation rate enhancement in massive galaxies is shown for comparison in black. Note: The $d_{\text{host}}$ isolation criteria was used to classify the TNT galaxies for this figure. Figures from Stierwalt et al. (2015). . . . .	22

1.15	A view of the SDSS fiber placement and size on a subset of four TNT galaxy pairs at various stages of interaction. The fibers are placed at the center of each galaxy or on an individually bright star forming region and do not encompass all of the emission. Figure modified from Stierwalt et al. (2015). . . . .	24
2.1	The TNT dwarf pair dm1357+54 shown in each wavelength used in this SED analysis. Dashed red circles in each frame indicate the individual galaxies in the pair. . . . .	27
2.2	Example of the resolution of SDSS optical image of a TNT pair (left) vs. WISE infrared image of the same pair (right). The blue arrows are pointing to the dwarf galaxies in both panels, and the red arrow to a nearby star. The WISE infrared emission of this star overlaps the southern galaxy in the pair, thus contaminating the measured flux in these bands. . . . .	29
2.3	Histograms for pair properties: $r_{\text{sep}}$ , $v_{\text{sep}}$ , mass ratio, and tidal index. Bins are colored to correspond to the grouped SEDs below. . . . .	31
2.4	Histograms for galaxy properties: metallicity and star formation rate. Bins are colored to correspond to the grouped SEDs below. . . . .	31
2.5	Left: The SED for each TNT galaxy separated by projected pair separation (red - close pairs; green - moderately separated pairs; blue - far pairs). The bottom panel is a combination of the top three panels for the sake of direct comparison. Right: Same as left, normalized to the SDSS $z$ -band measurement for each galaxy as a proxy for stellar mass. . . . .	32
2.6	Same as bottom right panel of Figure 2.5 with all points in a single frame and the mean of each radial separation bin overplotted as a square. . . . .	33
2.7	Left: The SED for each TNT galaxy separated by projected velocity separation (red - slow relative motion; green - moderate relative motion; blue - fast relative motion). The bottom panel is a combination of top three panels for the sake of direct comparison. Right: Same as left, normalized to the SDSS $z$ -band measurement for each galaxy as a proxy for stellar mass. . . . .	34
2.8	Same as bottom right panel of Figure 2.7 with all points in a single frame and the mean of each velocity separation bin overplotted as a square. . . . .	35
2.9	Left: The SED for each TNT galaxy separated by mass ratio (red - major ‘merger’; green - moderate ‘merger’; blue - minor ‘merger’). The bottom panel is a combination of top three panels for the sake of direct comparison. Right: Same as left, normalized to the SDSS $z$ -band measurement for each galaxy as a proxy for stellar mass. . . . .	36
2.10	Same as bottom right panel of Figure 2.9 with all points in a single frame and the mean of each mass ratio bin overplotted as squares. . . . .	37
2.11	Left: The SED for each TNT galaxy separated by metallicity (red - low metallicity pairs; green - moderate metallicity pairs; blue - high metallicity pairs). The bottom panel is a combination of top three panels for the sake of direct comparison. Right: Same as left, normalized to the SDSS $z$ -band measurement for each galaxy as a proxy for stellar mass. . . . .	38
2.12	Same as bottom right panel of Figure 2.11 with all points in a single frame and the mean of each metallicity bin overplotted as a square. . . . .	39

2.13	Left: The SED for each TNT galaxy separated by star formation rate (red - high SFR; green - moderate SFR; blue - low SFR). The bottom panel is a combination of top three panels for the sake of direct comparison. Right: Same as left, normalized to the SDSS $z$ -band measurement for each galaxy as a proxy for stellar mass. . . . .	41
2.14	Same as bottom right panel of Figure 2.13 with all points in a single frame and the mean of each star formation rate bin overplotted as a square. . . . .	42
2.15	Left: The SED for each TNT galaxy separated by tidal index (red - isolated; green - marginally isolated; blue - nonisolated). The bottom panel is a combination of top three panels for the sake of direct comparison. Right: Same as left, normalized to the SDSS $z$ -band measurement for each galaxy as a proxy for stellar mass. . . . .	43
2.16	Same as bottom right panel of Figure 2.15 with all points in a single frame and the mean of each tidal index bin overplotted as a square. . . . .	44
2.17	The mean of the TNT galaxy SEDs colored by tidal index (isolated in red; marginally isolated in green; non-isolated in blue) and the SEDs of a SBd (open grey triangle), a BCD (open grey square) and a ULIRG (open grey diamond). The dashed lines are only meant to help connect the data points of each comparison object and should not be interpreted as a fit to the SEDs. . . . .	45
2.18	SDSS ugriz image of NGC 0337, a star-forming barred spiral galaxy, for comparison to TNT galaxies in Appendix A. NGC 0337 is approximately 15 kpc in diameter. . . . .	46
2.19	SDSS ugriz image of UGCA 219, a blue compact dwarf galaxy, for comparison to TNT galaxies in Appendix A. UGCA 219 is approximately 9 kpc in diameter. . . . .	47
2.20	SDSS ugriz image of Arp 220, an ultraluminous infrared galaxy, for comparison to TNT galaxies in Appendix A. Arp 220 is approximately 40 kpc in diameter. . . . .	47
3.1	Three color images of the TNT Gemini sample. Continuum-subtracted $H\alpha$ in red, $H\alpha$ + continuum in green, r-band in blue. . . . .	56
3.2	SDSS optical spectra for dm1219+06a and dm1219+06b, demonstrating the noise levels. . . . .	59
3.3	Star formation rate comparison for (a) isolated (red), (b) marginally isolated (green), (c) non-isolated (blue), and (d) all dwarf galaxy pairs (for ease of direct comparison) colored by the tidal index with each dwarf's nearest massive neighbor. <b>Left:</b> Gemini SFRs compared to the SFR measured from the SDSS fiber-based spectra. <b>Right:</b> Gemini SFRs compared to the total SFR extrapolated from the SDSS fiber-based spectra. . . . .	61

3.4	Star formation rate comparison for (a) isolated (light red), (b) marginally isolated (light green), (c) non-isolated (light blue), and (d) all dwarf galaxy pairs (for ease of direct comparison) colored by the tidal index with each dwarf's pair member. As expected, none of the TNT dwarf galaxies in this subsample are isolated from the galaxy it is paired with. <b>Left:</b> Gemini SFRs compared to the SFR measured from the SDSS fiber-based spectra. <b>Right:</b> Gemini SFRs compared to the total SFR extrapolated from the SDSS fiber-based spectra. . . . .	62
3.5	The star formation rate of each galaxy as a function of stellar mass colored by the massive host tidal index (red - isolated galaxies; green - marginally isolated galaxies; blue - nonisolated galaxies). The LMC (which includes the 30Dor star forming region) is shown as a diamond and the galaxies from the Zaragoza-Cardiel et al. (2018) interacting sample are shown as dark grey squares. The light grey line is the star forming main sequence as defined in Zaragoza-Cardiel et al. (2018). . . . .	63
3.6	The star formation rate of each galaxy as a function of stellar mass colored by the dwarf pair tidal index (light red - isolated galaxies; light green - marginally isolated galaxies; light blue - nonisolated galaxies). The LMC (which includes the 30Dor star forming region) is shown as a diamond and the galaxies from the Zaragoza-Cardiel et al. (2018) interacting sample are shown as dark grey squares. The light grey line is the star forming main sequence as defined in Zaragoza-Cardiel et al. (2018). . . . .	64
3.7	Ratio of the $H\alpha$ luminosity in discrete regions to the total $H\alpha$ luminosity of each galaxy as a function of tidal index. Vertical lines mark the boundaries between isolated, marginally isolated, and nonisolated galaxies. <b>Left:</b> Ratio as a function massive host tidal index colored by dwarf pair tidal index. The fraction of light in regions increases with increasing isolation. <b>Right:</b> Ratio as a function of dwarf pair tidal index colored by massive host tidal index. There is no strong trend of the $H\alpha$ region ratio with $\Theta_D$ . Further, there does not appear to be a clear correlation among $\Theta_H$ , $\Theta_D$ , and the ratio. . . . .	65
3.8	$H\alpha$ region ratio as a function of galaxy stellar mass colored by tidal index with respect to the nearest massive galaxy (left) and dwarf companion (right). In both panels, red points are isolated, green are marginally isolated, and blue are non-isolated from the relevant companion. . . . .	65
3.9	$H\alpha$ region ratio as a function of total galaxy star formation rate colored by tidal index with respect to the nearest massive galaxy (left) and dwarf companion (right). In both panels, red points are isolated, green are marginally isolated, and blue are non-isolated from the relevant companion. Grey triangles show the ratios and star formation rates from Oey et al. (2007). . . . .	66

- 3.10 The number of regions identified by HIIphot in each TNT dwarf galaxy as a function of tidal index. The dashed vertical lines show the separation between the isolation classifications as defined by the tidal index parameter. **Left:** Number as a function massive host tidal index colored by dwarf pair tidal index. Though there is scatter, the number of regions tends to increase with increasing isolation. **Right:** Number as a function of dwarf pair tidal index colored by massive host tidal index. With the exception of one galaxy, there is a noticeable separation between dwarfs that are marginally isolated from their dwarf companion and those that are not isolated; the nonisolated galaxies have, on average, more discrete star-forming regions. . . . . 67
- 3.11 The number of H $\alpha$  regions identified by HIIphot in each TNT dwarf galaxy as a function of galaxy stellar mass, colored by tidal index with respect to the nearest massive galaxy (left) and dwarf companion (right). In both panels, red points are isolated, green are marginally isolated, and blue are non-isolated from the relevant companion. The Zaragoza-Cardiel et al. (2018) sample for 1 kpc regions (dark grey squares) and 2.5 kpc regions (light grey diamonds) is plotted for comparison. The number of regions across both the TNT and Zaragoza-Cardiel et al. (2018) samples are scattered between zero and 30, with outliers in each. For the Zaragoza-Cardiel et al. (2018) sample, the outliers are in the number of 1 kpc region. For the TNT sample, the outliers are primarily isolated from a massive galaxy and not isolated from their dwarf companion. . . . . 68
- 3.12 The number of H $\alpha$  regions identified by HIIphot in each TNT dwarf galaxy as a function of global galaxy star formation rate, colored by tidal index with respect to the nearest massive galaxy (left) and dwarf companion (right). In both panels, red points are isolated, green are marginally isolated, and blue are non-isolated from the relevant companion. The Zaragoza-Cardiel et al. (2018) sample for 1 kpc regions (dark grey squares) and 2.5 kpc regions (light grey diamonds) is plotted for comparison. We see a slight correlation between the number of regions and increasing star formation rate. . . . . 69
- 3.13 The luminosity of the brightest region identified by HIIphot in each TNT dwarf galaxy as a function of tidal index. The LMC (which includes the 30Dor star forming region) is shown as a diamond. The dashed vertical lines show the separation between the isolation classifications as defined by the tidal index parameter. **Left:** Luminosity as a function of massive host tidal index. The luminosity of the brightest region tends to increase with increasing isolation from a massive galaxy. **Right:** Luminosity as a function of dwarf pair tidal index. There is no strong correlation between region luminosity and dwarf pair tidal index. . . . . 69

3.14	The luminosity of the brightest region in each galaxy identified by HI-Iphot in each TNT dwarf galaxy as a function of stellar mass. The LMC (which includes the 30Dor star forming region) is shown as a diamond. The Zaragoza-Cardiel et al. (2018) sample for 1 kpc regions (dark grey squares) and 2.5 kpc regions (light grey diamonds) is plotted for comparison. <b>Left:</b> Luminosity as a function of galaxy stellar mass colored by massive host tidal index. <b>Right:</b> Luminosity as a function of galaxy stellar mass colored by dwarf pair tidal index. The luminosity of the brightest region increases with increasing stellar mass. . . . .	70
3.15	The luminosity of the brightest region in each galaxy as a function of star formation rate. The LMC (which includes the 30Dor star forming region) is shown as a diamond. Zaragoza-Cardiel et al. (2018) comparison sample for 1kpc regions (dark grey squares) and 2.5kpc regions (light grey diamonds). <b>Left:</b> Luminosity as a function of star formation rate colored by massive host tidal index. <b>Right:</b> Luminosity as a function of star formation rate colored by dwarf pair tidal index. . . . .	71
3.16	The luminosity of the brightest region in each galaxy as a function of specific star formation rate. The LMC (which includes the 30Dor star forming region) is shown as a diamond. Zaragoza-Cardiel et al. (2018) comparison sample for 1kpc regions (dark grey squares) and 2.5kpc regions (light grey diamonds). <b>Left:</b> Luminosity as a function of specific star formation rate colored by massive host tidal index. <b>Right:</b> Luminosity as a function of specific star formation rate colored by dwarf pair tidal index. . . . .	72
4.1	SDSS stamps of the seven TNT low-mass group candidates. Blue arrows indicate the location of the SDSS-identified TNT pair members. Red arrows indicate the candidate group members. . . . .	76
4.2	<b>a:</b> Projected radial separation from the centroid of the group versus difference in group member line-of-sight velocity from the group mean. The groups are filled stars (dm1049+09); filled circles (dm1623+15); open circles (dm1403+41); filled triangles (dm1440+14); open triangles (dm1718+30); filled squares (dm0909+06); and open squares (dm1349-02). <b>b:</b> One-dimensional velocity dispersions and 2D projected sizes for the TNT dwarf groups presented here (red circles) and dwarf associations from the literature (orange squares and yellow star). Groups $<1.5$ Mpc from a massive ( $M \simeq 10^{10} M_{\odot}$ ) host are marked with crosses. In both panels, uncertainties are smaller than symbol sizes (see Table 1 for uncertainties in individual TNT velocity measurements). . . . .	83
4.3	Three color RGB images of four of the dwarf groups obtained with the MarylandMagellan Tunable Filter (MMTF) Fabry Perot and with the Gemini Multi-Object Spectrograph (bottom right). Red corresponds to H $\alpha$ emission, green corresponds to MMTF or Gemini r-band, and blue corresponds to SDSS g-band. Velocities derived from optical spectroscopy are noted for each group member in white. . . . .	84
A.1	Isolated galaxy SDSS images. . . . .	92
A.2	Isolated galaxy SDSS images. . . . .	93

---

A.3	Isolated galaxy SDSS images. . . . .	94
A.4	Isolated galaxy SDSS images. . . . .	95
A.5	Marginally isolated galaxy SDSS images. . . . .	96
A.6	Nonisolated galaxy SDSS images. . . . .	97
B.1	Example of the resolution of SDSS optical image of a TNT pair (left) vs. WISE infrared image of the same pair (right). The blue arrows are pointing to the dwarf galaxies in both panels, and the red arrow to a nearby star. The WISE infrared emission of this star overlaps the southern galaxy in the pair, thus contaminating the measured flux in these bands. . . . .	119
B.2	TNT infrared colors in context: Modified figure from Smith and Hancock (2009) showing the metallicity of a sample of dwarf galaxies as a function of infrared color with the TNT interacting dwarf galaxies shown as solid black circles. The green hatched region indicates the range of expected colors if all IR emission was due to contributions from unextincted starlight. The TNT dwarfs occupy a similar color space that Smith & Hancock (2009) observe the interacting dwarfs in their sample and span a larger range of metallicities. . . . .	121
B.3	TNT infrared colors dependence on pair properties. The filled green region indicates the range of expected colors if all IR emission was due to contributions from unextincted starlight. Top left: IR color as a function of projected pair separation. Top right: IR color as a function of projected velocity separation. Bottom left: IR color as a function of mass ratio. Bottom right: IR color as a function of pair redshift. . . . .	122

# List of Tables

1.1	TiNy Titans Low-z Sample Properties . . . . .	17
1.2	TiNy Titans Low-z Sample Isolation Bin Counts . . . . .	18
2.1	Galex UV Filter Characteristics . . . . .	27
2.2	SDSS <i>ugriz</i> Filter Characteristics . . . . .	28
2.3	Wise Infrared Filter Characteristics . . . . .	29
2.4	TNT Target Binning Summary . . . . .	30
2.5	Comparison Object Details . . . . .	44
3.1	Observing Target Details . . . . .	53
3.2	Measured Properties of TNT Gemini Sample . . . . .	58
4.1	TNT isolated dwarf group candidate members . . . . .	81
4.2	TNT isolated dwarf group candidate properties . . . . .	82
A.1	TNT Pair Properties . . . . .	98
A.2	TNT Galaxy Properties . . . . .	101
A.3	TNT Galaxy Photometry . . . . .	107

*“You’re braver than you believe, and stronger than you seem, and smarter than you think.” – Christopher Robin*

# Acknowledgements

The acknowledgements section of my doctoral dissertation in astronomy is not something I ever thought I would be writing. I have many people to thank for helping me get here because I couldn't have done this alone.

First and foremost, thank you to my family for putting up with me for the last six years, which must have felt like the reemergence of my moody teenage phase. Grandma, thanks for being the best cheerleader anyone could ever ask for. Thank you dad for inspiring my love for science and for making sure I kept going, especially when I *really* didn't want to. Thanks mom for watching Brian Greene documentaries and for sending me every STEM article you could find. Thank you Becca for always reminding me how nerdy I am, and for going through this whole 'graduate degree defense' thing first so that I could learn from you. Jenn, Dan, Aric, and Natasha – thank you for the good advice and fun distractions.

To my mentors and friends in Florida, and at Swarthmore and Penn State: Thank you for helping me to build both the academic and emotional foundation I needed to succeed in graduate school.

To my thesis advisor, Kelsey Johnson: Thank you for all of your encouragement, for advising me beyond academics, and for showing me the importance of respect and balance.

To the other members of my thesis committee – Nitya, Aaron, and Claire: Thank you for your guidance and for supporting my passion for education and outreach.

To all of the other 'grown-ups' in the UVa Department of Astronomy – Sabrina, Mike, Steve, Whitney, Danielle, Janice, Ed, David, Ricky, Jackie: You have all helped me in a million different ways, and I can't thank you enough!

To Lisa May, Kim, Lauren, and Allison: Thank you for knowing that I could do it when I was certain I couldn't. You are my sisters in every way but genetics.

To Andrew, Brian, Matt, Chris, Thankful, Rachael, Kristen, Allison, Dylan, Trey, Sean, Robby, Jake (both redbear and blackbear), Loreto, and the other graduate students who I'm sure I forgot to name: Thank you all for supporting me through both academic and personal troubles, and for celebrating successes in both (and for rescuing me when I got locked out while dog sitting...).

To DSBK: Thank you for reminding me that science is fun!

To the rest of my Cville community – Cathy, Claire, Denise, Lili, Jeanette, Sandra, and Emily: Thank you for building my confidence, expanding my horizons, and keeping me grounded.

Finally, I would like to thank all of my astrodogs (and their families) for keeping me somewhat sane: Freckles the Wonderdog, Aiden, Bailey, Bear, Bo, Bubba, Carmella, Chewie, Cooper, Dobby, Dougie, Ducky, Easton, Emrys, Ezreal, Fira, Ginny, Hannah, Ivy, JD, Laika, Lilly, Loken, Lyra, Max, Maya/Noodle, Nicole, Nora, Roux (both of them!), Sadie, Samson, Sirius, Soren, and Storm.

# Chapter 1

## Introduction

### 1.1 Overview of Galaxies

#### 1.1.1 “The Great Debate” and Our Place in the Universe

Some of the most important unanswered questions in astronomy center around cosmic origins – the formation and subsequent evolution of the components of our universe. Modern day astronomers estimate that the universe is 13.7 billion years old and 93 billion light-years in diameter (the size of the observable Universe). These numbers are difficult for most people to comprehend as they are far beyond the realm of everyday human experience. In fact, astronomical scales were at the center of a paradigm-shifting controversy in the early- and mid-1900s. By that time, our view of the Universe had shifted from believing that the Earth was at the center of everything to understanding that the Earth orbits around the Sun, which is one of many stars in the Milky Way. The next step was to determine the Milky Way’s place in the universe. On one side were the scientists who argued that our Milky Way galaxy was the extent of the entire universe; every other astronomical object was contained within it. Others proposed that the Milky Way was one of many ‘island universes,’ a term coined by German philosopher Emanuel Kant in the 1800s ([Kant & L. Jaki, 1981](#)). From this perspective, the nebulae that astronomers observed (faint, diffuse objects that could be resolved into individual stars; see [Figure 1.1](#)) were not small and nearby, but far away and similar in size to the Milky Way (our island universe).



Figure 1.1 The ‘Great Andromeda Nebula’ as observed by Isaac Roberts in 1899. Public domain photo of from *A Selection of Photographs of Stars, Star-clusters and Nebulae*, Volume II, The Universal Press, London, 1899.

While this debate lasted decades, the “Great Debate” between Harlow Shapley and Herber Curtis in 1920 is often cited as a defining and representative moment in the narrative. Shapley believed that the Milky Way was all-encompassing. He used Cepheid variable stars (stars that vary in brightness with a period proportional to their intrinsic brightness) as standard candles to measure the distances to 69 globular clusters and mapped their distribution relative to the Sun (Figure 1.2; [Shapley \(1919\)](#)). From these observations, he determined that the Galaxy was approximately 100 kpc ( $3 \times 10^{18}$  km) in diameter with the Sun offset from the center by almost 20 kpc. His measurement of the Galaxy’s size was an order of magnitude larger than previously thought (10 kpc; [Kapteyn & van Rhijn \(1920\)](#)). He therefore argued that, were the nebulae in question truly island universes, they would have to be located at unimaginably great distances from the Milky Way. Thus, they must be contained within our Galaxy’s boundaries.

On the other side of the debate, Curtis argued in favor of the island universe theory. His research, based on star counts and distances determined via stellar spectral types, indicated that the Milky Way’s size was consistent with Kapteyn’s measurements of 10 kpc in diameter ([Kapteyn & van Rhijn, 1920](#)). Further, he argued that observations

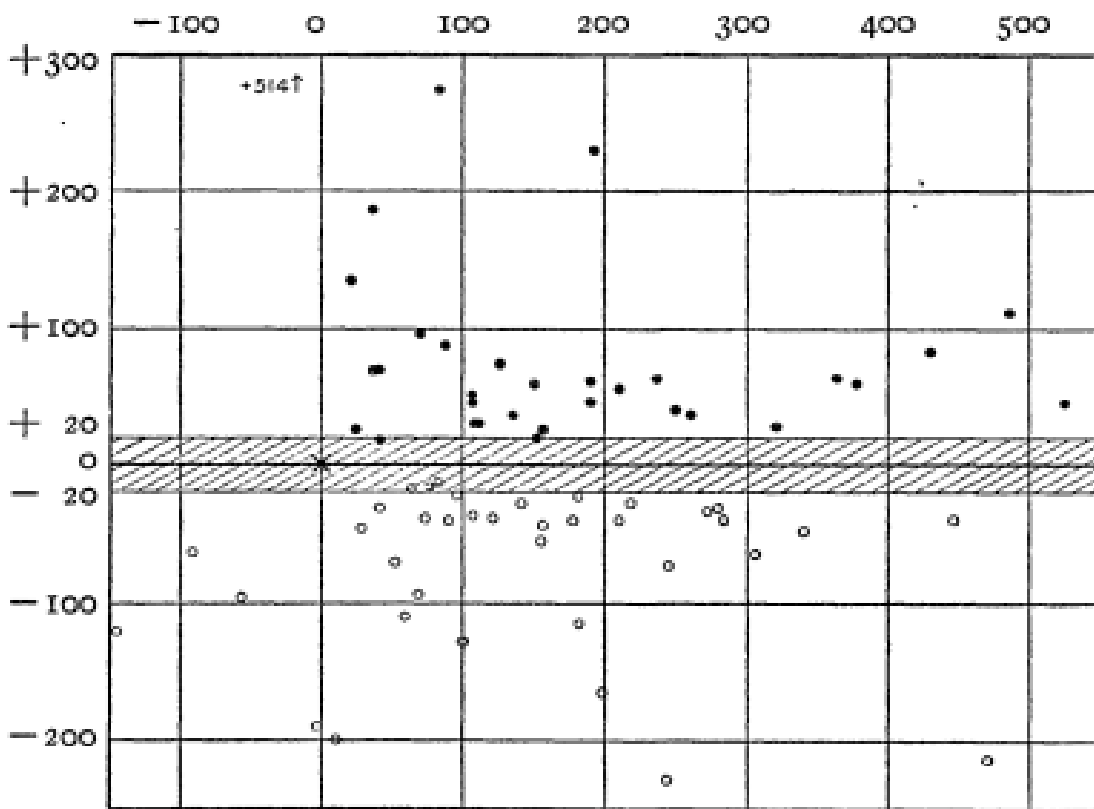


Figure 1.2 From [Shapley \(1919\)](#), the observed distribution of globular clusters relative to the plane of the Milky Way. The distance units are 100 pc. The Sun's position is shown as an X at the origin.

of transient novae events (stellar explosions) in the nebulae were evidence of their location beyond the Galaxy. These novae were intrinsically similar to those observed in the Milky Way except that they appeared significantly dimmer than local observations. Curtis interpreted this to mean that the nebulae must be far away, beyond the 10 kpc extent of the Milky Way.

Based on what we know today, neither Shapley nor Curtis was fully accurate in his model of the Universe. While Shapley was correct in saying that the Milky Way was much larger than previously thought, Curtis correctly identified the nebulae as extragalactic sources. Two primary scientific advances made resolving the debate possible. In the 1930s, astronomers were beginning to understand the role that interstellar dust plays in observational astronomy. While it had previously been treated as unimportant, it was becoming clear that this dust actually blocks some of the light of astronomical objects before we can observe it on Earth ([Trumpler, 1930](#)). The effect is especially prevalent when observing in the dusty plane of the Galaxy, and the light from distant stars and clusters has been completely absorbed by dust. Astronomers recognized that this meant they had



Figure 1.3 From left to right: representative examples of the morphologies of an elliptical galaxy, a lenticular galaxy, a spiral galaxy, and an irregular galaxy.

been underestimating the size of the Milky Way, as they had assumed there were no objects beyond what could be observed. Telescopes, the tools of observational astronomers, were also improving. In 1924, Edwin Hubble used Mount Wilson Observatory's new and powerful 100-inch Hooker Telescope to resolve individual stars in our neighboring galaxy, Andromeda. By observing specific variable stars in this system, he determined that the distance between Andromeda and the Milky Way was 275 kpc ( $\sim 90,000$  light years), putting it outside of the bounds of even the larger Milky Way (Hubble, 1925). The resolution of the decades-long debate was that the Milky Way is only one of many spiral galaxies, and spiral galaxies are just one of the many types of galaxies in the Universe. This realization revealed the true diversity of galaxies across cosmic time.

### 1.1.2 Galaxy Classification

Hubble (1926) classified galaxies into four primary morphological types: spiral, lenticular, elliptical, and irregular. Spiral galaxies consist of flat disks with a central stellar bulge and a surrounding halo. They are named for their spiral arms, which are located in the plane of the disk. They are further subdivided by the presence or absence of a bar and by how tightly coiled their spiral arms appear. Beyond morphology, spiral galaxies are actively forming stars in their disks, particularly in the arms. These young stars give spiral galaxies a blue color.

Elliptical galaxies, similar in shape to the central bulge in spiral galaxies, appear smooth and featureless. They are typically not star forming, and their older populations of stars give them a red color.

Lenticular galaxies have prominent disks and stellar bulges, but lack the spiral arm structure of spiral galaxies. While similar in structure to spiral galaxies, their properties are more closely related to ellipticals. Like ellipticals, they appear red in color and are not actively star-forming.

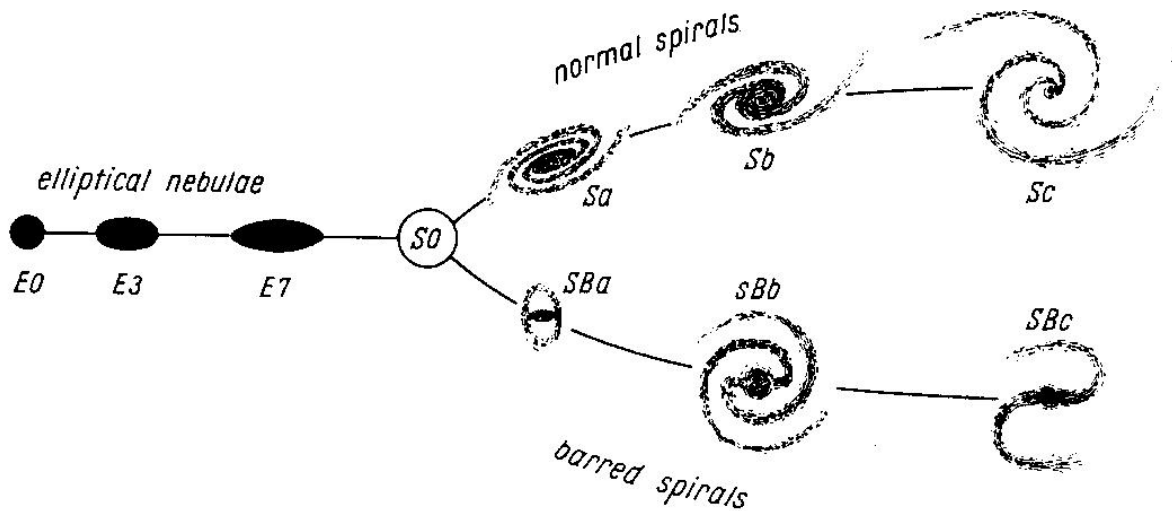


Figure 1.4 As described in [Hubble \(1926\)](#), the original galaxy classification ‘tuning fork’ diagram. Elliptical galaxies appear on the left, spirals on the right (split in to barred and unbarred), and lenticular (S0) in the center. Note that this schematic does not include irregular or peculiar galaxies, as they were not considered to be part of the sequence.

The final category of irregular or peculiar galaxies encompasses those that do not fit in the previous three. These galaxies are asymmetric and do not have a consistent or easily categorized morphology. [Figure 1.3](#) shows an example of each morphological type.

### 1.1.3 Galaxy Evolution via Interactions and Mergers

Though mergers are less common today, they were prevalent in the early universe where the high number density of galaxies led to frequent and prolonged galaxy interactions ([Malhotra et al., 2005](#)). While directly observing these systems is difficult due to their large distances, merging galaxies in the nearby universe can provide an optical local analog of the early universe. With the introduction of the tuning fork classification scheme, astronomers theorized an evolutionary connection among elliptical, lenticular, and spiral galaxies (see [Figure 1.4](#)). It was believed that spirals evolved from elliptical galaxies, developing their disk and spiral arm structure over time. Lenticulars were the proposed intermediate phase of this transition, first theorized to exist by Hubble and then directly observed through a dedicated imaging campaign ([Hubble, 1936](#)).

### 1.1.3.1 Massive Galaxy Interactions

While the sequence described above is no longer considered as a logical path of galaxy evolution, it is likely that there is a connection between spiral galaxies and elliptical galaxies; elliptical galaxies are the end state of a merger between two spiral disk galaxies (concept first introduced in [Toomre \(1977\)](#)).

Interactions among massive galaxies provide an important mode of galaxy evolution that results in a range of observable galaxy properties, including diluted metals, enhanced star formation, bluer colors, and higher Active Galactic Nuclei fractions (AGN, a black hole that is in the process of accreting gas), when compared to non-interacting galaxies (e.g., [Patton et al., 2011](#); [Ellison et al., 2011](#); [Scudder et al., 2012](#)). Like the Moon around the Earth and the Earth around the Sun, two spiral galaxies can orbit around their common center of mass. Over time ( $\sim 10^8$  years), the tidal friction between the two galaxies will dissipate the angular momentum of the system leading the galaxies closer to one another. After several passages between the two galaxies, their morphologies become notably disturbed as the tidal forces alter the disk and spiral arm structure. Star formation is increased due to the interaction ([Patton et al., 2011](#)), and stellar winds from the end stages of the resultant massive stars act as a source of feedback that perpetuates the formation of new stars. As the merger progresses, the dust and cool star forming gas is funneled towards the center of mass of the system ([Moreno et al., 2015](#)). This leads to (1) a concentrated burst of star formation and (2) the growth of a central AGN. As the AGN grows, the radiation it emits heats and expels the remaining gas and dust from the galaxy, essentially stopping most future star formation. The merged system will be spheroidal and red due to the remaining older stellar population; in other words, the end state is an elliptical galaxy.

### The Milky Way - Andromeda Galaxy System as an Example of Interacting Massive Galaxies

Our galaxy, the Milky Way, is in close proximity to another spiral galaxy known as Andromeda, or M31. Andromeda is often referred to as the sister galaxy of the Milky Way, as they are similar in size and structure. Currently located 2.5 million light years away, Andromeda is moving closer to the Milky Way at a rate of 70 miles per second. Over the next 4 billion years, the Milky Way and Andromeda will interact and go through the sequence of events pictured in [Figure 1.5](#) to form an elliptical galaxy to be

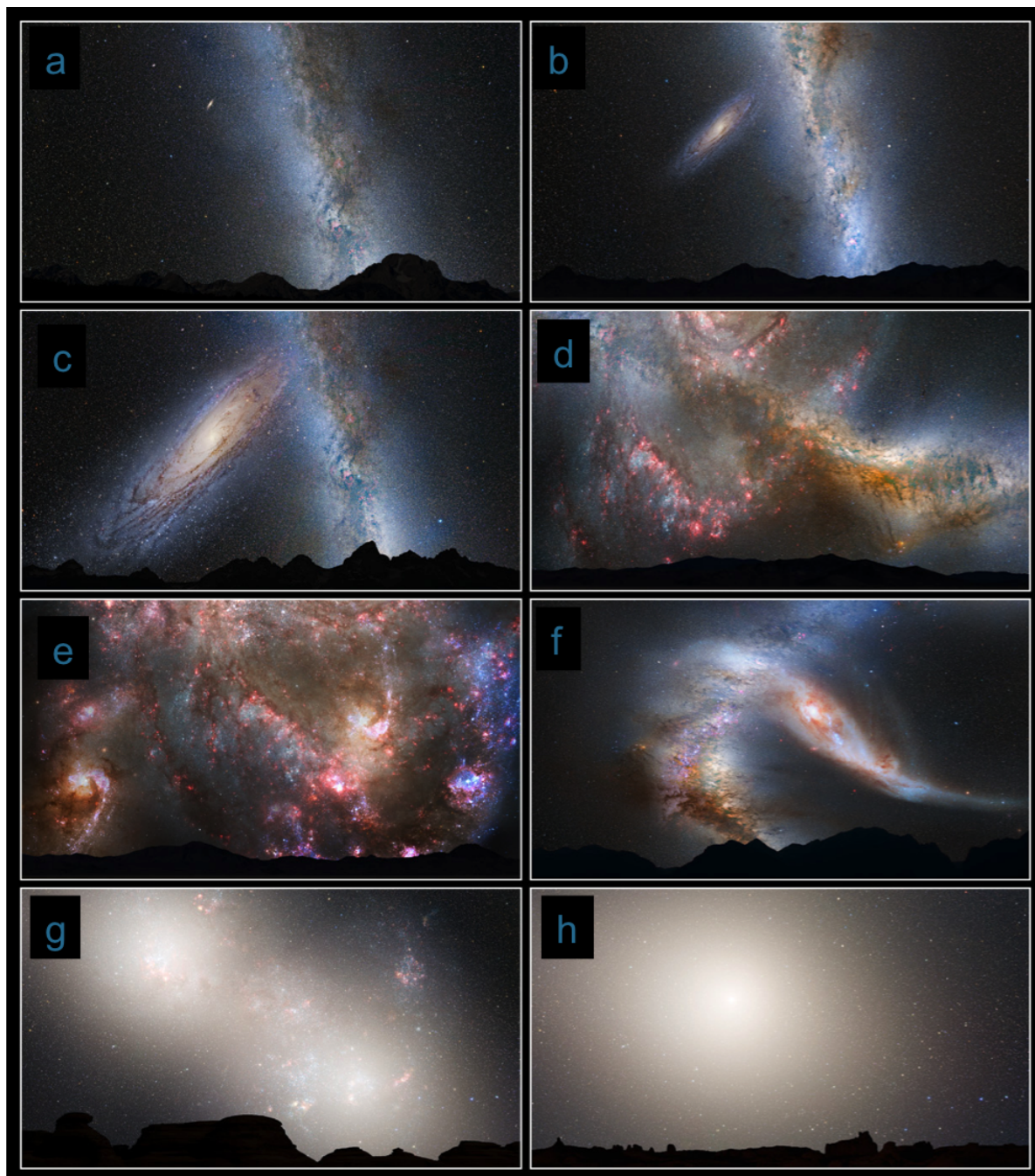


Figure 1.5 A *conceptual* view of the future Milky Way-Andromeda merger as seen from the point of view of an observer on Earth. **a**: Present day spirals. Andromeda is the bright extended feature to the top left of the Milky Way Band. **b+c**: The distance between galaxies decreasing, increasing the angular size of Andromeda. **d+e+f**: Gas and dust is funneled to center, burst of star formation begins, and the central AGN is fueled. **g**: The remaining gas used up or expelled and star formation decreases, eventually stopping. **h**: The end state of the system is a red elliptical galaxy. Image adapted from NASA; ESA; Z. Levay and R. van der Marel, STScI; T. Hallas, and A. Mellinger [Public domain], via Wikimedia Commons.

called Milkmeda or Milkdromeda. Unlike the original dynamic spiral galaxies which are actively turning gas in to stars, the resultant elliptical galaxy will be quenched – it will no longer be forming new stars.

### 1.1.3.2 Low Mass Galaxy Interactions

There may also be an evolutionary connection between low mass galaxies and spiral galaxies. Massive spiral galaxies like our own Milky Way are believed to have formed hierarchically through the merging of smaller irregular dwarf galaxies that are hundreds to thousands to millions of times less massive than the Milky Way or Andromeda. In fact, by number, the majority of galaxies in the universe are believed to be these low mass dwarf galaxies (Ramos et al., 2011). As shown in Figure 1.6, low mass irregular galaxies dominate the galaxy number density at all redshifts<sup>1</sup>. Further, the relative number of these dwarf galaxies increases with increasing redshift. It is therefore believed that low mass irregular systems may have been the dominant, if not only, type of galaxy present in the early Universe.

Today, we observe low mass galaxies in a range of environments: as satellites around massive galaxies, in large galaxy clusters, and in the field. The proximity of a dwarf galaxy to more massive galaxies has a significant impact on their evolution. Specifically, the presence of a high mass galaxy can effectively stop star formation from proceeding in dwarfs.

Looking at the ‘Local Group,’ the group of galaxies containing the Milky Way, Andromeda, M33, and their satellite dwarf galaxies (see Figure 1.7, left panel), we observe star forming dwarf irregulars located on the outskirts of the group, farthest from the massive spiral galaxies. The dwarf spheroidals that are close to the larger galaxies, on the other hand, are quenched and have stopped forming stars.

We also observe this phenomenon in the field (see Figure 1.7, right panel). The distance of 1.5 Mpc from a massive host marks an important boundary between the evolution of satellite dwarf galaxies versus field dwarf galaxies. Beyond 1.5 Mpc, the observed quenched fraction of dwarfs falls to zero (Geha et al., 2012), indicating the end of the sphere of influence of the massive host. Also beyond 1.5 Mpc, the escape velocity of a galaxy with  $M_* \approx 10^{10} M_\odot$  falls below the typical sound speed of  $10 \text{ km s}^{-1}$  in the interstellar medium, thus decreasing the possibility for disruption.

---

<sup>1</sup>Redshifts’ ( $z$ ) are a way to describe the age and/or size of the Universe, with larger values indicating larger distances from the Milky Way and earlier times in the Universe’s history.

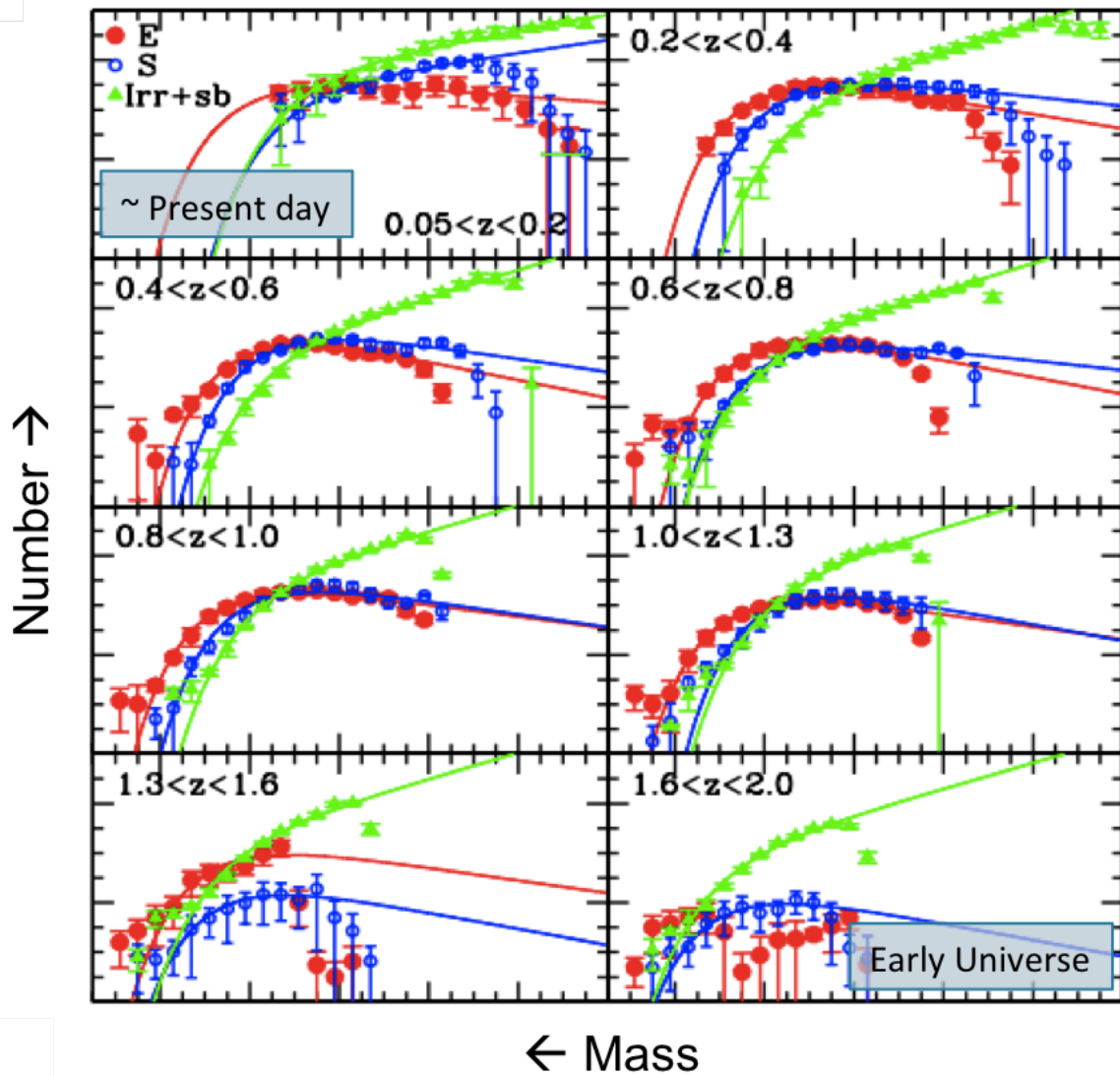


Figure 1.6 The luminosity function (number of galaxies per unit luminosity/stellar mass) of galaxies at a variety of redshifts, broken down by galaxy type (elliptical – red; spiral – blue; irregular – green). The redshift increases from left to right and top to bottom. In each panel, the low luminosity (low mass) galaxies dominate in number. The relative number of these dwarf galaxies increases with redshift. Figure adapted from [Ramos et al. \(2011\)](#).

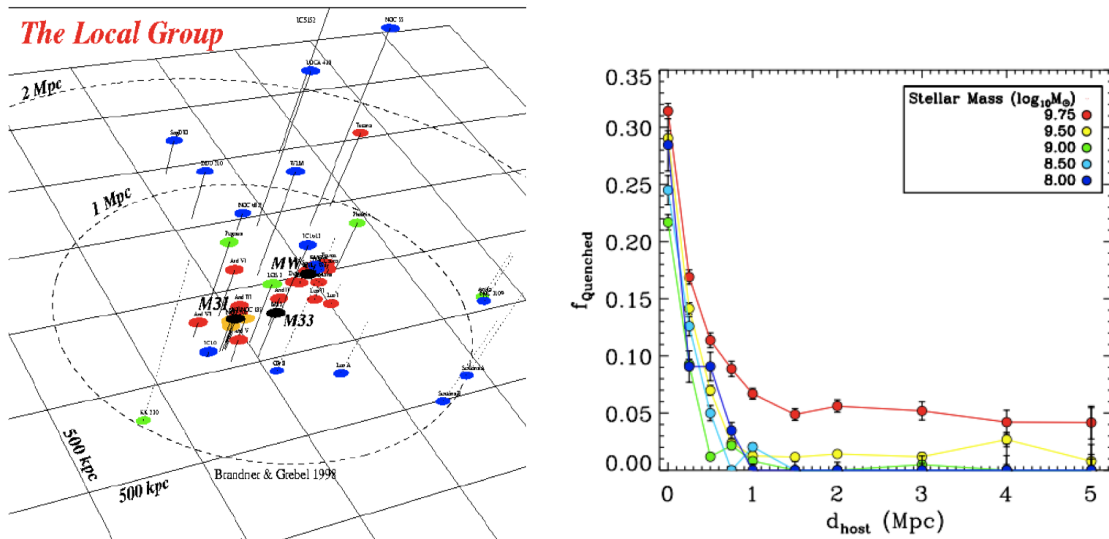


Figure 1.7 **Left:** A 3-dimensional schematic of the Local Group of galaxies. Black ellipses indicate the location of massive spiral galaxies (the Milky Way, Andromeda, and M33. Red and orange ellipses mark the location of quenched dwarf galaxies. Blue and green ellipses represent star forming dwarf galaxies. The distribution of dwarf galaxies is such that the star forming galaxies tend to be located far from the massive spirals, while those dwarfs that are close to these galaxies have stopped forming stars. From Grebel et al. (1999). **Right:** The fraction of quenched galaxies as a function of distance from their nearest massive neighbor. The different color bins represent different galaxy stellar masses, decreasing from red to blue. Beyond a distance of 1.5 Mpc from a massive galaxy there are no quenched low mass ( $M_* < 10^9 M_\odot$ ) galaxies. From Geha et al. (2012).

### The LMC - SMC System as an Example of Interacting Low Mass Galaxies

One area that has been largely unexplored is interactions *between* dwarf galaxies. The role that dwarf galaxy interactions play in a cosmological context remains unsolved because they are incredibly difficult to observe and to simulate. These galaxies are small and faint, requiring access to powerful telescopes that are capable of detecting their diffuse emission and small-scale structures ( $\lesssim 1 - 10$  pc). Similarly, their small mass and size scales require high resolution N-body simulations to study.

The closest local example of interacting dwarf galaxies is the Magellanic Cloud system consisting of the Large Magellanic Cloud (LMC) and the Small Magellanic Cloud (SMC) (see Figure 1.8), a pair of low mass galaxies located in the halo of the Milky Way. At  $5 \times 10^9 M_\odot$ , the LMC is considered to be on the upper end of the mass range for dwarf galaxies. The SMC is less massive at  $\sim 7 \times 10^8 M_\odot$ . Both galaxies exhibit irregular morphologies, though the LMC also has a stellar disk and spiral arms. The two galaxies are connected by both a tidal stream (the Magellanic Stream) and a tidal bridge (the Magellanic Bridge). Taken together, these features suggest that the Magellanic Clouds

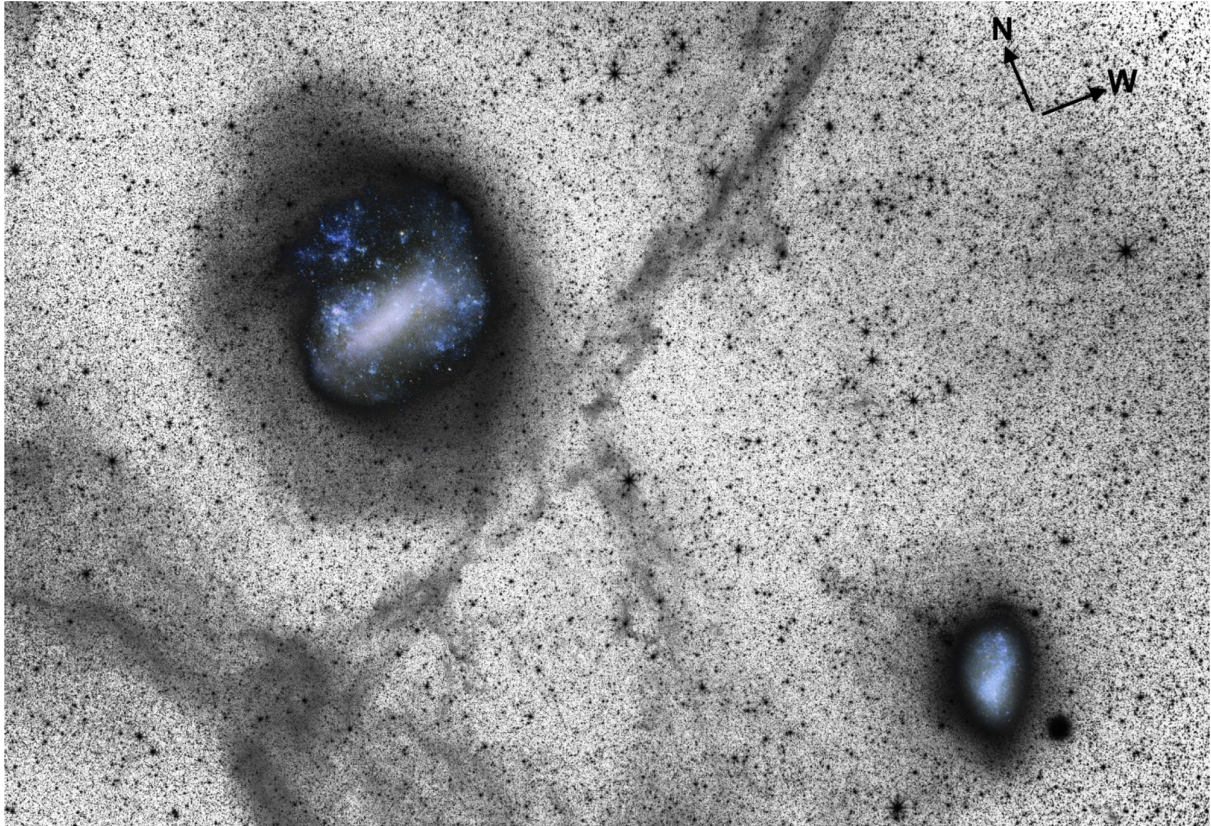


Figure 1.8 Wide-field image of the Large and Small Magellanic Clouds from [Besla et al. \(2016\)](#). The black and white background image was taken with an extremely broad Baader Luminance filter designed to detect incredibly faint structures. A deep optical image of the Magellanic Clouds is shown against the Luminance data for reference.

are bound and gravitationally influenced by one another, and it is believed that this interaction began before the Clouds fell into the Milky Way's halo ([Besla et al., 2012](#)). Furthermore, models and simulations that are able to reproduce the Clouds' observed features require that the LMC and SMC have had repeated tidal interactions, possibly including the SMC directly colliding with the LMC's disk ( $\sim 100$  Myr ago, [Besla et al. \(2012\)](#)).

However, while this is powerful as a nearby example of interacting dwarfs, its location in the halo of the Milky Way makes it completely nonisolated. Given that environment has been shown to strongly effect the evolution of dwarf galaxies, the LMC/SMC system is therefore an imperfect laboratory in which to observe the effects that low mass galaxies have on one another in the absence of a massive companion (as is likely the case at high redshift).

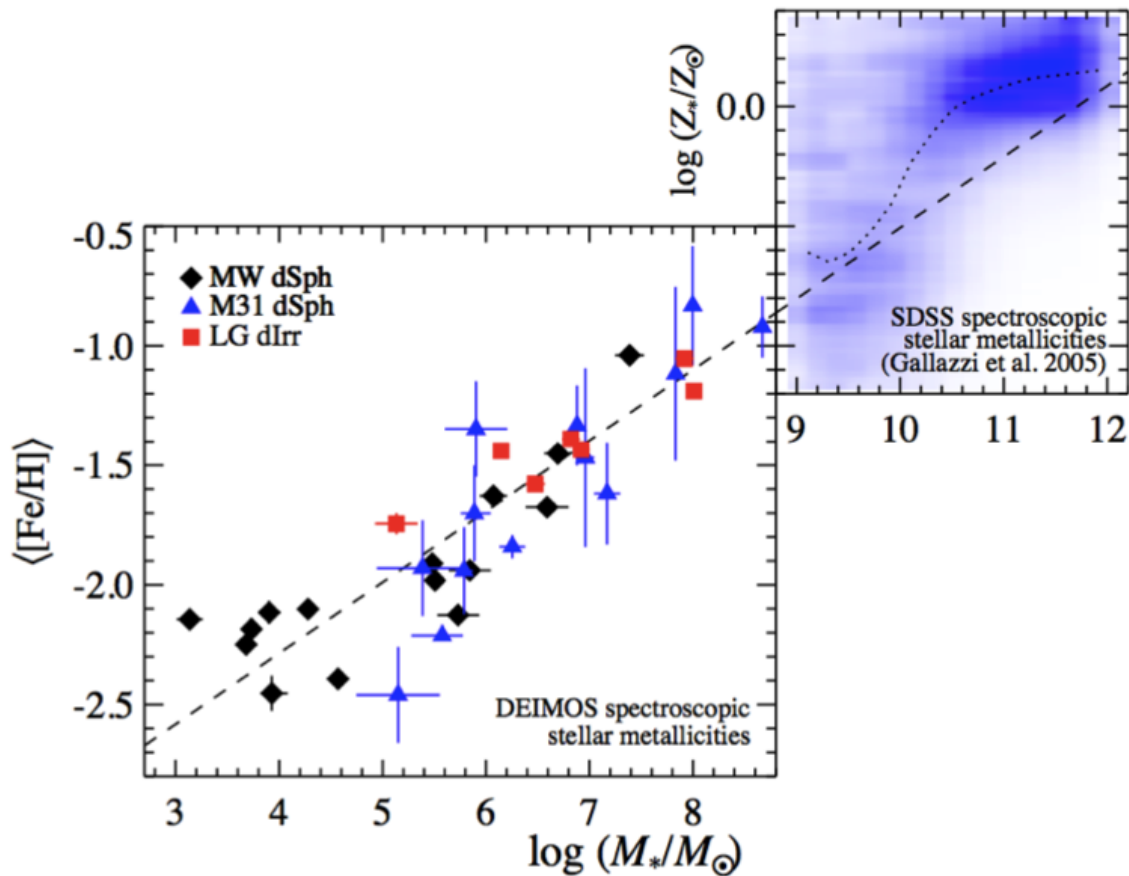


Figure 1.9 The observed metallicity of galaxies as a function of their stellar mass. Metallicity increases with increasing stellar mass over several orders of magnitude in mass. Figure from Kirby et al. (2013).

### 1.1.3.3 Comparing Massive Galaxies and Low Mass Galaxies

While we have a fairly clear picture of how massive galaxy interactions proceed, we can not necessarily use this information to understand the lower mass systems that are the building blocks of today’s massive galaxies. There are several significant ways in which low mass galaxies differ from massive galaxies. First, dwarf galaxies by definition are lower mass and therefore have shallower gravitational potential wells. They are therefore more susceptible to losing their star forming gas due to energetic events such as supernova explosions, galactic-scale winds, or interactions with other galaxies.

Dwarf galaxies are also observed to have lower metallicities (the ratio of heavy elements to hydrogen in the system) than massive galaxies (see Figure 1.9, Kirby et al. (2013)). Metals are largely responsible for gas cooling to temperatures at which the clouds can collapse to form stars. Having fewer metals therefore restricts the channels through which stars can form (see Section 3.1).

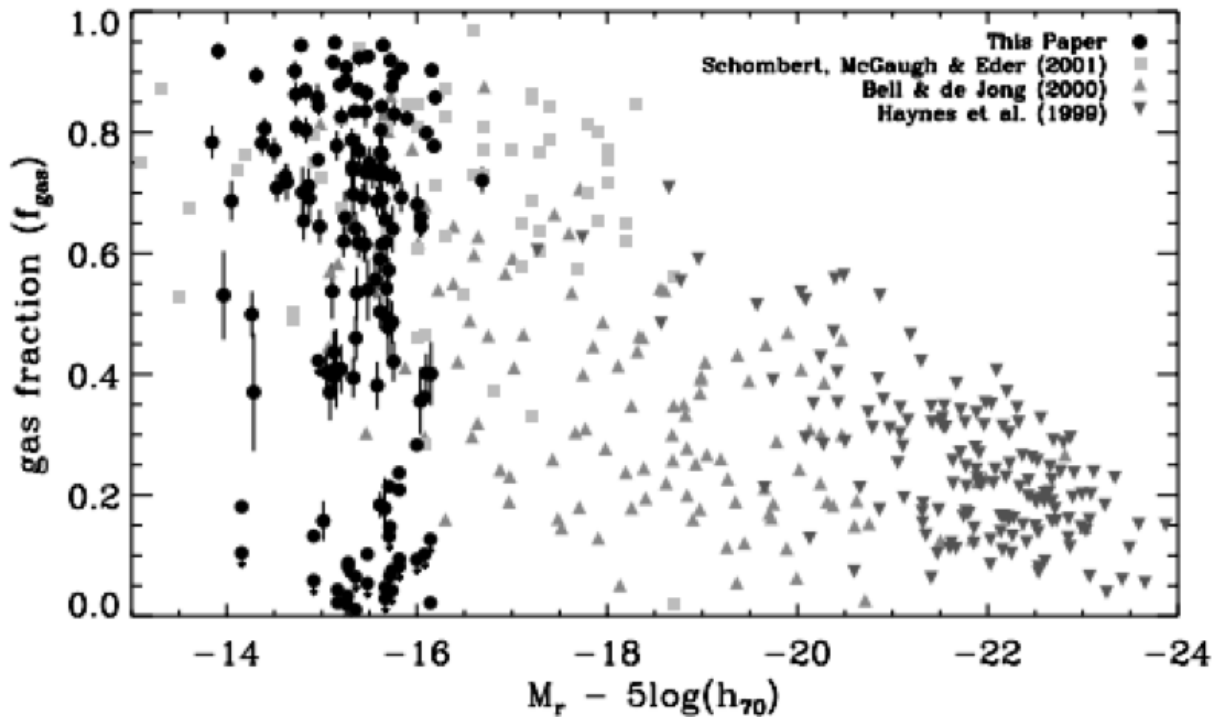


Figure 1.10 The ratio of gas mass to total baryonic mass in a galaxy as a function of the galaxy’s stellar mass. The gas fraction increases with decreasing stellar mass. Figure from [Geha et al. \(2006\)](#).

Massive galaxies have notably different gas fractions than dwarf galaxies (see Figure 1.10, [Geha et al. \(2006\)](#)). The gas fraction, defined in [Geha et al. \(2006\)](#) as

$$f_{\text{gas}} = \frac{M_{\text{gas}}}{M_{\text{gas}} + M_{\text{star}}}, \quad (1.1)$$

is a measurement of what fraction of the baryonic material in a galaxy is comprised of gas by mass. By comparing the HI masses (the primary component of neutral gas in galaxies) to the stellar masses of a sample of galaxies, [Geha et al. \(2006\)](#) found that gas fraction tends to decrease with increasing baryonic mass. As this sample contained 101 galaxies spanning a range of masses and environments, this finding suggests that the dwarf galaxies we observe locally are less efficient at converting gas in to stars than more massive galaxies.

However, while dwarf galaxies in the local universe are among the least efficient sites of star formation ([Geha et al., 2006](#)), this may not have been the case at higher redshifts. Combining star formation histories from observational data with the mass assembly history of dark matter halos from the Millennium and Millennium-II simulations ([Springel](#)

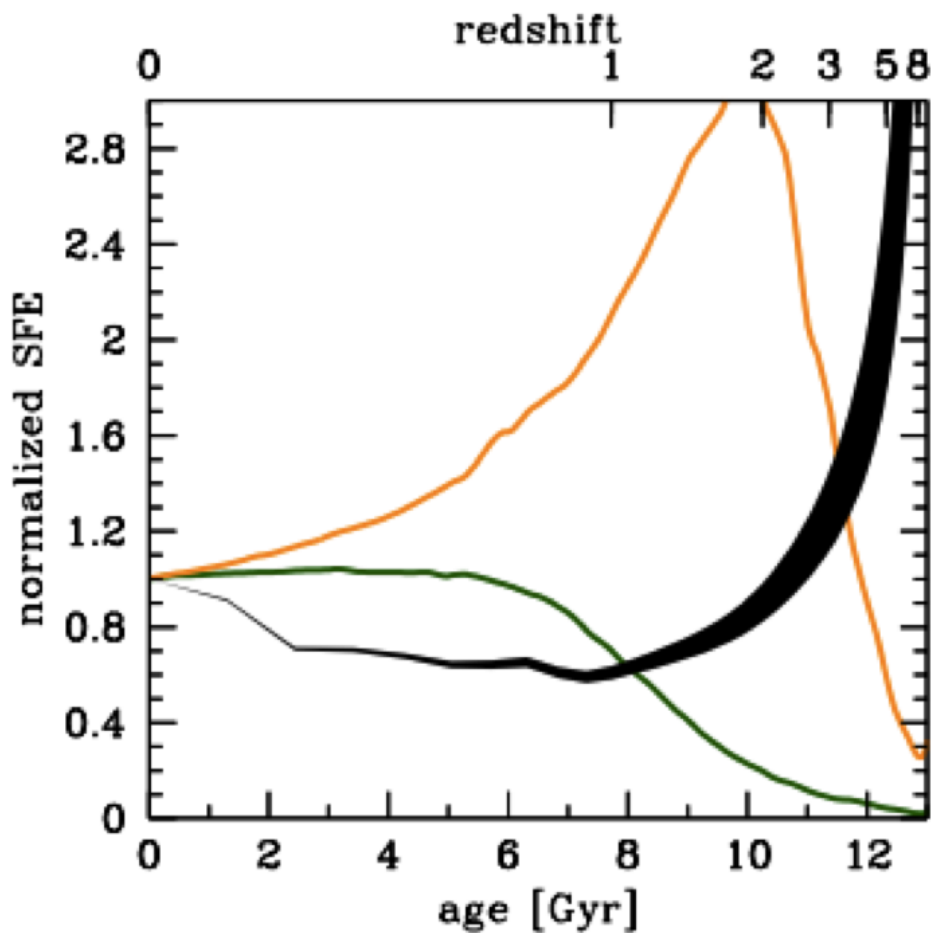


Figure 1.11 The star formation efficiency of a dwarf galaxy (black), a Milky Way-like galaxy (green), and an elliptical galaxy (orange) as a function of redshift or lookback time. Figure from [Madau et al. \(2014\)](#).

[et al., 2005](#)), [Madau et al. \(2014\)](#) examined the star formation efficiency history of dwarf galaxies, a Milky Way analog, and a representative elliptical galaxy (see Figure 1.11). Notably, they found that dwarf galaxies (black curve) go through markedly different phases of growth from the more massive counterparts (Milky Way - green curve; elliptical galaxy - orange curve). The dwarfs are seen to be much more efficient at forming stars at higher redshifts, while the massive galaxies are more efficient today.

Taken together, we see that it is not necessarily appropriate to assume that the properties of dwarf galaxies and the interactions between them can be extrapolated from those of massive galaxy interactions. Despite the fact that dwarf galaxy interactions are likely the most common type of interaction throughout cosmic time, relatively little is known about how these interactions proceed compared to more massive galaxy mergers. Until now there have not been comparable systematic studies of dwarf galaxy interactions.

## 1.2 The TiNy Titans Survey Overview

The TiNy Titans (TNT) survey is the first systematic study of interacting dwarf galaxies. A combined theoretical and multiwavelength observational campaign, it is designed to understand the role that interactions between low mass galaxies play in the larger context of galaxy formation and evolution. The TNT survey consists of three primary components: theoretical, local volume, and low- $z$ . These programs are described below.

### 1.2.1 TNT Theory Program

The theoretical component of the TiNy Titans Survey (Besla et al. 2018, *in prep*) is rooted in the N-body cosmological simulation *Illustris* (Vogelsberger et al., 2014). Using this simulation, a mock catalog of simulated dark matter halos is created and the stellar masses of these halos is determined through abundance matching (the process of matching an observed stellar luminosity function with a simulated dark matter halo mass function). This catalog is then searched for galaxies between redshifts  $0.013 < z < 0.252$  with  $2 \times 10^8 M_{\odot} < M_{*} < 5 \times 10^9 M_{\odot}$  who have companions within the same redshift and mass ranges within  $r_{\text{sep}} < 150$  kpc and  $v_{\text{sep}} < 150$  km s $^{-1}$ . These same criteria are also applied to the Sloan Digital Sky Survey catalog. By comparing these two samples, this component will address the following questions (from Besla et al. 2018, *in prep*):

1. What is the observed fraction of dwarfs in a pair or group vs. cosmological expectations?
2. What is the contamination fraction of dwarf multiples owing to projection effects?
3. What do cosmological simulations predict for the frequency of dwarf multiples in the era of deep photometric surveys like LSST?
4. What is the  $z \sim 0$  fraction of dwarf ‘‘Major Pairs’’ (stellar mass ratio  $> 1 : 4$ )?
5. What is the observed frequency of Magellanic Cloud analogs in the field vs. cosmological expectations?
6. Are the recently-discovered TNT dwarf groups (Stierwalt et al., 2017) consistent with cosmological expectations?

Early results from this study suggest that cosmologically-based simulations can provide accurate constraints for the prevalence of interacting dwarf galaxies across cosmic time.

### 1.2.2 TNT Local Volume Program

The focus of the TNT Local Volume program is to investigate the gas properties in dwarf-dwarf interactions, including the relative impact of dwarf-dwarf versus dwarf-massive galaxy interactions in stripping dwarf galaxies of their diffuse gas. Specifically, it seeks to answer the following questions (from [Pearson et al. \(2016\)](#)):

1. What is more important – environment or dwarf-dwarf interactions in removing gas to large radii?
2. How much material can be removed in this way and does this material remain bound to the pairs?

The TNT Local Volume sample consists of 10 dwarf galaxy pairs near the Milky Way ( $d < 30$  Mpc). These pairs and the galaxies within them span a range of properties; they have stellar mass ratios  $M_1/M_2 < 20$ , projected radial separations  $r_{\text{sep}} < 100$  kpc, and individual stellar masses  $M_* < 10^{9.9} M_\odot$ . They further span a range of gravitational environments in terms of their distance from a galaxy more massive than  $M_* > 10^{9.9} M_\odot$ .

In order to determine the gas properties, each TNT Local Volume pair has a resolved map of its hydrogen gas content, which allows for a detailed investigation of the gas distribution and morphology. Specifically, these maps can be used to measure how much of the detected gas is unbound (enriching the intergalactic medium) or bound (potentially available for star formation in the low-mass galaxies). Early results from this program indicate that the presence of a nearby massive galaxy leads to a higher fraction of unbound gas in dwarfs compared to low mass galaxies that are more isolated. As this gas is lost to the surrounding intergalactic medium, it is no longer available to be re-accreted by the dwarf galaxies for future star formation.

### 1.2.3 TNT Low-z Program

The TNT Low-z Program has three primary goals (from [Stierwalt et al. \(2015\)](#)):

1. To define the dwarf-dwarf merger sequence at  $z = 0$  (present day)
2. To use nearby dwarf pairs as local analogs to high redshift interacting dwarf galaxies
3. To explore extreme, interaction-driven modes of star formation in low metallicity systems

Table 1.1. TiNy Titans Low-z Sample Properties

Property	Range
Stellar mass	$10^7 M_{\odot} < M_* < 5 \times 10^9 M_{\odot}$
Projected $r_{\text{sep}}$	$< 50 \text{ kpc}$
Projected $v_{\text{sep}}$	$< 300 \text{ km s}^{-1}$
Redshift	$0.005 > z > 0.07$

The Low-z sample was selected by searching the Sloan Digital Sky Survey (SDSS, [Abazajian et al. \(2009\)](#)) spectroscopic catalogue for nearby dwarf galaxy pairs (see Table 1.1). SDSS imaged over 35% of the Northern sky at optical wavelengths, cataloging over 500 million objects. A follow-up spectroscopic campaign collected optical spectra for 3 million of these objects, from which properties such as spectral classification and redshift can be determined.

For the TNT low-z sample, the upper stellar mass limit is set to  $5 \times 10^9 M_{\odot}$ , the stellar mass of the LMC. The lower mass is set to  $10^7 M_{\odot}$  in order for the sample to be complete out to a redshift of  $z = 0.07$ . The lower redshift limit of  $z = 0.005$  ensures that the TNT galaxies are outside of the gravitational influence of the massive galaxies in our Local Group of galaxies. In order to be considered a dwarf pair, we further place constraints on the projected radial separation and projected velocity separation of the paired galaxies, such that they must be within 50 kpc of one another and must not be moving more than  $300 \text{ km s}^{-1}$  relative to one another. These ranges are based on those used to identify samples of bound pairs of massive galaxies based on their dark matter halo masses and virial radii ([Patton et al., 2013](#)), and are visually supported by the irregular morphologies of the galaxies selected. With these selection criteria applied to the SDSS spectroscopic catalog, we identified 104 candidate pairs of interacting dwarf galaxies.

### A note on isolation criteria

The TNT low-z sample was originally subdivided based on the pair’s distance from a nearby massive galaxy ( $M_* > 5 \times 10^9 M_{\odot}$ ) due to the environmental effects described above. Pairs beyond 1.5 Mpc from a massive neighbor were classified as ‘isolated’ and those within that distance as ‘nonisolated.’ Based on this definition, 60 of the 104 TNT Low-z pairs are isolated, and the remaining 44 pairs are nonisolated.

Another way to define isolation is to calculate the tidal index,  $\Theta_H$ , of a galaxy and its nearest massive neighbor. This parameter accounts for both the stellar mass and

Table 1.2. TiNy Titans Low-z Sample Isolation Bin Counts

	$d_{\text{host}}$ Criteria	$\Theta$ Criteria
Isolated	60	72
Marginally isolated	–	18
Nonisolated	44	14

the projected distance of the massive galaxy when determining the local gravitational environment. The massive host tidal index is defined as

$$\Theta_H = \log \left( \frac{M_H(M_\odot)}{[D_H(\text{Mpc})]^3} \right) + C, \quad (1.2)$$

where  $M_H$  is the stellar mass of the nearby massive host,  $D$  is the distance between the galaxy and the host, and  $C$  is a constant with a value of  $-10.96^2$  (Karachentsev et al., 2013). The galaxies are considered isolated if their tidal index value is  $< 0$ , non-isolated if the value is  $> 1.5$ , and marginally isolated in between these values. The TNT sample consists of 72 isolated pairs, 18 marginally isolated pairs, and 14 nonisolated pairs based on the tidal index definition.

We can also define  $\Theta_D$  to quantify the gravitational influence of each dwarf galaxy's pair member.

$$\Theta_D = \log \left( \frac{M_D(M_\odot)}{[r_{\text{sep}}(\text{Mpc})]^3} \right) + C, \quad (1.3)$$

where  $M_D$  is the stellar mass of the galaxy's dwarf pair member,  $r_{\text{sep}}$  is the projected radial separation the galaxy and its TNT pair, and  $C$  is again a constant with a value of  $-10.96$ . Using the same definition as above, none of the TNT dwarf galaxies are considered isolated from their paired dwarf companion; all pairs are either marginally isolated or nonisolated.

Figure 1.12 and Table 1.2 shows the difference between the two isolation criteria ( $d_{\text{host}}$  and  $\Theta$ ) when applied to the TNT low-z sample. Square points are considered isolated based on distance from a massive host and circles are nonisolated in  $d_{\text{host}}$  scheme. The tidal index parameter, plotted on the x-axis, gives red points as isolated, green as marginally isolated, and blue as nonisolated. The red squares are dwarf galaxies that are isolated

<sup>2</sup>This constant is defined such that a galaxy with  $\Theta = 0$  will be located at the boundary of the sphere of influence of the neighboring galaxy with the maximal tidal influence on the galaxy in question

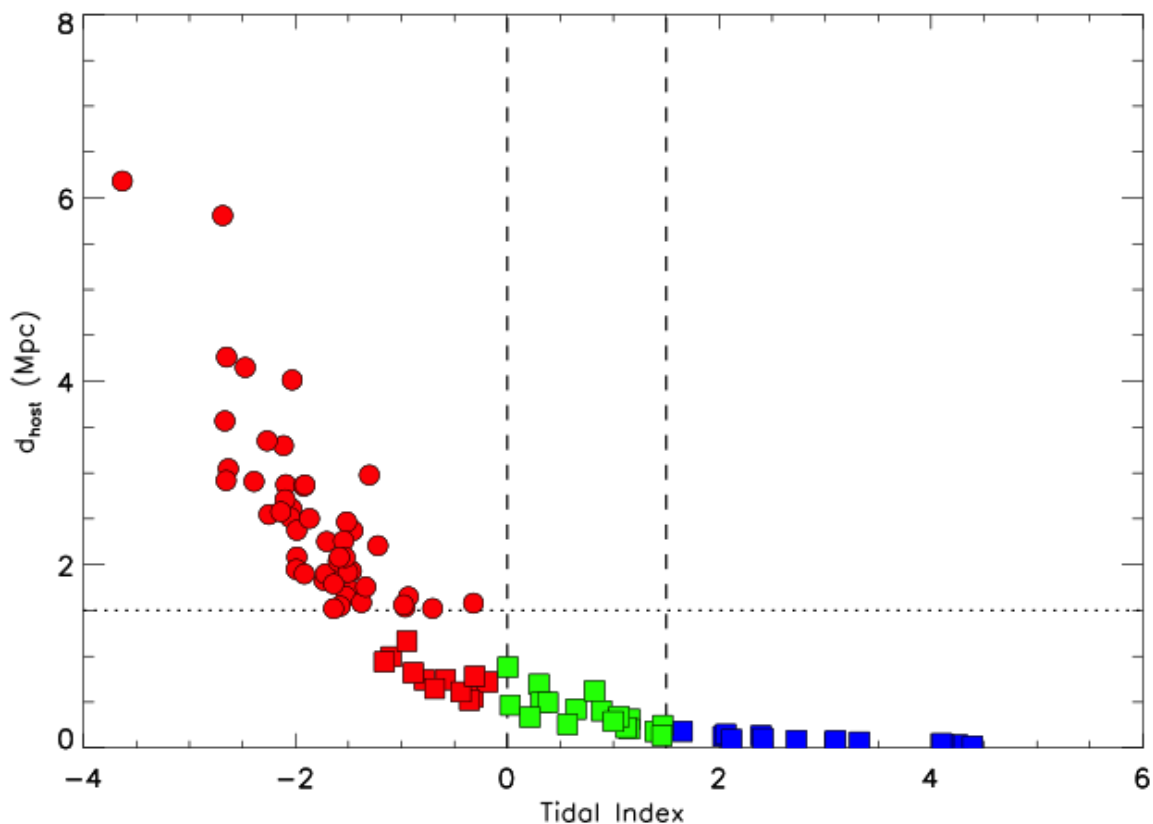


Figure 1.12 Visualization of the two isolation criteria ( $d_{\text{host}}$  and  $\Theta$ ) applied to the TiNy Titans dwarf galaxies. Square points are considered isolated based on distance from a massive host and circles are nonisolated in  $d_{\text{host}}$  scheme. The tidal index parameter, plotted on the x-axis, gives red points as isolated, green as marginally isolated, and blue as nonisolated. Dashed lines show the boundaries between the isolation category for each definition.

according to tidal index, but not by the projected separation between them and their nearest massive neighbor. Thus, these galaxies have lower mass neighbors than their distance-isolated counterparts (red circles).

In this thesis, we adopt the tidal index classification system as a more comprehensive determination of the local gravitational environment of each galaxy pair.

### 1.3 Early Results from the TNT Low-z Program

Stars are one of the fundamental components that make up galaxies, along with gas, dust, and dark matter. Understanding how these stars form in the early universe is a necessary foundation for topics ranging from planet formation to galaxy evolution. While

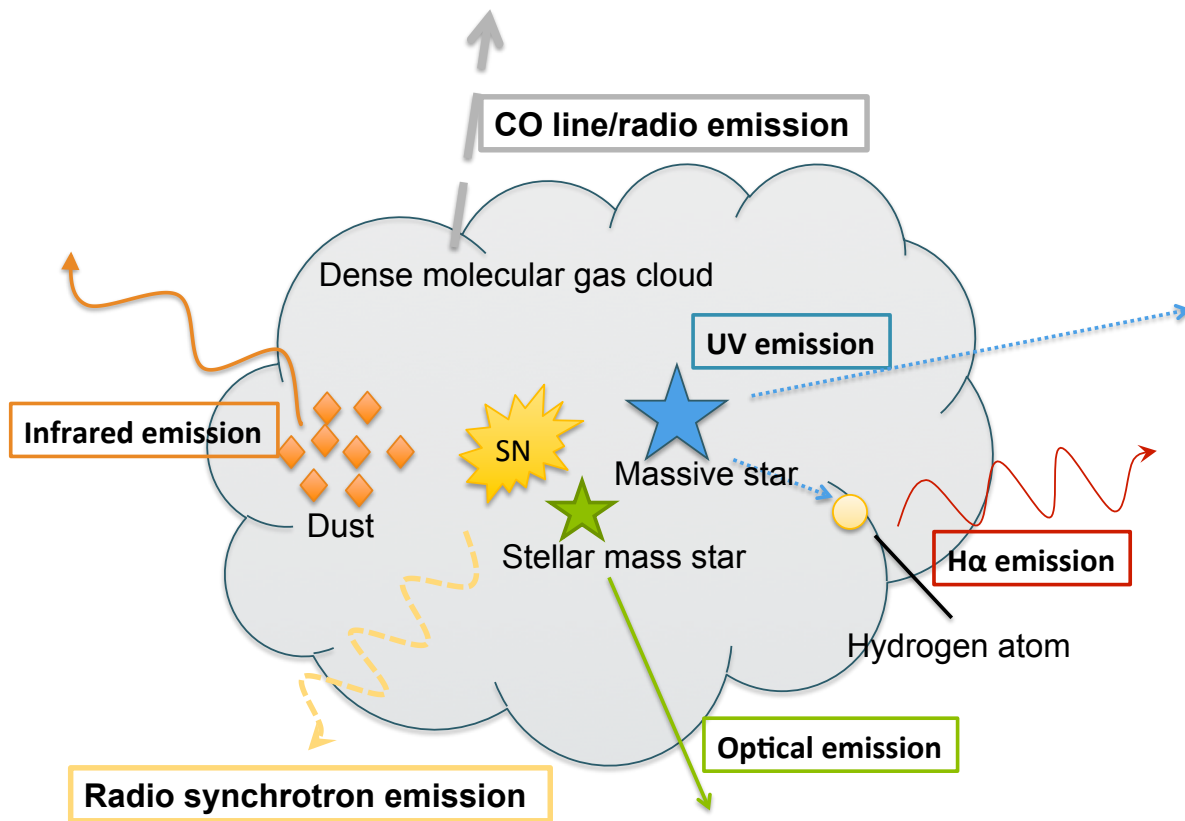


Figure 1.13 A schematic of the sources of electromagnetic emission during the star formation process.

the specifics of star formation vary as a function of stellar mass, the general process proceeds as follows. Stars form from cold ( $\sim 10 - 20$  Kelvin), dense ( $> 10 \times 4 \text{ cm}^{-3}$ ) clouds of molecular gas, primarily composed of molecular Hydrogen ( $\text{H}_2$ ). This gas begins in hydrostatic equilibrium with the pressure caused from the motion of the gas balancing out the gravitational force, which would otherwise lead it to collapse. Once a region of the gas reaches a certain density, however, the gas pressure is not able to withstand the gravitational force leading to the collapse of the so-called ‘core.’ The cores are approximately 0.1 parsec (0.3 lightyears) in diameter, with a mass of tens of solar masses. The collapse of these regions cause the center of the core to heat up, eventually resulting in fusion of the hydrogen gas. This process releases kinetic energy, which then balances and halts the gravitational collapse. The fusion also produces a stellar wind that expels much of the remaining gas and sets the eventual stellar mass of the forming star. In order to conserve angular momentum during the collapse, an accretion disk may form around the protostar, and the material in these disks may eventually form planets.

The star formation process emits light across the electromagnetic spectrum, the characteristics of which change over time as the system evolves. The initial molecular clouds are dark at almost all wavelengths, but regions of diffuse emission from carbon monoxide (CO) can be directly detected through rotational spectroscopy at radio wavelengths. As the clouds collapse the CO emission is observed to become more compact, and at the onset of star formation they begin emitting at radio and infrared wavelengths due to the resultant heat. As the hydrogen fusion leads to the removal of the surrounding natal gas and dust, optical and ultraviolet light from the young stars becomes observable. A schematic of these late-stage emission mechanisms is shown in Figure 1.13.

The spectral data from SDSS has allowed us to begin exploring the nature of star formation in the TNT Low- $z$  sample. Early TNT results include the finding that fiber-based  $H\alpha$  fluxes (the amount of light emitted by the galaxy at  $6563 \text{ \AA}$  within the  $3''$  SDSS fiber) suggested an enhancement in the star formation rates (SFRs) of paired versus unpaired dwarf galaxies (see Figure 1.14, Stierwalt et al. (2015)). To calculate the SFR enhancement, a control sample of matched unpaired dwarf galaxies was generated from SDSS data. For each TNT galaxy, we identified other galaxies that differ only in the fact that they are not nearby (as defined by the TNT pair criteria) another low mass galaxy; they are matched in redshift, stellar mass, and gravitational environment (i.e. isolated vs. nonisolated).

The SFRs for both the paired and unpaired galaxies were measured from the  $H\alpha$  emission line in the SDSS spectra ( $\lambda = 6563 \text{ \AA}$ ), and plotted as a function of projected radial separation (the unpaired dwarfs are plotted at the radial separation of the TNT dwarf to which they are matched). In both the isolated ( $d_{\text{host}} > 1.5 \text{ Mpc}$ ) and nonisolated ( $d_{\text{host}} < 1.5 \text{ Mpc}$ ) pairs of TNT interacting dwarf galaxies, we find increased SFRs in the paired galaxies with decreasing distance between the pair members.

The star formation enhancement is the ratio of these two lines, and is plotted in blue in the top panels of Figure 1.14. A SFR enhancement of 1 indicates that there is no difference in the rate of star formations between the paired and unpaired galaxies. A similar examination of the SDSS fiber-based star formation rates in paired versus unpaired massive galaxies is shown for comparison in black. We also see an enhancement in the star formation rates of paired massive galaxies with decreasing pair separation. Compared to the low mass TNT galaxy pairs, we see that, within errors, the enhancement in the paired dwarfs may be more significant in dwarfs than in their more massive counterparts, both in terms of magnitude and distance (relative to stellar mass) out to which the enhancement is observed.

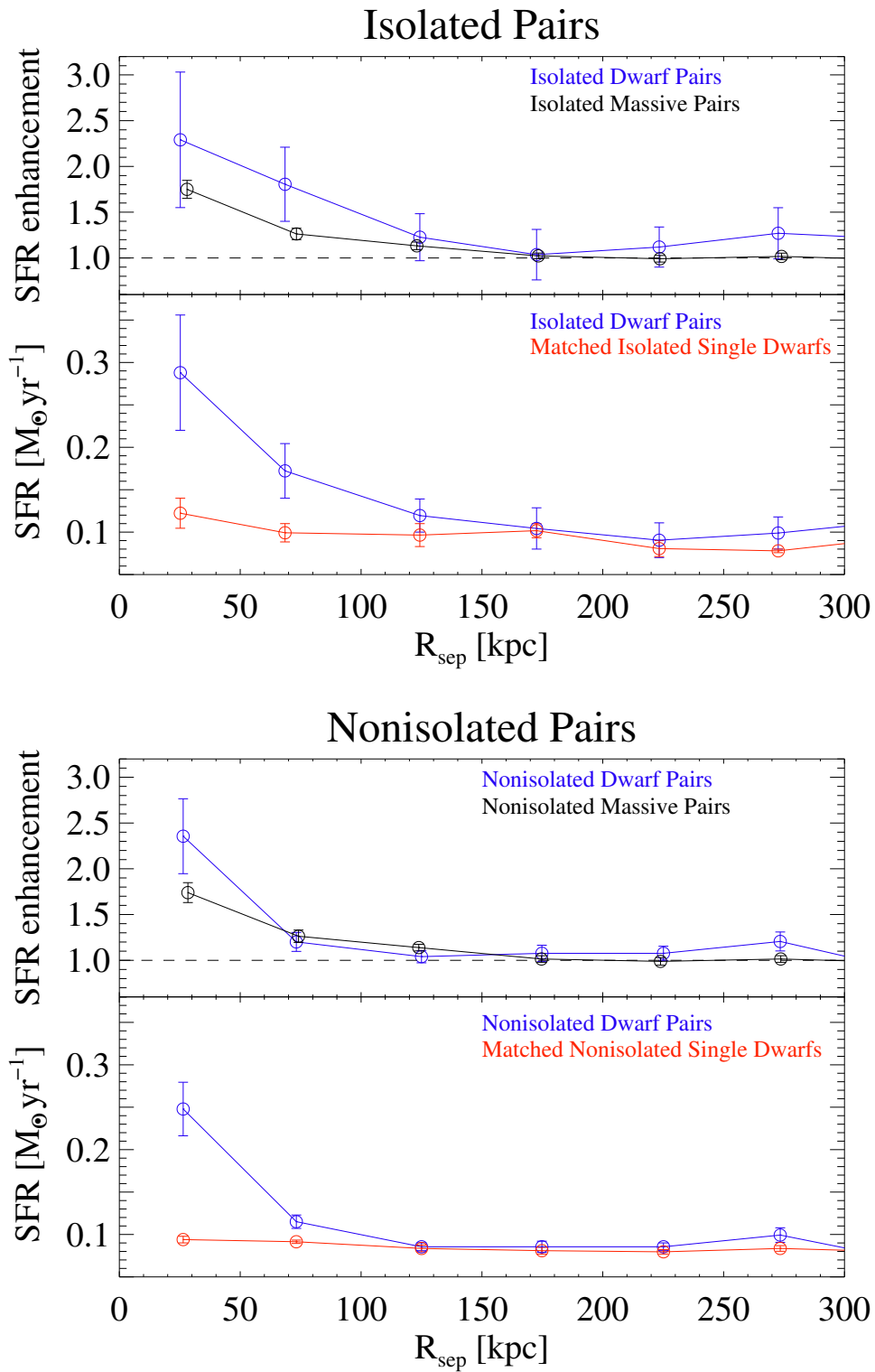


Figure 1.14 The star formation rate enhancement for the isolated (top) and nonisolated (bottom) TNT interacting dwarf galaxies as a function of projected radial separation. The bottom portion of each panel shows the star formation rates for paired (blue) and unpaired (red) dwarf galaxies, the ratios of which is used to calculate the enhancements for the dwarf pairs in the top panel (blue). A similar analysis of the star formation rate enhancement in massive galaxies is shown for comparison in black. Note: The  $d_{\text{host}}$  isolation criteria was used to classify the TNT galaxies for this figure. Figures from [Stierwalt et al. \(2015\)](#).

Though interesting, this analysis is presented with an important caveat: the star formation rates only include emission from within the area of the SDSS 3" optical fiber. As shown in Figure 1.15, these fibers do not encompass the entirety of the TNT galaxies. With covering fractions (the ratio of the area of the fiber to the area of the galaxy) ranging from 2% to 55% with a median of 17%, a significant amount of the star formation is not included in the enhancement calculation for both the paired and unpaired galaxies (Stierwalt et al., 2015). Thus, the results derived from the H $\alpha$  emission line in this data may not be truly representative of the star formation in these systems.

## 1.4 Thesis Overview

In this thesis, I examine the ongoing star formation in the TNT interacting dwarf galaxies in unprecedented detail, taking into account the full galaxy beyond the SDSS spectroscopic fibers. In Chapter 2, I present the ultraviolet through mid-infrared spectral energy distributions (SEDs) of the TNT sample, generated from publicly available data. In addition to allowing for the comparison of multiwavelength tracers of SFRs, these SEDs are used to quantify the ‘typical’ SED of interacting dwarf-dwarf interactions. In Chapter 3, I present a quantitative analysis of the star formation morphology in a subset of the TNT Low- $z$  sample as gleaned from high-resolution H $\alpha$  imaging. I further discuss the impact of the distribution and packaging of the star formation on these low mass dwarf galaxies and their environments. In Chapter 4, I examine an important subset of the TNT interacting dwarf sample – groups of three or more low mass interacting galaxies isolated from massive galaxies. This work was done in close collaboration with the TiNy Titans team, specifically Sabrina Stierwalt. We have identified the first such candidate dwarf groups, and, through followup narrowband imaging and optical spectroscopy, have confirmed that they are likely truly gravitationally bound systems. I present these data as well as a discussion of the cosmological context and role of the groups.

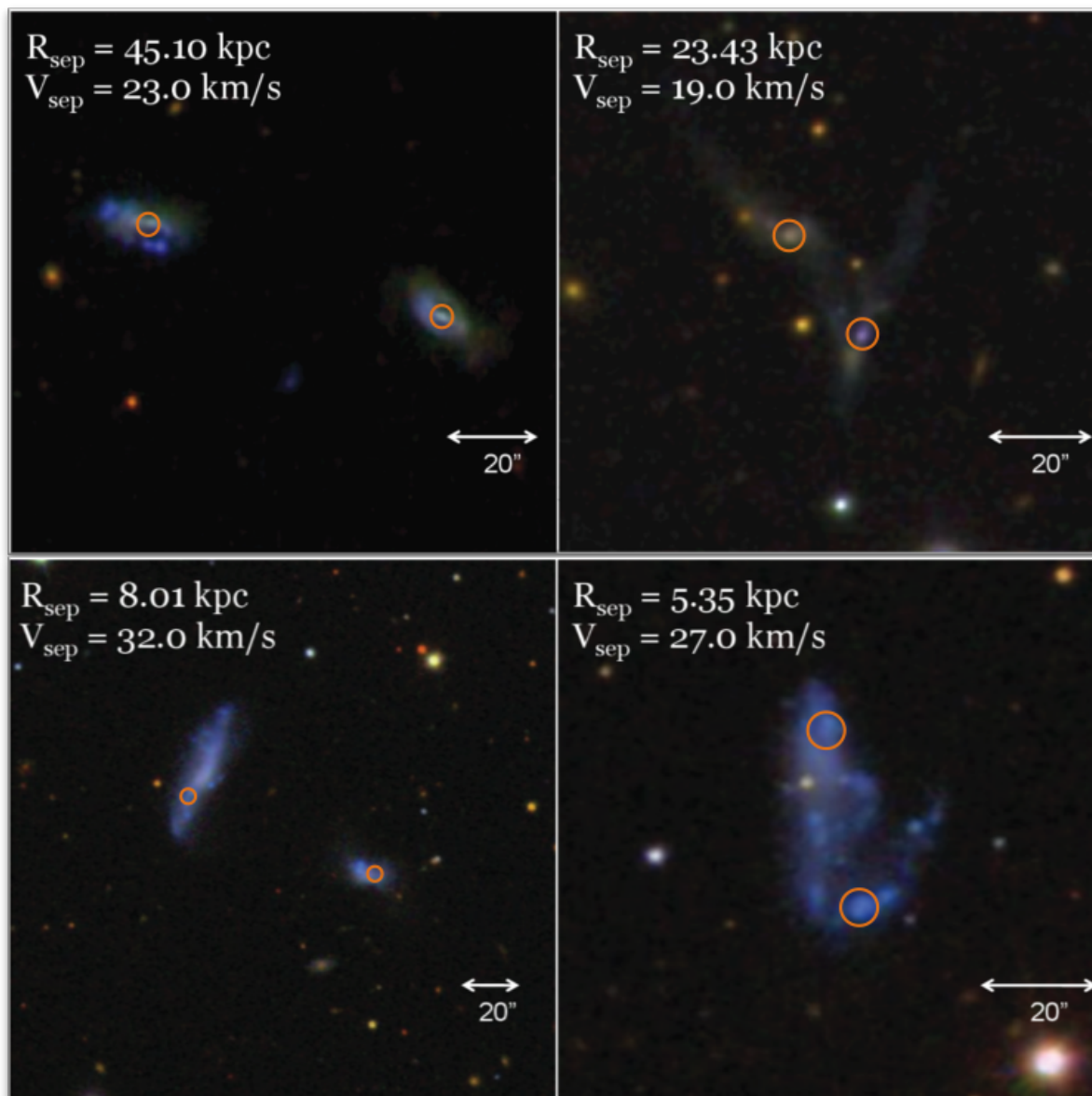


Figure 1.15 A view of the SDSS fiber placement and size on a subset of four TNT galaxy pairs at various stages of interaction. The fibers are placed at the center of each galaxy or on an individually bright star forming region and do not encompass all of the emission. Figure modified from [Stierwalt et al. \(2015\)](#).

# Chapter 2

## The Spectral Energy Distributions of Interacting Dwarf Galaxies

### 2.1 Introduction

Unlike most fields of natural science, astronomical hypotheses typically cannot be tested in laboratories through standard empirical methods. Instead, astronomers must pursue investigations remotely. We are able to physically examine only the closest astronomical objects, those in our Solar System. Studying anything else, from the nearest star to the furthest galaxies, relies on collecting and interpreting the light they emit during the course of their formation and evolution. The light produced by these processes is not limited to the optical wavelengths we can see, but spans the entire electromagnetic spectrum from low frequency radio waves to high energy gamma rays.

Spectral energy distributions (SEDs) are powerful tools that can be used to characterize astronomical objects. Through quantifying the amount of energy a galaxy emits as a function of wavelength, we can determine properties such as mass, age, and star formation rate (SFR). Further, these SEDs can be used to explore the relative contributions of different star formation mechanisms and can be used to infer the presence of active galactic nuclei (AGN). As part of an ongoing multi-wavelength campaign to understand the star formation and gas processing in interacting dwarf galaxies, we have generated ultraviolet through mid-infrared SEDs of the dwarf galaxies in the TNT sample.

Ultraviolet (UV) light ( $\sim 10 - 100$  nm) traces O-stars, which are hot ( $T > 10^5$  K) and massive ( $M > 16 M_{\odot}$ ). As these stars live less than 10 million years, UV emission

originates only from sites of recent star formation. UV light is also highly susceptible to dust attenuation. Thus, it is only observed from O-stars that have emerged from their natal molecular clouds and are no longer obscured.

Optical emission ( $\sim 400 - 700$  nm) is produced by stars of various ages, sizes, and temperatures in both unobscured and partially obscured environments. Optical light can therefore be used not only to map a galaxy's underlying, older stellar population but also to locate sites of recent star formation (though it is not particularly sensitive to the latter). It can further be used along with models to determine the age and stellar mass of a galaxy.

Infrared light ( $\sim 750 - 10^4$  nm) reveals both obscured sites of star formation and the dust in which they are embedded. At these longer wavelengths, infrared emission from the young stars is able to penetrate the natal dust that otherwise obscures the light at shorter wavelengths (optical and ultraviolet). Further, the enshrouding dust itself emits infrared light. Ultraviolet emission from embedded stars is absorbed by the dust, which heats it up. The dust then emits like a blackbody with a peak wavelength in the infrared.

In this chapter, we present trends in the SEDs of the TNT interacting dwarf galaxies as a function of pair properties (projected radial separation, projected velocity separation, mass ratio) individual galaxy properties (metallicity and star formation rate) and tidal index (a quantification of the local gravitational environment). We then compare the interacting dwarf SEDs to other astronomical objects in order to contextualize the TNT results.

## 2.2 Data and Methods

The SED of each individual galaxy in the TNT pair sample was generated using archival data from three publicly available surveys: Galaxy Evolution Explorer (GALEX, [Bianchi et al. \(2014\)](#)), Sloan Digital Sky Survey (SDSS, [Abazajian et al. \(2009\)](#)), and Wide-field infrared Survey Explorer (WISE, [Wright et al. \(2010\)](#)). The data from each survey was processed through the telescope's standard data reduction pipeline to combine multiple exposures of the same fields, remove spurious signals from cosmic rays, and account for sources of background and instrument noise. Figure 2.1 shows an example of one of the TNT galaxy pairs at all wavelengths, demonstrating the resolution and depth of each survey, as well as how the structures vary in each band.

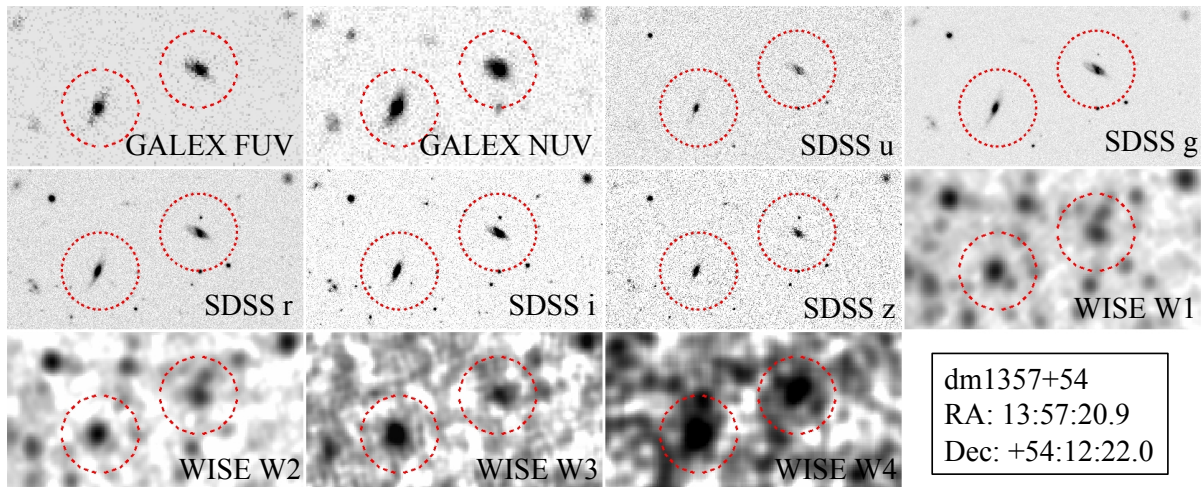


Figure 2.1 The TNT dwarf pair dm1357+54 shown in each wavelength used in this SED analysis. Dashed red circles in each frame indicate the individual galaxies in the pair.

Table 2.1. Galex UV Filter Characteristics

Filter name	Effective Wavelength ( $\text{\AA}$ )	Filter Width ( $\text{\AA}$ )
Far Ultraviolet (FUV)	1540	228
Near Ultraviolet (NUV)	2270	796

Note. — The filter width is given as the full width at half of the maximum throughput of the filter (FWHM). From the SVO Filter Profile Service.

### 2.2.1 Ultraviolet data from GALEX

The near- and far-ultraviolet (UV) data presented here came from the Galaxy Evolution Explorer (GALEX), a space-based telescope designed to probe the evolution of galaxies. The mission consists of (1) an imaging campaign that mapped the entire night sky at  $1600 \text{ \AA}$  (Near UV) and  $2500 \text{ \AA}$  (Far UV), and (2) a spectroscopic survey through which UV spectra of over 100,000 galaxies were obtained. The imaging survey reached a resolution of  $4.3''$  and  $5.3''$  in the FUV and NUV, respectively. The FUV and NUV catalog fluxes of the TNT galaxies were obtained through the MultiMission Archive at Space Telescope Science Institute (MAST) GALEX archive. Each field was then checked by eye for potential interlopers, such as stars or nearby galaxies, that might impact the reported values. Further, as many of the TNT dwarf galaxies are partially resolved, they are often split in to multiple catalog entries. The visual inspection ensures that the total flux of each galaxy is included in the measurements for these SEDs.

Table 2.2. SDSS *ugriz* Filter Characteristics

Filter name	Effective Wavelength (Å)	Filter Width (Å)
Ultraviolet ( <i>u</i> )	3600	582
Green ( <i>g</i> )	4640	1260
Red ( <i>r</i> )	6120	1150
Near Infrared ( <i>i</i> )	7440	1240
Infrared ( <i>z</i> )	8900	995

Note. — The filter width is given as the full width at half of the maximum throughput of the filter (FWHM). From the SVO Filter Profile Service.

### 2.2.2 Optical data from SDSS

The optical data utilized in this analysis was obtained through the Sloan Digital Sky Survey (SDSS). SDSS imaged approximately 35% of the night sky in five broad optical bands commonly referred to as the ‘ugriz’ filters (see Table 2.2). As part of this survey, SDSS captured approximately 500 million astronomical objects with an angular resolution of  $\sim 1.5''$ . SDSS also includes optical spectra for over 3 million of these objects. As mentioned previously, the TNT sample was built from the SDSS spectroscopic catalog. For the SEDs, we use the custom aperture photometric measurements from [Stierwalt et al. \(2015\)](#). The photometry was performed on processed, calibrated SDSS images that were downloaded from the online database. The apertures are based on the  $2\sigma$  contour of each galaxy’s *r*-band image. This aperture was then used on the the remaining four bands. Each value was corrected for extinction due to dust along the line-of-sight to the galaxy, which varies as a function of wavelength.

### 2.2.3 Infrared data from WISE

The infrared data was obtained through the Wide-field Infrared Survey Explorer (WISE). WISE imaged the full night sky in four infrared bands – W1 ( $3.4 \mu\text{m}$ ), W2 ( $4.6 \mu\text{m}$ ), W3 ( $12 \mu\text{m}$ ), and W4 ( $22 \mu\text{m}$ ) – observing over 750 million astronomical objects at an angular resolution of  $6''$ . In the WISE IR bands, W1 and W2 primarily contain emission from stellar photospheres. At slightly longer wavelengths, W3 is sensitive to polycyclic aromatic hydrocarbons (PAHs, ring-shaped dust molecules containing only hydrogen and carbon atoms that are thought to be fundamental in the origin of life) and W4 is dominated by emission from warm dust. Catalog flux values of the TNT

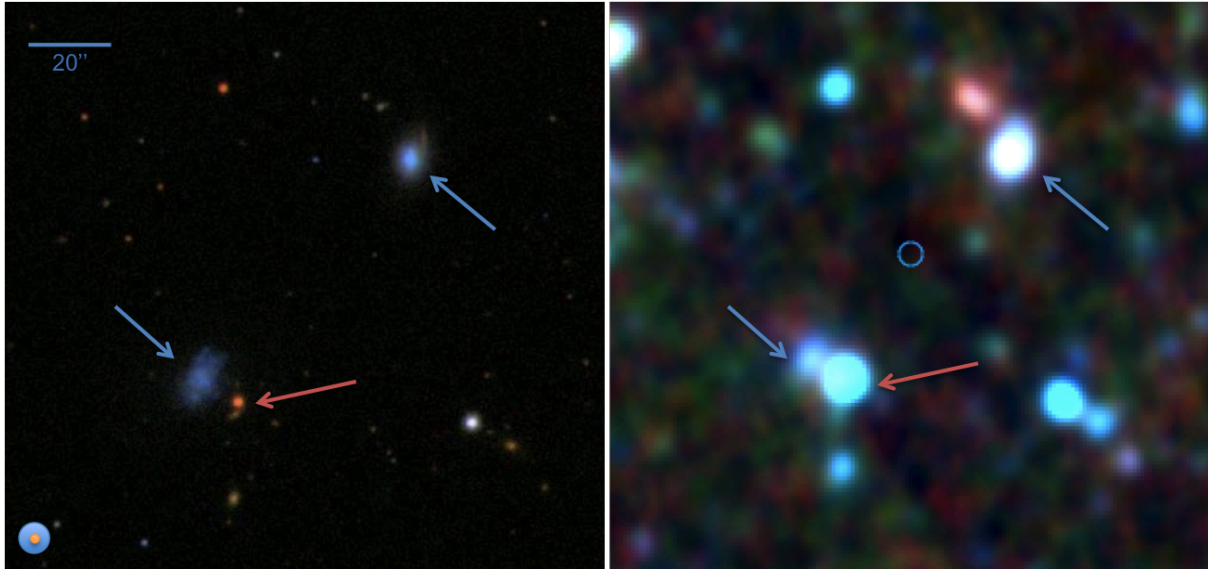


Figure 2.2 Example of the resolution of SDSS optical image of a TNT pair (left) vs. WISE infrared image of the same pair (right). The blue arrows are pointing to the dwarf galaxies in both panels, and the red arrow to a nearby star. The WISE infrared emission of this star overlaps the southern galaxy in the pair, thus contaminating the measured flux in these bands.

Table 2.3. Wise Infrared Filter Characteristics

Filter name	Effective Wavelength (nm)	Filter Width (nm)
W1	33500	636
W2	46000	11100
W3	116000	62800
W4	221000	47400

Note. — The filter width is given as the full width at half of the maximum throughput of the filter (FWHM). From the SVO Filter Profile Service.

galaxies were obtained through the NASA/IPAC Infrared Science Archive (IRSA). Each field was then checked by eye for potential interlopers that might impact the reported values (see Figure 2.2). Many of the TNT dwarf galaxies are only marginally resolved in the WISE imaging (resolution of  $6''$ ), thus making investigations of the nuclear versus extended emission difficult. In a small number of cases ( $\sim 5$ ), contamination from a bright foreground star or a red background galaxy as revealed by the optical SDSS imaging are clearly blended in the WISE photometry.

Table 2.4. TNT Target Binning Summary

Property	Low	Mid	High
$r_{\text{sep}}$	50	82	76
$v_{\text{sep}}$	90	96	20
Mass Ratio	130	64	14
Tidal Index ( $\Theta_H$ )	144	36	28
Metallicity ( $Z$ )	80	95	33
Star Formation Rate	40	134	24

## 2.2.4 Binning targets by pair and galaxy properties

For this analysis, we will bin the TNT galaxies based on both their pair ( $r_{\text{sep}}$ ,  $v_{\text{sep}}$ , mass ratio, and tidal index) and individual galaxy (metallicity and star formation rate) properties. For each property, a histogram was generated and the galaxies were split into three bins: low, mid-range, and high (see Figures 2.3 and 2.4). For tidal index, we used the definition of isolation described in Chapter 1 for binning. For the rest of the properties, galaxies were binned based on a visual inspection of the histograms. Where there were no evident natural groupings, the galaxies were binned such that there were approximately equal numbers in each property bin.

## 2.3 Results

### 2.3.1 SEDs as a function of projected radial separation

The SEDs for the TNT dwarf galaxies were first analyzed as a function of projected radial separation, a proxy for interaction stage. Figure 2.6 shows the SED for individual dwarf galaxies colored by their projected radial separations, with close pairs ( $r_{\text{sep}} < 15$  kpc) in red, moderately separated pairs ( $15 \text{ kpc} < r_{\text{sep}} < 35$  kpc) in green, and widely separated pairs ( $35 \text{ kpc} < r_{\text{sep}} < 50$  kpc) in blue. All fluxes have been normalized to the SDSS z-band flux. The average of each radial separation bin is shown as a square. The close pairs have a higher average flux across the SED, notably in the near- and far-ultraviolet.

As mentioned in Section 1.3, Stierwalt et al. (2015) noted that the star formation rate of the TNT dwarf pairs increased with decreasing projected pair separation. The trend seen

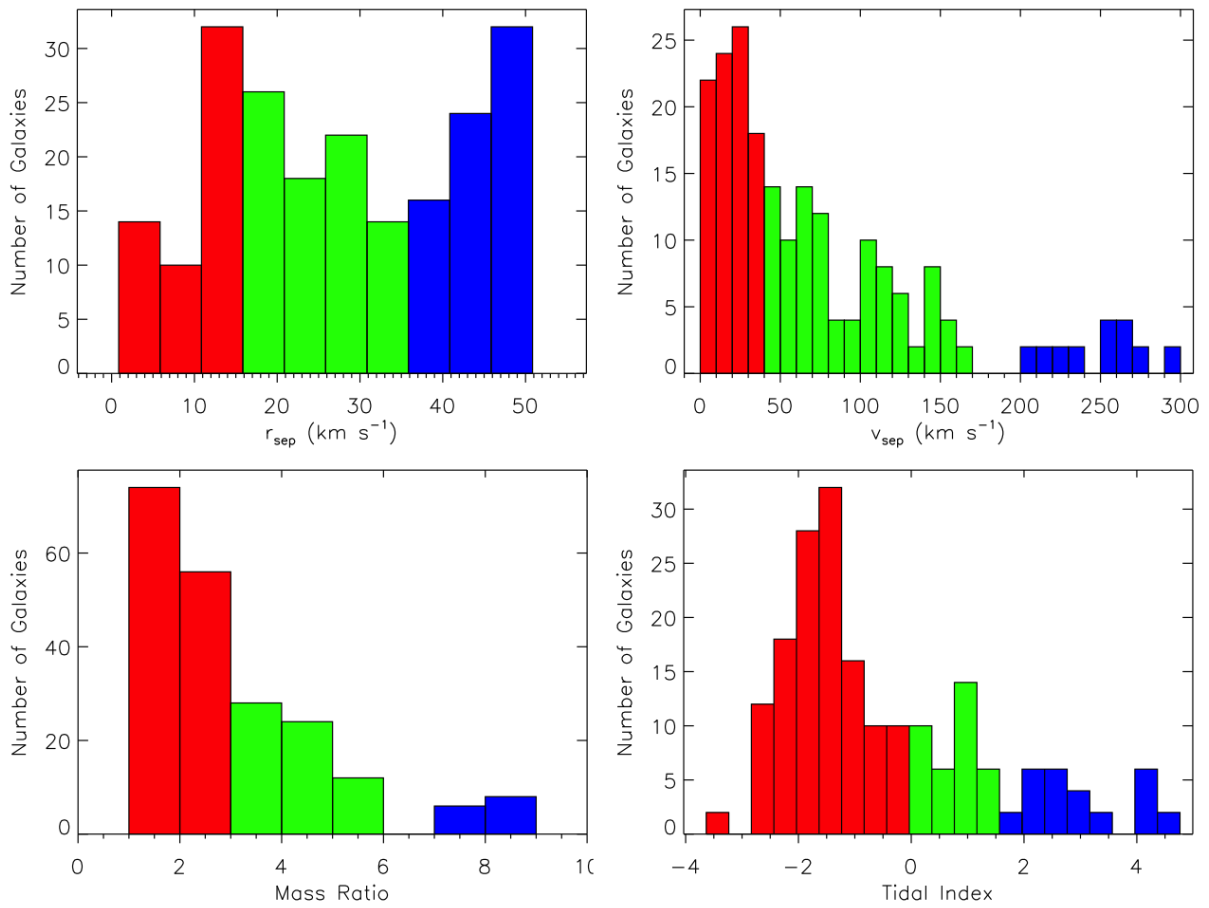


Figure 2.3 Histograms for pair properties:  $r_{\text{sep}}$ ,  $v_{\text{sep}}$ , mass ratio, and tidal index. Bins are colored to correspond to the grouped SEDs below.

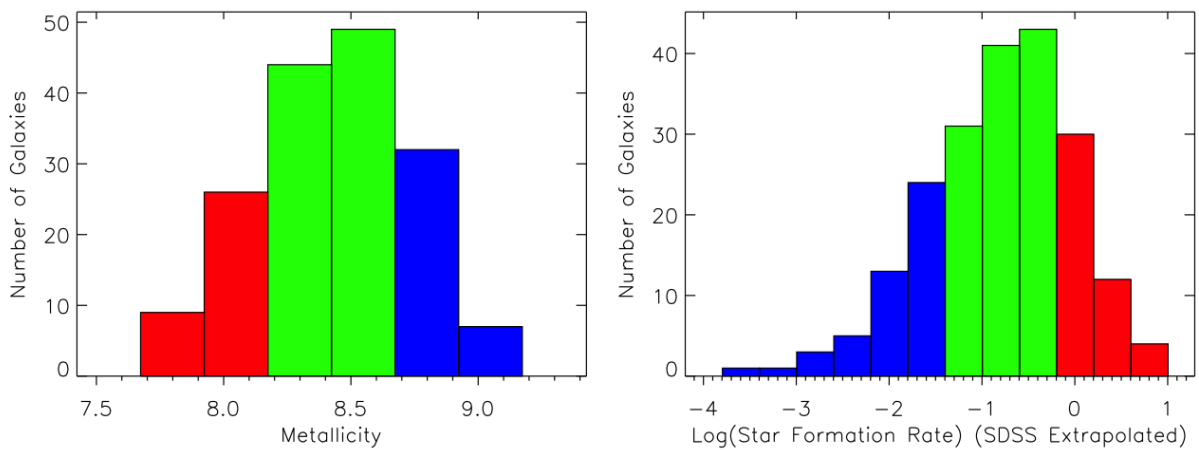


Figure 2.4 Histograms for galaxy properties: metallicity and star formation rate. Bins are colored to correspond to the grouped SEDs below.

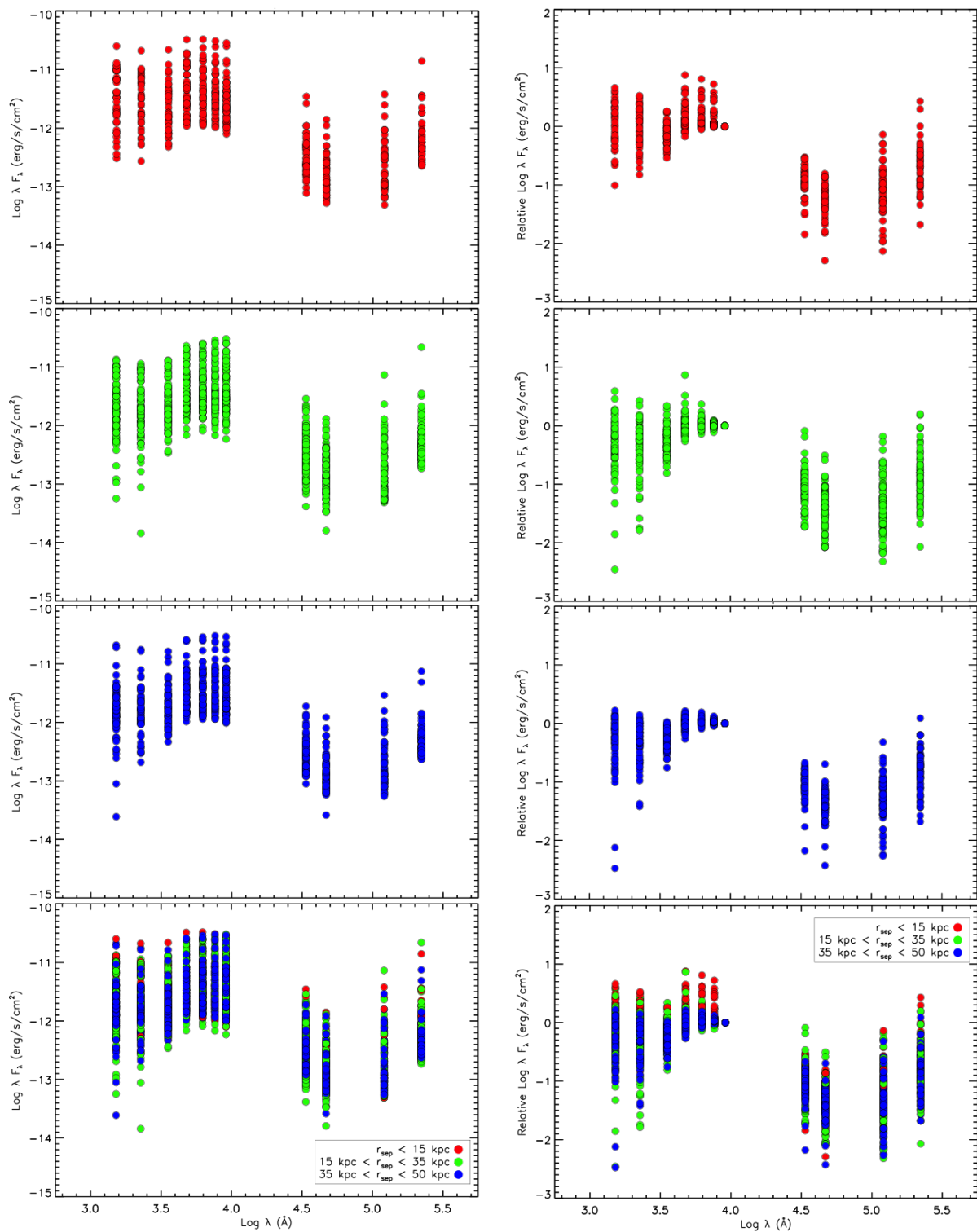


Figure 2.5 Left: The SED for each TNT galaxy separated by projected pair separation (red - close pairs; green - moderately separated pairs; blue - far pairs). The bottom panel is a combination of the top three panels for the sake of direct comparison. Right: Same as left, normalized to the SDSS  $z$ -band measurement for each galaxy as a proxy for stellar mass.

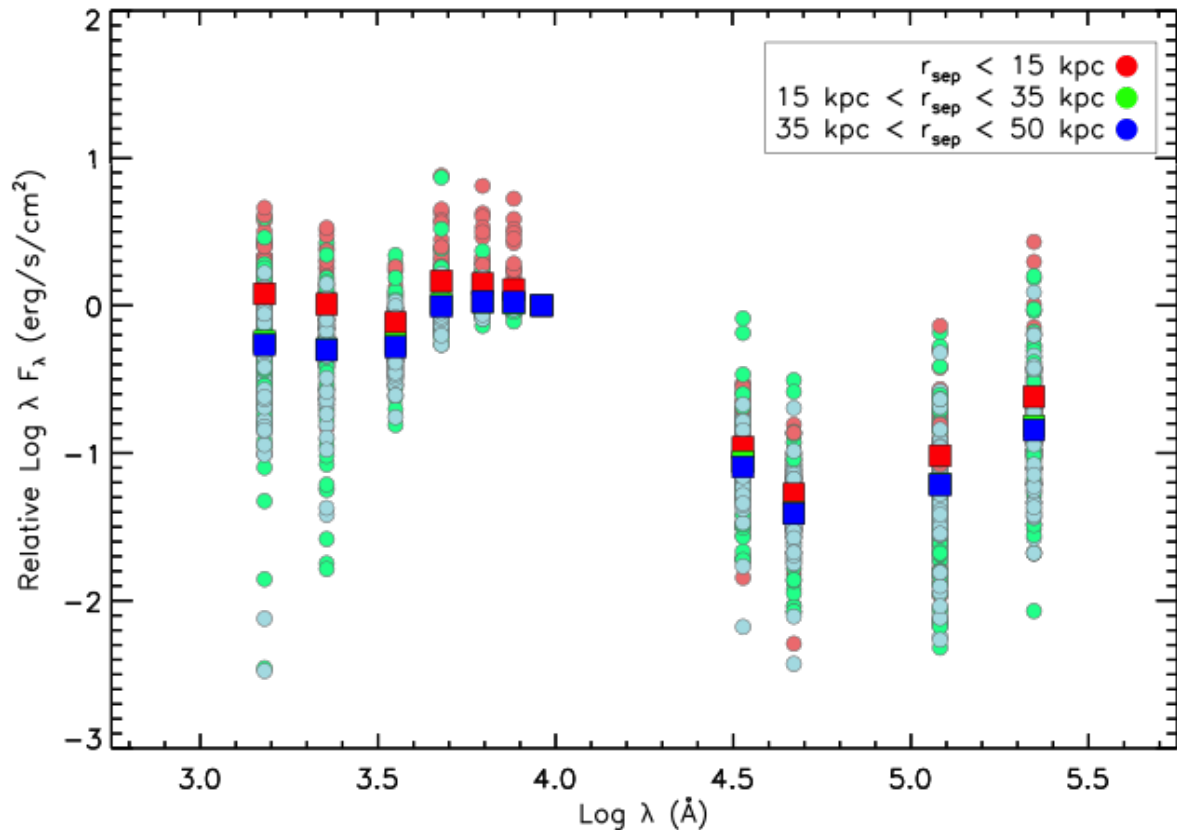


Figure 2.6 Same as bottom right panel of Figure 2.5 with all points in a single frame and the mean of each radial separation bin overplotted as a square.

here supports that result, as the dwarf galaxies that are closer to one another have more ultraviolet emission from young massive stars than those pairs that are widely separated.

### 2.3.2 SEDs as a function of projected velocity separation

Figure 2.8 shows the SED for individual dwarf galaxies colored by their projected velocity separations, with close pairs ( $v_{\text{sep}} < 40 \text{ km s}^{-1}$ ) in red, moderately separated pairs ( $40 \text{ km s}^{-1} < v_{\text{sep}} < 170 \text{ km s}^{-1}$ ) in green, and widely separated pairs ( $170 \text{ km s}^{-1} < v_{\text{sep}} < 300 \text{ km s}^{-1}$ ) in blue. All fluxes have been normalized to the SDSS z-band flux. The average of each velocity separation bin is shown as a square. The close and moderately separated pairs have, on average, higher relative fluxes across the SEDs. This is most notable in the ultraviolet and infrared.

Galaxies that are moving slowly relative to one another (those with small  $v_{\text{sep}}$ ) are subjected to a prolonged influence of one another's gravitational pull. Here, we see that these same galaxies have both higher levels of both star formation (ultraviolet) and warm dust

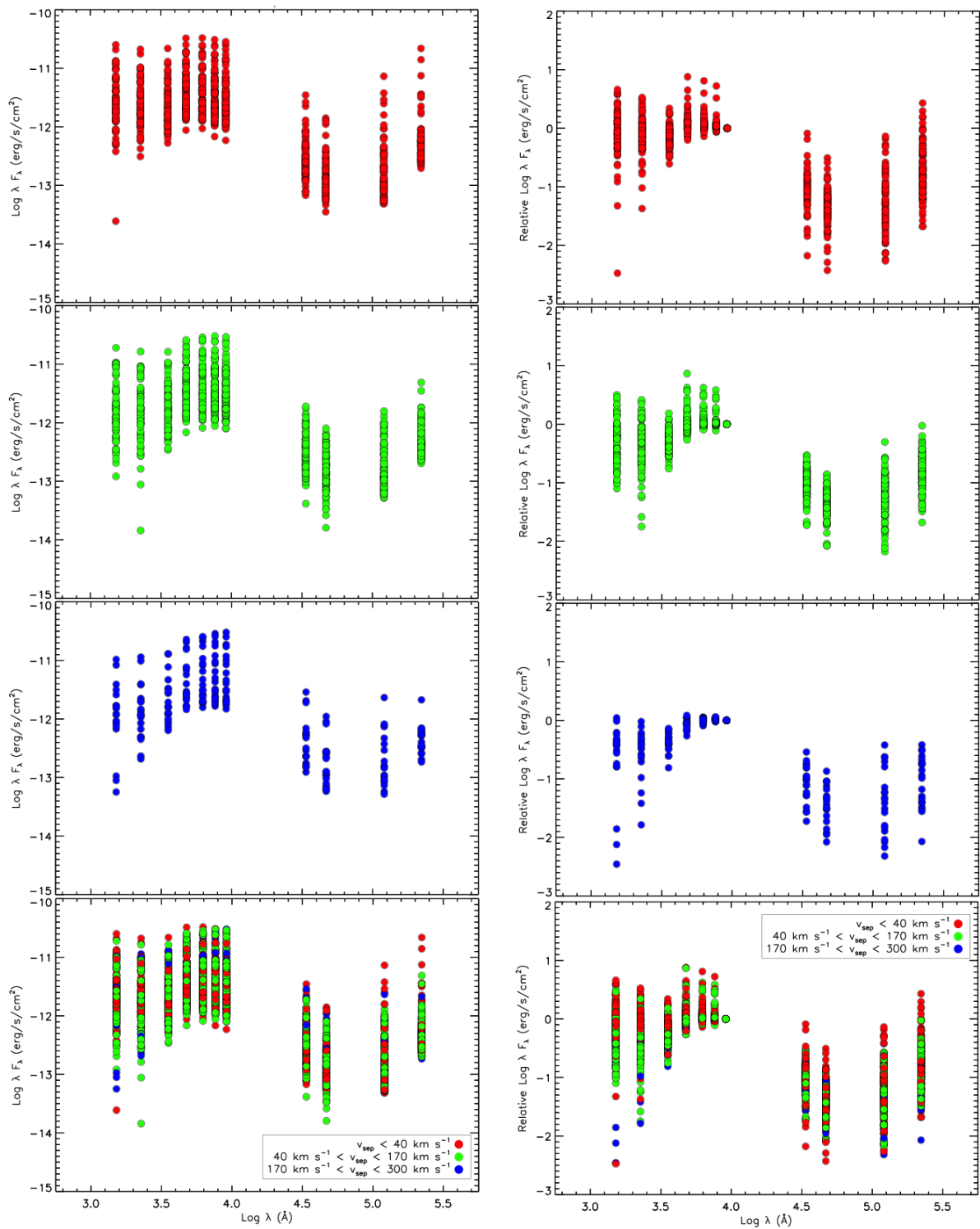


Figure 2.7 Left: The SED for each TNT galaxy separated by projected velocity separation (red - slow relative motion; green - moderate relative motion; blue - fast relative motion). The bottom panel is a combination of top three panels for the sake of direct comparison. Right: Same as left, normalized to the SDSS  $z$ -band measurement for each galaxy as a proxy for stellar mass.

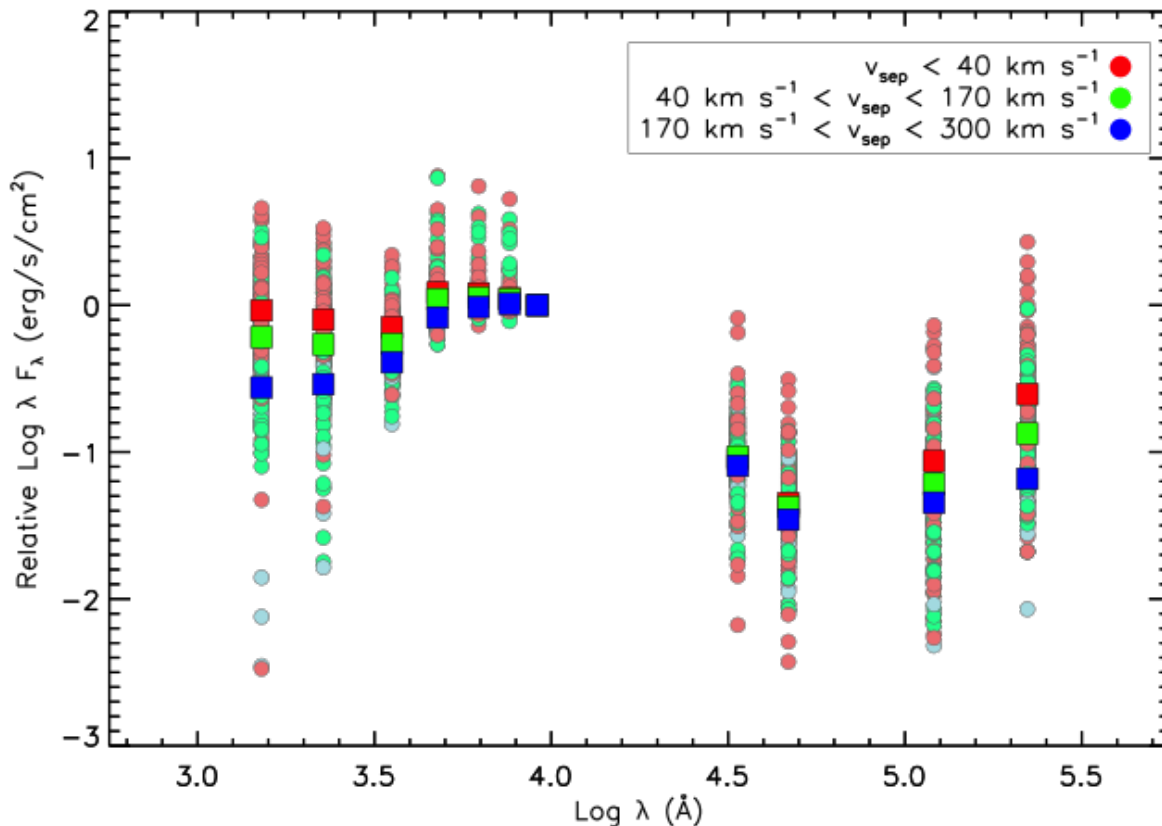


Figure 2.8 Same as bottom right panel of Figure 2.7 with all points in a single frame and the mean of each velocity separation bin overplotted as a square.

(infrared) tracers. This suggests a relationship between the duration of an interaction and the rate of ongoing star formation. The gas in a galaxy must reach a certain density before it will collapse and form stars. The tidal forces involved in an extended interaction between two dwarf galaxies may play an important role in creating these conditions.

### 2.3.3 SEDs as a function of pair mass ratio

Figure 2.10 shows the SED for individual dwarf galaxies color coded by their mass ratios, with low mass ratios ( $M_1/M_2 < 3$ ) in red, mid mass ratios ( $3 < M_1/M_2 < 6$ ) in green, and high mass ratios ( $6 < M_1/M_2 < 10$ ) in blue, normalized to the SDSS z-band flux. The average of each mass ratio bin is shown as squares. The pairs with small to moderate mass ratios (both galaxies are of similar stellar mass) have, on average, higher relative fluxes across the SEDs than those with greater mass ratios. This is most notable in the ultraviolet and far-mid infrared.

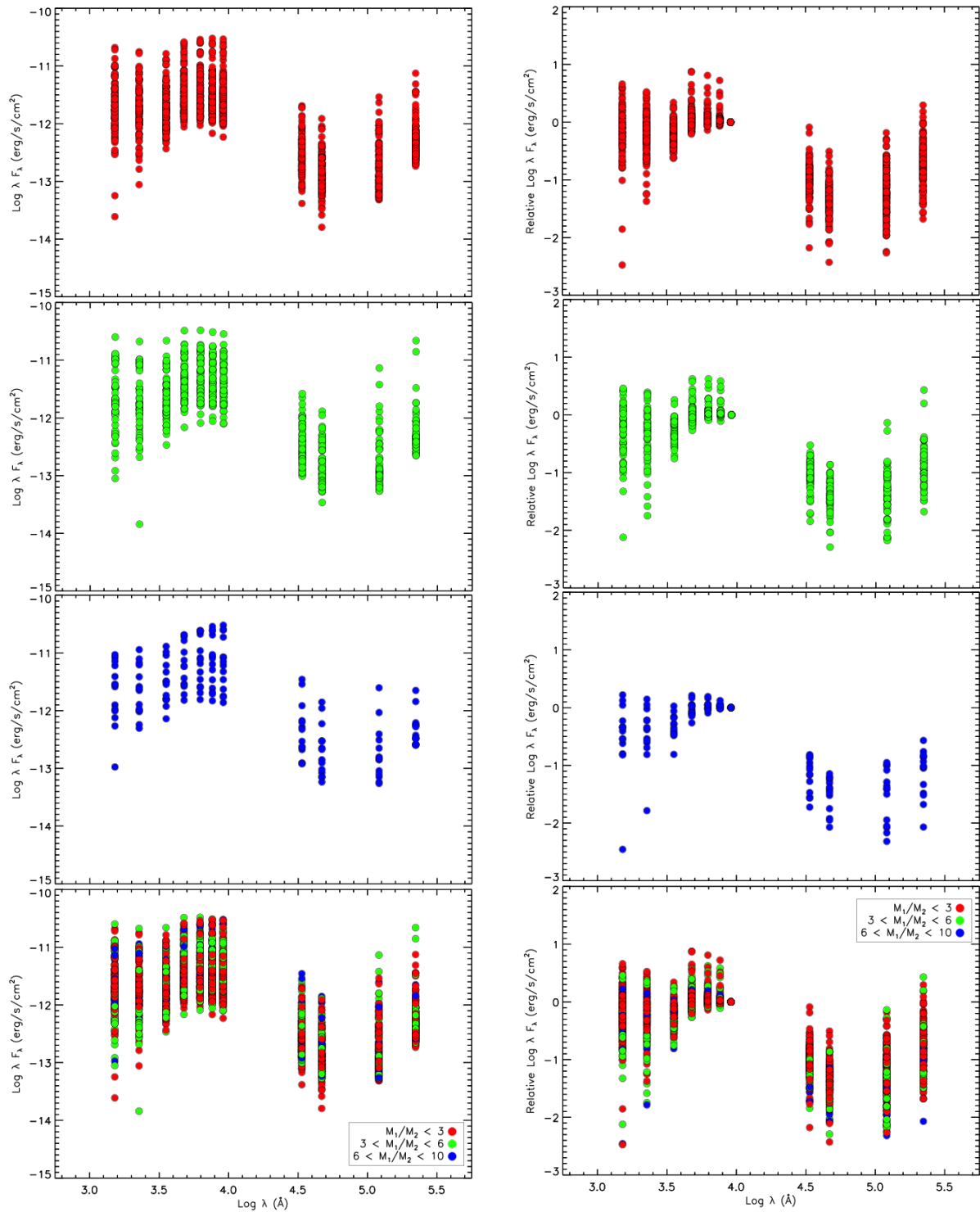


Figure 2.9 Left: The SED for each TNT galaxy separated by mass ratio (red - major ‘merger’; green - moderate ‘merger’; blue - minor ‘merger’). The bottom panel is a combination of top three panels for the sake of direct comparison. Right: Same as left, normalized to the SDSS  $z$ -band measurement for each galaxy as a proxy for stellar mass.

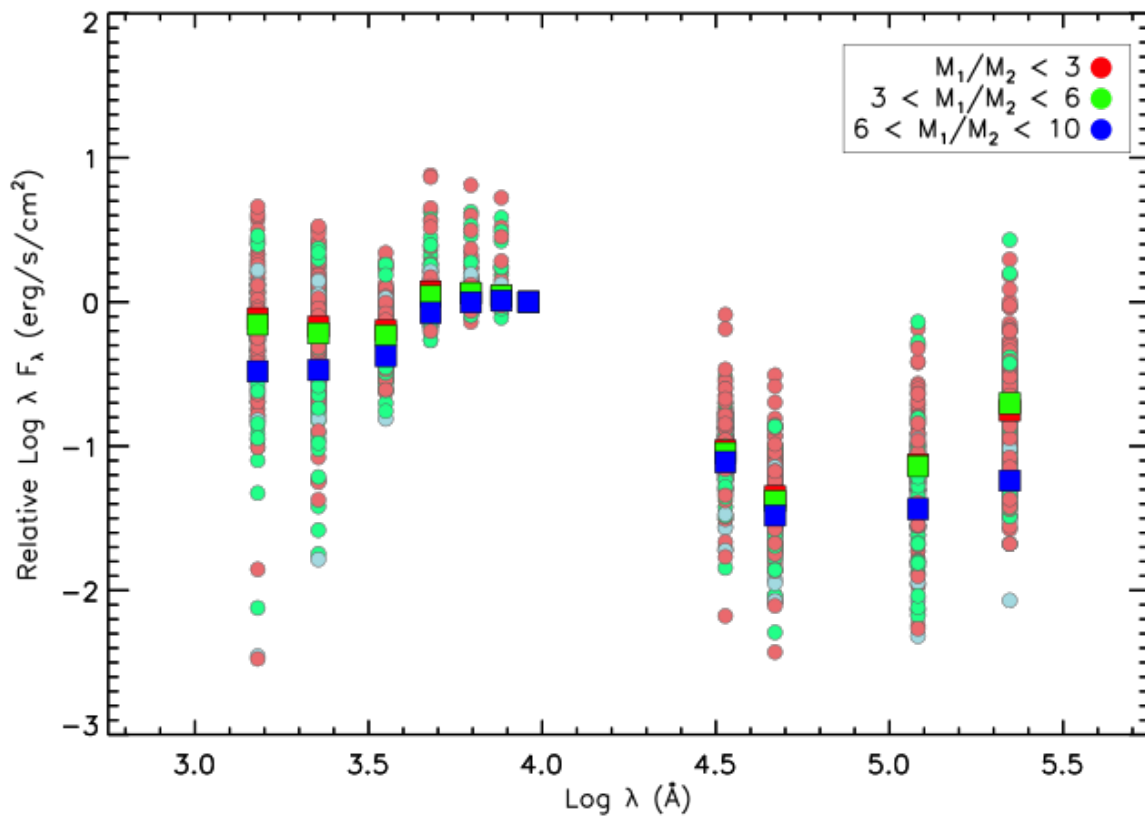


Figure 2.10 Same as bottom right panel of Figure 2.9 with all points in a single frame and the mean of each mass ratio bin overplotted as squares.

The enhanced UV flux suggests that pairs with mass ratio  $< 6$  are forming more high mass stars than those with larger mass ratios. Like pairs with small  $v_{\text{sep}}$ , the dwarf pairs with galaxies of similar masses do not contain a host-like galaxy that is strongly influencing a satellite galaxy. Rather, the small mass ratios creates a system in which neither galaxy dominates in terms of tidal forces. This allows both galaxies involved in the interaction to hold on to their interstellar medium and form stars.

### 2.3.4 SEDs as a function of galaxy metallicity

Figure 2.12 shows the SED for individual dwarf galaxies color coded by their metallicity, with low metallicity ( $Z < 8.2$ ) in red, moderate metallicity ( $8.2 < Z < 8.7$ ) in green, and high metallicity ( $Z > 8.7$ ) in blue, normalized to the SDSS z-band flux. The average of each metallicity bin is shown as squares. The SEDs for the TNT galaxies at short wavelengths reveal that there is a correlation between metallicity and UV emission, with UV flux increasing with decreasing metallicity. At the long wavelength end, we see that

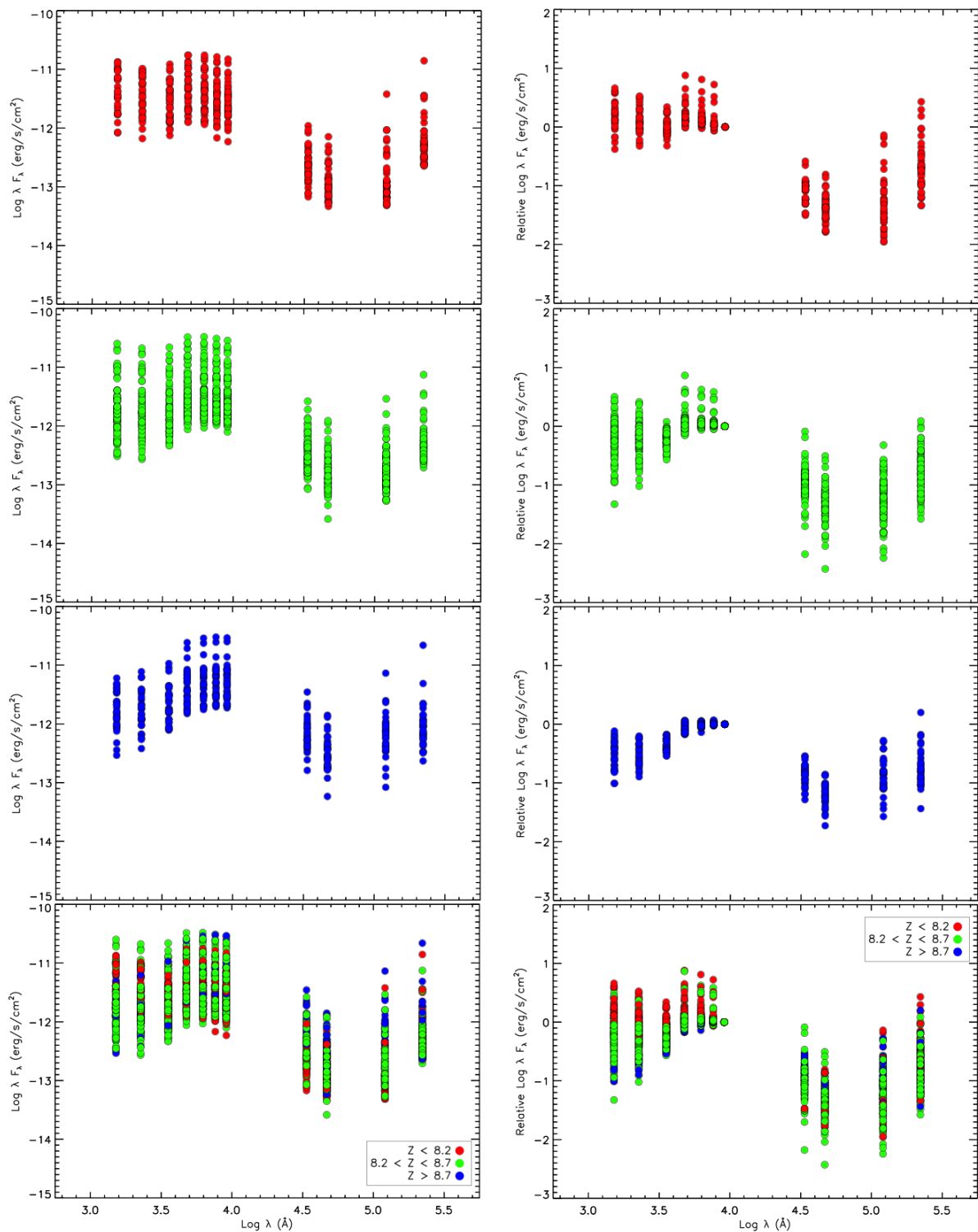


Figure 2.11 Left: The SED for each TNT galaxy separated by metallicity (red - low metallicity pairs; green - moderate metallicity pairs; blue - high metallicity pairs). The bottom panel is a combination of top three panels for the sake of direct comparison. Right: Same as left, normalized to the SDSS  $z$ -band measurement for each galaxy as a proxy for stellar mass.

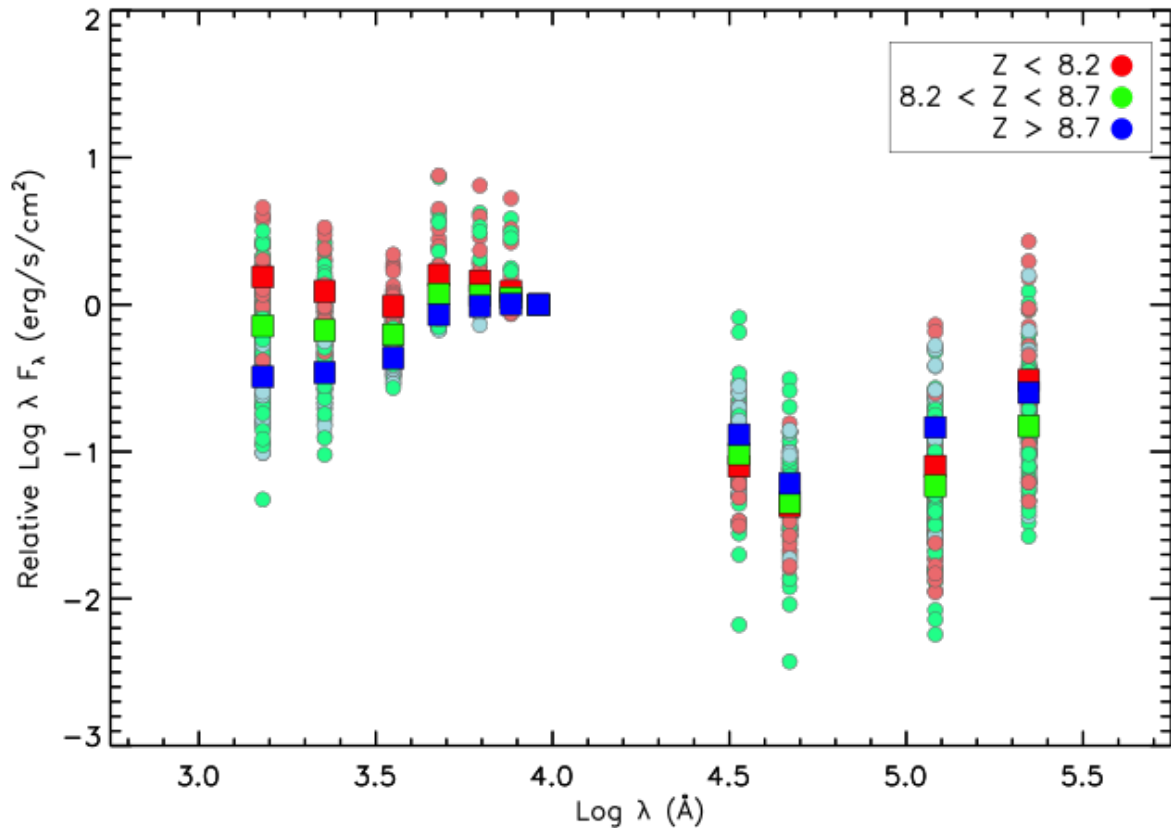


Figure 2.12 Same as bottom right panel of Figure 2.11 with all points in a single frame and the mean of each metallicity bin overplotted as a square.

the high metallicity galaxies have more flux in the W1, W2, and W3 WISE bands, while the intermediate metallicity galaxies fall below both the low and high metallicity galaxies in W4.

The UV enhancement of the low metallicity galaxies likely points to the relationship between stellar UV luminosity and metallicity; low metallicity stars are more luminous at UV wavelengths. This is because high metallicity stars are subject to the effects of ‘line blanketing’ whereby the UV radiation from the star is absorbed by the metals and re-emitted at longer wavelengths (Mokiem et al., 2004). The difference in emission at W1 and W2 suggests that the lower metallicity systems may have an older and/or cooler underlying stellar population. The relatively low emission from the low metallicity galaxies in W3 indicates that these systems form fewer PAHs than higher metallicity galaxies. In W4, we see that the lowest and highest metallicity systems have comparable fluxes, with the intermediate-metallicity galaxies emitting less at this wavelength. There are likely two different processes contributing to the observed W4 elevation of these metallicity groups. Gas in low metallicity galaxies cools less efficiently leading to higher

temperatures and thus more W4 emission. On the other hand, high metallicity galaxies have larger dust masses, which also leads to more W4 emission (Rémy-Ruyer et al., 2013).

### 2.3.5 SEDs as a function of galaxy star formation rate

Figure 2.14 shows the SED for individual dwarf galaxies color coded by their star formation rates, with low star formation rates ( $\log(SFR) < -1.5$ ) in red, moderate star formation rates ( $-1.5 < \log(SFR) < 0$ ) in green, and high star formation rates ( $\log(SFR) > 0$ ) in blue, normalized to the SDSS z-band flux. The average of each star formation rate bin is shown as squares. The pairs with high and moderate star formation rates are somewhat brighter on average in the UV than the low star formation galaxies, and are significantly brighter in the IR.

The enhanced W1 and W2 indicates either hotter stellar photospheres and/or a larger number of stars in the high star formation rate galaxies, either of which would be expected. Considering W3, with higher star formation rates, there are more stars heating the dust, thus leading to an increased IR luminosity.

### 2.3.6 SEDs as a function of massive host tidal index

As discussed in Section 1.1.3.2, massive galaxies can have a significant impact on the evolution of low mass galaxies. Specifically, the presence of a massive galaxy has been shown to quench the star formation in dwarf galaxies, through a combination of stripping the smaller galaxy of its star forming gas or heating it so that it cannot collapse to form stars. In order to explore the impact of this process in the TNT sample, we examined their SEDs as a function of tidal index (see Section 1.2.3).

Figure 2.16 shows the SED for individual dwarf galaxies color coded by their tidal index, with isolated galaxies ( $\Theta_H < 0$ ) in red, moderately isolated galaxies ( $0 < \Theta_H < 1.5$ ) in green, and non-isolated galaxies ( $\Theta_H > 1.5$ ) in blue, normalized to the SDSS z-band flux. The average of each tidal index bin is shown as squares. The isolated and marginally isolated pairs have, on average, higher relative fluxes in the ultraviolet and far-mid infrared portions of the SEDs.

We see evidence of environmental quenching, with TNT galaxies that are nearby a massive galaxy exhibiting less ongoing star formation relative to those that are more isolated from

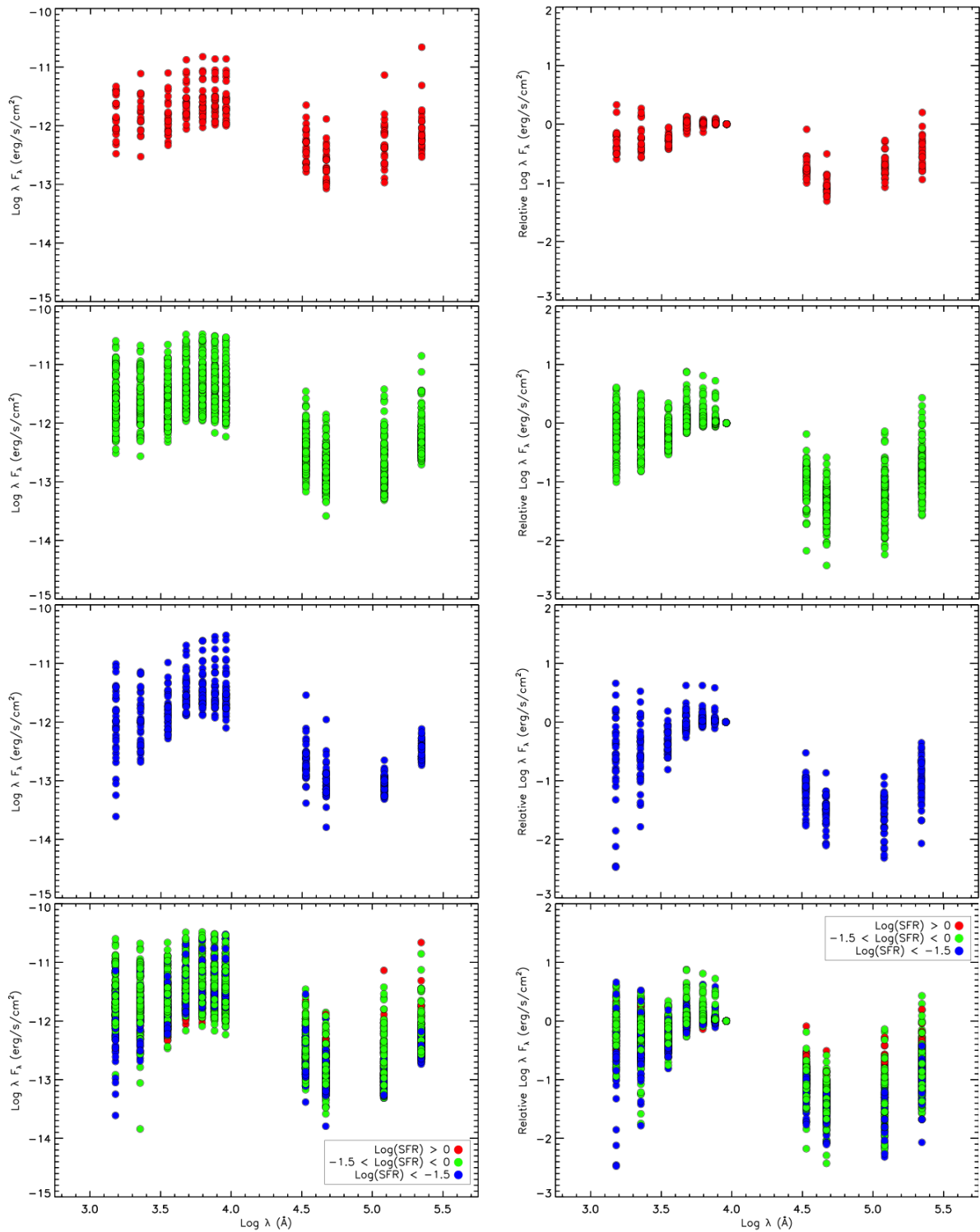


Figure 2.13 Left: The SED for each TNT galaxy separated by star formation rate (red - high SFR; green - moderate SFR; blue - low SFR). The bottom panel is a combination of top three panels for the sake of direct comparison. Right: Same as left, normalized to the SDSS  $z$ -band measurement for each galaxy as a proxy for stellar mass.

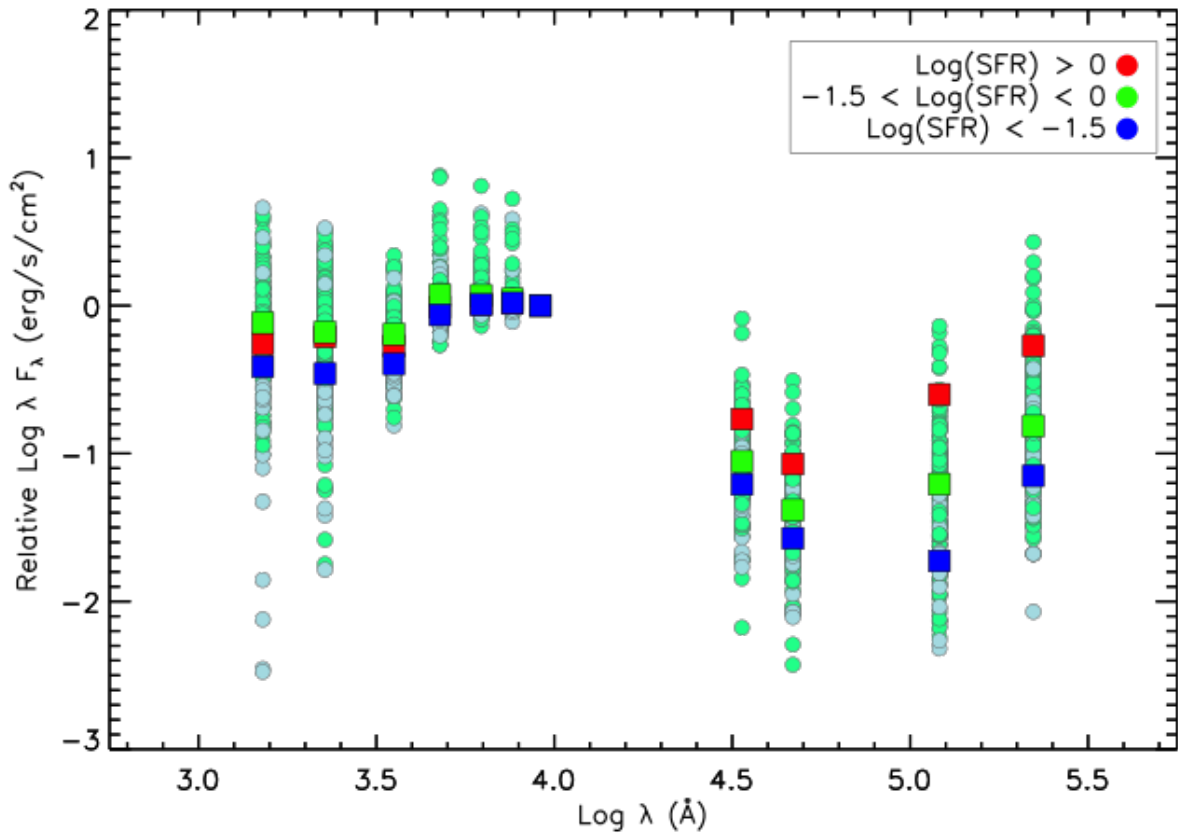


Figure 2.14 Same as bottom right panel of Figure 2.13 with all points in a single frame and the mean of each star formation rate bin overplotted as a square.

such an influence. As discussed in Section 1.1.3.2, massive galaxies are largely absent in the high redshift universe. Thus, the first dwarf galaxies, those that we believe to be the fundamental building blocks of more massive galaxies, would not have been impacted by massive galaxies. This highlights the importance of building up a sample of *isolated* dwarf galaxies in the local universe; if we are attempting to understand the processing and evolution of dwarf galaxies in the early universe by observing analogous local systems, we must account for the large scale gravitational environment of nearby galaxies.

### 2.3.7 Comparison to other astronomical systems

Brown et al. (2014) presented over 100 galaxy SEDs from the UV to the mid-IR using both spectroscopic and photometric data. This sample spans the range of morphologies, including elliptical galaxies, spiral galaxies, merging galaxies, and dwarf galaxies. Using data from 26 filters, some redundant, they were able to constrain systematic errors in their diverse set of SEDs with high accuracy ( $< 10\%$  deviations).

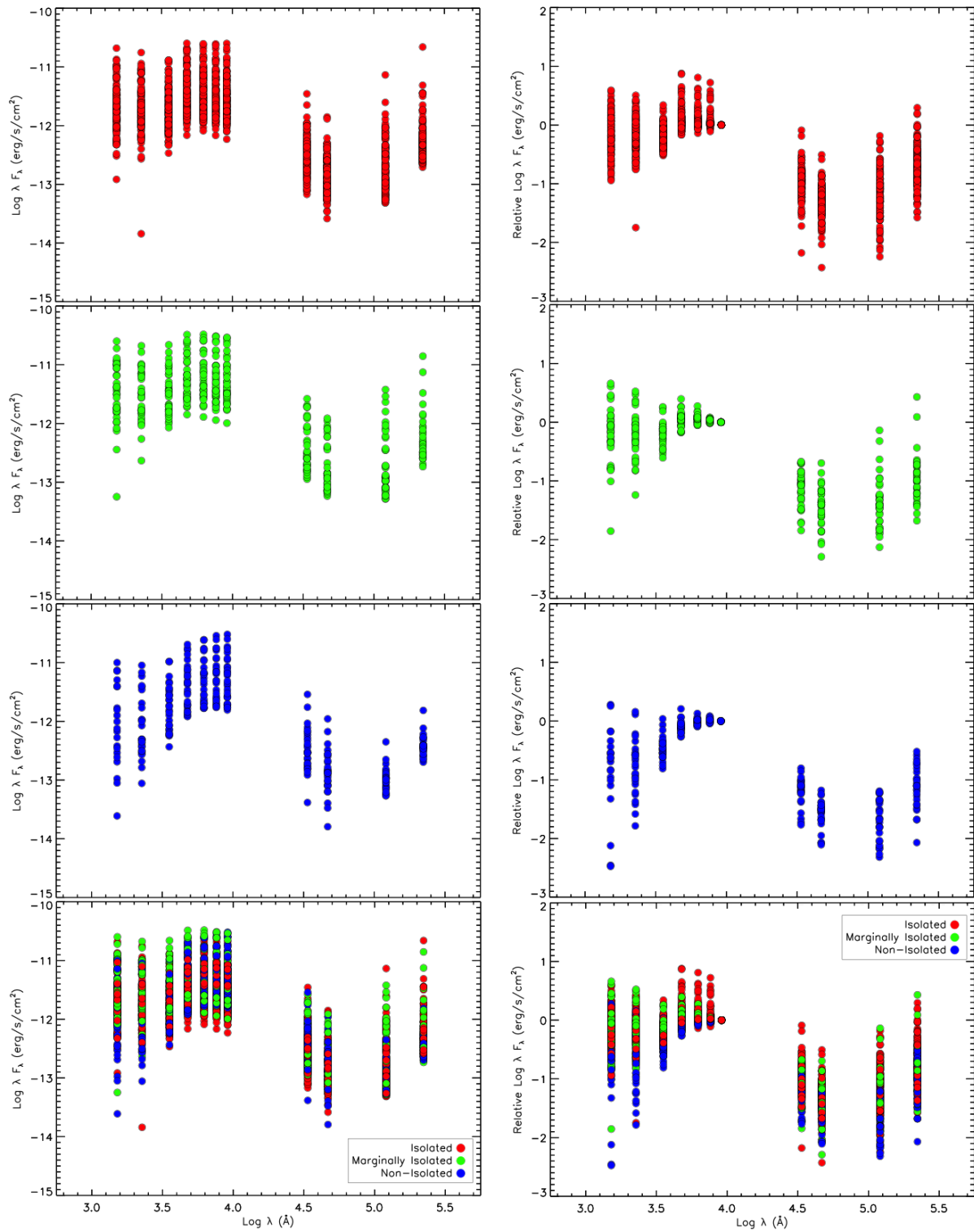


Figure 2.15 Left: The SED for each TNT galaxy separated by tidal index (red - isolated; green - marginally isolated; blue - nonisolated). The bottom panel is a combination of top three panels for the sake of direct comparison. Right: Same as left, normalized to the SDSS  $z$ -band measurement for each galaxy as a proxy for stellar mass.

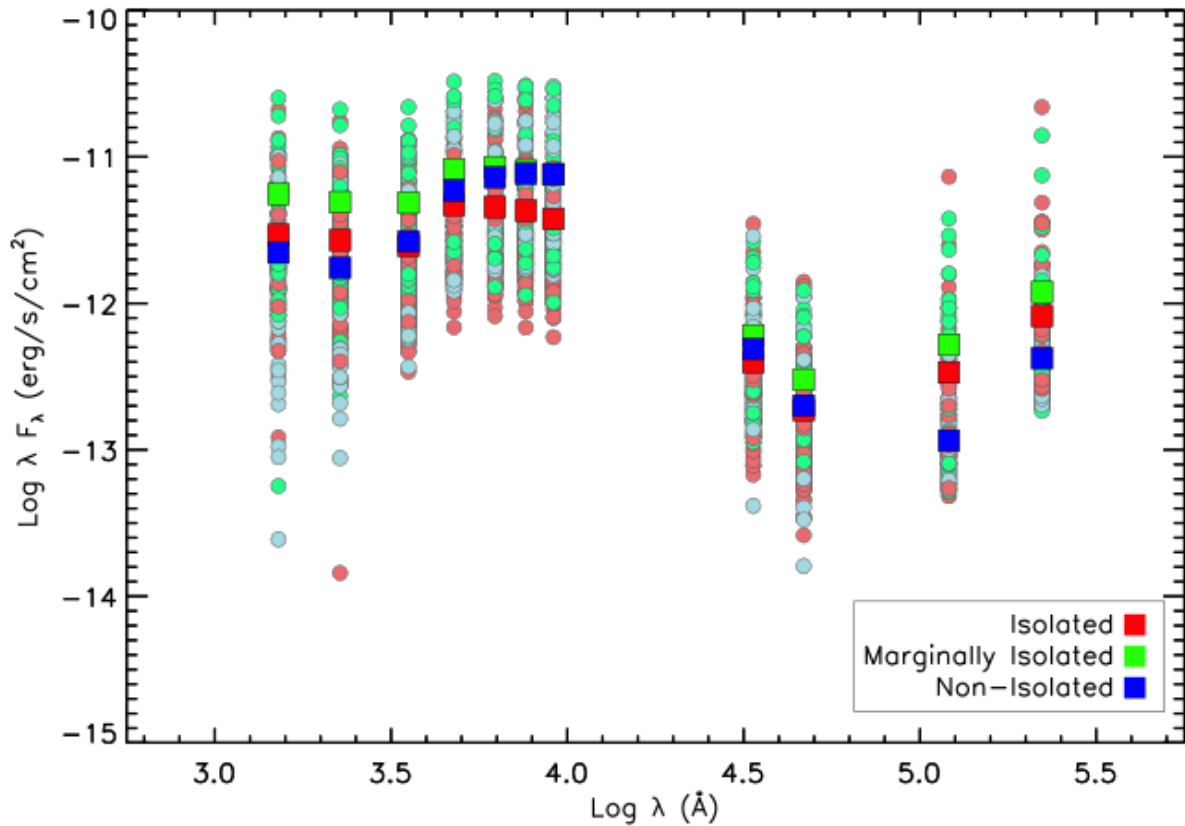


Figure 2.16 Same as bottom right panel of Figure 2.15 with all points in a single frame and the mean of each tidal index bin overplotted as a square.

Table 2.5. Comparison Object Details

Galaxy Name	Galaxy Type	Stellar Mass ( $M_{\odot}$ )	Redshift	Physical Size (Optical) (kpc)
NGC 0337	SBd	$1.6 \times 10^{10}$	0.00549	15
UGCA 219	BCD	$\sim 10^8$	0.00797	9
Arp 220	ULIRG	$\sim 10^{11} M_{\odot}$	0.0181	40

Note. — Properties of the comparison objects from [Brown et al. \(2014\)](#). Values from SIMBAD Astronomical Database and NASA/IPAC Extragalactic Database.

Shown in Figure 2.17 are the SEDs for a representative barred spiral galaxy (SBd; triangles), blue compact dwarf (BCD; squares), and an ultraluminous infrared galaxy (ULIRG; diamonds) from [Brown et al. \(2014\)](#). The photometric values for each type of galaxy is connected by a dashed line for ease of viewing. This should not be considered a physically motivated SED fit.

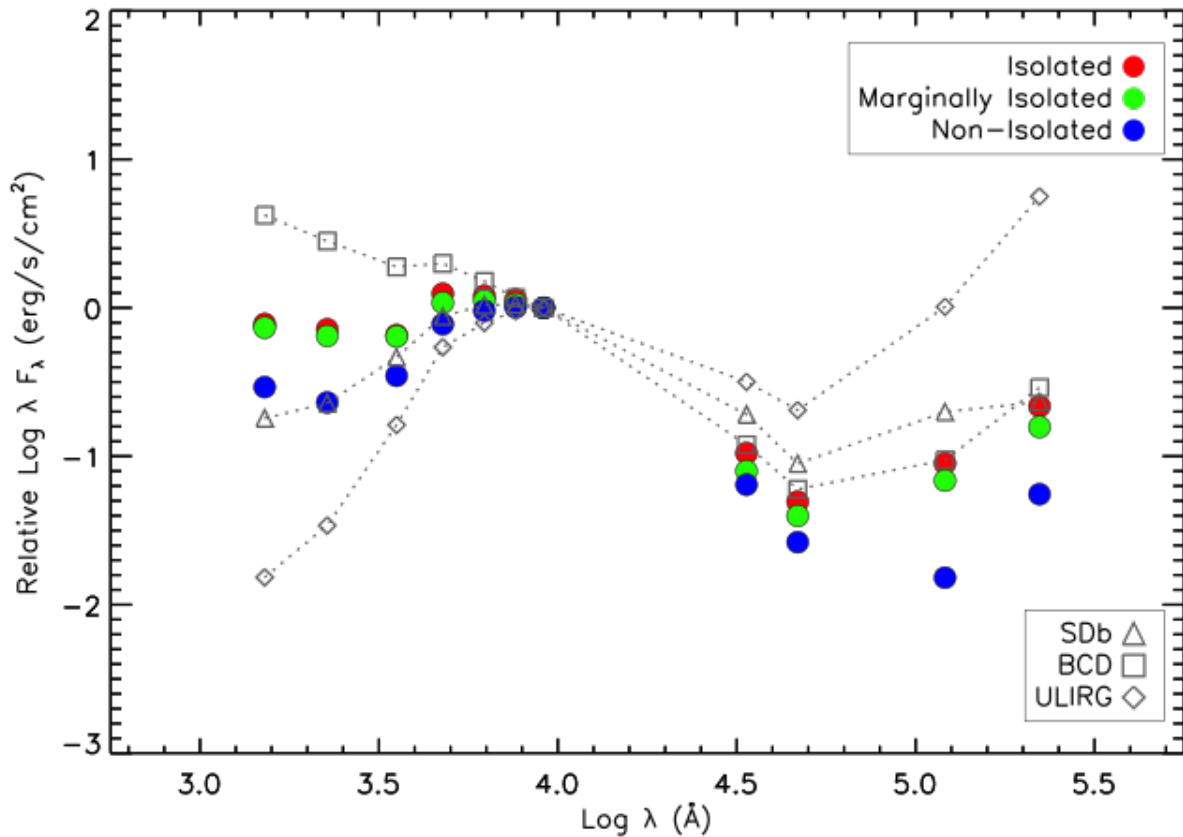


Figure 2.17 The mean of the TNT galaxy SEDs colored by tidal index (isolated in red; marginally isolated in green; non-isolated in blue) and the SEDs of a SDb (open grey triangle), a BCD (open grey square) and a ULIRG (open grey diamond). The dashed lines are only meant to help connect the data points of each comparison object and should not be interpreted as a fit to the SEDs.

### 2.3.7.1 NGC 0337 - A barred spiral galaxy

NGC 0337 (Figure 2.18) is a typical example of a star-forming galaxy with loosely coiled spiral arms. Located at a redshift of 0.00549 (within the redshift range of the TNT sample), new stars are forming in both its spiral arms and its bar. The shape of the SED of NGC 0337 is similar to that of the TNT galaxies at long wavelengths. At shorter wavelengths, in the near- and far-UV, the TNT galaxies have larger relative fluxes.

Both the TNT dwarf galaxies and the barred spiral galaxy exhibit signs of active star formation. The relative amount of UV radiation from the dwarf galaxies suggests a larger population of young massive stars. A number of dwarf galaxies are known to host statistically anomalous numbers of massive star clusters given their overall cluster population and star formation rate (e.g., NGC1705, O’Connell et al. (1994)). This SED comparison suggests a similar conclusion, namely that the star-forming low mass galaxies



Figure 2.18 SDSS ugriz image of NGC 0337, a star-forming barred spiral galaxy, for comparison to TNT galaxies in Appendix A. NGC 0337 is approximately 15 kpc in diameter.

have higher specific star formation rates (rate of star formation per unit mass) than star-forming massive galaxies. In other words, they have more massive stars than would be expected based on their physical size.

### 2.3.7.2 UGCA 219 - A blue compact dwarf galaxy

UGCA 219 (Figure 2.19) is a blue compact dwarf (BCD) located at a redshift of 0.00797, within the range of the TNT sample. BCDs are a specific class of low-mass, high surface brightness galaxies characterized by a large number of star-forming clusters. These galaxies are theorized to be a potential end-state of a merger between two dwarf galaxies (Bekki, 2008). Thus, BCDs may represent TNT galaxies at the end of their interaction, with both  $r_{\text{sep}}$  and  $v_{\text{sep}} \simeq 0$ . UGCA 219 has notably more UV flux than the TNT galaxies, with comparable optical and IR emission. In the context of the dwarf galaxy merger sequence described in Stierwalt et al. (2015), this supports the TNT findings that star formation (as traced by the presence of massive O-stars) is enhanced with decreasing pair separation.

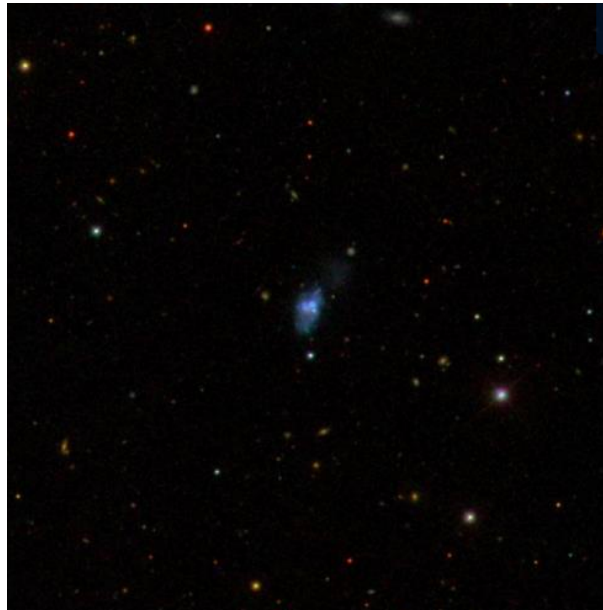


Figure 2.19 SDSS ugriz image of UGCA 219, a blue compact dwarf galaxy, for comparison to TNT galaxies in Appendix A. UGCA 219 is approximately 9 kpc in diameter.

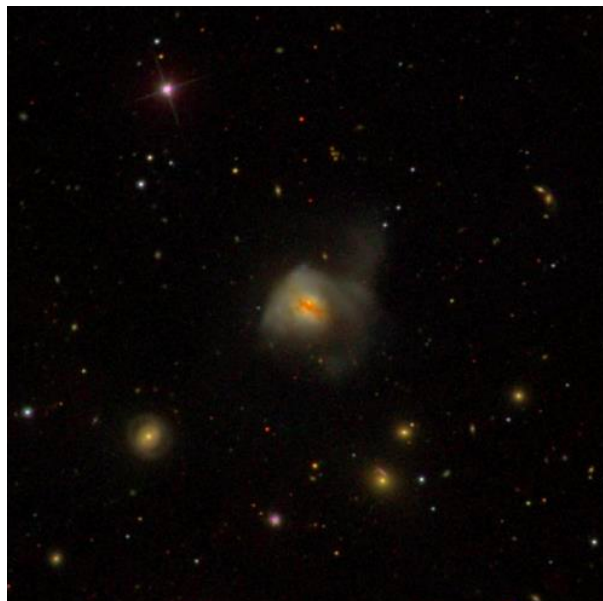


Figure 2.20 SDSS ugriz image of Arp 220, an ultraluminous infrared galaxy, for comparison to TNT galaxies in Appendix A. Arp 220 is approximately 40 kpc in diameter.

### 2.3.7.3 Arp 220 - An ultra-luminous infrared galaxy

One of primary goals of the TNT Low- $z$  program is to determine the dwarf-dwarf merger sequence, and see where it matches and where it deviates from what is known about massive galaxy mergers. Most galaxies that are classified as ‘ultraluminous infrared galaxies’ (ULIRGs) are observed to be interacting and merging massive spiral galaxies ( $> 50\%$ , Sanders et al. (1988)) and can therefore be thought of as the massive analogs of the interacting TNT dwarf galaxies (see Section 1.1.3.3 for a more thorough discussion of the similarities and differences between interacting massive galaxies and interacting dwarf galaxies). This population of galaxies is defined by infrared luminosity,  $L_{\text{IR}} > 10^{12} L_{\odot}$ , which is typically the result of a large amount of dust that has been heated by young stars. ULIRGs have irregular morphologies, indicative of interactions and mergers between massive galaxies (e.g., Armus et al. (2009)).

Arp 220 (Figure 2.20) is thought to be a prototypical ULIRG, and is the closest one to the Milky Way at  $z = 0.0181$ . From the SEDs, Arp 220 has significantly less relative UV flux and considerably more IR flux than the average TNT dwarf galaxies. The differences in the SEDs of the two types of systems can be attributed to several factors. ULIRGs contain more dust than the TNT galaxies, accounting for their high IR emission. This is either the result of higher dust production by supernovae in massive galaxy mergers, the relatively weak hold that the gravitational potential wells of dwarf galaxies have on their dust (i.e. low mass galaxies lose what dust does form through SNe during the interaction process), or a combination of these effects. This could also be indicative of the relative timescales of the burst of star formation that is inspired in interacting massive galaxies versus interacting dwarf galaxies; the dwarf galaxies may form their stars over a shorter period of time than the massive galaxies, which would mean that we would be unlikely to observe the short, dusty stage of the star formation process in these systems. Furthermore, this implies a potentially different mode of gas processing in the interstellar medium of these two types of galaxy pairs – massive galaxy interactions appear to produce and/or retain more dust than their low mass counterparts.

## 2.4 Discussion and Conclusion

The spectral energy distributions of the TNT interacting dwarf galaxies reveal many important features of their evolution. In considering pair properties, we observe a higher rate of star formation (as indicated by UV emission) in pairs that are close and moving

slow relative to one another. Based on their projected radial and velocity separations, these galaxy pairs have likely completed several passages and are in the late stages of their interaction. As is seen in other examples of galaxy mergers, the interactions between these galaxies have inspired bursts of star formation throughout their merging process (e.g., [Patton et al. \(2011\)](#)). We also observe that galaxies with low mass ratios (not a host/satellite system) exhibit higher tracers of star formation. Their similar masses make it such that neither galaxy dominates in terms of tidal forces, allowing both galaxies involved in the interaction to hold on to their interstellar medium and form stars.

In considering the properties of each galaxy, we note the interplay between metallicity and star formation rate, and their collective impact on the galaxy's dust. Higher star formation rates leads to more dust heating. It also increases the metallicity of the ISM, which is correlated with higher dust mass. These processes are reflected primarily in the WISE IR emission of the SEDs.

We further explored the impact of the dwarf galaxy's global gravitational environment, finding that paired dwarf galaxies that are isolated from massive galaxies have enhanced star formation indicators over those that are not. This is indicative of the effect that massive galaxies have on the physical processes taking place in low mass systems. Specifically, nearby massive galaxies can halt star formation, leading to quenched dwarf galaxies.

In the context of other astronomical objects, we can paint a picture of where the interacting dwarf galaxies fit in in the larger context of galaxy evolution. Dwarf galaxies appear to be most similar to star-forming spiral galaxies, though possibly more efficient at forming stars per unit mass. We see that blue compact dwarf galaxies follow the star formation trend seen in interacting dwarfs, with star formation rates increasing with decreasing pair separation. Nominally the BCDs have a projected  $r_{\text{sep}} = 0$ , and their star formation rates are accordingly higher. We also gain insight in to how interactions between dwarf galaxies differ from interaction between massive galaxies (ULIRGs). ULIRGs are significantly dustier leading to both an increase in IR flux relative to the TNT dwarfs and a decrease in UV flux, likely due to the volume of UV-absorbing dust in the more massive galaxies.

Future work will begin with extending the range of wavelengths included in the SED analysis. At the short wavelength end, gamma ray and x-ray observations will allow for the study of AGN, dense objects like pulsars and neutron stars, and transient high-energy bursts. On the other end of the electromagnetic spectrum, submillimeter and radio observations will add to our understanding of dust, obscured star formation, and molecular gas.

# Chapter 3

## Narrowband H $\alpha$ Imaging with Gemini/GMOS-N

### 3.1 Introduction

While the processes regulating star formation and the interstellar medium (ISM) in massive interacting galaxies have been studied extensively, little is known about the extent to which these processes occur in the low metallicity, shallow gravitational potential wells of dwarf galaxies. Moreover, we do not know how the star formation is distributed in interacting low mass galaxies. In massive galaxy interactions, star formation tends to be centrally concentrated (e.g., [Patton et al., 2013](#); [Moreno et al., 2015](#)). However, the shallower gravitational potentials of dwarf galaxies ( $M_* < 5 \times 10^9 M_\odot$ ) may not allow for the funneling of the ISM towards the global center of mass of the system, and thus not lead to the triggering of similarly concentrated star formation.

Furthermore, dwarf galaxies lack large-scale shear from differential rotation ( $v_{\text{rot}} < 100 \text{ km s}^{-1}$  compared to several  $100 \text{ km s}^{-1}$  for massive galaxies; [Lelli et al. \(2014\)](#)). Differential rotation describes a galaxy in which the material in the inner regions of a galaxy orbit at faster speeds than in the outer regions. It is responsible for the formation of spiral arms in disk galaxies<sup>1</sup>, which is where many of the stars form in spiral galaxies. Dwarf galaxies that lack this rotation must rely on a different process to condense gas for star formation.

---

<sup>1</sup>Though the arms can be formed by differential rotation, they are maintained as density waves.

Dwarf galaxies also generally have lower metal abundances than their massive counterparts, which can impact cooling (Kirby et al., 2013). In terms of star formation, the temperature ( $T$ ) of a molecular cloud is related to its Jeans mass ( $M_J$ , the fundamental mass at which a gas cloud with density  $n$  will collapse to form a protostar) as

$$M_J \propto \left( \frac{T^3}{n} \right)^{1/2}. \quad (3.1)$$

Other properties being equal, a hotter cloud requires more mass before it can collapse to form a star. Thus, dwarf galaxies with fewer metals may tend to form more high mass stars than massive galaxies. On the other hand, a low metal abundance can also lead to more significant expulsion of gas outflows via stellar winds, which in turn can accelerate quenching.

All of these factors could lead to substantially different star formation in dwarf galaxies than is seen in massive galaxy interactions. Where star formation takes place and the extent to which it is distributed or clumped has important implications for feedback processes throughout galaxy evolution.

One specific area of star formation that might be different in dwarf galaxies is the formation of massive ( $\sim 10^5 - 10^6 M_\odot$ ) star clusters. These star-forming regions have large populations of high mass-stars and represent extreme environments with star formation similar to that in the early universe. Further, they are the proposed progenitors of globular clusters (GCs), which are some of the oldest structures in the universe (Johnson et al., 2009; Gallagher & Grebel, 2002). GCs are detected in most nearby large galaxies, including our own Milky Way. These massive clusters are therefore essential components to galaxies, and their formation is fundamental to understanding galaxy evolution.

A range of studies of massive galaxies have demonstrated that star clusters appear to follow a power-law mass distribution of  $\alpha \sim -2$  (e.g., Whitmore et al., 2014), which suggests that the most massive clusters are simply the tail end of a continuous mass distribution. In contrast, a number of dwarf galaxies are known to host statistically anomalous numbers of massive star clusters given their overall cluster population and star formation rate (e.g., NGC1705, O’Connell et al. (1994)). Whether or not these clusters have a power-law mass distribution in these environments has fundamental implications for the formation of globular clusters and the impact of stellar feedback at early times in the universe. For example, feedback from young massive clusters (in the form of ionizing radiation, supernovae explosions, and stellar winds from massive stars) may either (1)

compress surrounding gas and trigger additional star formation, or (2) heat or expel the gas, making it unavailable for star formation. Which process occurs will be impacted by the environment in which the clusters are in; the gas in low density environments may be more susceptible to escape and heating, while gas that is in environments that are of high enough density will be compressed in to new regions of star formation.

While the Sloan Digital Sky Survey (SDSS, [Abazajian et al. \(2009\)](#)) archival data available for the TNT interacting dwarf galaxies allows us to estimate the rate of star formation in each galaxy, these results are based only on the star formation rates as determined from the SDSS 3'' optical fibers (see [Section 1.3](#)). The fibers are typically placed either in the center of a galaxy or on an individually bright knot of star formation, with covering fractions (the ratio of the area of the fiber to the area of the galaxy) ranging from 2% to 55% with a median of 17% ([Stierwalt et al., 2015](#)). Thus, the results derived from the H $\alpha$  emission line in this data does not give an indication of the star formation and star cluster distribution (see [Figure 1.15](#)).

In order to study the cluster population of the TNT galaxies, we have undertaken an H $\alpha$  narrowband imaging campaign. By observing entire galaxies in this star formation tracer, we are able to determine both the total amount of star formation and its distribution and packaging within the galaxy. In this chapter, we present narrowband H $\alpha$  imaging of a subset of the TNT sample with spatial resolution matched to the native size of giant molecular clouds ( $\sim 100$  pc, [Murray \(2011\)](#)). At this scale, we will be able to probe the character of individual massive star forming clusters in the dwarf galaxies and determine their location within their galaxy. From this, we can begin to understand what feedback from massive stars may have been like in early universe galaxies.

This chapter is organized as follows: in [Section 3.2](#) we describe the targets and observing strategy. In [Section 3.3](#) we present the results of the Gemini imaging, specifically the extent to which stellar mass, global star formation rate, and local gravitational environment impact the number and luminosities of HII regions identified in each dwarf galaxy. In [Section 3.4](#) we discuss the implications of these results.

Table 3.1. Observing Target Details

Pair Name	Redshift	$r_{\text{sep}}$ (kpc)	$v_{\text{sep}}$ (km s $^{-1}$ )	$\Theta_H$ (Host)	$\Theta_D$ (Dwarf)
dm0827+46	0.0074	0.850	54.0	-0.75	6.2
dm1031+41	0.0088	1.08	42.0	-2.1	5.4
dm1647+21	0.0088	5.35	27.0	1.3	3.0
dm1225+50	0.0083	14.0	19.0	-1.5	2.7
dm1242+34	0.014	15.8	40.0	-0.97	2.9
dm0916+06	0.012	17.7	228.	-2.7	3.1
dm0930+60	0.014	20.8	1.00	-2.7	1.9
dm1237+18	0.0085	20.8	18.0	-0.36	1.5
dm1418+21	0.0086	27.3	23.0	-3.7	0.44
dm1718+30	0.015	30.0	6.00	-1.4	2.1
dm1616+34	0.0089	33.5	22.0	-3.7	0.74
dm1314+35	0.0079	49.9	10.0	-2.2	0.44
dm1503+00	0.0053	1.38	25.0	1.1	4.6
dm1406+55	0.0068	19.4	252.	4.2	2.3
dm1505+01	0.0069	20.9	253.	1.4	1.8
dm1352+03	0.015	23.1	1.00	0.64	2.4
dm1219+06	0.0066	23.3	135.	4.4	1.4
dm1032+28	0.0054	29.6	17.0	3.1	1.8
dm1427+56	0.0065	30.7	108.	3.1	1.8
dm1220+08	0.015	37.7	121.	1.6	1.4
dm1214+49	0.014	38.7	91.0	-0.034	1.2
dm1051+65	0.011	40.9	83.0	2.7	1.1
dm1218+05	0.0086	46.0	261.	2.1	0.77

Note. — Details on the subset of TNT dwarf galaxy pairs included in this study. For tidal index, a subscript of  $H$  refers to the influence of the nearest massive host and  $D$  refers to the dwarf pair member. A galaxy is isolated if  $\Theta < 0$ , nonisolated if  $\Theta > 1.5$ , and marginally isolated if it falls in between these values.

## 3.2 Observations

### 3.2.1 Sample Properties

The sample investigated here is selected from the full TNT sample to cover a range of projected radial and velocity separations (Stierwalt et al., 2015). It includes pairs between redshifts of  $z = 0.0053$  and  $z = 0.015$ , a range determined based on the width of the filter used for the observations. The pairs in this subsample exist in a range of environments as determined by their tidal indices with respect to their nearest massive host and their pair member (see Section 1.2.3). The redshift, projected radial separation, projected velocity separation, tidal index with respect to the nearest massive galaxy, and tidal index with respect to the pair member are reported in Table 3.1.

### 3.2.1.1 Optical imaging with Gemini North/GMOS-N

Detecting and resolving star forming regions in low mass galaxies requires large aperture telescopes (for their light collecting area and angular resolution, respectively). The Gemini North Telescope, located in Hawaii, has an 8.1-m mirror and can achieve an angular resolution of  $0.5''$  (115 pc at a distance of 48 Mpc, the mean distance of the subsample). Further, the site often experiences photometric conditions that allow for the accurate measurement of the star formation rates in the galaxies.

Observations were conducted with the Gemini Multi-Object Spectrograph (GMOS, [Hook et al. \(2004\)](#)) on Gemini North during dark photometric time during the first semester of 2016. The GMOS  $5.5'$  field of view ensured that the TNT dwarf pairs would be well-contained within the 5.5 square arcminute field of view of GMOS-N ( $\theta_{\text{sep}} \lesssim 4'$ ). A narrowband H $\alpha$  continuum filter (HaC,  $\lambda_{\text{central}} = 6620 \text{ \AA}$ , width= 60  $\text{\AA}$ ) was used as a redshifted H $\alpha$  filter, and an SDSS  $r'$  filter ( $\lambda_{\text{central}} = 6300 \text{ \AA}$ , width= 1360  $\text{\AA}$ ) for continuum subtraction. Each target field was observed for a total of 460 seconds in H $\alpha$  and 280 seconds in r-band, split into individual exposures of 115 seconds and 70 seconds, respectively. The individual exposures were dithered by  $5''$  in both the X- and Y-directions to allow for continuous coverage between the chip gaps. The data was reduced using the Gemini/GMOS IRAF package<sup>2</sup>. Flux calibration was done using observations of Landolt standard fields ([Landolt, 1992](#)) and confirmed using SDSS photometry and spectroscopy. The average PSF of the reduced images is  $0.63''$ , which corresponds to a physical scale of 150 pc at the mean distance of the observed TNT galaxy pairs (48 Mpc).

## 3.2.2 Comparison Systems

### 3.2.2.1 The Magellanic Clouds

The Large Magellanic Cloud (LMC) and Small Magellanic Cloud (SMC) system is the closest example of interacting dwarf galaxies. This well-studied pair is located just 50 kpc from the Milky Way and, with a  $\Theta_H = 3.7$  with respect to the Milky Way, is not isolated. The LMC/SMC system has been the subject of a vast range of multiwavelength studies, and, like the TNT galaxies, exhibits clearly asymmetric morphology indicative of tidal interactions ([Besla et al., 2007](#)). The LMC is home to 30 Doradus (30Dor), a massive HII region that is 200 pc in diameter ([Indebetouw et al., 2009](#)). As one of the largest and most

<sup>2</sup><http://www.gemini.edu/sciops/instruments/gmos/data-format-and-reduction>

massive star clusters forming in the nearby universe, 30Dor is the best example of a local super star cluster. While the formation of this cluster is still not fully understood, the feedback from the young stars in 30Dor has been observed triggering a new burst of star formation in the LMC (Walborn et al., 1999; Kalari, 2017). By including the properties of the Magellanic Clouds and 30Dor in our analysis on interacting dwarf galaxies, we may be able to address (1) what conditions are necessary to form a region like 30Dor, and (2) how prevalent are star forming regions like 30Dor. We may also be able to glean further insight in to the physical processes occurring in the TNT galaxies that we can not yet resolve at their redshifts.

### 3.2.2.2 Previous work on diffuse H $\alpha$ emission fraction

In addition to understanding the formation of and feedback from young stars in the TNT dwarf galaxies, we are also interested in how this star formation is packaged. Are stars forming uniformly throughout the systems, or are they distributed in more compact configurations? One way to quantify this is to determine what fraction of the light is contained in distinct regions as opposed to a diffuse component of the ISM.

Similar work has been done using the Survey for Ionization in Neutral Gas Galaxies (SINGG) H $\alpha$  survey of HI-selected galaxies (Meurer et al., 2006). The SINGG galaxies are all gas rich systems that span a range of stellar masses ( $10^7 M_{\odot} < M_{HI} < 10^{11} M_{\odot}$ ) and radial velocities ( $v_r < 1.27 \times 10^4 \text{ km s}^{-1}$ ), as well as exhibit a variety of star forming characteristics. Oey et al. (2007) investigated the fraction of H $\alpha$  emission that is contained in the diffuse component of the warm interstellar medium ( $f_{\text{WIM}}$ ) in these systems in order to understand how this fraction is related to the physical properties of the galaxies. Comparing the TNT star formation packaging properties to this diverse population of galaxies will afford us insight in to how the interacting dwarf galaxies compare to other star forming galaxies.

### 3.2.2.3 Previous work on galaxy-wide star formation properties

Along with the star formation packaging, once identified we can also explore the properties of the compact star forming regions themselves. The number of star forming clumps, how bright they are, and how these features vary with galaxy and environmental properties are all important for understanding how stellar feedback may guide the evolution of interacting low mass galaxies.

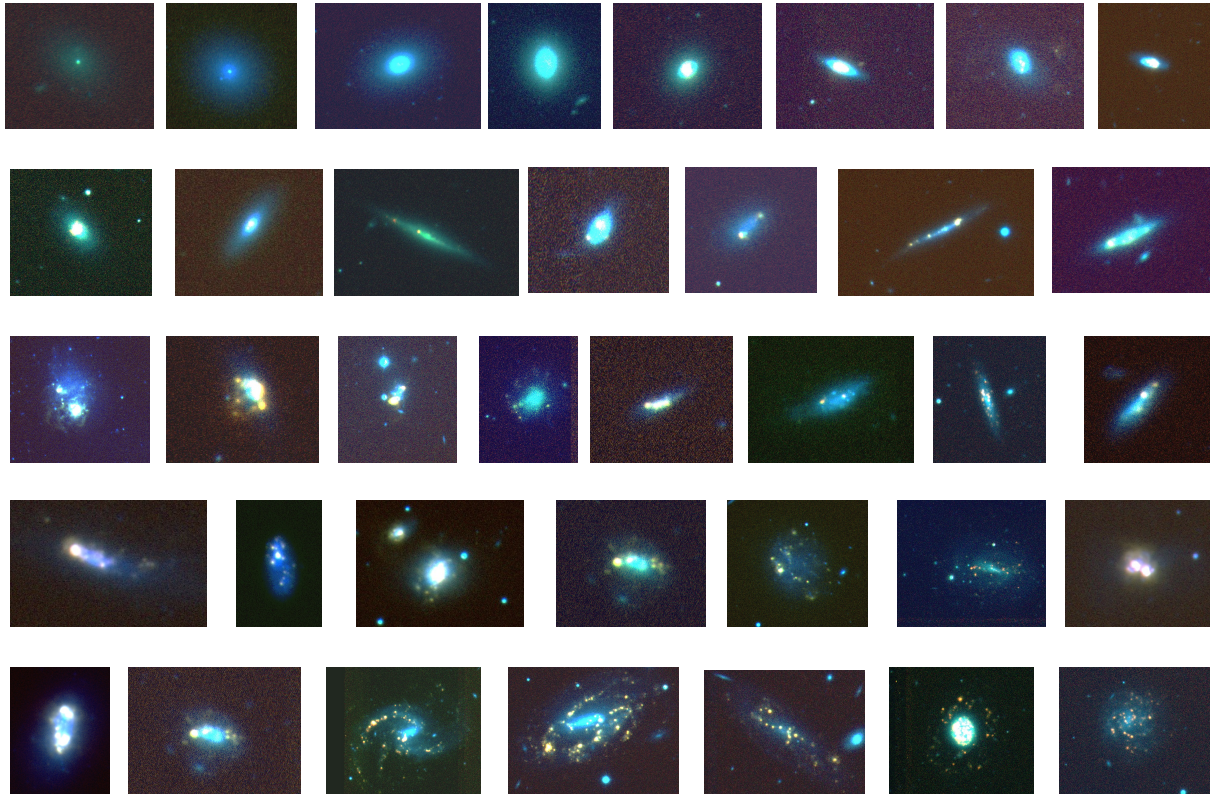


Figure 3.1 Three color images of the TNT Gemini sample. Continuum-subtracted H $\alpha$  in red, H $\alpha$  + continuum in green, r-band in blue.

[Zaragoza-Cardiel et al. \(2018\)](#) looked at star forming clumps in a sample of galaxies that includes both interacting pairs and non-interacting systems. They used archival ultraviolet, optical, and infrared data to examine the global star formation properties of these galaxies, and also considered the properties of over 1500 individual star forming complexes across the entire sample: 46 galaxies selected from the Spirals, Bridges, and Tails (SBT) sample of interacting galaxies (see [Smith et al. \(2010\)](#) for sample details) and 30 non-interacting spiral galaxies identified in archival *Spitzer* data. These results will allow us to interpret the properties of the TNT star forming regions identified in the narrowband H $\alpha$  data. Specifically, we will use the [Zaragoza-Cardiel et al. \(2018\)](#) sample to contextualize the number and luminosity of clumps in our TNT galaxies.

### 3.3 Results

The reduced Gemini/GMOS data can be seen in Figure 3.1. These three color images use red for continuum-subtracted H $\alpha$  emission, green for H $\alpha$  + continuum, and blue for

$r$ -band emission for blue. We observe a range of morphologies in these galaxies ranging from smooth and centrally concentrated to irregular and clumpy.

### 3.3.1 Star Formation Rates

Surphot (Reines et al., 2008) was used to perform custom aperture photometry on both the calibrated  $r$ -band and  $H\alpha$  images (See Table 3.2). Measured  $H\alpha$  luminosities were used to compute star formation rates (SFR), applying the Kennicutt (1998) relation:

$$\text{SFR}(M_{\odot} \text{ yr}^{-1}) = 7.9 \times 10^{-42} L(H\alpha) \text{ (ergs s}^{-1}\text{)} \quad (3.2)$$

These measured properties are given in Table 3.2.

Table 3.2. Measured Properties of TNT Gemini Sample

Galaxy ID	$L_r$ (ergs s <sup>-1</sup> )	$L_{H\alpha}$ (ergs s <sup>-1</sup> )	log(SFR) ( $M_{\odot} yr^{-1}$ )	log(sSFR) ( $yr^{-1}$ )
dm0827+46a	41.1	39.7	-1.4	-9.2
dm0827+46b	41.1	39.8	-1.3	-9.3
dm1031+41a	40.7	38.9	-2.2	-10
dm1031+41b	40.9	39.2	-1.9	-11
dm1647+21a	41.4	40.0	-1.1	-9.4
dm1647+21b	41.2	40.2	-0.87	-8.7
dm1225+50a	42.0	40.6	-0.5	-7.6
dm1225+50b	41.3	39.8	-1.3	-8.8
dm1242+34a	41.8	40.1	-0.96	-8.4
dm1242+34b	41.9	40.3	-0.81	-9
dm0916+06a	41.5	40.2	-0.9	-9.1
dm0916+06b	42.2	40.6	-0.48	-8.4
dm0930+60a	41.7	40.4	-0.68	-8.2
dm0930+60b	41.7	40.8	-0.27	-8.2
dm1237+18a	40.9	39.7	-1.4	-10
dm1237+18b	40.8	39.4	-1.7	-9.5
dm1418+21a	40.9	39	-2.1	-9.7
dm1418+21b	40.7	40	-1.1	-8.6
dm1718+30a	42.3	40.9	-0.16	-9
dm1718+30b	41.7	39.9	-1.2	-9.2
dm1616+34a	41.1	39.6	-1.5	-10
dm1616+34b	40.9	39.7	-1.4	-9.5
dm1314+35a	42.0	40.4	-0.72	-7.9
dm1314+35b	41.1	39.3	-1.8	-9.2
dm1503+00a	40.7	39.5	-1.6	-9.9
dm1503+00b	40.3	39	-2.1	-11
dm1406+55a	41.6	38.6	-2.5	-11
dm1406+55b	41.3	39.5	-1.6	-9.2
dm1505+01a	41.1	38.9	-2.2	-10
dm1505+01b	41.1	39.6	-1.5	-10
dm1352+03a	41.6	39.9	-1.2	-10
dm1352+03b	41.9	40.2	-0.91	-9
dm1219+06a*	–	–	–	–
dm1219+06b*	–	–	–	–
dm1032+28a	40.7	38.8	-2.3	-10

Table 3.2 (cont'd)

Galaxy ID	$L_r$ (ergs s $^{-1}$ )	$L_{H\alpha}$ (ergs s $^{-1}$ )	log(SFR) ( $M_{\odot}yr^{-1}$ )	log(sSFR) ( $yr^{-1}$ )
dm1032+28b	41.2	37.9	-3.2	-11
dm1427+56a	40.8	38.8	-2.3	-9.3
dm1427+56b	41.2	39.1	-2	-9.1
dm1220+08a	41.9	40.2	-0.87	-8.9
dm1220+08b	41.6	40.1	-1	-8.8
dm1214+49a	41.1	39.4	-1.7	-9.4
dm1214+49b	41.4	40	-1.1	-8.4
dm1041+65a	41.3	39.5	-1.6	-9.5
dm1041+65b	41.0	39.2	-2	-9.2
dm1218+05a	41.7	39.6	-1.5	-10
dm1218+05b	41.2	39.5	-1.6	-10

Note. — \*For one of our pairs (dm1219+06), no H $\alpha$  emission was detected above the noise in the Gemini/GMOS-N data.

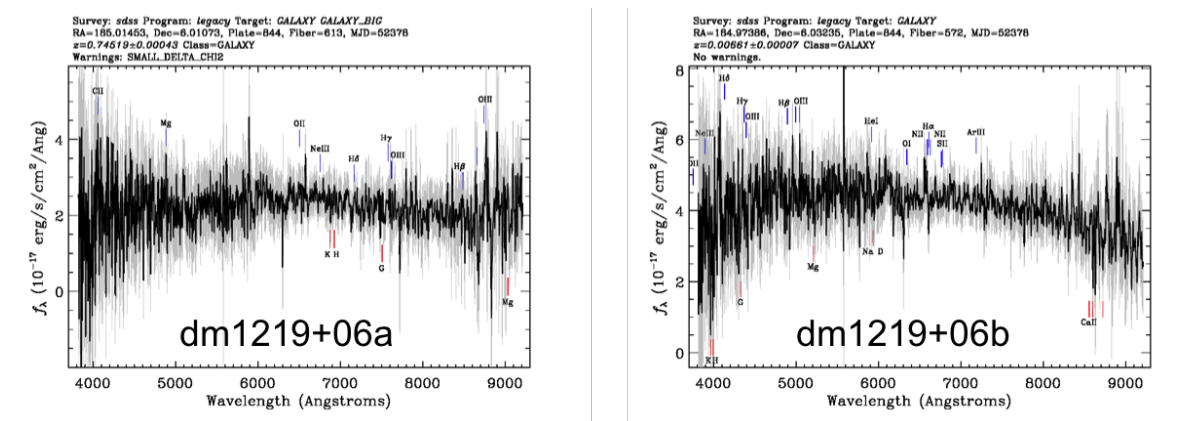


Figure 3.2 SDSS optical spectra for dm1219+06a and dm1219+06b, demonstrating the noise levels.

**A note on TNT dwarf pair dm1219+06:** For one of our pairs (dm1219+06), no H $\alpha$  emission was detected above the noise in the Gemini/GMOS-N data. The original selection criterion for the TNT sample required a signal-to-noise ratio  $> 1$  in each emission line used to measure the galaxy properties. Based on the high noise level in their spectra (see Figure 3.2), it is possible that the original H $\alpha$  luminosities may have been overestimated.

In Figure 3.3 we show how our measured Gemini SFRs compare to both the SDSS fiber SFRs (left) and the SDSS extrapolated SFRs (right). As expected, the total SFRs from the Gemini data are greater than the star formation rates derived from the SDSS 3'' fiber. They are also generally consistent with the SDSS extrapolated values. Of note are two outliers in which the total SFR measured with Gemini is lower than the fiber-based value

from SDSS. This appears to be due to an error in the SDSS reported values from DR7. We further investigate the impact of a massive gravitational force on the TNT dwarf galaxy SFRs. The galaxies are plotted in panels according to their isolation from nearby massive galaxies ( $\Theta_H$ ) and colored accordingly (red - isolated galaxies; green - marginally isolated galaxies; blue - nonisolated galaxies). We see that dwarf galaxies with larger  $\Theta_H$  (less isolated) tend to have lower SFRs than their more isolated counterparts.

Figure 3.4 shows the effect of each dwarf's pair galaxy on the SFR. The galaxies are plotted in panels according to their isolation from their SDSS-identified pair member ( $\Theta_D$ ) and colored accordingly (light red - isolated galaxies; light green - marginally isolated galaxies; light blue - nonisolated galaxies). Note that, as expected, none of the galaxies are identified as isolated from their dwarf pair member. While we could hypothesize that dwarfs that are more strongly interacting with their pair member (higher tidal indices) would have higher star formation rates, we do not see strong evidence of that here.

Figure 3.5 shows the measured star formation rates as a function of the galaxy's stellar mass and colored by  $\Theta_H$  (red - isolated galaxies; green - marginally isolated galaxies; blue - nonisolated galaxies). As expected based on the star formation main sequence, the star formation rate of the galaxies increases with stellar mass. The tendency for dwarf galaxies near massive hosts to have lower star formation rates is evident. For reference, the LMC is shown as a diamond and the Zaragoza-Cardiel et al. (2018) interacting sample is shown as dark grey squares. The light grey line is the star forming main sequence as defined in Zaragoza-Cardiel et al. (2018). The TNT dwarf galaxies almost all have elevated star formation rates with respect to their stellar mass. Those that fall near the main sequence are primarily not isolated from their nearest massive neighbor.

Figure 3.6 again shows the measured star formation rates as a function of the galaxy's stellar mass, this time colored by  $\Theta_D$ . In contrast to the previous plot, there does not appear to be a correlation between  $\Theta_D$  and the total SFR of each galaxy.

### 3.3.2 H $\alpha$ Region Ratios

H $\alpha$  regions were identified and defined using HIIphot (Thilker et al. (2000)) with a signal-to-noise detection threshold of 20 and a terminal gradient of  $1 \text{ cm}^{-6} \text{ pc}$  corresponding to an H $\alpha$  surface brightness of  $2.06 \times 10^{-18} \text{ erg s}^{-1} \text{ cm}^{-2} \text{ arcsec}^{-2}$ . We used data products from HIIphot to generate region-only images of each dwarf galaxy, and then used Surphot

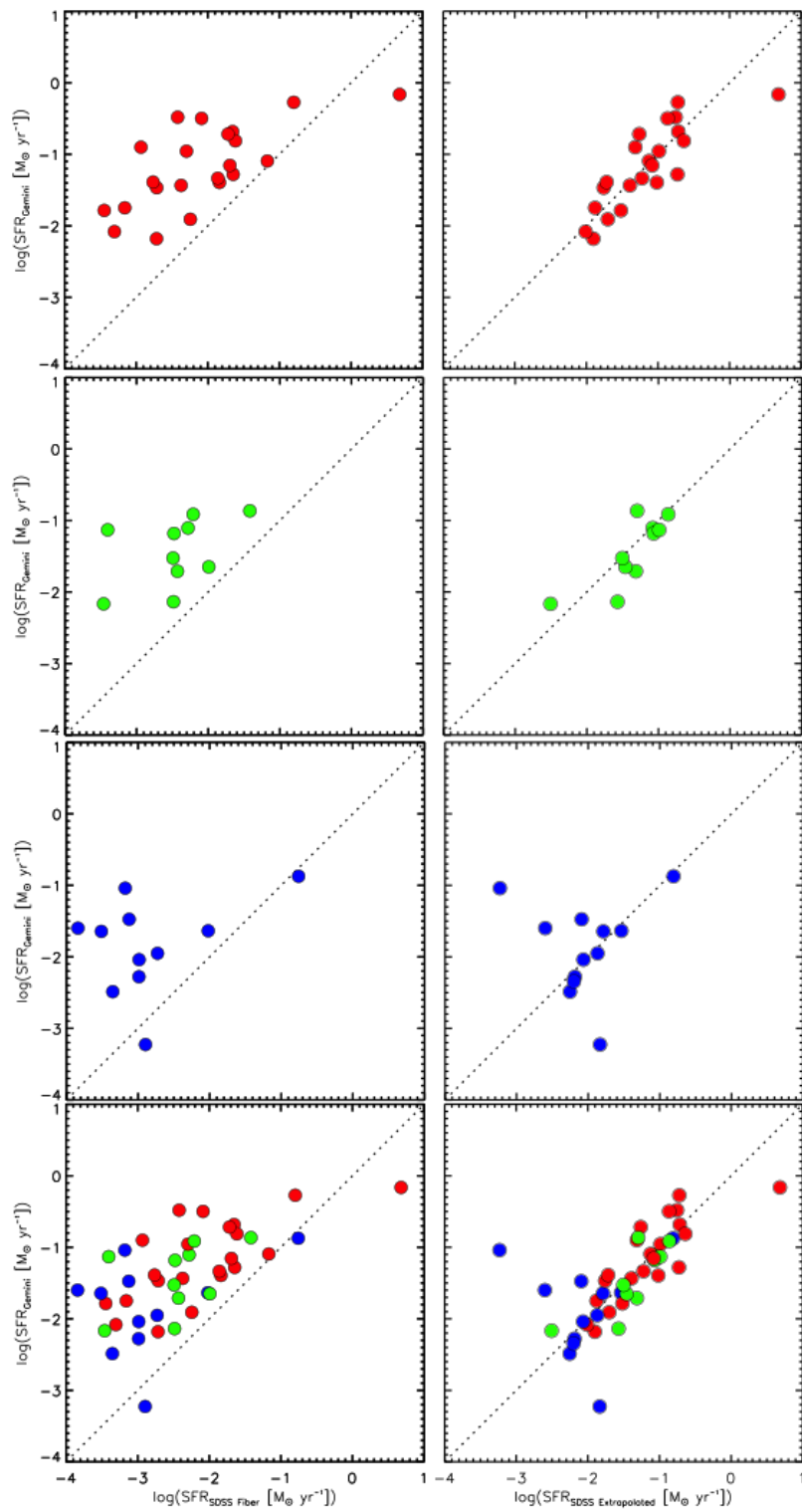


Figure 3.3 Star formation rate comparison for (a) isolated (red), (b) marginally isolated (green), (c) non-isolated (blue), and (d) all dwarf galaxy pairs (for ease of direct comparison) colored by the tidal index with each dwarf's nearest massive neighbor. **Left:** Gemini SFRs compared to the SFR measured from the SDSS fiber-based spectra. **Right:** Gemini SFRs compared to the total SFR extrapolated from the SDSS fiber-based spectra.

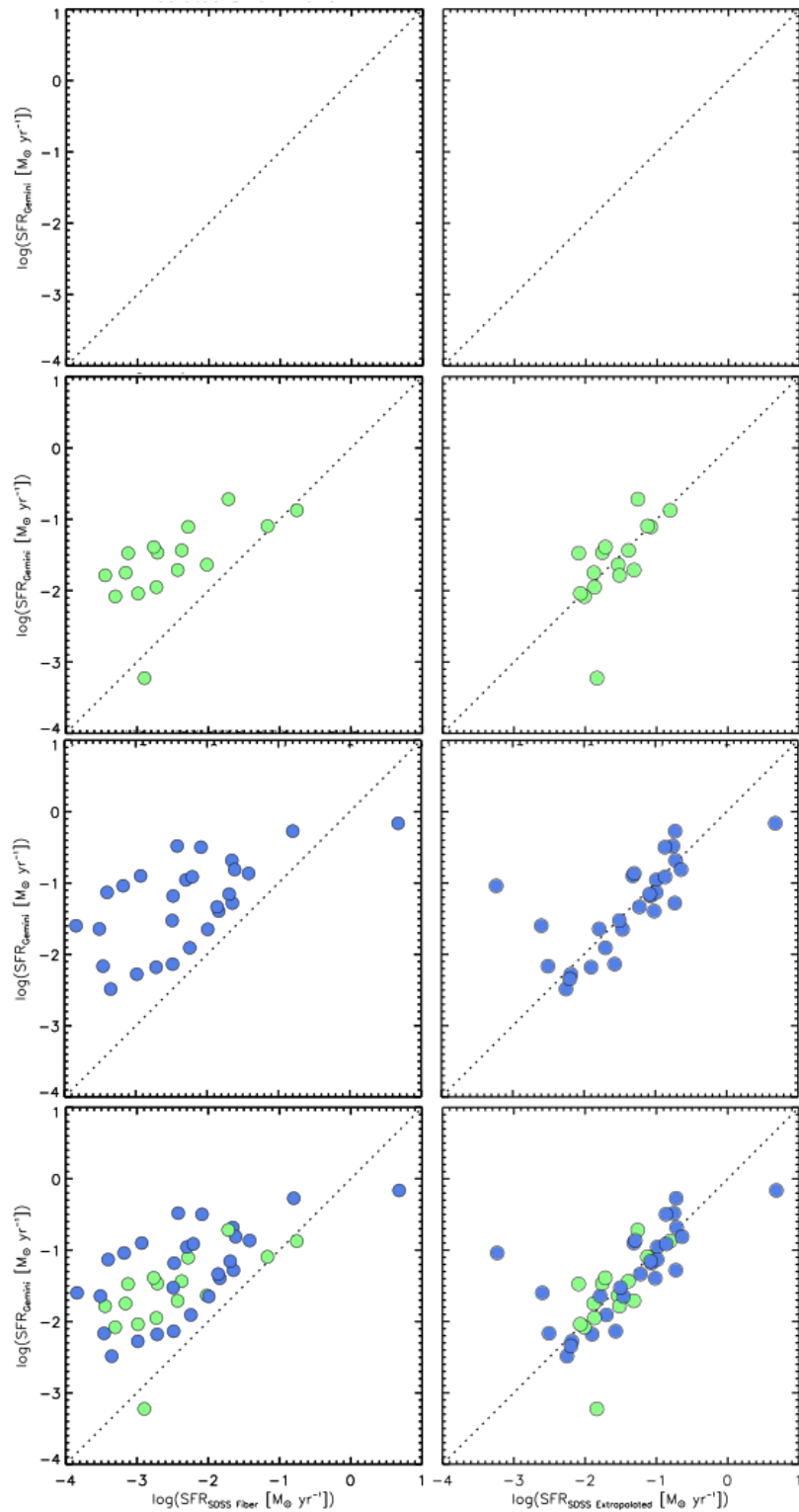


Figure 3.4 Star formation rate comparison for (a) isolated (light red), (b) marginally isolated (light green), (c) non-isolated (light blue), and (d) all dwarf galaxy pairs (for ease of direct comparison) colored by the tidal index with each dwarf's pair member. As expected, none of the TNT dwarf galaxies in this subsample are isolated from the galaxy it is paired with. **Left:** Gemini SFRs compared to the SFR measured from the SDSS fiber-based spectra. **Right:** Gemini SFRs compared to the total SFR extrapolated from the SDSS fiber-based spectra.

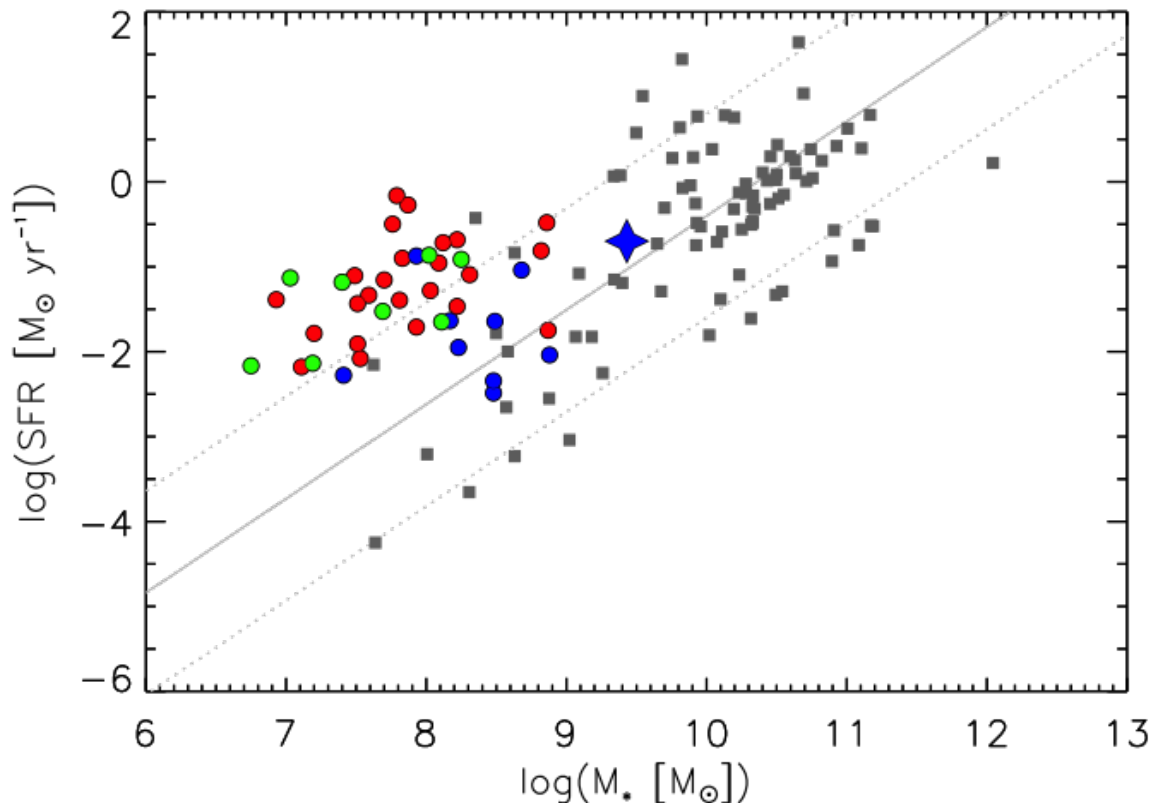


Figure 3.5 The star formation rate of each galaxy as a function of stellar mass colored by the massive host tidal index (red - isolated galaxies; green - marginally isolated galaxies; blue - non-isolated galaxies). The LMC (which includes the 30Dor star forming region) is shown as a diamond and the galaxies from the Zaragoza-Cardiel et al. (2018) interacting sample are shown as dark grey squares. The light grey line is the star forming main sequence as defined in Zaragoza-Cardiel et al. (2018).

to perform aperture photometry on both a total H $\alpha$  image of each galaxy and a region-only image. From these we calculated an H $\alpha$  region ratio (the percentage of H $\alpha$  emission identified as coming from HIIphot-identified regions compared to total H $\alpha$  emission from that galaxy).

Figure 3.7 shows the H $\alpha$  region ratios as a function of tidal index with respect to the nearest massive galaxy (left) and with respect to the dwarf companion (right). Points are colored by  $\Theta_D$ (left) and  $\Theta_H$ (right) to look for trends among all three parameters. By comparing these two distributions, we can describe the relative impact of the host and the dwarf pair member on the packaging of the star formation in the TNT sample. We see that, while there is scatter in the ratio, galaxies that are more isolated from a nearby companion are able to achieve higher H $\alpha$  region ratios. We also see that the isolated galaxies with larger ratios are primarily non-isolated from their low-mass companion. Further, while there is no strong correlation between dwarf pair tidal index and H $\alpha$  region

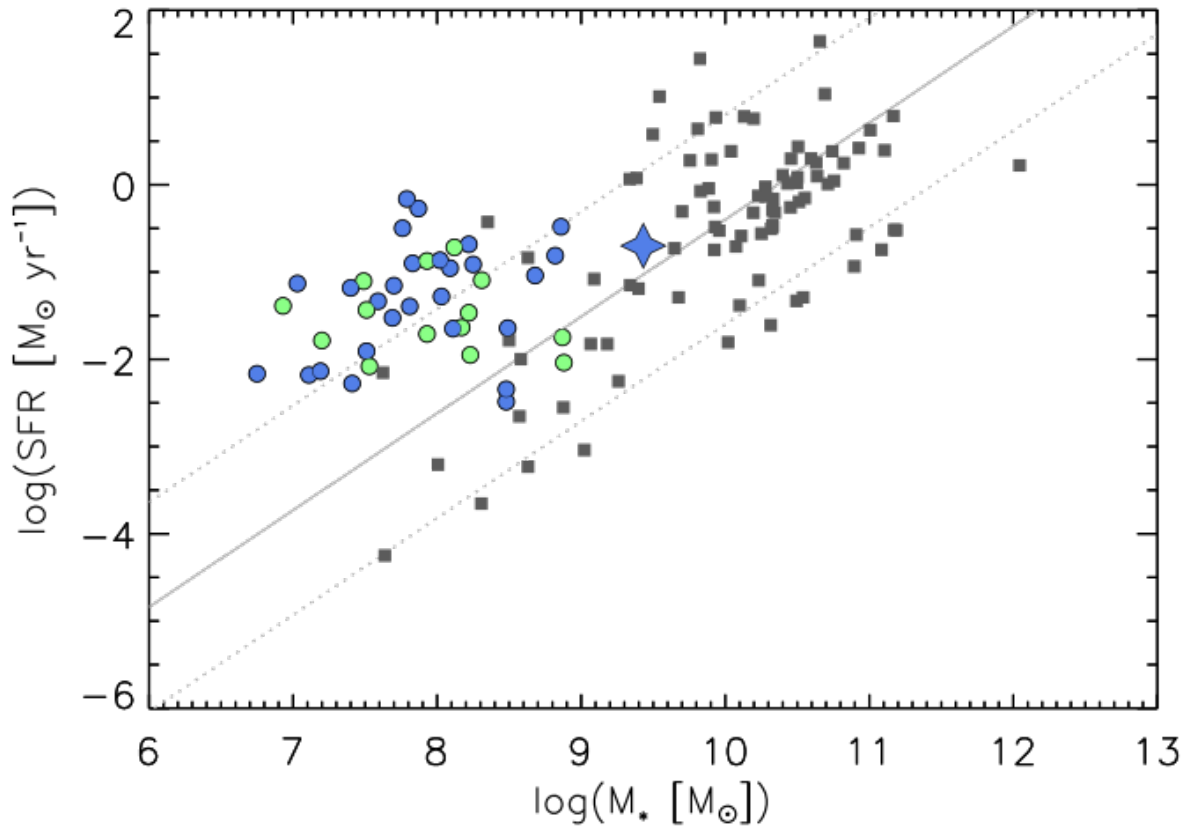


Figure 3.6 The star formation rate of each galaxy as a function of stellar mass colored by the dwarf pair tidal index (light red - isolated galaxies; light green - marginally isolated galaxies; light blue - nonisolated galaxies). The LMC (which includes the 30Dor star forming region) is shown as a diamond and the galaxies from the [Zaragoza-Cardiel et al. \(2018\)](#) interacting sample are shown as dark grey squares. The light grey line is the star forming main sequence as defined in [Zaragoza-Cardiel et al. \(2018\)](#).

ratios, galaxies that are both isolated from a massive host (red and green, marginally) and non-isolated from their paired dwarf galaxy are scattered to larger ratio values. Taken together, this suggests that a nearby massive galaxy has more impact over the concentration of star formation than the low mass companion, though the companion may also play a role in this process.

In Figure 3.8 we show the H $\alpha$  region ratio as a function of galaxy stellar mass colored by tidal index with respect to nearest massive galaxy (left) and with respect to low mass companion (right). There is no significant relationship between the H $\alpha$  region ratio and the galaxy stellar mass. Nor is there a trend with tidal index with respect to massive or low-mass companion.

In Figure 3.9 we show the H $\alpha$  region ratio as a function of total galaxy star formation rate colored by tidal index with respect to nearest massive galaxy (left) and with respect

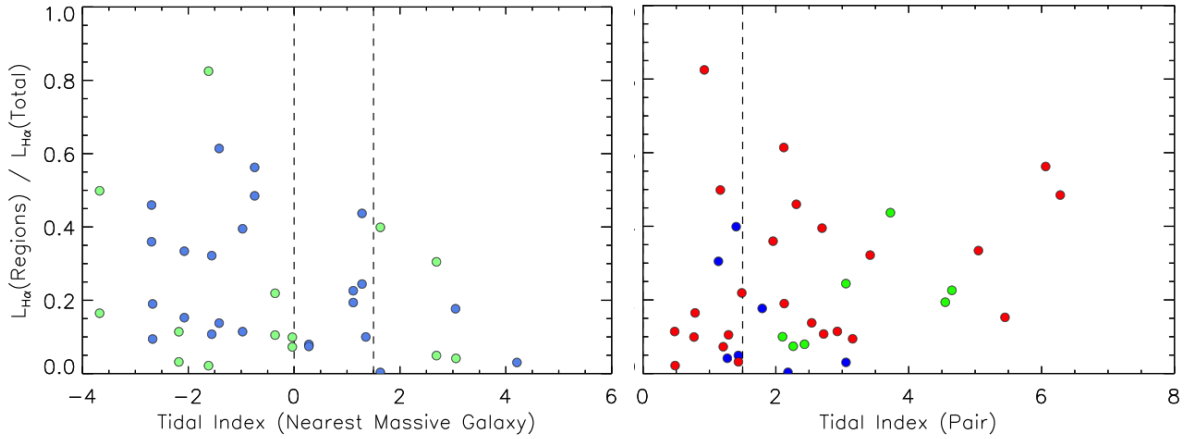


Figure 3.7 Ratio of the H $\alpha$  luminosity in discrete regions to the total H $\alpha$  luminosity of each galaxy as a function of tidal index. Vertical lines mark the boundaries between isolated, marginally isolated, and nonisolated galaxies. **Left:** Ratio as a function massive host tidal index colored by dwarf pair tidal index. The fraction of light in regions increases with increasing isolation. **Right:** Ratio as a function of dwarf pair tidal index colored by massive host tidal index. There is no strong trend of the H $\alpha$  region ratio with  $\Theta_D$ . Further, there does not appear to be a clear correlation among  $\Theta_H$ ,  $\Theta_D$ , and the ratio.

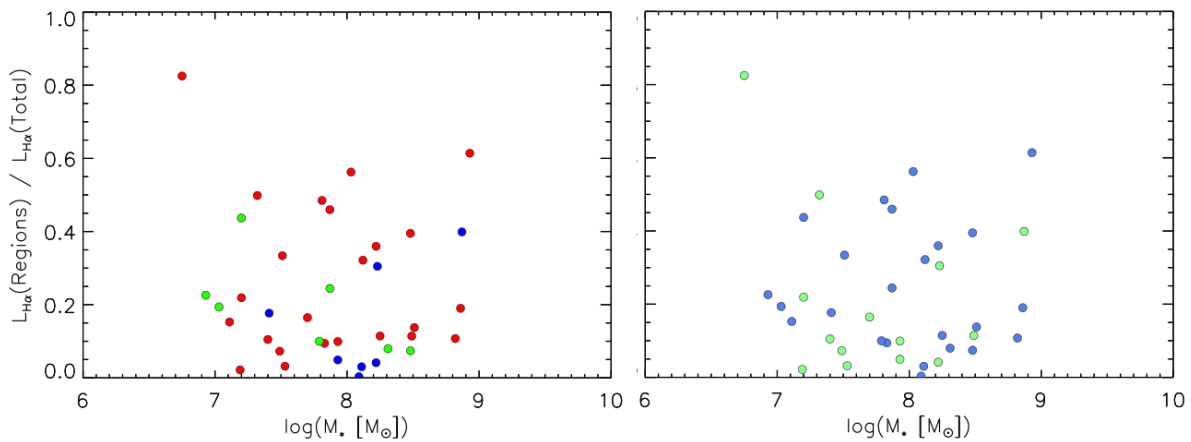


Figure 3.8 H $\alpha$  region ratio as a function of galaxy stellar mass colored by tidal index with respect to the nearest massive galaxy (left) and dwarf companion (right). In both panels, red points are isolated, green are marginally isolated, and blue are non-isolated from the relevant companion.

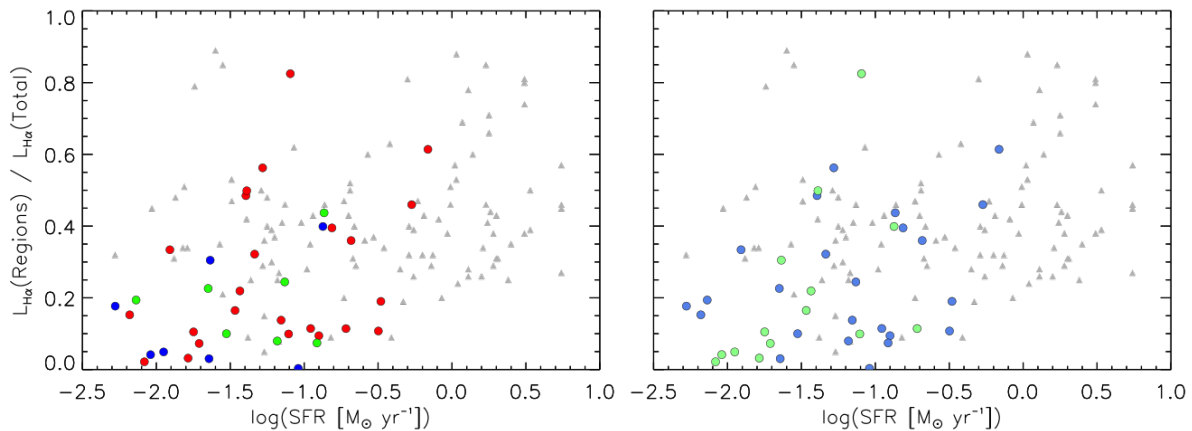


Figure 3.9 H $\alpha$  region ratio as a function of total galaxy star formation rate colored by tidal index with respect to the nearest massive galaxy (left) and dwarf companion (right). In both panels, red points are isolated, green are marginally isolated, and blue are non-isolated from the relevant companion. Grey triangles show the ratios and star formation rates from Oey et al. (2007).

to dwarf pair galaxy (right). The TNT sample is compared to the sample from Oey et al. (2007). As they used the same software (HIIPhot, Thilker et al. (2000)) to distinguish between diffuse and concentrated regions of H $\alpha$  emission, we will compare these values ( $1-f_{\text{WIM}}$ ) to the fraction of H $\alpha$  emission found in clumps in the TNT sample. Oey et al. (2007) find an average  $f_{\text{WIM}}$  value of  $0.59 \pm 0.19$  across the sample, and this value decreases to  $0.36 \pm 0.18$  for starbursting galaxies ( $\log(\Sigma_{\text{H}\alpha}) > 39.4$ ). Considering only galaxies in the Oey et al. (2007) sample with star formation rates in the range of the TNT galaxies,  $f_{\text{WIM}} = 0.62 \pm 0.10$ . The TNT average  $f_{\text{WIM}}$  is  $0.77 \pm 0.12$ . In general, the TNT region ratios follow the same trend as the Oey (2007) sample. The TNT sample is additionally probing galaxies with lower star formation rates.

### 3.3.3 Number of HIIPhot-Identified Regions

Using the region catalog produced by HIIPhot, we determined the total number of discrete H $\alpha$  regions identified in each TNT galaxy. Figure 3.10 shows this number as a function of tidal index with respect to the nearest massive galaxy (left) and with respect to the dwarf companion (right). Points are colored by  $\Theta_D$ (left) and  $\Theta_H$ (right) to look for trends among all three parameters. The dashed lines show the separation between the isolation classifications as defined by the tidal index parameter. Across all three massive galaxy isolation bins, the majority of galaxies have fewer than 30 identified regions. Each isolation bin also has outliers, with the highest number of regions appearing in the most

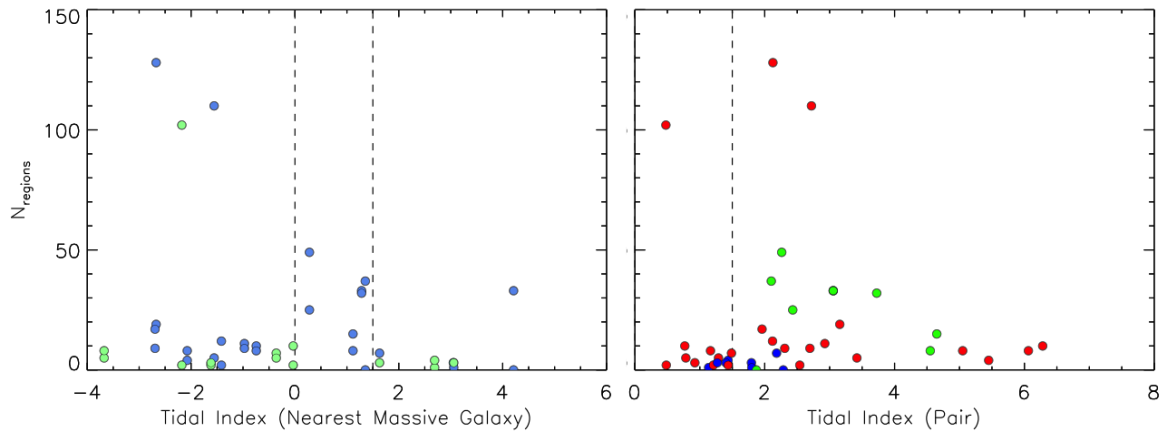


Figure 3.10 The number of regions identified by HIIphot in each TNT dwarf galaxy as a function of tidal index. The dashed vertical lines show the separation between the isolation classifications as defined by the tidal index parameter. **Left:** Number as a function massive host tidal index colored by dwarf pair tidal index. Though there is scatter, the number of regions tends to increase with increasing isolation. **Right:** Number as a function of dwarf pair tidal index colored by massive host tidal index. With the exception of one galaxy, there is a noticeable separation between dwarfs that are marginally isolated from their dwarf companion and those that are not isolated; the nonisolated galaxies have, on average, more discrete star-forming regions.

isolated galaxies. When considering  $\Theta_D$ , the dwarfs that are more strongly interacting with their dwarf companion span a wider range of number of H $\alpha$  regions and appear, on average, to have more regions than the galaxies that are marginally isolated from their companion.

In Figure 3.11 we plot the number of H $\alpha$  regions as a function of galaxy stellar mass, colored by tidal index with respect to the nearest massive galaxy (left) and dwarf companion (right). The Zaragoza-Cardiel et al. (2018) sample for 1 kpc regions (dark grey squares) and 2.5 kpc regions (light grey diamonds) is plotted for comparison. There is a loose correlation between region number and galaxy mass, in that the number of regions increase slightly with increasing stellar mass. This trend is more evident among the dwarf galaxies than the Zaragoza-Cardiel et al. (2018) interacting galaxies. The two samples are generally consistent, with the number of regions across both the TNT and Zaragoza-Cardiel et al. (2018) samples between zero and 30, and outliers scattered to high numbers in each. For the Zaragoza-Cardiel et al. (2018) sample, the outliers are in the number of 1 kpc region rather than the 2.5 kpc regions, which would be expected; within a given galaxy that can be resolved at these scales, there should be more small star-forming regions than larger ones (which may themselves be comprised of several smaller complexes).

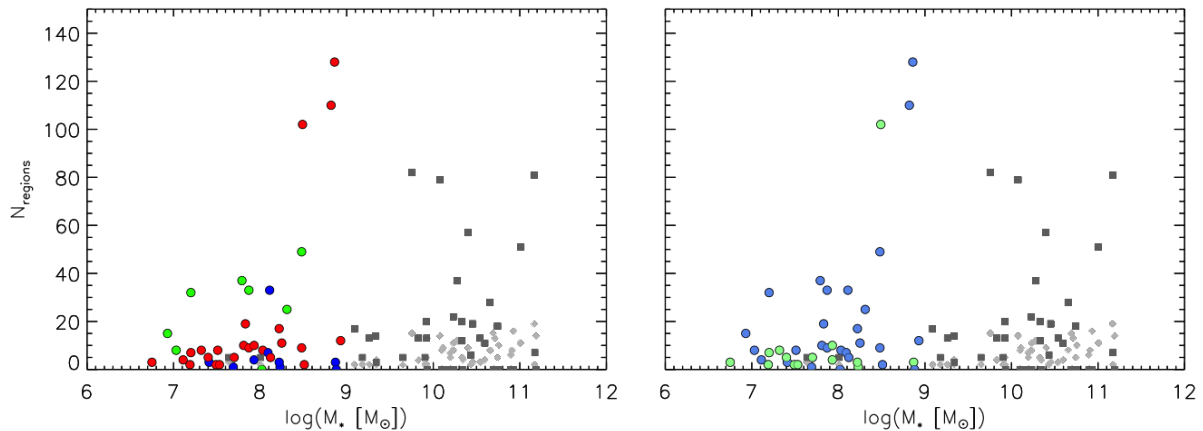


Figure 3.11 The number of H $\alpha$  regions identified by HIIphot in each TNT dwarf galaxy as a function of galaxy stellar mass, colored by tidal index with respect to the nearest massive galaxy (left) and dwarf companion (right). In both panels, red points are isolated, green are marginally isolated, and blue are non-isolated from the relevant companion. The Zaragoza-Cardiel et al. (2018) sample for 1 kpc regions (dark grey squares) and 2.5 kpc regions (light grey diamonds) is plotted for comparison. The number of regions across both the TNT and Zaragoza-Cardiel et al. (2018) samples are scattered between zero and 30, with outliers in each. For the Zaragoza-Cardiel et al. (2018) sample, the outliers are in the number of 1 kpc region. For the TNT sample, the outliers are primarily isolated from a massive galaxy and not isolated from their dwarf companion.

For the TNT sample, the outliers are primarily isolated from a massive galaxy and not isolated from their dwarf companion, consistent with Figure 3.10.

Figure 3.12 shows the number of regions as a function of the total SFR in each galaxy, colored by tidal index with respect to the nearest massive galaxy (left) and dwarf companion (right). The Zaragoza-Cardiel et al. (2018) sample for 1 kpc regions (dark grey squares) and 2.5 kpc regions (light grey diamonds) is plotted for comparison. As with stellar mass, we see a slight correlation in that the number of regions increases with increasing star formation rate. This similarity is expected given the relationship between stellar mass and star formation rate (see Figure 3.5).

### 3.3.4 Brightest Region Luminosity

From the HIIphot-generated region catalogs, we identified the most luminous HII region in each galaxy.

Figure 3.13 shows the luminosity of the brightest region in each galaxy as a function of massive neighbor tidal index (left) and dwarf pair tidal index (right). There is a tendency

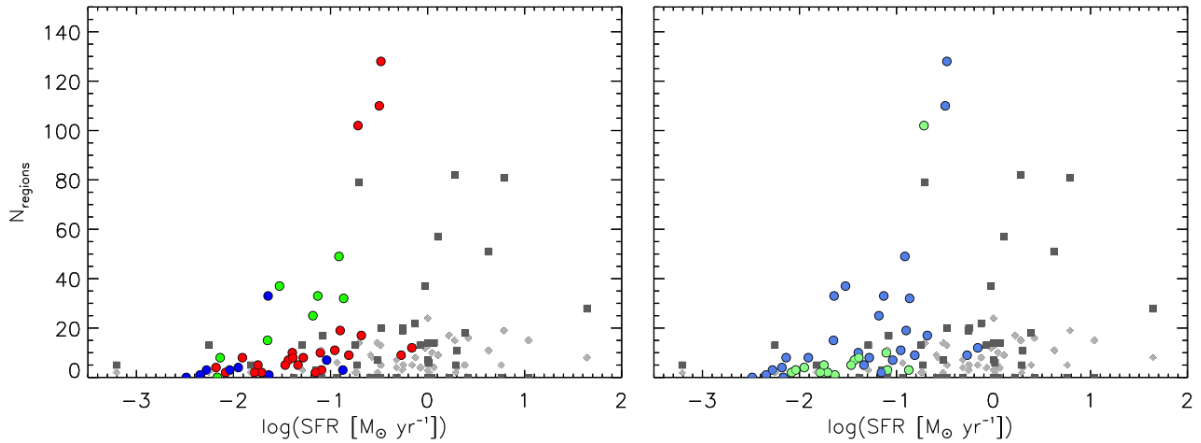


Figure 3.12 The number of H $\alpha$  regions identified by HIphot in each TNT dwarf galaxy as a function of global galaxy star formation rate, colored by tidal index with respect to the nearest massive galaxy (left) and dwarf companion (right). In both panels, red points are isolated, green are marginally isolated, and blue are non-isolated from the relevant companion. The Zaragoza-Cardiel et al. (2018) sample for 1 kpc regions (dark grey squares) and 2.5 kpc regions (light grey diamonds) is plotted for comparison. We see a slight correlation between the number of regions and increasing star formation rate.

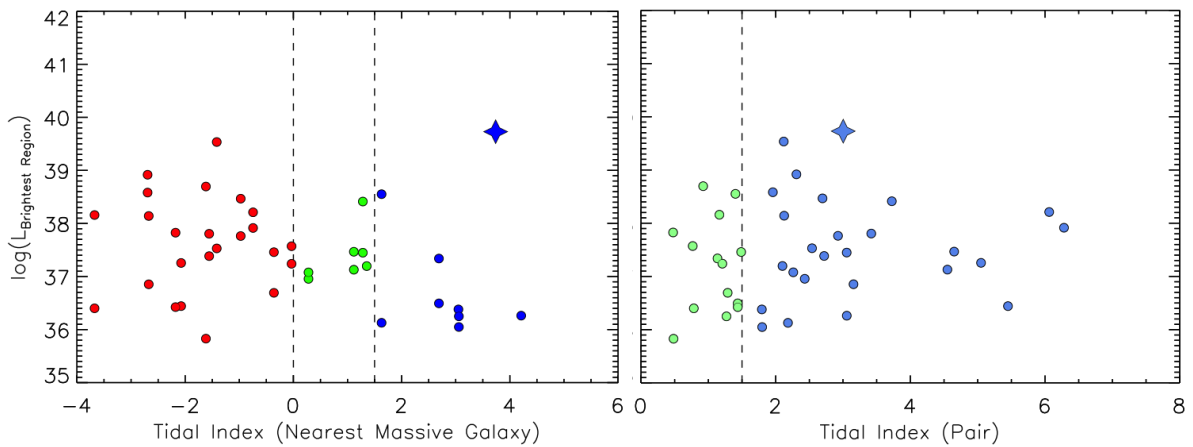


Figure 3.13 The luminosity of the brightest region identified by HIphot in each TNT dwarf galaxy as a function of tidal index. The LMC (which includes the 30Dor star forming region) is shown as a diamond. The dashed vertical lines show the separation between the isolation classifications as defined by the tidal index parameter. **Left:** Luminosity as a function of massive host tidal index. The luminosity of the brightest region tends to increase with increasing isolation from a massive galaxy. **Right:** Luminosity as a function of dwarf pair tidal index. There is no strong correlation between region luminosity and dwarf pair tidal index.

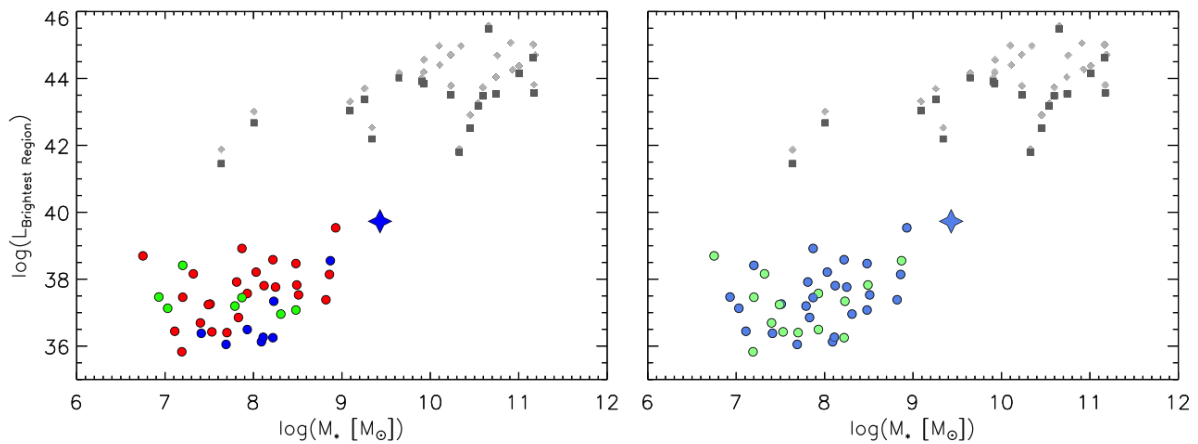


Figure 3.14 The luminosity of the brightest region in each galaxy identified by HIIphot in each TNT dwarf galaxy as a function of stellar mass. The LMC (which includes the 30Dor star forming region) is shown as a diamond. The Zaragoza-Cardiel et al. (2018) sample for 1 kpc regions (dark grey squares) and 2.5 kpc regions (light grey diamonds) is plotted for comparison. **Left:** Luminosity as a function of galaxy stellar mass colored by massive host tidal index. **Right:** Luminosity as a function of galaxy stellar mass colored by dwarf pair tidal index. The luminosity of the brightest region increases with increasing stellar mass.

for dwarf galaxies that are more isolated from a massive galaxy to have the most luminous H $\alpha$  regions, while there is no obvious trend with respect to the gravitation influence within the pair. The LMC/30Dor system appears to be consistent with the TNT sample. This suggests that the presence of a massive galaxy can limit the brightness of star forming clumps in a dwarf galaxy. We also see that it is not necessary to be interacting with a Milky Way sized galaxy in order for a dwarf galaxy to form regions as luminous as 30Dor, as luminous regions are forming in isolation. These regions also form in environments that span the range of environments with respect to the low mass companions, suggesting that these dwarfs may play a role in the formation of luminous clusters in even marginally isolated companions.

Figure 3.14 shows the brightest region luminosities as a function of galaxy stellar mass. The luminosities of the Zaragoza-Cardiel et al. (2018) sample are several orders of magnitude larger than the luminosities of the TNT sample's brightest regions, even within similar mass ranges. This is likely due to the difference in the region sizes; the TNT regions have a maximum radius of 250 pc while the Zaragoza-Cardiel et al. (2018) region radii are 1 kpc or 2.5 kpc. In both samples, we see an increase in the luminosity of the brightest region with increasing stellar mass, anchored by the LMC/30Dor system properties. Though there is a positive correlation, we also see that even low mass galaxies can

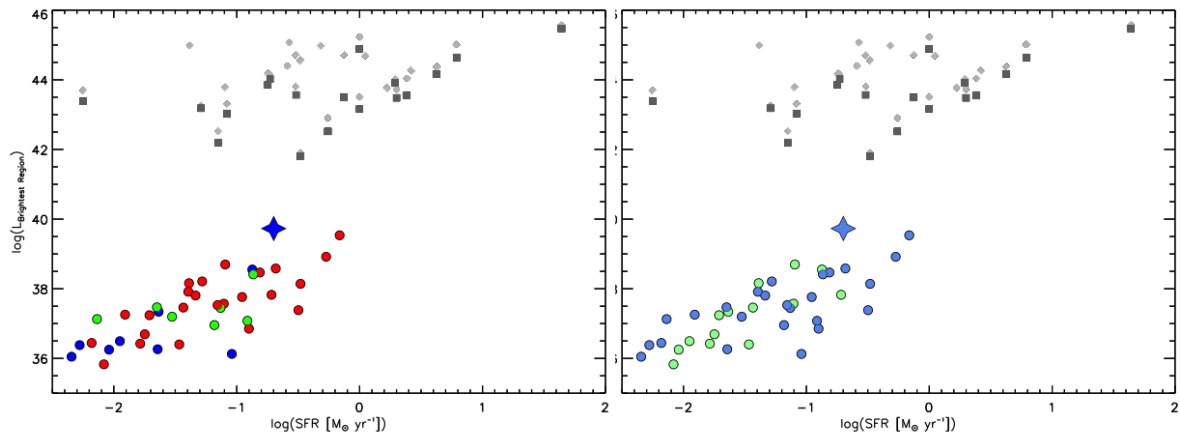


Figure 3.15 The luminosity of the brightest region in each galaxy as a function of star formation rate. The LMC (which includes the 30Dor star forming region) is shown as a diamond. Zaragoza-Cardiel et al. (2018) comparison sample for 1kpc regions (dark grey squares) and 2.5kpc regions (light grey diamonds). **Left:** Luminosity as a function of star formation rate colored by massive host tidal index. **Right:** Luminosity as a function of star formation rate colored by dwarf pair tidal index.

form comparably luminous regions, particularly if they are isolated from a more massive galaxy (in this sense, the LMC/30Dor system is somewhat of an outlier).

Figure 3.15 shows the luminosity of each galaxy’s brightest H $\alpha$  region as a function of SFR. Galaxies with larger global SFRs tend to have brighter regions, and SFR is much more strongly correlated with brightest region luminosity than stellar mass. The LMC/30Dor system appears to fall in line with the trend seen in the TNT galaxies, though it stands out as a non-isolated galaxy in this regime with just one other non-isolated TNT galaxy. Again, the luminosities of the Zaragoza sample are several orders of magnitude larger than the luminosities of the TNT sample’s brightest regions and the LMC/30Dor system, even within similar star formation rate ranges. As above, this is likely due to the difference in the region sizes.

Figure 3.16 shows the luminosity of each galaxy’s brightest H $\alpha$  region as a function of specific star formation rate (sSFR), the star formation rate normalized by galaxy stellar mass. Within the TNT sample, there is still a correlation between sSFR and region luminosity, though with the introduction of stellar mass the correlation is weaker. The LMC/30Dor system (diamond) becomes an outlier here when the LMC’s mass is taken in to account.

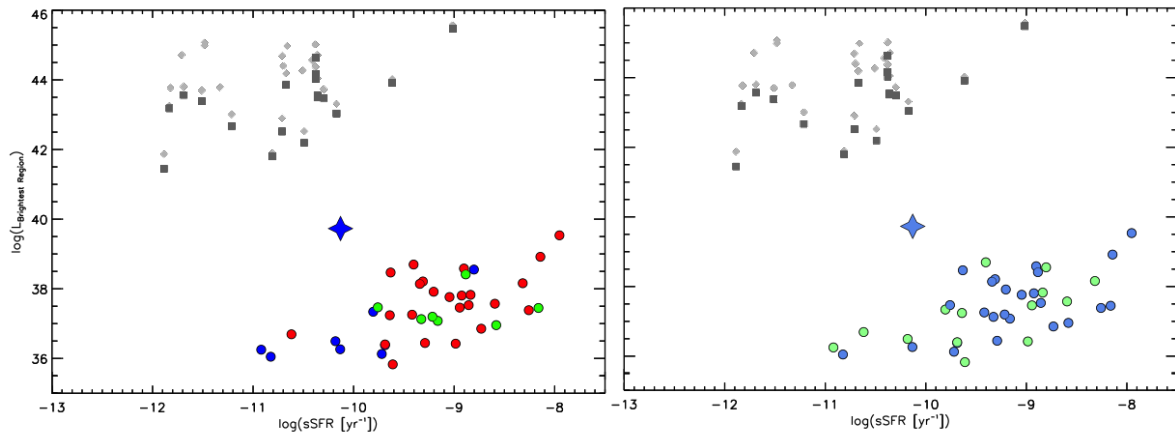


Figure 3.16 The luminosity of the brightest region in each galaxy as a function of specific star formation rate. The LMC (which includes the 30Dor star forming region) is shown as a diamond. [Zaragoza-Cardiel et al. \(2018\)](#) comparison sample for 1kpc regions (dark grey squares) and 2.5kpc regions (light grey diamonds). **Left:** Luminosity as a function of specific star formation rate colored by massive host tidal index. **Right:** Luminosity as a function of specific star formation rate colored by dwarf pair tidal index.

### 3.4 Discussion and Conclusion

We have presented Gemini/GMOS H $\alpha$  imaging of 23 galaxy pairs from the TNT sample of interacting dwarf galaxies. We find that the star formation rates measured using the galaxy-integrated H $\alpha$  Gemini luminosities are generally consistent with those extrapolated from the 3'' SDSS spectroscopic values. We further show that the star formation rates in these galaxies are primarily influenced by nearby massive neighbors rather than their low-mass companion.

The SFRs of the TNT galaxies put them above the star formation main sequence (SFMS, Stierwalt et al. *in prep*). Using narrowband imaging to measure SFRs as opposed to extrapolating fiber-based values is important for using local interacting dwarf systems as analogs for high redshift processes. Specifically, the integrated values allow us to more accurately determine the extent to which the galaxies deviate from the  $z = 0$  MS, and whether they more accurately follow trends seen in observations of higher redshift systems ([Mancuso et al., 2016](#)).

The fraction of H $\alpha$  luminosity contained within discrete regions increases with decreasing  $\Theta_H$  and increases with increasing SFR. There is no correlation with galaxy stellar mass. We also find that the number of discrete H $\alpha$  regions is generally scattered below 30 in all galaxies with respect to tidal index, SFR, and stellar mass. The outliers with many more regions ( $> 80$ ) tend to be isolated from a massive galaxy, and have relatively large SFRs

and stellar masses. Taken together, these results suggest that we have more localized SF in dwarf galaxy pairs that are more isolated from massive galaxy hosts, conditions similar to those at high redshift (Ramos et al., 2011). As localized star formation can lead to enhanced feedback effects, these distributions can be used to infer the evolution of dwarf galaxies at high redshifts.

The luminosity of the brightest  $H\alpha$  region in each galaxy increases with increasing stellar mass and SFR. It does not appear to be influenced by nearby massive galaxies as measured by the tidal index parameter. When comparing the TNT star forming regions to 30Dor in the LMC (often considered the template for high redshift star forming dwarfs), we see that in some respects 30Dor is ‘typical’ (luminosity as a function of both environment and galaxy stellar mass) and in others it is an outlier (luminosity as a function of specific star formation rate). Dwarf galaxies with star forming regions as bright as 30Dor appear to be relatively rare, but we find that they are not necessarily found near a Milky Way analog. Further observations and comparison are necessary to evaluate the ways in which the LMC/SMC/30Dor system is and is not an appropriate analog for high redshift dwarf galaxy interactions.

# Chapter 4

## The Discovery of Compact Groups of Dwarf Galaxies

### 4.1 Introduction

In the case of massive galaxies, it has been shown that galaxy evolution proceeds differently in interacting pairs than it does in interacting groups of three or more galaxies; pair interaction increases the galaxies' star formation rates (SFRs), while group interactions accelerate the quenching of ongoing star formation (Alatalo et al., 2015; Walker et al., 2010; Johnson et al., 2007). Though interactions may initially increase the SFRs in compact group galaxies, the combined impact from multiple nearby, slow-moving galaxies may introduce other processes (gas stripping and heating) that can quickly use up the star-forming gas, or otherwise make it unavailable for star formation.

Walker et al. (2010) examined the *Spitzer* mid-infrared colors of Hickson Compact Groups (HCGs, Hickson (1982)), which reflect the properties of the dust in these systems. They noted a statistically significant dearth of galaxies in this color space when compared to other galaxy environments (galaxy clusters, interacting galaxies, and field galaxies), which they attribute to a rapid evolution of these compact group galaxies from actively star forming to quenched (and thus spending little time forming stars at moderate rates). This gap was also seen in a larger sample of HCGs identified in the whole-sky Wide-field Infrared Survey Explorer (WISE) (Zucker et al., 2016). Further, HCGs have a higher fraction of galaxies with red optical colors when compared to galaxies in other gravitational environments, indicating that they are more evolved than these comparison samples (Walker et al., 2013).

One explanation for this observed difference between interacting pairs and interacting groups is the presence of a significant intergalactic medium (IGM) that surrounds these massive groups of galaxies. As the galaxies move through this material, their molecular gas is shocked and heated, making it unavailable to collapse in to stars and clusters (Alatalo et al., 2015). Alternatively, the galaxies are subjected to continuous and variable tidal torquing, which is likely to introduce more chaotic motion into the gas, again making it unavailable to form stars (Coziol & Plauchu-Frayn, 2007).

As the  $\Lambda$  Cold Dark Matter ( $\Lambda$ CDM) theory of hierarchical structure formation predicts that primordial density fluctuations should be scale-free, groups of low mass galaxies with their own lower mass satellites should also exist (Davis et al., 1985). These groups are thought to represent the fundamental building blocks of more massive galaxies like our Milky Way. However, probing low mass galaxies presents a severe observational challenge as identifying such systems requires access to powerful, large-aperture telescopes capable of observing a significant fraction of the night sky. Dwarf galaxies also present a major theoretical challenge, as modern cosmological simulations are not yet robust at these mass and size scales beyond the smallest systems (individual star-forming clouds and clusters, Hopkins et al. (2014)).

As is the case with many aspects of understanding the formation and evolution of low mass galaxies, it is unclear that the same dichotomy observed between pairs and groups of massive galaxies can be extrapolated down to the low mass galaxy regime. Thus, the first step in understanding the role that groups of dwarfs play in the hierarchical assembly of massive galaxies is to identify a sample of these groups of galaxies comprised of only low mass members. Here we describe observations of a set of such groups identified from the TiNy Titans survey low- $z$  sample. Each group contains three to five known members, has a total group baryonic mass (gas and stars) between  $\sim 4.4 \times 10^9 M_\odot$  and  $2 \times 10^{10} M_\odot$  (individual galaxies have baryonic masses between  $2 \times 10^6 M_\odot$  and  $2 \times 10^9 M_\odot$ ), and require mass-to-light ratios  $< 100 M_\odot/L_\odot$  (see Section 4.3.1 for definitions and details). We present how the group candidates were selected and the observations used to confirm their physical reality. We then discuss how they compare to both observed massive groups of galaxies and theoretical predictions of low mass groups.

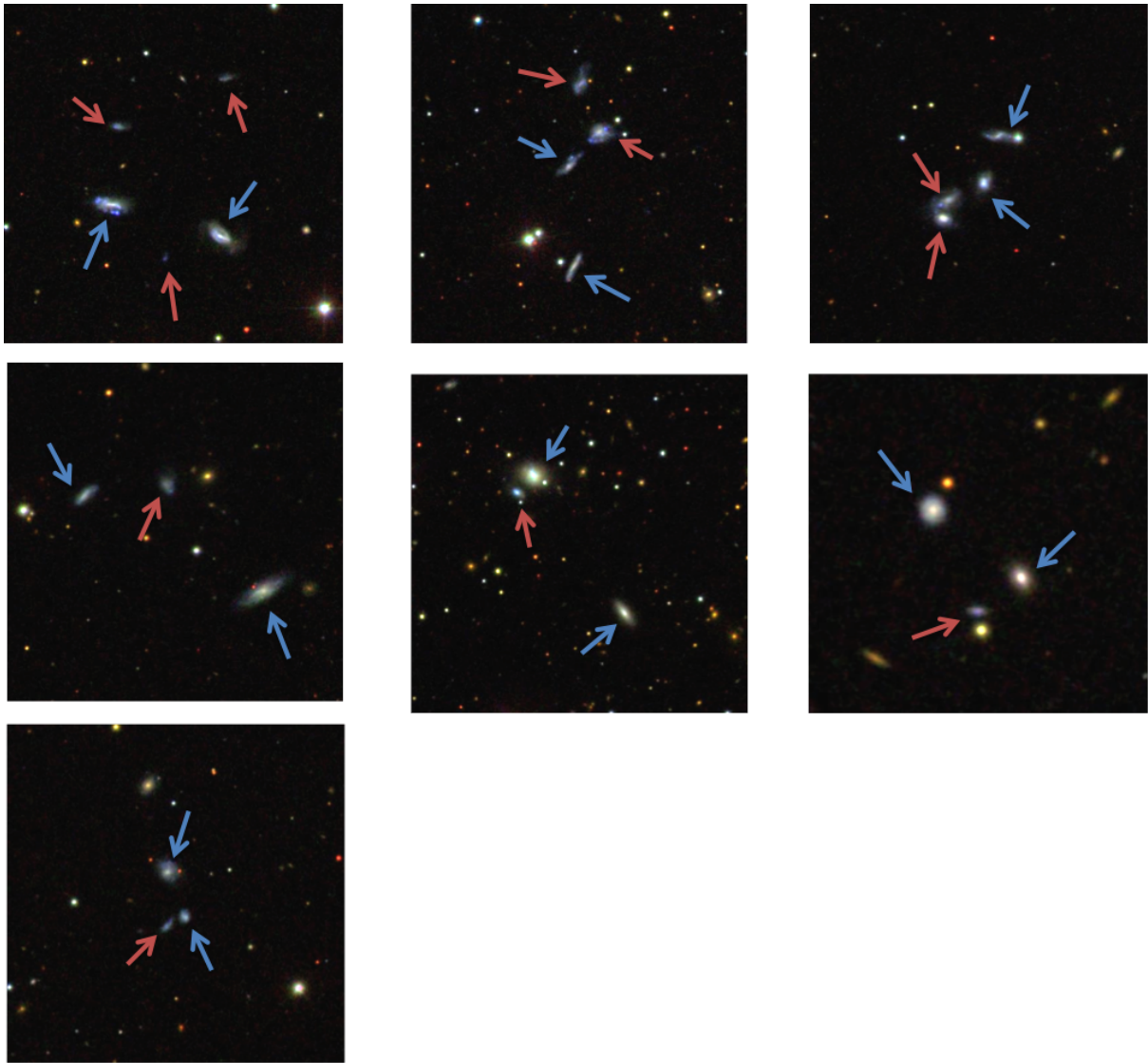


Figure 4.1 SDSS stamps of the seven TNT low-mass group candidates. Blue arrows indicate the location of the SDSS-identified TNT pair members. Red arrows indicate the candidate group members.

## 4.2 Methods

### 4.2.1 Group Candidate Selection

Seven group candidates were serendipitously discovered while investigating dwarf-dwarf galaxy interactions in the multiwavelength TNT survey (Stierwalt et al., 2015). The SDSS images for all 60 isolated ( $d_{\text{host}} < 1.5$  Mpc, see Section 1.2.3) TNT pairs were visually inspected for any potential low-mass neighbors (see Figure 4.1). Such neighbors were initially not included in the TNT sample because they did not have SDSS spectra (spectroscopic fibers were placed on bright objects and thus lower mass dwarf

galaxies are often excluded) or because our TNT selection algorithm removed the known pairs from consideration to avoid over-counting. Seven candidate groups were identified, and follow-up observations were obtained in order to determine whether or not they are gravitationally bound systems (Stierwalt et al., 2017).

## 4.2.2 Follow-up observations

When SDSS spectra were not available, group member candidates were targeted for follow up optical spectroscopy using the long-slit optical spectrograph on the 3.5-m telescope at the Apache Point Observatory. We further obtained very narrowband (10Å) H $\alpha$  imaging for three of the groups with the MarylandMagellan Tunable Filter (MMTF) Fabry Perot (Veilleux et al., 2010). One additional group was observed with the narrow-band (60 Å) H $\alpha$  filter on the Gemini Multi-Object Spectrograph at Gemini-North as part of a larger TNT H $\alpha$  narrow-band imaging campaign (see Chapter 3). These observations are described in detail below.

### 4.2.2.1 Optical imaging with the Maryland-Magellan Tunable Filter

The MMTF Fabry Perot filter (Veilleux et al., 2010) on Magellan Baade’s Inamori-Magellan Areal Camera and Spectrograph (IMACS, Dressler et al. (2011)) allows for the simultaneous identification of potential group members (the extremely narrow band-pass constrains projected radial separations among the galaxy group candidates) and high resolution view of the galaxies’ star formation morphologies (which can provide further evidence of galaxy interactions).

We obtained narrowband H $\alpha$  and continuum observations for three of our candidate groups (dm1049+09, dm1349-02, and dm1623+15) on 20-21 April 2015 using IMACS/MMTF on Magellan Baade. The groups selected for imaging were observable from Magellan in April and within the redshift range of 0.0220 to 0.0549 so that the H $\alpha$  emission line would fall within a single MMTF order-blocking filter centered at 6815 Å with a total available width of  $\sim 200$  Å. Each field was observed using staring mode with the 10 Å tunable portion of the filter centred on the average wavelength of the H $\alpha$  emission line from the original TNT pair. Images of the continuum in all fields were taken by shifting the filter off the H $\alpha$  emission by 25-50 Å while avoiding night sky lines. The total exposure time ranged from 80 to 120 minutes for both H $\alpha$  and off-band continuum, split into individual exposures of 20 minutes each. The individual exposures were dithered by

between 30" and 300" to fill in inter-chip gaps, and care was taken to ensure all targets fell within the Fabry Perot's central monochromatic spot. We reduced the data using IRAF and the MMTF pipeline (Veilleux et al., 2010), which includes bias subtraction, flat fielding, bad pixel masking (including cosmic rays), sky background subtraction, image registration and chip mosaicing, point-spread-function matching and image stacking. Images were flux-calibrated using Oke standard stars (Oke, 1990) observed with the same filters as the science targets.

#### 4.2.2.2 Optical imaging with the Gemini Multi-Object Spectrograph

Not all of the candidate dwarf groups were within the range of the 6.5-meter Magellan Baade Telescope and the MMTF filter, either due to their position in the sky or their redshift. However, H $\alpha$  and r-band continuum observations of an additional group candidate (dm1718+30) were obtained as part of a larger TNT follow-up program (Liss 2018, *in prep*; see Chapter 3) using the Gemini Multi-Object Spectrograph on the 8.1-m Gemini-North Telescope (Hook et al., 2004). We observed the field for a total of 460 seconds for H $\alpha$  and 280 seconds for r-band. The observations were split into individual exposures of 115 seconds and 70 seconds for  $r$  and H $\alpha$ , respectively. Individual exposures were dithered by 5" in the X- and Y-directions to allow for continuous coverage between chip gaps. We reduced the observations using the Gemini/GMOS IRAF package which includes bias subtracting, flat fielding, chip mosaicing, and image alignment and combining. Flux calibration was done using observations of Landolt standard fields (Landolt, 1992).

#### 4.2.2.3 Optical spectroscopy with the Apache Point Dual Imaging Spectrograph

In order to further constrain the redshifts of the group member candidates identified in the narrowband H $\alpha$  data, we obtained long-slit optical spectra of the group candidate members without SDSS spectroscopic observations throughout 2015 and 2016 using the Dual Imaging Spectrograph (DIS) on the Apache Point Observatory (APO) 3.5-m telescope. Each target was observed using both the red and blue channels with high-resolution R1200 and B1200 gratings and a 2.0" x 6' slit. Targets were observed at the parallactic angle with total exposure times ranging from 25 to 160 minutes and individual exposure times ranging between 5 and 10 minutes depending on weather conditions. The red and blue channels were centered at the approximate wavelength of H $\alpha$  (red)

or  $H\beta$  (blue) of the group members that were already confirmed by SDSS spectroscopy. We reduced the spectra using standard IRAF tools, including bias subtraction, scattered light correction, and flat fielding. Wavelength calibration was done using helium, neon and argon arc lamps. We measured velocities from Gaussian fits to the  $H\alpha$  emission line, and the uncertainties derived from the fit parameters are very low ( $\sim 12 \text{ km s}^{-1}$ ) owing to the high-resolution spectra.

## 4.3 Results

### 4.3.1 Redshifts and boundedness

Though the three-dimensional (3D) structure of the groups is not known, all seven groups are observed to be within roughly a virial radius of the most massive group member. Furthermore, all candidate group members, which range in stellar mass from  $2 \times 10^6 M_\odot$  to  $2 \times 10^9 M_\odot$  (Stierwalt et al., 2017), were confirmed to have velocities within  $200 \text{ km s}^{-1}$  of the mean group velocity and thus fall within the TNT interaction criteria (Column 2, Table 1). The results of the optical spectroscopy are shown in Table 4.1. This velocity information allows us to determine the physical size of each group – all observed group members are within roughly a virial radius of the most massive group member (Column 4, Table 1;  $\sim 100 \text{ kpc}$  for a dark halo mass of  $10^{11} M_\odot$ ).

In order to determine group boundedness, the 3D velocity,  $\sigma_{3D}$  of each group was calculated using the line-of-sight velocities:

$$\sigma_{3D} = \sqrt{3} \times \sqrt{\langle v^2 \rangle - \langle v \rangle^2}, \quad (4.1)$$

where  $v$  is line-of-sight velocity for the group members. We then equated this velocity dispersion to the escape velocity of each group:

$$v_{esc} = \sqrt{\frac{2GM}{r}} \rightarrow \sigma_{3D} = \sqrt{\frac{2GM}{r}} \quad (4.2)$$

where  $G = 6.67 \times 10^{-11} \text{ m}^3 \text{ kg}^{-1} \text{ s}^{-2}$  is the gravitational constant,  $M$  is the combined mass of the group members, and  $r$  is the group size, taken to be largest projected 2D distance between any two group members. Solving this equation for mass, we can place a lower

limit on the total mass (stars, gas, dust, and dark matter) required for each group to be gravitationally bound:

$$M_{Bound,1} = \frac{\sigma_{3D}^2 r}{2G}. \quad (4.3)$$

The total masses required to be gravitationally bound exceed the known baryonic masses for each group<sup>1</sup>.

By comparing these known masses to the minimum bounded mass from Equation 4.3, we can determine the amount of dark matter (matter that does not emit light and is thus not directly detectable, but does interact gravitationally with baryonic matter leading us to infer its presence). This ratio is often reported as a mass-to-light (M/L) ratio, the ratio between the total mass of a system (including its dark matter) to the total luminosity of the system from the matter that radiates. This ratio varies across astronomical systems. For example, individual massive O-stars having  $M/L \simeq 0.005 M_{\odot}/L_{\odot}$  and sun-like stars have  $M/L \simeq 1 M_{\odot}/L_{\odot}$ . At galaxy scales, spiral disks have  $M/L \simeq 2 - 4 M_{\odot}/L_{\odot}$ , ellipticals have  $M/L \simeq 8 - 15 M_{\odot}/L_{\odot}$ , and dwarf irregular galaxies (like the TNT pairs) having  $M/L \simeq 10 - 100 M_{\odot}/L_{\odot}$  (the large range being a consequence of their wide range of morphologies). For the TNT dwarf galaxy group candidates, the resulting minimum required total mass-to-light (M/L) ratios range from  $\sim 0.7$  to  $11 M_{\odot}/L_{\odot}$  (see Table 4.2), which are consistent with the M/L ratios of 10100 that have previously been determined for individual dwarf galaxies (Spekkens et al., 2014).

We can also use our knowledge of the velocities and projected distances of individual group members (see Figure 2) to determine individual galaxy masses:

$$M_{gal} = \frac{v_{sep}^2 r}{2G}, \quad (4.4)$$

where  $G$  is again the gravitational constant,  $r$  is the distance between the individual galaxy and the center of mass of the dwarf group and  $v_{sep}$  is the difference in projected velocity between the individual galaxy and the average line-of-sight velocity of the group. When summed for all galaxies in a given group, this gives us a projected total mass (baryonic plus dark matter) estimate for each system. Comparing this mass to the observed luminosities, the resulting  $M/L$  ratios from those mass predictions range from 12 to 70

---

<sup>1</sup>Here, the known baryonic mass consists of stellar masses from SDSS SED fitting and HI masses from single dish radio observations taken with the Green Bank Telescope and the Arecibo Telescope.

Table 4.1. TNT isolated dwarf group candidate members

Name	$v_{\text{opt}}$ (km s <sup>-1</sup> )	$\log(M_*)$ ( $M_{\odot}$ )	$R_{\text{proj,prim}}$ (kpc)	Velocity source
dm1049+09a	10037 ( $\pm 3$ )	9.32 ( $\pm 0.1$ )	0.0	SDSS
dm1049+09b	10064 ( $\pm 2$ )	9.11 ( $\pm 0.1$ )	47.7	SDSS
dm1049+09c	10277 ( $\pm 1$ )	8.19 ( $\pm 0.2$ )	65.0	APO
dm1049+09d	10141 ( $\pm 1$ )	7.66 ( $\pm 0.3$ )	67.0	APO
dm1049+09e	9991 ( $\pm 1$ )	7.10 ( $\pm 0.3$ )	24.9	APO
dm1623+15a	10280 ( $\pm 2$ )	8.77 ( $\pm 0.1$ )	0.0	SDSS
dm1623+15b	10031 ( $\pm 2$ )	8.61 ( $\pm 0.1$ )	42.7	SDSS
dm1623+15c	10004 ( $\pm 1$ )	8.98 ( $\pm 0.2$ )	58.1	APO
dm1623+15d	10139 ( $\pm 1$ )	8.76 ( $\pm 0.3$ )	78.6	APO
dm1403+41a	10580 ( $\pm 2$ )	8.81 ( $\pm 0.1$ )	0.0	SDSS
dm1403+41b	10619 ( $\pm 2$ )	8.61 ( $\pm 0.1$ )	22.1	SDSS
dm1403+41c	10319 ( $\pm 2$ )	9.19 ( $\pm 0.1$ )	22.9	SDSS
dm1403+41d	10470 ( $\pm 1$ )	8.80 ( $\pm 0.1$ )	16.7	APO
dm1440+14a	5429 ( $\pm 3$ )	8.78 ( $\pm 0.1$ )	0.0	SDSS
dm1440+14b	5423 ( $\pm 2$ )	8.14 ( $\pm 0.1$ )	46.5	SDSS
dm1440+14c	5381 ( $\pm 1$ )	7.88 ( $\pm 0.2$ )	32.0	SDSS
dm1718+30a	4446 ( $\pm 2$ )	8.96 ( $\pm 0.1$ )	0.0	SDSS
dm1718+30b	4428 ( $\pm 2$ )	8.52 ( $\pm 0.1$ )	46.5	SDSS
dm1718+30c	4569 ( $\pm 1$ )	7.77 ( $\pm 0.1$ )	32.0	APO
dm0909+06a	14021 ( $\pm 2$ )	9.31 ( $\pm 0.1$ )	0.0	SDSS
dm0909+06b	13799 ( $\pm 2$ )	9.35 ( $\pm 0.1$ )	32.2	SDSS
dm0909+06c	13705 ( $\pm 1$ )	8.17 ( $\pm 0.3$ )	31.8	APO
dm1349-02a	6914 ( $\pm 3$ )	8.41 ( $\pm 0.1$ )	0.0	SDSS
dm1349-02b	6988 ( $\pm 2$ )	8.13 ( $\pm 0.1$ )	14.3	SDSS
dm1349-02c	6898 ( $\pm 1$ )	7.55 ( $\pm 0.3$ )	15.8	APO

Note. —  $v_{\text{opt}}$ : line-of-sight velocity measured from the optical spectra derived from the source in the last column.  $R_{\text{proj,prim}}$ : 2D projected distance between each group member and the primary or most massive group member in kpc. The last column notes the source of the velocity given in the second column, either from the SDSS spectroscopic catalogue or from original observations presented here using the Dual Imaging Spectrograph at the Apache Point Observatory.

$M_{\odot}/L_{\odot}$  and thus also suggest that the TNT dwarf groups do not require an unusual amount of dark matter to be bound systems.

### 4.3.2 Narrowband imaging and star formation morphology

The results of the H $\alpha$  imaging campaign are shown in Figure 4.3. Each observed group show significant H $\alpha$  emission in all candidate group members. Due to the extremely narrow bandwidth of the MMTF, these observations further support the finding from the

Table 4.2. TNT isolated dwarf group candidate properties

Group Name	Distance (Mpc)	$\sigma_{3D}$ (km s <sup>-1</sup> )	Size (kpc)	$(M/L)_{\text{bound}}$ ( $M_{\odot}/L_{\odot}$ )	$\log(M_{\text{tot,est}})$ ( $M_{\odot}$ )	$(M/L)_{\text{est}}$ ( $M_{\odot}/L_{\odot}$ )
dm1049+09	146 ( $\pm 5$ )	209 ( $\pm 1$ )	80.5	> 9.49	12.05	51.3
dm1623+15	147 ( $\pm 5$ )	188 ( $\pm 2$ )	78.5	> 10.46	11.92	53.8
dm1403+41	152 ( $\pm 5$ )	224 ( $\pm 2$ )	43.3	> 5.74	11.83	30.8
dm1440+14	78 ( $\pm 4$ )	37 ( $\pm 2$ )	32.2	> 0.79	10.60	12.3
dm1718+30	65 ( $\pm 5$ )	109 ( $\pm 1$ )	31.2	> 4.40	11.59	79.4
dm0909+06	201 ( $\pm 5$ )	230 ( $\pm 2$ )	32.3	> 7.45	11.83	50.1
dm1349-02	101 ( $\pm 4$ )	68 ( $\pm 2$ )	15.9	> 1.48	10.66	15.6

Note. — Adopted distances, 3D velocity dispersions ( $\sigma_{3D}$ ), group sizes, estimated total baryonic masses ( $M_{\text{tot,est}}$ ) and mass-to-light ratios required for the groups to be bound.

APO optical spectra that all suspected group members fall within  $\pm 200$  km s<sup>-1</sup> of the original TNT pair. In all but one of the observed galaxies (dm1718+30b), the morphology of the bright H $\alpha$  emission in these groups is clumpy and asymmetric. There are also faint tidal streams and bridges in the outskirts of the individual galaxies.

## 4.4 Discussion

### 4.4.1 Possible projection effects and interlopers

The morphology of the H $\alpha$  emission shows clear signs of galaxy interactions in our groups. However, without independent distance information, projection effects can affect both our distance and velocity estimates, either of which could lead to either interlopers or unbound groups. To address this potential issue, we compare the measured properties of the dwarf galaxy groups to those predicted by theory and simulations. The TNT groups have relative line-of-sight velocity differences ( $\Delta v_{\text{los}}$ ) between group members (Stierwalt et al., 2017) consistent with those measured for bound groups found in mock catalogues based on the Millennium-II simulation ( $\Delta v_{\text{los}}$  up to 200-300 km s<sup>-1</sup> for groups with masses between  $10^9 M_{\odot}$  and  $10^{9.5} M_{\odot}$ ) (Sales et al., 2013).

The observed groups could also be unbound systems caught at a moment of passing. An estimated 59% of simulated groups of more massive galaxies identified in a similar fashion to the TNT sample (from their projected radial and velocity separations) are

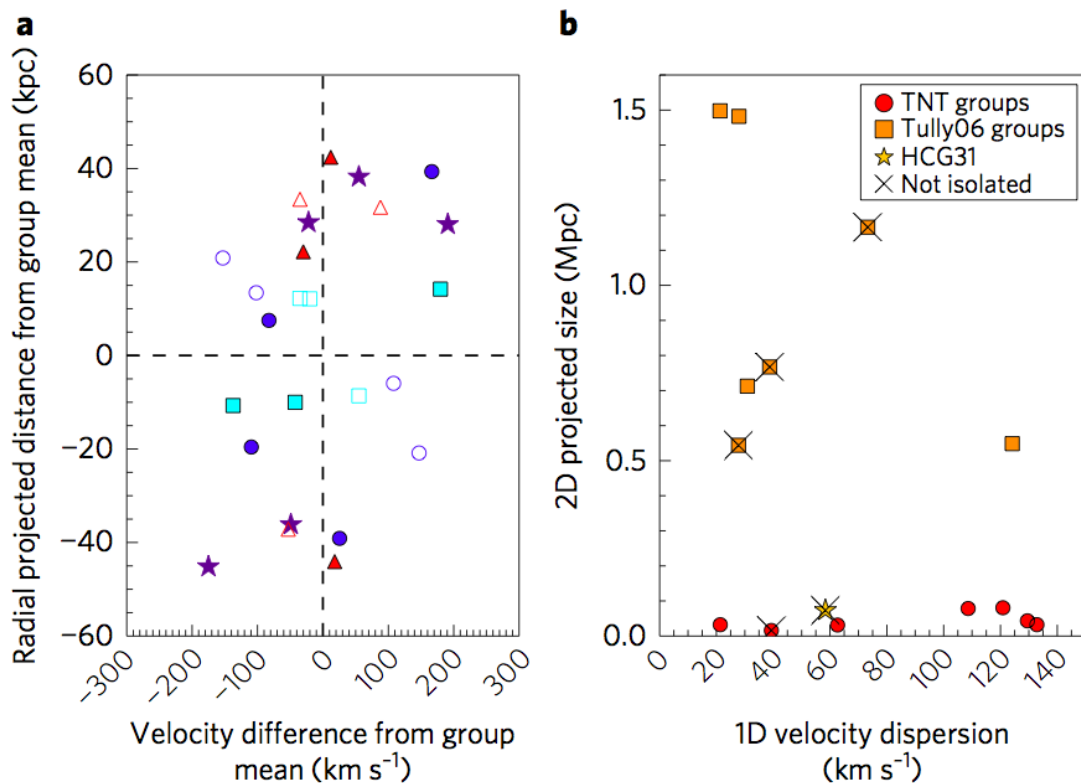


Figure 4.2 **a**: Projected radial separation from the centroid of the group versus difference in group member line-of-sight velocity from the group mean. The groups are filled stars (dm1049+09); filled circles (dm1623+15); open circles (dm1403+41); filled triangles (dm1440+14); open triangles (dm1718+30); filled squares (dm0909+06); and open squares (dm1349-02). **b**: One-dimensional velocity dispersions and 2D projected sizes for the TNT dwarf groups presented here (red circles) and dwarf associations from the literature (orange squares and yellow star). Groups  $<1.5$  Mpc from a massive ( $M \simeq 10^{10} M_{\odot}$ ) host are marked with crosses. In both panels, uncertainties are smaller than symbol sizes (see Table 1 for uncertainties in individual TNT velocity measurements).

actually physically associated (McConnachie et al., 2008). If this result holds to lower masses, a similar fraction (at least four of the seven) of the identified TNT groups are expected to be bound systems.

#### 4.4.2 Comparison to other associations of low mass galaxies

The compact dwarf groups identified here are distinct from previously known groups and loose associations of dwarf galaxies in two primary ways: previously known systems are (1) significantly more extended and/or (2) are in close proximity to a massive galaxy ( $< 1.5$  Mpc) and thus are subjected to strong external gravitational effects. Seven associations

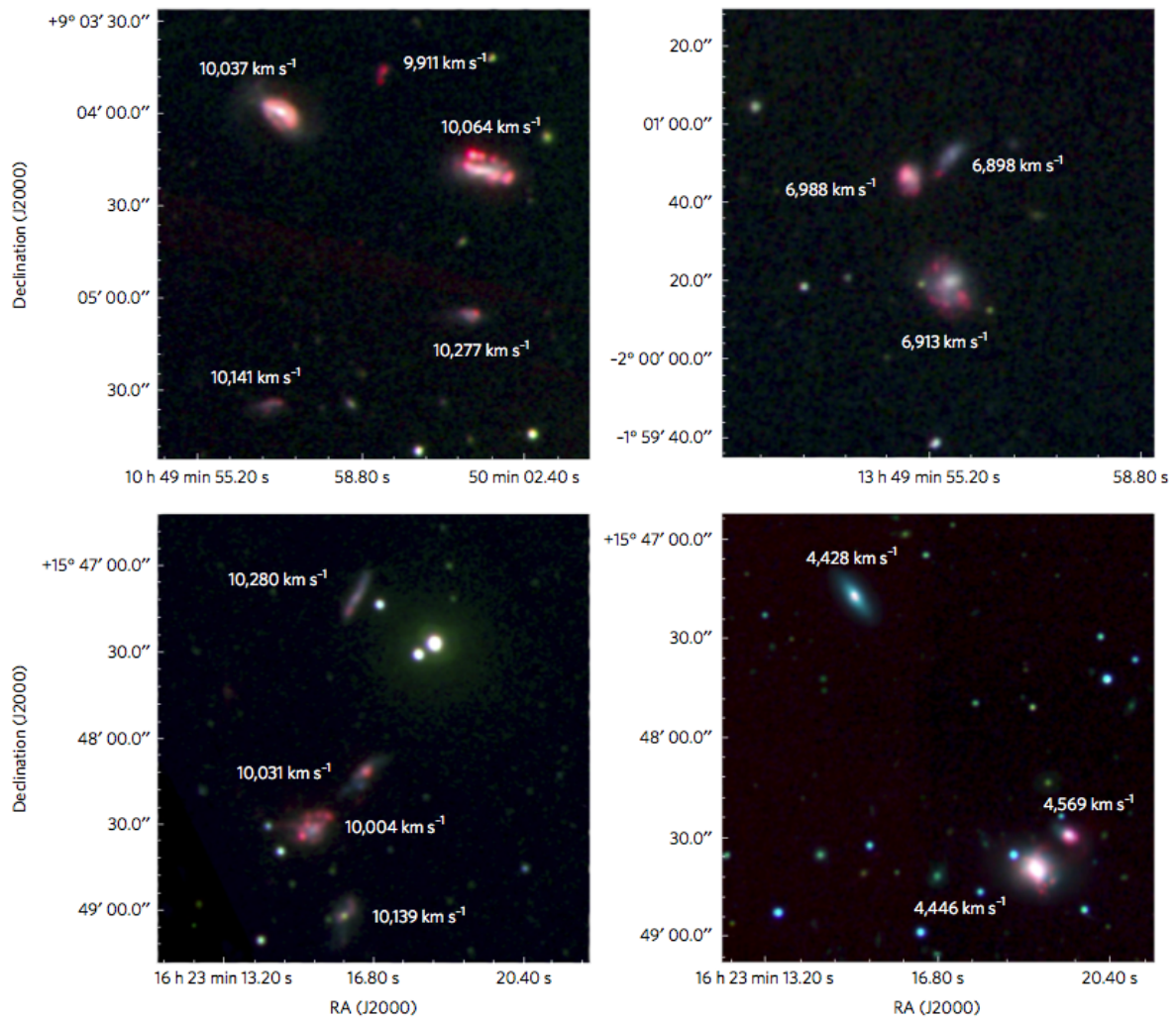


Figure 4.3 Three color RGB images of four of the dwarf groups obtained with the MarylandMagellan Tunable Filter (MMTF) Fabry Perot and with the Gemini Multi-Object Spectrograph (bottom right). Red corresponds to  $H\alpha$  emission, green corresponds to MMTF or Gemini r-band, and blue corresponds to SDSS g-band. Velocities derived from optical spectroscopy are noted for each group member in white.

of dwarf galaxies were identified in the Local Volume ( $D < 8$  Mpc) and are close enough for primary distance measurements using tip of the red giant branch stars<sup>2</sup> (Tully et al., 2006). These associations all have much larger projected and 3D sizes than the TNT groups (see Figure 2, red circles versus orange squares). A notable consequence of the larger observed sizes is the extremely large M/L ratios (all  $> 100M_{\odot}/L_{\odot}$  with some as high as  $700 M_{\odot}/L_{\odot}$ ) required for the known dwarf associations to be gravitationally bound.

<sup>2</sup>Red giants are evolved stars with inert helium cores surrounded by envelopes of hydrogen gas. These stars can be used as ‘standard candles’ to measure distances to nearby extragalactic objects, as their intrinsic brightness does not vary significantly with mass or composition. Thus, by comparing their observed luminosity to this known value, we can calculate how far away the host galaxy is.

Additionally, two of the seven associations are within 0.6 Mpc of a massive ( $M > 10^8 M_\odot$ ) host and a third is  $\sim 1.2$  Mpc from the Milky Way ( $M_* > 10^{11} M_\odot$ ).

Another previously known group that more closely resembles the TNT groups is Hickson Compact Group 31 (HCG31, [Gallagher et al. \(2010\)](#)). HCG31 includes seven to eight members within  $\sim 75$  kpc all with stellar masses of similar mass to the TNT groups ( $1 - 8 \times 10^9 M_\odot$ ). The five galaxies in the center of this compact group show clear morphological features of interaction. However, at least three massive galaxies reside within 1.5 Mpc of HCG31, the most massive ( $M_* = 10^{10.7} M_\odot$ ) at a projected distance of just under 1 Mpc and a velocity separation of only  $55 \text{ km s}^{-1}$ . Thus, the competing larger-scale environmental effects (including possible ram-pressure or tidal stripping) may be a challenge to disentangle. The TNT-selected dwarf groups are thus the first detection of dwarf-only groups whose isolation enables us to study hierarchical structure formation at low masses.

#### 4.4.3 Statistical comparison to theoretical predictions

The  $\Lambda$ CDM theory not only predicts the existence of dwarf groups but also provides statistics regarding how often they should be observed. According to the Millennium-II simulation ([Springel et al., 2005](#)), dwarf galaxies with  $M_* \simeq 10^9 M_\odot$ , the average for the TNT primary galaxies, have a 1-3% chance of having a companion of similar mass ([Sales et al., 2013](#)). This prediction is consistent with the upper limit that is estimated for the SDSS spectroscopic catalogue on the fraction of dwarfs observed to have a close companion of  $< 5\%$  ([Stierwalt et al., 2015, 2017](#)). The FIRE simulations, which push to even lower primary galaxy masses and focus specifically on isolated environments, produce consistent results, specifically that  $\sim 5\%$  of isolated dwarf galaxies are found to have a companion with a mass ratio of at least 1:3 ([Wheeler et al., 2015](#)).

The Millennium-II simulation results further predict that the same TNT primary group members have a 1-10% chance of hosting the second and third most massive satellites observed in the TNT groups; of the 60 systematically selected, isolated TNT pairs, seven have additional observable companions, or 11%. This fraction is consistent with the higher end of the range from predictions from simulations (10%). If only 59% of the TNT groups prove to be bound structures, as is observed for more massive galaxies, the observed fraction of 11% reduces to  $\sim 6\%$  and thus lies right within the predicted range.

#### 4.4.4 Qualitative comparison to massive galaxy groups

HCG galaxies are seen to occupy the ‘red sequence’ in optical color-space at a higher fraction than galaxies in other gravitational environments, suggesting that they have evolved from blue and star-forming to ‘red and dead’ (Walker et al., 2013). The low mass galaxies in the TNT groups presented here do not follow this pattern. The narrowband H $\alpha$  imaging from the MMTF and GMOS-N shows that, in the groups we were able to observe, there is ongoing star formation (age < 10 Myr) throughout the system. This is in contrast to what is found in massive galaxy groups, namely that the quenching of star formation in such environments is accelerated. In fact, we observe similar star formation rates in these TNT groups as is observed in the TNT pairs (Stierwalt et al. 2015; Liss et al. 2018, *in prep*). These data therefore suggest that evolution of groups of low mass galaxies does indeed proceed differently from their massive counterparts. These low mass groups may not contain a significant IGM capable of heating the galaxies’ gas to temperatures that are not conducive to forming stars.

### 4.5 Conclusion

We have presented the first confirmed compact groups of galaxies containing only low mass dwarf members. We see that these groups do not appear to evolve in the same way as massive groups of galaxies. Specifically, we observe no evidence of the accelerated star formation quenching observed in compact groups that include massive galaxies in the TNT dwarf galaxy groups. In contrast, the dwarf groups are forming stars at the same rates as dwarf pairs. This leaves open the possibility that low mass groups of galaxies are the potential building blocks of more massive galaxies, as they are able to continue growing in stellar mass during their interaction and merger process. In other words, the existence of these dwarf-only groups suggests that, given time, hierarchical merging will turn some of these groups into isolated intermediate-mass galaxies. Based on the estimated total stellar masses of the TNT groups (see Table 4.2), and allowing for some additional conversion of gas into stars, these groups could produce isolated galaxies with masses of  $\sim 10^9 - 10^{10} M_{\odot}$ . Thus, at least some of the galaxies observed to exist today in this mass range may have been built up from mergers within dwarf groups. The TNT dwarf groups presented here provide direct probes of this hierarchical structure formation in action at the low mass end, giving us a new window into a process expected to be common at earlier times, but nearly impossible to observe at such redshifts.

The future steps in this research require both improved simulations and new high-quality, multi-wavelength observations. Current theoretical models are just at the stage where we can begin to probe the low mass galaxies discussed in this chapter (e.g., [Hopkins et al., 2014](#); [Vogelsberger et al., 2014](#)). The increased mass, time, and spatial resolution of the next generation of simulations will allow for both more detailed studies of individual dwarf galaxies as well as a more accurate understanding of their formation and evolution in a complete cosmological context.

On the observational side, to further probe the 3D structure of our TNT groups, we have an ongoing radio VLA program to obtain a low-resolution neutral hydrogen gas map for each group to look for bridges, streams or other features directly connecting the group members physically to one another. We have also used the Large Binocular Camera on the twin 8.4-meter mirrors of the Large Binocular telescope to obtain deeper optical imaging of one of the groups presented here (dm1049+09). This high sensitivity data will be used to identify additional companions with even lower stellar masses ( $\sim 2 \times 10^5 M_{\odot}$ ). Probing these lower mass members will allow for a more direct comparison between our observations and theoretical predictions ([Wheeler et al., 2015](#)). Furthermore, new optical and infrared ground- and space-based observatories such as the Large Synoptic Survey Telescope and the James Webb Space Telescope will allow us to both increase our sample size and detect these faint galaxies out to higher redshifts.

# Chapter 5

## Summary and Conclusion

Dwarf galaxies are, by number, the most prevalent type of galaxy at all redshifts. Determining the characteristics of interactions between them is critical to understanding galaxy evolution. Massive galaxies, like our own Milky Way, are theorized to have formed hierarchically through the merging of these low mass galaxies. Thus, understanding the impact of dwarf galaxy interactions on how star formation proceeds in these systems will provide important insight into hierarchical galaxy formation.

The TiNy Titans (TNT) survey is the first systematic study of interacting dwarf galaxies. It is a combined multi-wavelength observational and theoretical campaign aimed at investigating the role that dwarf galaxy interactions play in the larger picture of galaxy evolution. We have used the spectroscopic portion of the Sloan Digital Sky Survey (SDSS) to identify a sample of 104 interacting dwarf galaxy ( $M_* < 5 \times 10^9 M_\odot$ ) pairs ( $r_{\text{sep}} < 50$  kpc &  $v_{\text{sep}} < 300 \text{ km s}^{-1}$ ) at low redshifts ( $0.007 < z < 0.05$ ). The survey has three primary goals: (1) define the dwarf-dwarf interaction sequence at  $z \simeq 0$ ; (2) use these low redshift merging systems to understand galaxy assembly at higher redshifts; and (3) determine the prevalent modes of star formation in the low metallicity environments of dwarf galaxies. This thesis has examined the ongoing star formation in the TNT interacting dwarf galaxies in unprecedented detail.

Using the wealth of data available from large surveys spanning ultraviolet (GALEX), optical (SDSS), and infrared (WISE) wavelengths, we have contextualized the place of dwarf galaxy interactions in the larger context of star-forming galaxies. The global star formation properties of the TNT pairs as determined by their spectral energy distributions (SEDs) put them in line with massive spiral galaxies, possibly even forming more stars per unit mass than their more massive counterparts. Further, the dwarf galaxies have

characteristically different signatures of star formation than massive interacting galaxies, which may indicate different modes of star formation in these systems; specifically, the dwarf galaxies typically contain less dust and thus exhibit (1) more ultraviolet and optical emission from the photospheres of young stars, and (2) less infrared emission from cooler stars and warm dust. These trends are consistent with the lower metal abundances typically found in dwarf galaxies.

We show the importance of environmental factors in determining how and where stars form in interacting dwarf galaxies. Using high-resolution, narrowband  $H\alpha$  imaging, we are able to measure the fraction of star formation occurring in compact environments, count the number of these discrete regions in each galaxy, and calculate how luminous the brightest of the clusters can be. We have found that dwarf galaxies that are isolated from massive galaxies have more star-forming regions that contain a larger fraction of  $H\alpha$  emission than non-isolated interacting dwarfs. We further see that the luminosity of the brightest clusters in each galaxy increases with increasing isolation. We also see an environmental impact when considering the gravitational influence on a dwarf galaxy by its low mass companion; dwarf galaxies that are *nonisolated* from their TNT pair member form more discrete  $H\alpha$  regions than those that are considered marginally isolated. Combined, these observations highlight the magnitude of the effects that dwarf galaxies can have on one another outside the gravitational influence of more massive galaxies (i.e. similar to the conditions found at high redshift in the early universe).

We also investigate groups of three or more dwarf galaxies, an important subset of the TNT sample. For massive galaxies, we find that their evolution in pairs proceeds in notably different ways from massive galaxy evolution in group environments. Specifically, groups of massive galaxies experience the accelerated quenching of star formation which is found to be enhanced in pairs. This would pose a problem for the theory of hierarchical galaxy evolution were this trend to follow for interactions among groups of dwarf galaxies; if such group interactions halted star formation in low mass galaxies then they could not build up the stellar populations we observe in today's massive galaxies and thus could not be the building blocks of these systems. We find no evidence of quenching in the TNT low mass compact galaxy groups, observing instead enhanced star formation like those with just one dwarf companion. Along with confirming that the members of these groups are likely to be gravitationally bound to one another, such groups remain well-poised to serve as the foundation of massive galaxy buildup.

It is important to remember that the work presented here is one piece in a large and fascinating puzzle that is being explored under the umbrella of the TNT interacting dwarf

galaxy survey. The UV, optical, and IR observations of stars and dust presented here are part of the TNT Low- $z$  sample, which also includes ongoing radio, submillimeter, and x-ray observations of atomic and molecular gas, active galactic nuclei, and x-ray binary star systems. Additionally, upcoming ground- and space-based observing programs with the Large Synoptic Survey Telescope and the James Webb Space Telescope will allow for the sample of 104 pairs to be significantly expanded, adding to the statistical power of this program. Furthermore, the TNT Low- $z$  Sample is just one of three components of the TNT Survey. Advances in both instrumentation and simulations are on the horizon for both the TNT Local Volume Program and the TNT Theory Program. We will be able to obtain higher resolution observations of even more local interacting low mass galaxies as well as accurately model these individual systems in an effort to understand their initial conditions. On the theoretical end, improvements in mass, size, and time resolution, as well as more complete inclusion of physical processes will allow for even more direct and realistic comparisons. And, as is the course of science, all of these future prospects and studies will inspire new and challenging questions to be answered.

Finally, as scientists, we have an obligation to share our work not only with others in the scientific community, but also with members of the general public. People are too often dissuaded from pursuing scientific research and careers because they are presented as entirely objective and solitary. This portrayal is especially discouraging for individuals from traditionally underrepresented backgrounds, as they cannot envision themselves as members of this group. In reality, science is *not* about getting the correct answers, as there rarely is a ‘correct answer’ to be found. It is an inherently creative process that relies on critical thinking, collaboration, and perseverance. We as scientists need to actively embrace and demonstrate these qualities in order to make our community more accepting. We will never reach our full scientific potentials without including as many points of view as possible.

# Appendix A

## TNT Low- $z$ Sample Properties and Photometry

In this appendix we include the pair properties and photometric data (including Sloan Digital Sky Survey 5-color *ugriz* images) for the TNT Low- $z$  sample.

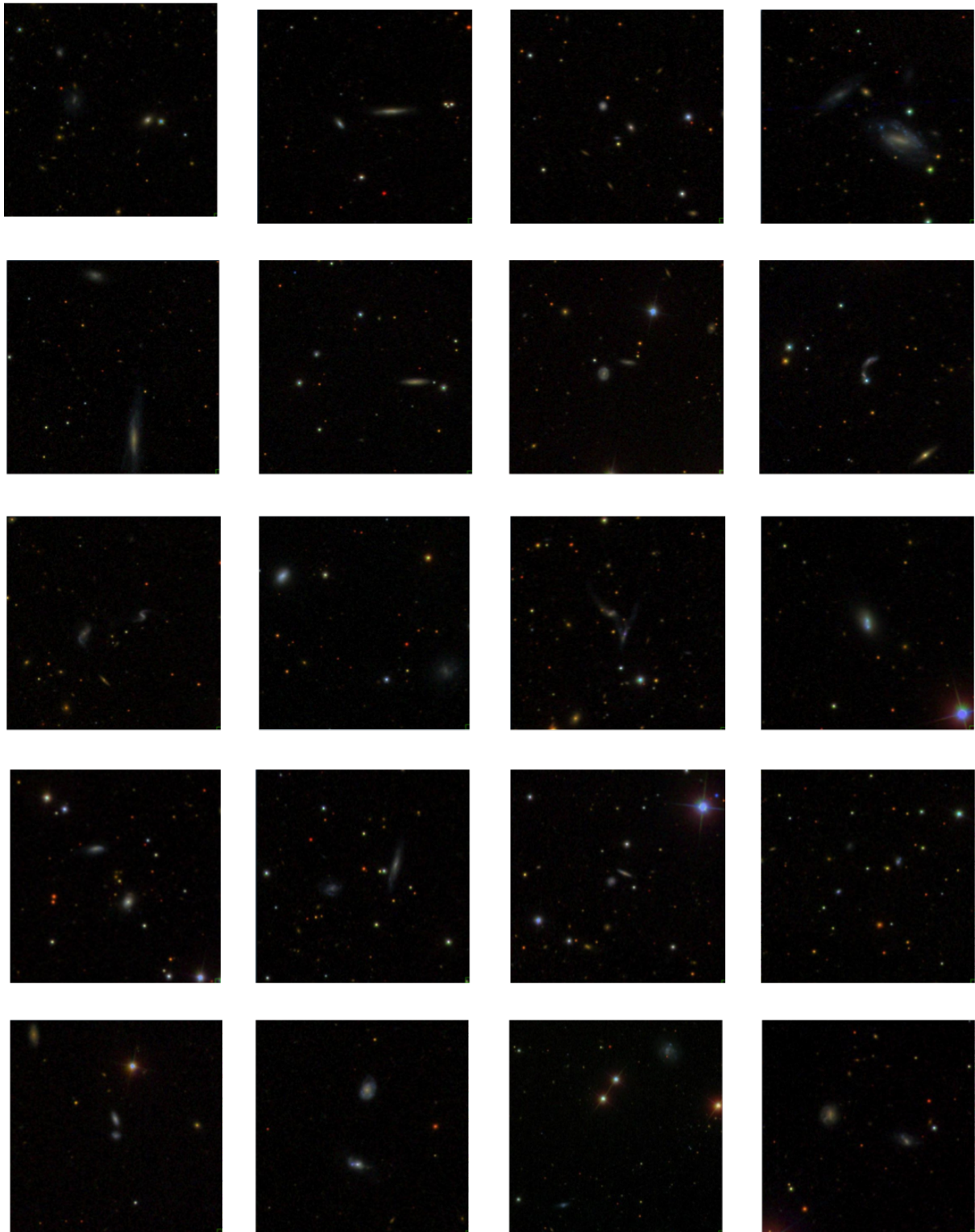


Figure A.1 Isolated galaxy SDSS images.

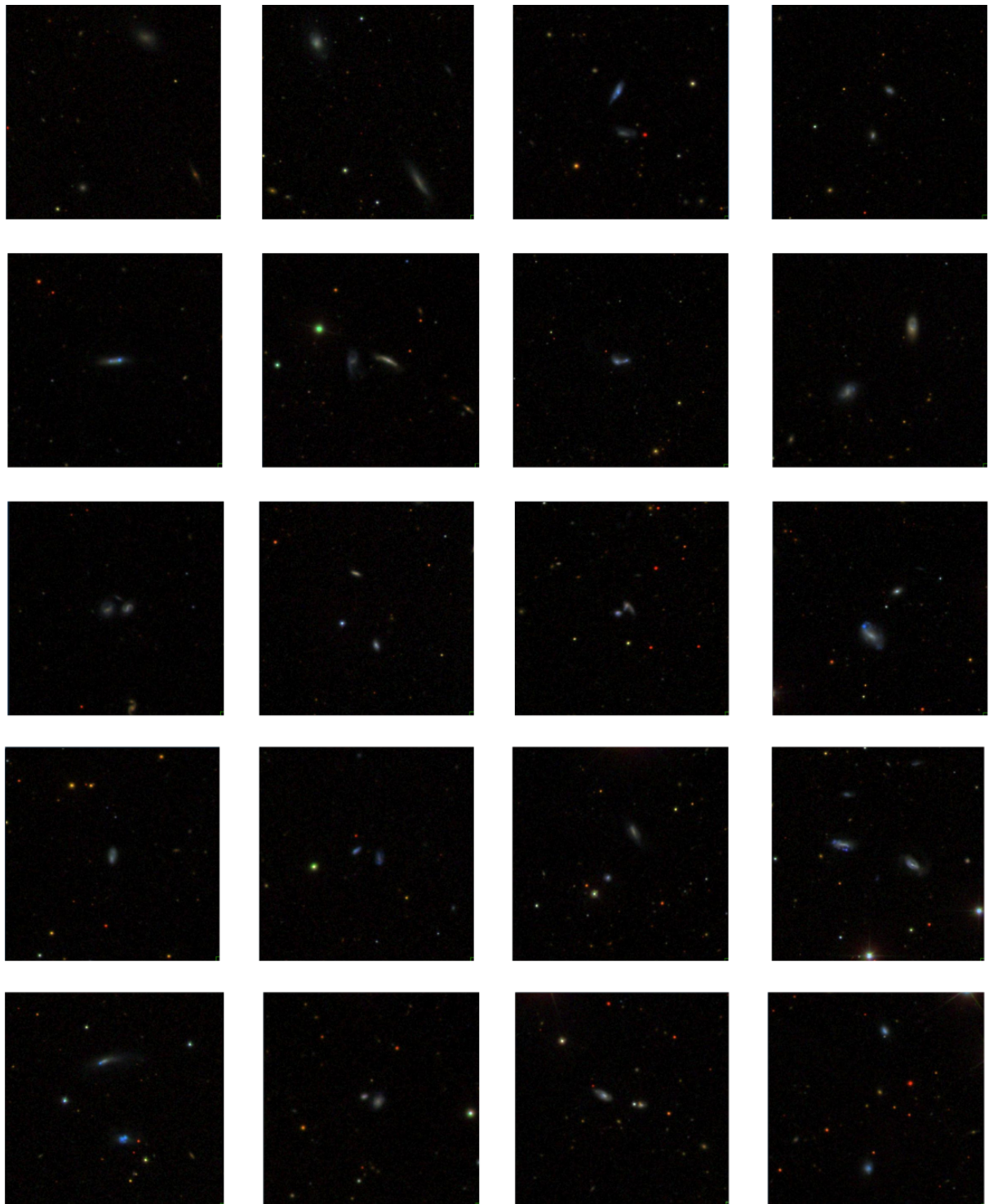


Figure A.2 Isolated galaxy SDSS images.

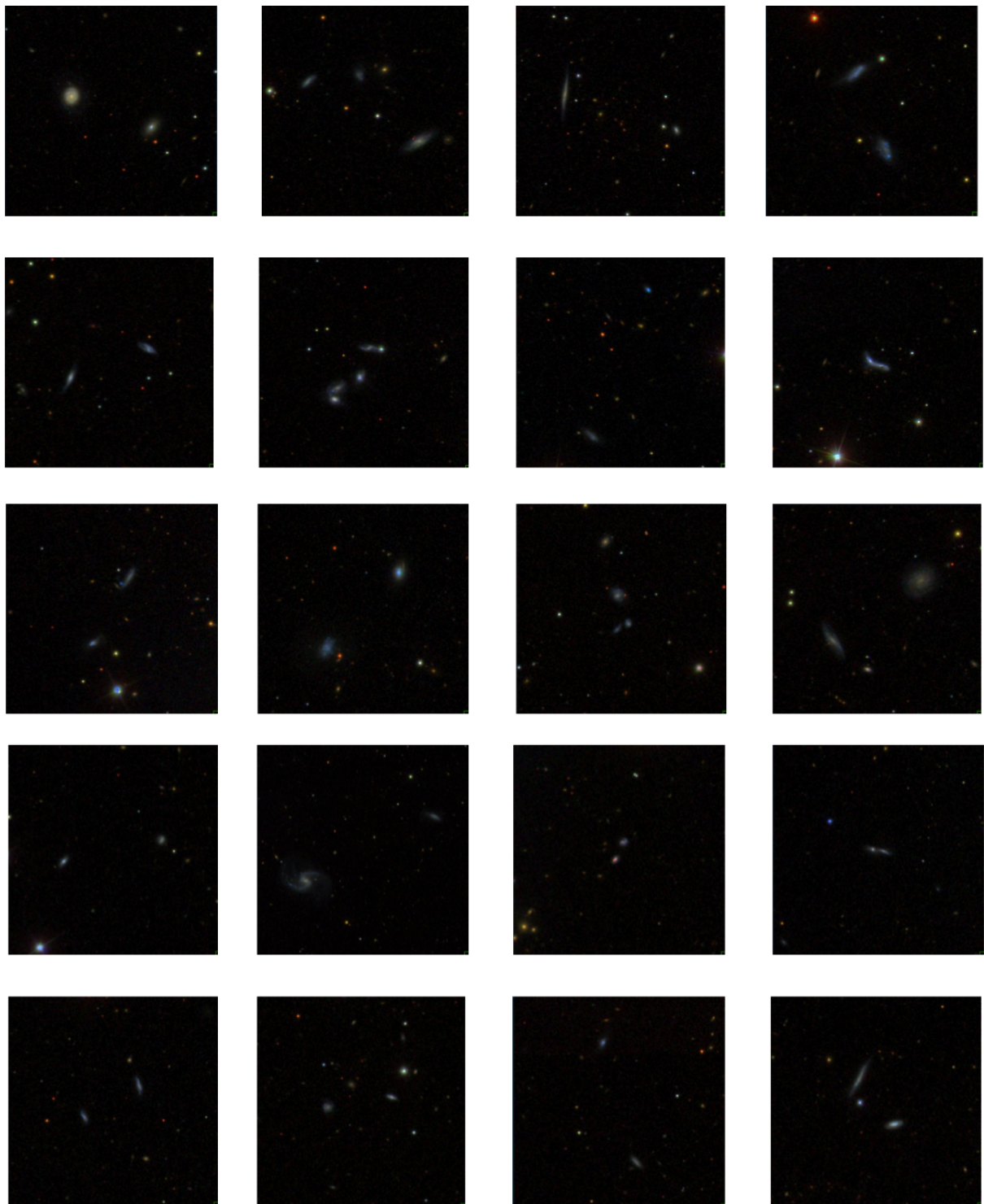


Figure A.3 Isolated galaxy SDSS images.

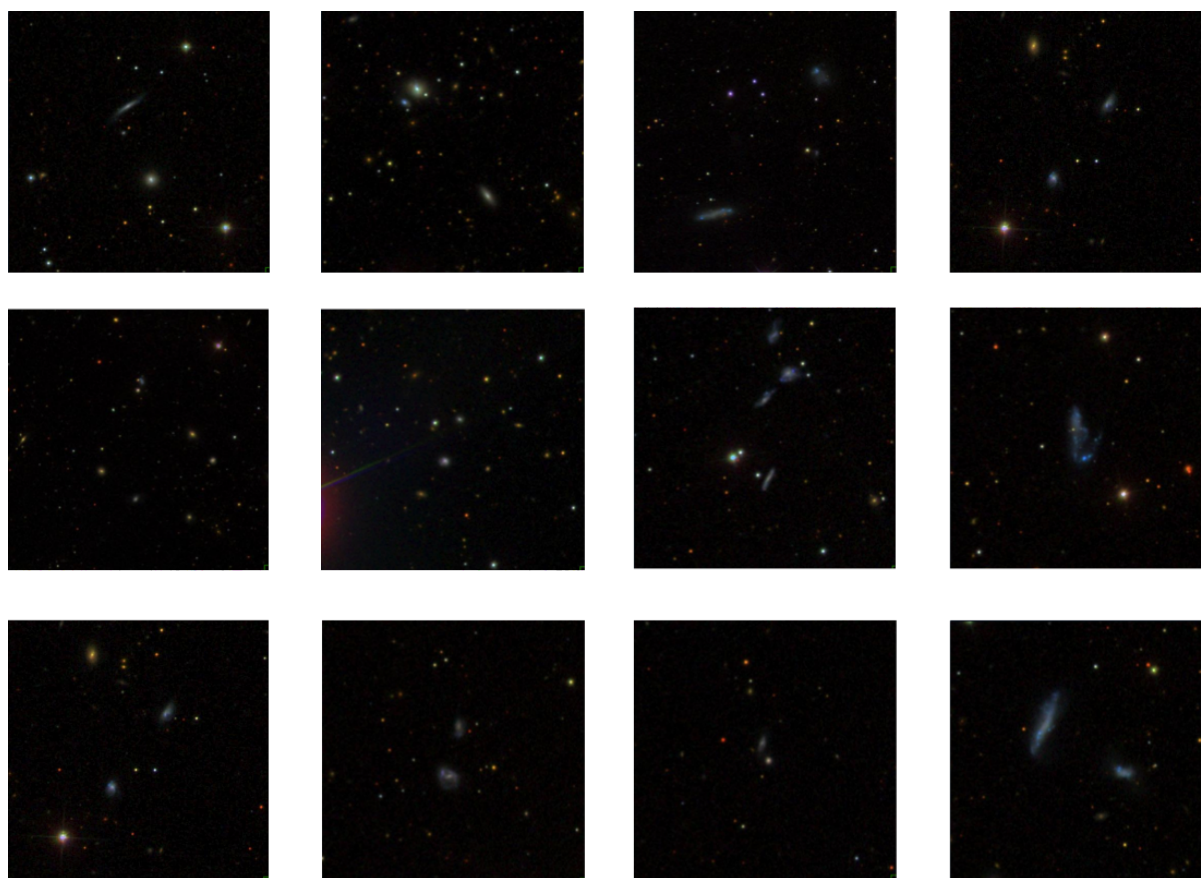


Figure A.4 Isolated galaxy SDSS images.

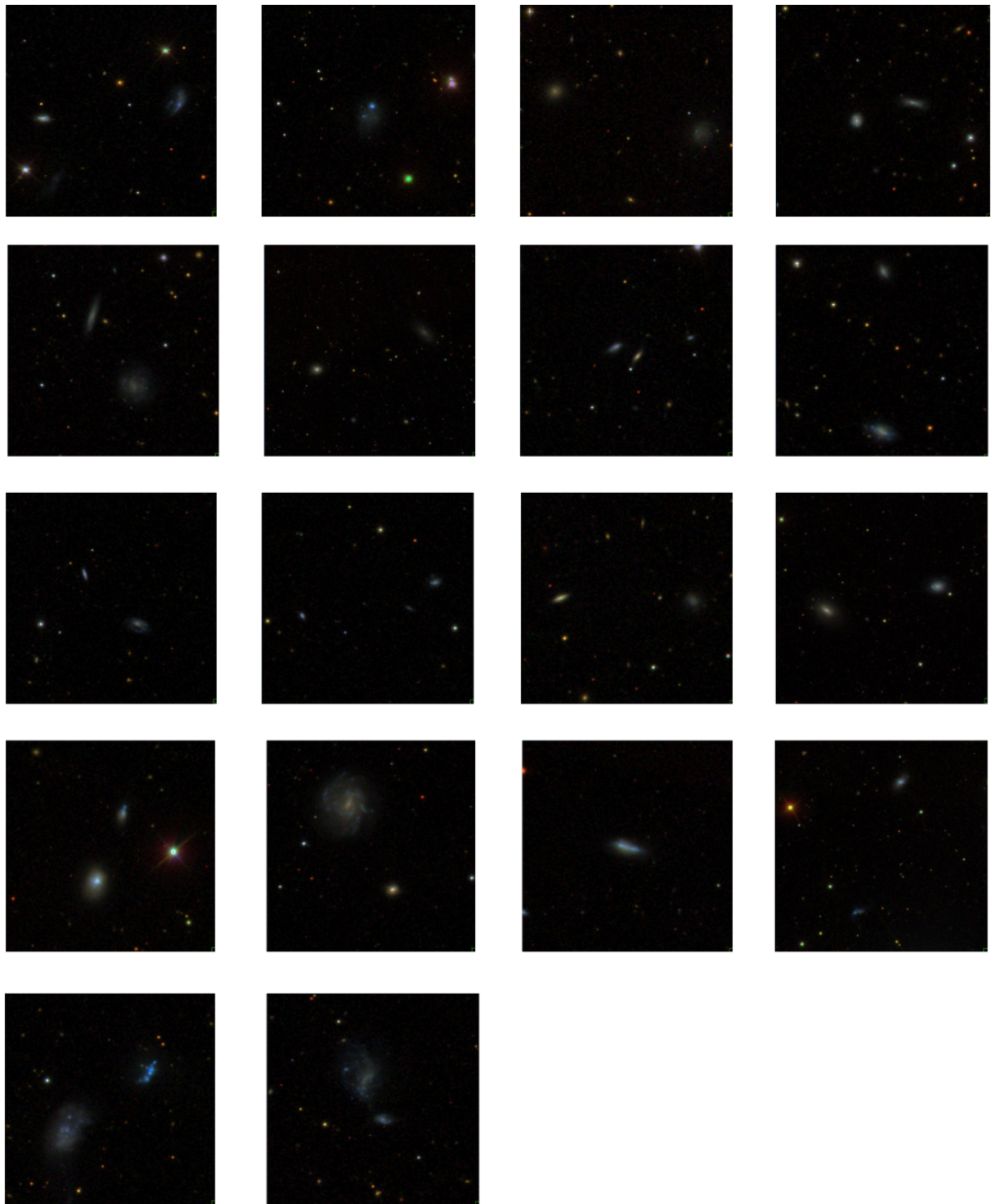


Figure A.5 Marginally isolated galaxy SDSS images.

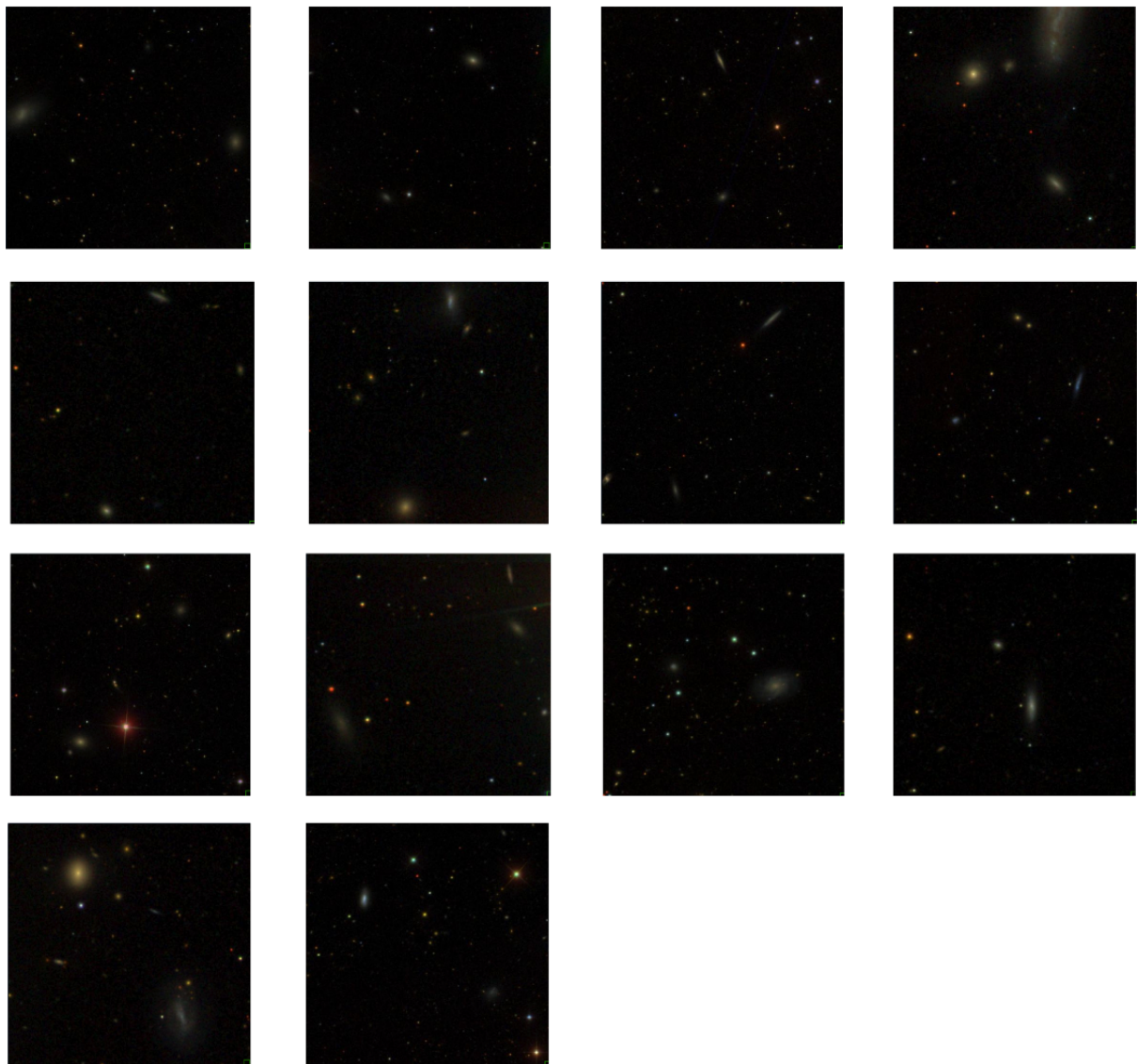


Figure A.6 Nonisolated galaxy SDSS images.

Table A.1. TNT Pair Properties

TNT Pair Name	$z$	$r_{\text{sep}}$ (kpc)	$v_{\text{sep}}$ (km s $^{-1}$ )	Mass Ratio	Log( $M_{\text{host}}$ ) ( $M_{\odot}$ )	$D_{\text{host}}$ (Mpc)	$\Theta_{\text{host}}$
dm0027+00	0.031	45.	140.	2.7	10.4	2.87	-1.9
dm0035-10	0.038	12.	112.	2.7	10.8	2.21	-1.2
dm0052+00	0.034	48.	154.	1.6	10.2	4.26	-2.6
dm0058+01	0.018	47.	16.0	1.8	9.76	0.257	0.57
dm0204-10	0.0061	44.	39.0	8.5	9.88	0.611	-0.44
dm0206-08	0.018	15.	111.	4.1	10.8	0.695	0.30
dm0346+00	0.031	47.	167.	2.8	–	> 10	–
dm0744+21	0.029	33.	78.0	4.0	10.1	2.37	-2.0
dm0759+15	0.036	46.	25.0	3.5	10.3	2.08	-1.6
dm0801+14	0.053	15.	271.	1.9	10.3	1.96	-1.6
dm0813+07	0.030	38.	23.0	1.1	9.76	0.523	-0.36
dm0815+42	0.044	50.	39.0	2.6	10.3	2.50	-1.9
dm0818+24	0.0073	27.	106.	3.4	10.2	1.17	-0.95
dm0820+03	0.052	23.	19.0	2.1	10.1	2.51	-2.0
dm0827+46	0.0072	0.85	54.0	4.6	10.8	1.52	-0.71
dm0828+20	0.015	49.	60.0	5.9	9.71	0.649	-0.69
dm0833+22	0.025	48.	73.0	8.2	10.4	1.76	-1.3
dm0844+20	0.027	13.	70.0	2.6	10.1	1.85	-1.7
dm0850+45	0.071	19.	34.0	2.4	–	> 10	–
dm0901+12	0.020	20.	122.	4.4	10.3	2.25	-1.7
dm0909+06	0.046	30.	210.	1.1	10.3	3.35	-2.3
dm0916+06	0.012	18.	228.	8.1	9.78	3.05	-2.6
dm0924+34	0.0063	46.	34.0	1.4	10.7	0.0652	3.3
dm0925+66	0.0057	18.	62.0	3.2	9.81	0.820	-0.89
dm0930+60	0.014	21.	1.00	3.0	9.70	2.92	-2.7
dm0944-00	0.0050	10.	10.0	3.5	10.1	0.222	1.1
dm0948+32	0.0052	7.4	7.00	5.0	10.1	0.207	1.2
dm0953+49	0.054	15.	75.0	2.4	10.6	1.54	-0.96
dm0957+15	0.014	26.	200.	1.5	10.4	0.497	0.38
dm1007+55	0.033	23.	50.0	1.4	10.3	4.15	-2.5
dm1014+59	0.0072	19.	43.0	1.6	10.3	0.719	-0.19
dm1022+21	0.014	32.	119.	4.6	11.0	0.0432	4.1
dm1031+41	0.0087	1.1	42.0	4.6	10.2	2.61	-2.0
dm1032+28	0.0054	30.	17.0	5.9	10.4	0.0624	3.1
dm1036+10	0.027	13.	13.0	1.1	10.6	2.37	-1.5

Table A.1 (cont'd)

TNT Pair Name	$z$	$r_{\text{sep}}$ (kpc)	$v_{\text{sep}}$ (km s $^{-1}$ )	Mass Ratio	$\text{Log}(M_{\text{host}})$ ( $M_{\odot}$ )	$D_{\text{host}}$ (Mpc)	$\Theta_{\text{host}}$
dm1048+32	0.045	43.	14.0	4.3	10.3	1.93	-1.5
dm1049+09	0.034	45.	23.0	1.4	9.88	1.90	-1.9
dm1051+65	0.011	41.	83.0	2.1	10.5	0.0834	2.7
dm1059+47	0.034	12.	111.	1.1	9.96	2.91	-2.4
dm1106+01	0.031	43.	145.	2.1	10.4	2.85	-1.9
dm1107+00	0.061	13.	17.0	2.9	–	> 10	–
dm1115+46	0.0096	2.2	3.00	5.5	10.5	0.423	0.65
dm1132+14	0.018	16.	42.0	5.5	9.84	1.95	-2.0
dm1132+57	0.0051	22.	5.00	1.1	10.4	0.182	1.7
dm1134+44	0.019	3.0	26.0	2.4	10.2	1.71	-1.5
dm1141+32	0.0059	31.	65.0	4.4	10.6	0.247	1.5
dm1142+52	0.030	20.	91.0	4.8	10.1	1.90	-1.7
dm1145+13	0.011	40.	147.	5.5	11.1	0.0486	4.1
dm1152+07	0.032	5.8	121.	4.0	9.93	2.08	-2.0
dm1155+43	0.036	49.	16.0	2.0	10.3	0.288	1.0
dm1202+33	0.024	41.	141.	3.2	10.6	1.56	-0.98
dm1204+17	0.014	47.	30.0	1.1	10.3	0.782	-0.31
dm1213+07	0.0073	49.	64.0	4.5	10.4	0.105	2.4
dm1214+49	0.014	39.	91.0	1.5	10.8	0.883	0.0062
dm1218+05	0.0081	46.	261.	3.7	9.97	0.0919	2.1
dm1218+45	0.019	15.	49.0	1.2	9.79	0.743	-0.78
dm1219+06	0.0069	23.	135.	2.6	10.3	0.0201	4.4
dm1220+08	0.015	38.	121.	8.0	9.81	0.135	1.5
dm1220+20	0.021	19.	53.0	3.8	10.0	1.83	-1.7
dm1225+50	0.0083	14.	19.0	7.5	10.6	2.47	-1.5
dm1231+06	0.031	37.	29.0	1.6	9.95	3.57	-2.7
dm1235+57	0.038	46.	5.00	1.0	10.4	2.08	-1.5
dm1237+18	0.0085	21.	18.0	2.8	11.2	1.58	-0.32
dm1242+34	0.014	16.	40.0	1.3	10.7	1.65	-0.93
dm1246+32	0.023	45.	24.0	1.0	9.87	1.52	-1.6
dm1247-01	0.0092	33.	102.	7.8	10.5	0.150	2.1
dm1254+58	0.0084	37.	108.	2.2	10.6	0.342	1.1
dm1312+34	0.017	20.	293.	2.1	10.7	0.134	2.4
dm1314+35	0.0079	50.	10.0	2.3	10.1	2.58	-2.1
dm1319+55	0.076	26.	0.00	2.0	–	> 10	–

Table A.1 (cont'd)

TNT Pair Name	$z$	$r_{\text{sep}}$ (kpc)	$v_{\text{sep}}$ (km s $^{-1}$ )	Mass Ratio	Log( $M_{\text{host}}$ ) ( $M_{\odot}$ )	$D_{\text{host}}$ (Mpc)	$\Theta_{\text{host}}$
dm1337+18	0.065	13.	56.0	1.6	—	> 10	—
dm1338+22	0.016	24.	21.0	2.8	10.1	1.65	-1.5
dm1342+52	0.0060	12.	72.0	1.5	9.99	0.745	-0.58
dm1349-02	0.023	14.	65.0	3.3	9.88	0.558	-0.32
dm1350-02	0.024	50.	64.0	2.5	9.72	0.940	-1.2
dm1352+03	0.015	23.	1.00	2.4	10.4	0.497	0.32
dm1357+54	0.026	41.	34.0	1.7	10.2	2.71	-2.1
dm1402+50	0.0064	29.	264.	1.1	10.7	0.405	0.89
dm1403+41	0.035	21.	37.0	1.1	10.4	3.30	-2.1
dm1406+55	0.0064	19.	252.	8.2	10.7	0.0322	4.2
dm1418+21	0.0087	27.	23.0	3.0	9.95	1.55	-1.6
dm1419+50	0.0055	30.	76.0	2.5	10.3	0.128	2.0
dm1422+18	0.029	13.	153.	4.0	11.2	0.623	0.82
dm1422+22	0.032	10.	46.0	1.3	10.3	2.03	-1.6
dm1427+56	0.0066	31.	108.	3.3	10.8	0.0805	3.1
dm1429+40	0.0090	28.	80.0	1.8	9.75	0.335	0.21
dm1440+14	0.018	45.	3.00	4.7	10.3	1.91	-1.5
dm1447+17	0.021	48.	100.	3.9	10.1	1.79	-1.6
dm1449+36	0.0062	10.	18.0	1.2	9.86	0.995	-1.1
dm1503+00	0.0053	1.4	25.0	2.0	10.6	0.313	1.2
dm1505+01	0.0072	21.	253.	2.6	10.1	0.181	1.4
dm1520+01	0.026	31.	60.0	3.0	10.5	2.26	-1.5
dm1523+36	0.023	34.	9.00	1.7	10.2	2.87	-2.1
dm1526+24	0.053	40.	7.00	1.6	9.93	2.55	-2.2
dm1526+41	0.053	15.	53.0	1.9	10.6	5.81	-2.7
dm1529+26	0.0068	10.	32.0	1.2	—	> 10	—
dm1539+34	0.022	24.	24.0	2.1	9.99	0.467	0.027
dm1616+34	0.0090	34.	22.0	2.2	9.70	6.18	-3.6
dm1620+25	0.064	42.	43.0	1.4	—	> 10	—
dm1623+15	0.034	41.	235.	1.8	10.3	2.04	-1.6
dm1647+21	0.0090	5.3	27.0	1.9	—	> 10	—
dm1718+30	0.015	30.	6.00	4.0	10.2	1.59	-1.4
dm2227-09	0.0056	31.	34.0	4.6	10.7	4.01	-2.0
dm2358+14	0.027	38.	27.0	1.1	11.1	2.98	-1.3

Note. — If no massive galaxy was found within 10 Mpc ( $D_{\text{host}} > 10$ ), then the mass of the host and  $\Theta_{\text{host}}$  are undefined.

Table A.2. TNT Galaxy Properties

TNT Pair Name	ID1	ID2	$\log(M_*)$ ( $M_\odot$ )	$z$	Metallicity
dm0027+00	dm0027+00a	I097	8.6	0.031	8.4
dm0027+00	dm0027+00b	I098	9.3	0.031	8.9
dm0035-10	dm0035-10a	I015	9.1	0.037	8.7
dm0035-10	dm0035-10b	I016	8.6	0.038	8.4
dm0052+00	dm0052+00a	I115	9.3	0.034	8.7
dm0052+00	dm0052+00b	I116	9.5	0.035	8.9
dm0058+01	dm0058+01a	N077	8.7	0.018	8.6
dm0058+01	dm0058+01b	N078	8.2	0.018	8.1
dm0204-10	dm0204-10a	N071	7.0	0.0063	–
dm0204-10	dm0204-10b	N072	7.7	0.0064	8.0
dm0206-08	dm0206-08a	N019	8.9	0.018	8.4
dm0206-08	dm0206-08b	N020	8.2	0.018	8.2
dm0346+00	dm0346+00a	I109	9.3	0.030	8.9
dm0346+00	dm0346+00b	I110	8.9	0.031	8.5
dm0744+21	dm0744+21a	I073	8.8	0.029	8.7
dm0744+21	dm0744+21b	I074	9.4	0.029	8.8
dm0759+15	dm0759+15a	I107	8.8	0.036	8.3
dm0759+15	dm0759+15b	I108	9.2	0.036	8.6
dm0801+14	dm0801+14a	I031	9.1	0.054	8.7
dm0801+14	dm0801+14b	I032	9.3	0.053	8.7
dm0813+07	dm0813+07a	N063	8.4	0.030	8.5
dm0813+07	dm0813+07b	N064	8.3	0.030	8.2
dm0815+42	dm0815+42a	I117	9.2	0.044	8.7
dm0815+42	dm0815+42b	I118	8.9	0.044	8.7
dm0818+24	dm0818+24a	N041	7.7	0.0070	–
dm0818+24	dm0818+24b	N042	8.2	0.0074	8.2
dm0820+03	dm0820+03a	I057	9.3	0.052	8.8
dm0820+03	dm0820+03b	I058	9.0	0.052	8.6
dm0827+46	dm0827+46a	I001	7.8	0.0074	8.0
dm0827+46	dm0827+46b	I002	8.0	0.0072	8.3
dm0828+20	dm0828+20a	N081	8.1	0.015	–
dm0828+20	dm0828+20b	N082	8.8	0.015	8.6
dm0833+22	dm0833+22a	I113	8.3	0.025	8.5
dm0833+22	dm0833+22b	I114	9.2	0.025	8.8
dm0844+20	dm0844+20a	I025	9.0	0.027	8.8

Table A.2 (cont'd)

TNT Pair Name	ID1	ID2	$\log(M_*)$ ( $M_\odot$ )	$z$	Metallicity
dm0844+20	dm0844+20b	I026	8.6	0.026	8.4
dm0850+45	dm0850+45a	I041	9.4	0.070	8.7
dm0850+45	dm0850+45b	I042	9.1	0.071	8.6
dm0901+12	dm0901+12a	I047	8.5	0.020	8.6
dm0901+12	dm0901+12b	I048	9.0	0.019	8.7
dm0909+06	dm0909+06a	I067	9.3	0.047	8.9
dm0909+06	dm0909+06b	I068	9.4	0.046	8.8
dm0916+06	dm0916+06a	I039	7.8	0.012	–
dm0916+06	dm0916+06b	I040	8.9	0.012	8.5
dm0924+34	dm0924+34a	N075	8.5	0.0061	–
dm0924+34	dm0924+34b	N076	8.1	0.0062	–
dm0925+66	dm0925+66a	N021	7.0	0.0042	–
dm0925+66	dm0925+66b	N022	7.5	0.0056	8.4
dm0930+60	dm0930+60a	I049	8.2	0.014	8.2
dm0930+60	dm0930+60b	I050	7.9	0.014	8.1
dm0944-00	dm0944-00a	N009	7.7	0.0047	–
dm0944-00	dm0944-00b	N010	7.2	0.0048	7.9
dm0948+32	dm0948+32a	N005	8.3	0.0051	8.6
dm0948+32	dm0948+32b	N006	7.3	0.0053	8.2
dm0953+49	dm0953+49a	I029	9.1	0.054	8.6
dm0953+49	dm0953+49b	I030	9.4	0.054	9.0
dm0957+15	dm0957+15a	N039	9.2	0.014	–
dm0957+15	dm0957+15b	N040	8.9	0.014	9.0
dm1007+55	dm1007+55a	I055	9.2	0.033	8.7
dm1007+55	dm1007+55b	I056	9.1	0.033	8.3
dm1014+59	dm1014+59a	N023	7.2	0.0072	8.0
dm1014+59	dm1014+59b	N024	7.5	0.0073	8.1
dm1022+21	dm1022+21a	N055	9.2	0.014	–
dm1022+21	dm1022+21b	N056	8.6	0.014	–
dm1031+41	dm1031+41a	I003	7.1	0.0088	8.2
dm1031+41	dm1031+41b	I004	7.5	0.0086	8.0
dm1032+28	dm1032+28a	N047	7.4	0.0054	8.4
dm1032+28	dm1032+28b	N048	8.2	0.0053	8.4
dm1036+10	dm1036+10a	I019	8.1	0.027	7.9
dm1036+10	dm1036+10b	I020	8.0	0.027	8.1

Table A.2 (cont'd)

TNT Pair Name	ID1	ID2	$\log(M_*)$ ( $M_\odot$ )	$z$	Metallicity
dm1048+32	dm1048+32a	I093	8.7	0.045	8.4
dm1048+32	dm1048+32b	I094	9.2	0.044	8.5
dm1049+09	dm1049+09a	I103	9.1	0.034	8.6
dm1049+09	dm1049+09b	I104	9.3	0.033	8.8
dm1051+65	dm1051+65a	N069	8.2	0.011	8.8
dm1051+65	dm1051+65b	N070	7.9	0.011	8.5
dm1059+47	dm1059+47a	I017	8.8	0.033	8.6
dm1059+47	dm1059+47b	I018	8.9	0.034	8.7
dm1106+01	dm1106+01a	I095	8.9	0.031	8.8
dm1106+01	dm1106+01b	I096	8.8	0.031	8.4
dm1107+00	dm1107+00a	I021	9.1	0.061	8.6
dm1107+00	dm1107+00b	I022	9.4	0.061	8.7
dm1115+46	dm1115+46a	N003	8.2	0.0095	8.1
dm1115+46	dm1115+46b	N004	7.8	0.0096	8.3
dm1132+14	dm1132+14a	I037	8.4	0.018	8.6
dm1132+14	dm1132+14b	I038	8.8	0.018	8.4
dm1132+57	dm1132+57a	N031	7.3	0.0042	–
dm1132+57	dm1132+57b	N032	7.1	0.0050	7.7
dm1134+44	dm1134+44a	I005	8.1	0.019	8.2
dm1134+44	dm1134+44b	I006	8.3	0.019	8.5
dm1141+32	dm1141+32a	N053	7.2	0.0060	–
dm1141+32	dm1141+32b	N054	8.0	0.0060	8.3
dm1142+52	dm1142+52a	I045	8.6	0.030	–
dm1142+52	dm1142+52b	I046	9.3	0.030	8.8
dm1145+13	dm1145+13a	N067	8.8	0.0011	–
dm1145+13	dm1145+13b	N068	8.3	0.0011	–
dm1152+07	dm1152+07a	I009	8.5	0.032	–
dm1152+07	dm1152+07b	I010	8.5	0.032	8.3
dm1155+43	dm1155+43a	N085	8.7	0.036	8.3
dm1155+43	dm1155+43b	N086	8.7	0.036	8.3
dm1202+33	dm1202+33a	I085	8.8	0.024	8.7
dm1202+33	dm1202+33b	I086	9.3	0.024	8.9
dm1204+17	dm1204+17a	N079	8.5	0.014	8.4
dm1204+17	dm1204+17b	N080	8.4	0.014	8.2
dm1213+07	dm1213+07a	N083	7.6	0.0071	–

Table A.2 (cont'd)

TNT Pair Name	ID1	ID2	$\log(M_*)$ ( $M_\odot$ )	$z$	Metallicity
dm1213+07	dm1213+07b	N084	8.1	0.0073	8.7
dm1214+49	dm1214+49a	N065	7.5	0.014	–
dm1214+49	dm1214+49b	N066	7.9	0.015	8.2
dm1218+05	dm1218+05a	N073	8.7	0.0086	–
dm1218+05	dm1218+05b	N074	7.8	0.0076	–
dm1218+45	dm1218+45a	N017	8.3	0.019	8.1
dm1218+45	dm1218+45b	N018	8.1	0.019	8.4
dm1219+06	dm1219+06a	N035	7.6	0.0066	–
dm1219+06	dm1219+06b	N036	7.5	0.0065	–
dm1220+08	dm1220+08a	N061	8.9	0.015	8.7
dm1220+08	dm1220+08b	N062	8.1	0.015	–
dm1220+20	dm1220+20a	I043	8.3	0.021	8.4
dm1220+20	dm1220+20b	I044	8.3	0.021	8.5
dm1225+50	dm1225+50a	I027	8.8	0.0083	9.0
dm1225+50	dm1225+50b	I028	8.1	0.0084	8.6
dm1231+06	dm1231+06a	I079	8.1	0.031	8.3
dm1231+06	dm1231+06b	I080	8.3	0.030	8.2
dm1235+57	dm1235+57a	I105	8.6	0.038	–
dm1235+57	dm1235+57b	I106	8.7	0.038	8.6
dm1237+18	dm1237+18a	I051	7.2	0.0085	7.9
dm1237+18	dm1237+18b	I052	7.4	0.0085	8.2
dm1242+34	dm1242+34a	I035	8.3	0.014	8.3
dm1242+34	dm1242+34b	I036	8.5	0.014	–
dm1246+32	dm1246+32a	I099	8.4	0.023	8.2
dm1246+32	dm1246+32b	I100	8.3	0.023	8.4
dm1247-01	dm1247-01a	N057	8.0	0.0094	8.6
dm1247-01	dm1247-01b	N058	8.9	0.0090	–
dm1254+58	dm1254+58a	N059	9.0	0.0086	8.7
dm1254+58	dm1254+58b	N060	8.6	0.0082	8.7
dm1312+34	dm1312+34a	N027	8.4	0.018	8.6
dm1312+34	dm1312+34b	N028	8.8	0.017	8.6
dm1314+35	dm1314+35a	I119	8.5	0.0079	8.2
dm1314+35	dm1314+35b	I120	7.5	0.0078	–
dm1319+55	dm1319+55a	I061	9.8	0.076	9.0
dm1319+55	dm1319+55b	I062	9.1	0.076	8.6

Table A.2 (cont'd)

TNT Pair Name	ID1	ID2	$\log(M_*)$ ( $M_\odot$ )	$z$	Metallicity
dm1337+18	dm1337+18a	I023	9.1	0.065	8.6
dm1337+18	dm1337+18b	I024	9.0	0.065	8.6
dm1338+22	dm1338+22a	I059	8.1	0.016	8.1
dm1338+22	dm1338+22b	I060	8.2	0.016	8.1
dm1342+52	dm1342+52a	N011	7.6	0.0059	8.1
dm1342+52	dm1342+52b	N012	7.2	0.0060	8.0
dm1349-02	dm1349-02a	N015	8.4	0.023	8.3
dm1349-02	dm1349-02b	N016	8.1	0.023	8.2
dm1350-02	dm1350-02a	N087	8.7	0.024	8.6
dm1350-02	dm1350-02b	N088	9.2	0.024	–
dm1352+03	dm1352+03a	N033	8.3	0.015	8.3
dm1352+03	dm1352+03b	N034	8.5	0.015	8.5
dm1357+54	dm1357+54a	I089	8.8	0.026	8.6
dm1357+54	dm1357+54b	I090	8.5	0.026	8.3
dm1402+50	dm1402+50a	N045	8.4	0.0064	8.6
dm1402+50	dm1402+50b	N046	8.0	0.0069	–
dm1403+41	dm1403+41a	I053	8.8	0.035	8.2
dm1403+41	dm1403+41b	I054	8.6	0.035	8.3
dm1406+55	dm1406+55a	N025	8.9	0.0068	–
dm1406+55	dm1406+55b	N026	8.1	0.0061	–
dm1418+21	dm1418+21a	I063	7.2	0.0086	–
dm1418+21	dm1418+21b	I064	6.8	0.0085	7.7
dm1419+39	dm1419+39a	N049	8.0	0.0054	8.1
dm1419+39	dm1419+39b	N050	7.3	0.0056	–
dm1422+18	dm1422+18a	N013	8.7	0.029	8.4
dm1422+18	dm1422+18b	N014	9.1	0.028	8.8
dm1422+22	dm1422+22a	I013	8.8	0.032	–
dm1422+22	dm1422+22b	I014	8.8	0.032	8.3
dm1427+56	dm1427+56a	N051	7.7	0.0065	–
dm1427+56	dm1427+56b	N052	8.2	0.0068	8.5
dm1429+40	dm1429+40a	N043	8.2	0.0090	–
dm1429+40	dm1429+40b	N044	7.8	0.0088	–
dm1440+14	dm1440+14a	I101	8.2	0.018	8.3
dm1440+14	dm1440+14b	I102	8.8	0.018	8.6
dm1447+17	dm1447+17a	I111	8.3	0.021	8.3

Table A.2 (cont'd)

TNT Pair Name	ID1	ID2	$\log(M_*)$ ( $M_\odot$ )	$z$	Metallicity
dm1447+17	dm1447+17b	I112	8.8	0.021	8.6
dm1449+36	dm1449+36a	N007	7.5	0.0062	7.9
dm1449+36	dm1449+36b	N008	7.2	0.0063	8.0
dm1503+00	dm1503+00a	N001	6.9	0.0053	8.0
dm1503+00	dm1503+00b	N002	7.0	0.0053	8.1
dm1505+01	dm1505+01a	N029	8.0	0.0069	—
dm1505+01	dm1505+01b	N030	7.8	0.0077	8.7
dm1520+01	dm1520+01a	I069	8.6	0.026	8.3
dm1520+01	dm1520+01b	I070	9.1	0.026	8.7
dm1523+36	dm1523+36a	I077	8.5	0.023	8.2
dm1523+36	dm1523+36b	I078	8.7	0.023	8.2
dm1526+24	dm1526+24a	I083	9.4	0.053	8.8
dm1526+24	dm1526+24b	I084	9.1	0.053	8.6
dm1526+41	dm1526+41a	I033	8.9	0.053	8.6
dm1526+41	dm1526+41b	I034	9.3	0.053	9.1
dm1529+26	dm1529+26a	I011	8.0	0.0067	8.1
dm1529+26	dm1529+26b	I012	7.6	0.0068	7.9
dm1539+34	dm1539+34a	N037	8.9	0.022	8.7
dm1539+34	dm1539+34b	N038	8.6	0.022	8.6
dm1616+34	dm1616+34a	I075	7.7	0.0089	7.9
dm1616+34	dm1616+34b	I076	7.3	0.0090	8.0
dm1620+25	dm1620+25a	I091	9.4	0.064	8.7
dm1620+25	dm1620+25b	I092	9.1	0.064	8.6
dm1623+15	dm1623+15a	I087	8.8	0.034	8.4
dm1623+15	dm1623+15b	I088	8.6	0.033	8.2
dm1647+21	dm1647+21a	I007	7.9	0.0088	—
dm1647+21	dm1647+21b	I008	7.2	0.0091	7.8
dm1718+30	dm1718+30a	I065	8.9	0.015	8.9
dm1718+30	dm1718+30b	I066	8.5	0.015	8.6
dm2227-09	dm2227-09a	I071	7.9	0.0055	—
dm2227-09	dm2227-09b	I072	7.7	0.0057	8.0
dm2358+14	dm2358+14a	I081	8.7	0.027	8.1
dm2358+14	dm2358+14b	I082	8.7	0.027	8.4

Note. — Some of the TNT dwarf galaxies do not have reported metallicities because there was too much uncertainty in their spectra to accurately calculate them (e.g., weak line strength and/or faint continuum).

Table A.3. TNT Galaxy Photometry

Pair Name	ID1	ID2	$\log F_F$	$\log F_N$	$\log F_u$	$\log F_g$	$\log F_r$	$\log F_i$	$\log F_z$	$\log F_{W1}$	$\log F_{W2}$	$\log F_{W3}$	$\log F_{W4}$
(erg cm <sup>-2</sup> s <sup>-1</sup> Å <sup>-1</sup> )													
dm0027+00	dm0027+00a	I097	-11.9	-12.0	-12.1	-11.9	-11.9	-11.9	-11.9	-13.0	-13.6	-12.9	-12.4
dm0027+00	dm0027+00b	I098	-12.0	-11.9	-11.7	-11.4	-11.3	-11.3	-11.3	-12.1	-12.4	-12.1	-12.2
dm0035-10	dm0035-10a	I015	-11.7	-11.7	-11.7	-11.5	-11.5	-11.5	-11.5	-12.3	-12.7	-12.4	-12.4
dm0035-10	dm0035-10b	I016	-11.9	-12.0	-12.1	-11.9	-11.9	-11.9	-11.9	-12.8	-13.1	-13.1	-12.5
dm0052+00	dm0052+00a	I115	-11.4	-11.4	-11.3	-11.1	-11.1	-11.1	-11.1	-12.1	-12.3	-11.8	-11.3
dm0052+00	dm0052+00b	I116	-11.4	-11.4	-11.4	-11.1	-11.1	-11.1	-11.1	-12.3	-12.6	-12.3	-12.1
dm0058+01	dm0058+01a	N077	-11.6	-11.6	-11.4	-11.2	-11.2	-11.2	-11.2	-11.9	-11.9	-11.5	-11.1
dm0058+01	dm0058+01b	N078	-11.4	-11.5	-11.5	-11.3	-11.4	-11.4	-11.5	-12.8	-13.0	-12.9	-12.2
dm0204-10	dm0204-10a	N071	-11.5	-11.6	-11.7	-11.5	-11.6	-11.7	-11.8	-12.9	-13.2	-13.3	-12.6
dm0204-10	dm0204-10b	N072	-11.0	-11.1	-11.2	-11.0	-11.0	-11.0	-11.2	-12.6	-12.9	-13.1	-12.5
dm0206-08	dm0206-08a	N019	-11.0	-11.0	-11.2	-10.9	-11.0	-11.0	-11.0	-12.7	-13.0	-12.9	-12.4
dm0206-08	dm0206-08b	N020	-11.4	-11.6	-11.7	-11.5	-11.6	-11.6	-11.6	-12.7	-13.0	-13.2	-12.5
dm0346+00	dm0346+00a	I109	-12.0	-12.0	-11.8	-11.4	-11.3	-11.3	-11.3	-12.3	-12.7	-12.4	-12.2
dm0346+00	dm0346+00b	I110	-12.0	-12.0	-11.9	-11.6	-11.6	-11.6	-11.6	-12.6	-12.9	-12.9	-12.3
dm0744+21	dm0744+21a	I073	-11.7	-11.7	-11.7	-11.5	-11.5	-11.5	-11.5	-12.4	-12.8	-12.5	-12.4
dm0744+21	dm0744+21b	I074	-11.5	-11.5	-11.4	-11.1	-11.1	-11.1	-11.1	-11.9	-12.2	-11.9	-11.9
dm0759+15	dm0759+15a	I107	-11.7	-11.8	-11.9	-11.7	-11.8	-11.8	-11.8	-12.9	-13.2	-12.9	-12.3
dm0759+15	dm0759+15b	I108	-11.7	-11.7	-11.7	-11.4	-11.4	-11.4	-11.4	-12.5	-12.8	-12.7	-12.3
dm0801+14	dm0801+14a	I031	-12.0	-12.1	-12.0	-11.8	-11.8	-11.8	-11.8	-12.6	-13.0	-12.5	-12.2
dm0801+14	dm0801+14b	I032	-12.1	-12.2	-12.1	-11.8	-11.7	-11.7	-11.7	-12.2	-12.6	-12.1	-12.2
dm0813+07	dm0813+07a	N063	-11.8	-11.9	-12.0	-11.8	-11.9	-11.9	-11.9	-12.7	-12.9	-12.6	-12.1

Table A.3 (cont'd)

Pair Name	ID1	ID2	$\log F_F$	$\log F_N$	$\log F_u$	$\log F_g$	$\log F_r$	$\log F_i$	$\log F_z$	$\log F_{W1}$	$\log F_{W2}$	$\log F_{W3}$	$\log F_{W4}$
dm0813+07	dm0813+07b	N064	-11.9	-11.9	-12.0	-11.8	-11.9	-11.9	-11.9	-12.8	-13.1	-12.8	-12.3
dm0815+42	dm0815+42a	I117	-11.9	-12.0	-12.0	-11.7	-11.7	-11.7	-11.7	-12.7	-13.0	-12.7	-12.5
dm0815+42	dm0815+42b	I118	-12.0	-12.0	-12.1	-11.8	-11.8	-11.9	-11.9	-12.7	-13.1	-12.9	-12.3
dm0818+24	dm0818+24a	N041	-	-	-11.9	-11.6	-11.6	-11.5	-11.5	-13.0	-13.3	-13.1	-12.3
dm0818+24	dm0818+24b	N042	-	-	-11.1	-10.9	-10.9	-10.9	-10.9	-12.0	-12.4	-12.6	-12.0
dm0820+03	dm0820+03a	I057	-12.0	-12.2	-12.0	-11.8	-11.7	-11.7	-11.7	-12.5	-12.8	-12.5	-12.1
dm0820+03	dm0820+03b	I058	-11.9	-11.9	-11.9	-11.6	-11.7	-11.7	-11.7	-12.6	-12.9	-12.4	-11.8
dm0827+46	dm0827+46a	I001	-11.0	-11.1	-11.4	-10.9	-10.8	-10.9	-11.3	-12.0	-12.3	-12.2	-11.7
dm0827+46	dm0827+46b	I002	-11.0	-11.1	-11.3	-10.9	-10.8	-10.9	-11.1	-12.0	-12.3	-12.2	-11.7
dm0828+20	dm0828+20a	N081	-12.3	-12.4	-12.1	-11.7	-11.7	-11.7	-11.8	-12.8	-13.2	-13.0	-12.2
dm0828+20	dm0828+20b	N082	-12.0	-11.4	-11.4	-11.1	-11.1	-11.0	-11.1	-12.4	-12.7	-12.9	-12.3
dm0833+22	dm0833+22a	I113	-12.3	-12.2	-12.1	-11.8	-11.8	-11.8	-11.9	-12.7	-13.1	-12.9	-12.4
dm0833+22	dm0833+22b	I114	-12.1	-12.0	-11.8	-11.4	-11.3	-11.3	-11.3	-12.2	-12.5	-12.4	-12.3
dm0844+20	dm0844+20a	I025	-11.8	-11.9	-11.7	-11.4	-11.4	-11.4	-11.4	-12.3	-12.7	-12.5	-12.0
dm0844+20	dm0844+20b	I026	-12.5	-12.6	-12.3	-11.9	-11.9	-11.8	-11.9	-12.8	-13.2	-12.8	-12.1
dm0850+45	dm0850+45a	I041	-11.9	-11.9	-11.9	-11.7	-11.7	-11.7	-11.7	-12.6	-12.9	-12.8	-12.3
dm0850+45	dm0850+45b	I042	-12.3	-12.1	-12.3	-12.1	-12.0	-12.0	-12.0	-12.1	-12.5	-12.7	-12.3
dm0901+12	dm0901+12a	I047	-11.8	-11.8	-11.8	-11.5	-11.5	-11.5	-11.6	-12.4	-12.7	-12.5	-12.3
dm0901+12	dm0901+12b	I048	-11.9	-11.8	-11.6	-11.3	-11.2	-11.2	-11.2	-12.2	-12.5	-12.2	-12.0
dm0909+06	dm0909+06a	I067	-11.9	-11.9	-11.8	-11.5	-11.5	-11.5	-11.5	-12.3	-12.6	-12.1	-12.3
dm0909+06	dm0909+06b	I068	-12.0	-11.9	-11.9	-11.6	-11.6	-11.5	-11.5	-12.3	-12.6	-12.3	-12.5

(erg cm<sup>-2</sup> s<sup>-1</sup> Å<sup>-1</sup>)

Table A.3 (cont'd)

Pair Name	ID1	ID2	$\log F_F$	$\log F_N$	$\log F_u$	$\log F_g$	$\log F_r$	$\log F_i$	$\log F_z$	$\log F_{W1}$	$\log F_{W2}$	$\log F_{W3}$	$\log F_{W4}$
			(erg cm <sup>-2</sup> s <sup>-1</sup> Å <sup>-1</sup> )										
dm0916+06	dm0916+06a	I039	-11.6	-11.6	-11.8	-11.6	-11.6	-11.6	-11.6	-12.9	-13.1	-13.0	-12.5
dm0916+06	dm0916+06b	I040	-11.1	-10.9	-10.9	-10.7	-10.7	-10.7	-10.7	-12.3	-12.6	-12.8	-12.2
dm0924+34	dm0924+34a	N075	-11.4	-11.4	-11.2	-10.9	-10.8	-10.8	-10.8	-12.5	-12.9	-13.0	-12.4
dm0924+34	dm0924+34b	N076	-13.6	-12.5	-11.7	-11.3	-11.2	-11.2	-11.1	-12.5	-12.9	-13.0	-12.6
dm0925+66	dm0925+66a	N021	-12.9	-13.8	-12.5	-12.2	-12.1	-12.1	-12.1	-13.0	-13.5	-13.1	-12.5
dm0925+66	dm0925+66b	N022	-12.2	-12.1	-12.0	-11.6	-11.5	-11.6	-11.6	-12.8	-13.1	-12.9	-12.6
dm0930+60	dm0930+60a	I049	-11.3	-11.4	-11.5	-11.3	-11.4	-11.4	-11.4	-12.5	-12.8	-12.7	-12.1
dm0930+60	dm0930+60b	I050	-10.9	-11.0	-11.2	-11.1	-11.2	-11.4	-11.5	-12.4	-12.6	-12.2	-11.5
dm0944-00	dm0944-00a	N009	-11.2	-11.2	-11.1	-10.7	-10.8	-10.8	-10.8	-12.7	-13.1	-13.0	-12.5
dm0944-00	dm0944-00b	N010	-10.9	-11.0	-11.0	-10.9	-11.0	-11.3	-11.3	-12.3	-12.1	-11.4	-10.9
dm0948+32	dm0948+32a	N005	-10.6	-10.7	-10.7	-10.5	-10.5	-10.5	-10.5	-11.6	-12.0	-11.8	-11.5
dm0948+32	dm0948+32b	N006	-11.4	-11.5	-11.5	-11.3	-11.4	-11.4	-11.4	-12.5	-12.9	-12.9	-12.6
dm0953+49	dm0953+49a	I029	-	-	-12.1	-11.8	-11.8	-11.8	-11.8	-12.4	-12.7	-12.4	-12.3
dm0953+49	dm0953+49b	I030	-	-	-11.8	-11.5	-11.5	-11.5	-11.5	-12.4	-12.7	-12.4	-12.2
dm0957+15	dm0957+15a	N039	-11.0	-11.0	-10.9	-10.6	-10.6	-10.6	-10.6	-12.3	-12.7	-12.4	-12.2
dm0957+15	dm0957+15b	N040	-11.8	-11.7	-11.5	-11.2	-11.0	-11.0	-11.0	-11.7	-12.0	-11.6	-11.7
dm1007+55	dm1007+55a	I055	-11.6	-11.6	-11.5	-11.2	-11.2	-11.2	-11.2	-12.1	-12.4	-12.1	-12.0
dm1007+55	dm1007+55b	I056	-12.2	-12.2	-12.1	-10.7	-11.6	-11.6	-11.6	-12.2	-12.5	-12.8	-12.4
dm1014+59	dm1014+59a	N023	-11.5	-11.6	-11.6	-11.4	-11.5	-11.6	-11.7	-12.7	-13.0	-13.2	-12.3
dm1014+59	dm1014+59b	N024	-11.4	-11.6	-11.7	-11.4	-11.5	-11.6	-11.6	-12.6	-13.0	-13.3	-12.5
dm1022+21	dm1022+21a	N055	-	-12.3	-11.4	-10.9	-10.8	-10.8	-10.7	-11.8	-12.2	-12.9	-12.2

Table A.3 (cont'd)

Pair Name	ID1	ID2	$\log F_F$	$\log F_N$	$\log F_u$	$\log F_g$	$\log F_r$	$\log F_i$	$\log F_z$	$\log F_{W1}$	$\log F_{W2}$	$\log F_{W3}$	$\log F_{W4}$
(erg cm <sup>-2</sup> s <sup>-1</sup> Å <sup>-1</sup> )													
dm1022+21	dm1022+21b	N056	-	-12.6	-11.9	-11.5	-11.4	-11.3	-11.4	-12.4	-12.8	-13.2	-12.4
dm1031+41	dm1031+41a	I003	-	-	-12.3	-11.5	-11.5	-11.5	-12.1	-12.6	-13.0	-13.2	-12.6
dm1031+41	dm1031+41b	I004	-	-	-11.9	-11.5	-11.5	-11.5	-11.7	-12.6	-13.0	-13.2	-12.6
dm1032+28	dm1032+28a	N047	-12.4	-12.4	-12.1	-11.7	-11.6	-11.6	-11.6	-12.8	-13.1	-13.3	-12.4
dm1032+28	dm1032+28b	N048	-12.3	-12.0	-11.5	-11.1	-11.0	-10.9	-11.0	-12.1	-12.5	-13.1	-12.1
dm1036+10	dm1036+10a	I019	-11.5	-11.6	-11.8	-11.7	-11.8	-11.8	-11.9	-12.9	-13.2	-13.0	-12.4
dm1036+10	dm1036+10b	I020	-11.6	-11.7	-11.9	-11.8	-11.9	-12.0	-12.0	-13.1	-13.3	-13.0	-12.2
dm1048+32	dm1048+32a	I093	-11.7	-11.9	-12.0	-11.7	-11.8	-11.8	-11.9	-12.7	-13.0	-12.9	-12.3
dm1048+32	dm1048+32b	I094	-11.9	-11.9	-11.9	-11.6	-11.5	-11.5	-11.6	-12.6	-13.0	-13.0	-12.3
dm1049+09	dm1049+09a	I103	-11.2	-11.2	-11.3	-11.1	-11.2	-11.2	-11.3	-12.4	-12.7	-12.3	-12.1
dm1049+09	dm1049+09b	I104	-11.4	-11.4	-11.4	-11.1	-11.1	-11.2	-11.2	-12.3	-12.6	-12.2	-12.0
dm1051+65	dm1051+65a	N069	-12.5	-12.4	-12.1	-11.7	-11.5	-11.5	-11.5	-12.4	-12.8	-12.9	-12.6
dm1051+65	dm1051+65b	N070	-12.5	-12.4	-12.2	-11.9	-11.8	-11.8	-11.8	-12.7	-13.0	-13.0	-12.4
dm1059+47	dm1059+47a	I017	-11.7	-11.8	-11.9	-11.7	-11.7	-11.7	-11.7	-12.7	-13.1	-13.0	-12.4
dm1059+47	dm1059+47b	I018	-11.7	-11.8	-11.8	-11.6	-11.6	-11.6	-11.6	-12.6	-12.9	-12.8	-12.6
dm1106+01	dm1106+01a	I095	-	-	-12.1	-11.8	-11.7	-11.7	-11.6	-12.4	-12.7	-12.6	-12.5
dm1106+01	dm1106+01b	I096	-	-	-11.7	-11.5	-11.5	-11.5	-11.6	-12.4	-12.7	-12.6	-12.1
dm1107+00	dm1107+00a	I021	-11.4	-11.5	-11.8	-11.6	-11.7	-11.7	-11.7	-12.5	-12.8	-12.5	-12.1
dm1107+00	dm1107+00b	I022	-11.4	-11.5	-11.9	-11.6	-11.6	-11.6	-11.6	-12.4	-12.7	-12.3	-12.2
dm1115+46	dm1115+46a	N003	-10.9	-11.0	-11.2	-11.0	-11.0	-11.0	-11.1	-12.1	-12.4	-12.5	-12.1
dm1115+46	dm1115+46b	N004	-10.9	-11.0	-11.4	-11.2	-11.3	-11.3	-11.4	-12.1	-12.4	-12.5	-12.1

Table A.3 (cont'd)

Pair Name	ID1	ID2	$\log F_F$	$\log F_N$	$\log F_u$	$\log F_g$	$\log F_r$	$\log F_i$	$\log F_z$	$\log F_{W1}$	$\log F_{W2}$	$\log F_{W3}$	$\log F_{W4}$
			(erg cm <sup>-2</sup> s <sup>-1</sup> Å <sup>-1</sup> )										
dm1132+14	dm1132+14a	I037	-11.9	-11.9	-11.7	-11.4	-11.4	-11.4	-11.5	-12.3	-12.6	-12.4	-11.9
dm1132+14	dm1132+14b	I038	-11.0	-11.0	-11.0	-10.8	-10.9	-10.9	-11.0	-12.1	-12.5	-12.5	-12.3
dm1132+57	dm1132+57a	N031	-11.3	-11.5	-11.6	-11.5	-11.6	-11.6	-11.6	-12.8	-13.1	-13.2	-12.4
dm1132+57	dm1132+57b	N032	-11.1	-11.2	-11.4	-11.2	-11.3	-11.3	-11.4	-12.6	-13.0	-13.1	-12.5
dm1134+44	dm1134+44a	I005	-11.2	-11.2	-11.8	-11.1	-11.1	-11.2	-11.7	-12.3	-12.5	-12.0	-11.4
dm1134+44	dm1134+44b	I006	-11.2	-11.2	-11.4	-11.1	-11.1	-11.2	-11.4	-12.3	-12.5	-12.0	-11.4
dm1141+32	dm1141+32a	N053	-11.1	-11.2	-11.3	-11.3	-11.4	-11.5	-11.5	-12.9	-13.1	-13.0	-12.4
dm1141+32	dm1141+32b	N054	-11.1	-11.1	-11.0	-10.8	-10.8	-10.9	-10.9	-12.4	-12.8	-12.7	-12.1
dm1142+52	dm1142+52a	I045	-11.8	-11.9	-11.9	-11.7	-11.7	-11.7	-11.7	-13.0	-13.3	-13.2	-12.6
dm1142+52	dm1142+52b	I046	-11.7	-11.7	-11.6	-11.3	-11.2	-11.2	-11.2	-12.0	-12.3	-12.0	-11.9
dm1145+13	dm1145+13a	N067	-	-	-11.8	-11.4	-11.2	-11.1	-11.1	-12.2	-12.6	-13.2	-12.5
dm1145+13	dm1145+13b	N068	-	-	-11.6	-11.4	-11.3	-11.3	-11.3	-12.4	-12.8	-12.9	-12.4
dm1152+07	dm1152+07a	I009	-11.5	-11.5	-11.8	-11.3	-11.4	-11.4	-11.6	-12.6	-12.9	-12.9	-12.3
dm1152+07	dm1152+07b	I010	-11.5	-11.5	-11.9	-11.3	-11.4	-11.4	-11.9	-12.6	-12.9	-12.9	-12.3
dm1155+43	dm1155+43a	N085	-11.8	-11.8	-11.8	-11.6	-11.7	-11.7	-11.8	-12.6	-12.9	-12.7	-12.5
dm1155+43	dm1155+43b	N086	-11.7	-11.8	-11.8	-11.6	-11.6	-11.6	-11.7	-12.7	-13.1	-13.1	-12.5
dm1202+33	dm1202+33a	I085	-11.5	-11.5	-11.5	-11.3	-11.3	-11.3	-11.3	-12.4	-12.7	-12.4	-12.4
dm1202+33	dm1202+33b	I086	-11.7	-11.7	-11.5	-11.2	-11.1	-11.1	-11.1	-12.0	-12.3	-12.1	-12.1
dm1204+17	dm1204+17a	N079	-11.4	-11.4	-11.5	-11.3	-11.2	-11.3	-11.3	-12.3	-12.6	-12.5	-12.2
dm1204+17	dm1204+17b	N080	-11.8	-11.8	-11.7	-11.5	-11.4	-11.4	-11.5	-12.6	-13.0	-13.0	-12.5
dm1213+07	dm1213+07a	N083	-12.6	-12.5	-12.2	-11.8	-11.7	-11.7	-11.8	-12.9	-13.2	-13.0	-12.5

Table A.3 (cont'd)

Pair Name	ID1	ID2	$\log F_F$	$\log F_N$	$\log F_u$	$\log F_g$	$\log F_r$	$\log F_i$	$\log F_z$	$\log F_{W1}$	$\log F_{W2}$	$\log F_{W3}$	$\log F_{W4}$
dm1213+07	dm1213+07b	N084	-11.8	-11.8	-11.6	-11.2	-11.2	-11.2	-11.2	-12.5	-12.9	-13.0	-12.4
dm1214+49	dm1214+49a	N065	-12.1	-12.0	-12.1	-11.8	-11.9	-11.9	-12.0	-12.9	-13.2	-13.2	-12.4
dm1214+49	dm1214+49b	N066	-11.8	-11.8	-11.9	-11.7	-11.7	-11.8	-11.8	-12.8	-13.1	-13.1	-12.5
dm1218+05	dm1218+05a	N073	-13.1	-12.3	-11.5	-11.1	-11.0	-10.9	-10.9	-12.2	-12.6	-13.0	-12.3
dm1218+05	dm1218+05b	N074	-	-12.7	-12.2	-11.8	-11.7	-11.6	-11.7	-12.8	-13.2	-13.0	-12.5
dm1218+45	dm1218+45a	N017	-11.2	-11.2	-11.3	-11.2	-11.3	-11.4	-11.4	-12.4	-12.6	-12.0	-11.5
dm1218+45	dm1218+45b	N018	-12.0	-11.9	-12.1	-11.8	-11.8	-11.8	-11.8	-13.1	-13.4	-13.1	-12.6
dm1219+06	dm1219+06a	N035	-	-12.8	-12.2	-11.9	-11.8	-11.7	-11.7	-12.9	-13.4	-12.9	-12.3
dm1219+06	dm1219+06b	N036	-	-13.1	-12.4	-11.9	-11.8	-11.7	-11.8	-12.8	-13.5	-13.1	-12.3
dm1220+08	dm1220+08a	N061	-11.9	-11.9	-11.5	-11.2	-11.1	-11.1	-11.1	-11.9	-12.2	-12.0	-11.8
dm1220+08	dm1220+08b	N062	-12.0	-12.0	-11.9	-11.7	-11.7	-11.7	-11.7	-12.9	-13.1	-13.1	-12.6
dm1220+20	dm1220+20a	I043	-12.3	-12.2	-12.1	-11.8	-11.8	-11.8	-11.8	-12.7	-13.0	-13.0	-12.5
dm1220+20	dm1220+20b	I044	-11.9	-11.9	-11.9	-11.8	-11.8	-11.8	-11.8	-12.6	-12.9	-13.0	-12.4
dm1225+50	dm1225+50a	I027	-11.2	-11.2	-11.0	-10.7	-10.6	-10.6	-10.6	-11.5	-11.9	-11.6	-11.6
dm1225+50	dm1225+50b	I028	-11.6	-11.6	-11.5	-11.2	-11.2	-11.2	-11.2	-12.2	-12.5	-12.5	-12.2
dm1231+06	dm1231+06a	I079	-11.8	-11.9	-12.0	-11.8	-11.9	-11.9	-12.0	-12.9	-13.2	-13.0	-12.2
dm1231+06	dm1231+06b	I080	-11.8	-11.8	-11.9	-11.7	-11.7	-11.8	-11.9	-12.8	-13.0	-12.8	-12.2
dm1235+57	dm1235+57a	I105	-11.9	-11.9	-12.1	-11.8	-11.8	-11.8	-11.9	-12.9	-13.2	-13.2	-12.4
dm1235+57	dm1235+57b	I106	-11.9	-12.0	-12.0	-11.7	-11.7	-11.8	-11.8	-12.5	-12.9	-12.6	-12.5
dm1237+18	dm1237+18a	I051	-11.7	-11.8	-11.9	-11.8	-11.9	-11.9	-12.0	-13.0	-13.3	-13.1	-12.2
dm1237+18	dm1237+18b	I052	-12.1	-12.2	-12.1	-11.9	-11.9	-11.9	-11.9	-12.9	-13.1	-13.2	-12.4

(erg cm<sup>-2</sup> s<sup>-1</sup> Å<sup>-1</sup>)

Table A.3 (cont'd)

Pair Name	ID1	ID2	$\log F_F$	$\log F_N$	$\log F_u$	$\log F_g$	$\log F_r$	$\log F_i$	$\log F_z$	$\log F_{W1}$	$\log F_{W2}$	$\log F_{W3}$	$\log F_{W4}$
			(erg cm <sup>-2</sup> s <sup>-1</sup> Å <sup>-1</sup> )										
dm1242+34	dm1242+34a	I035	-11.7	-11.7	-11.6	-11.4	-11.4	-11.4	-11.4	-12.6	-13.0	-13.0	-12.6
dm1242+34	dm1242+34b	I036	-11.4	-11.4	-11.4	-11.1	-11.1	-11.2	-11.2	-12.1	-12.5	-12.4	-12.1
dm1246+32	dm1246+32a	I099	-11.8	-11.8	-11.8	-11.6	-11.6	-11.6	-11.7	-12.6	-13.0	-13.1	-12.6
dm1246+32	dm1246+32b	I100	-12.1	-12.2	-12.1	-11.8	-11.8	-11.8	-11.8	-12.7	-13.0	-13.1	-12.6
dm1247-01	dm1247-01a	N057	-12.0	-12.0	-11.8	-11.5	-11.5	-11.5	-11.5	-12.5	-12.9	-12.8	-12.5
dm1247-01	dm1247-01b	N058	-11.1	-11.2	-11.0	-10.7	-10.6	-10.6	-10.6	-12.3	-12.7	-12.7	-12.3
dm1254+58	dm1254+58a	N059	-11.3	-11.2	-11.0	-10.6	-10.5	-10.5	-10.5	-11.7	-12.1	-12.0	-12.0
dm1254+58	dm1254+58b	N060	-10.7	-10.8	-10.8	-10.6	-10.6	-10.6	-10.6	-11.9	-12.2	-12.1	-11.9
dm1312+34	dm1312+34a	N027	-12.2	-12.3	-12.1	-11.8	-11.7	-11.7	-11.7	-12.5	-12.9	-13.0	-12.5
dm1312+34	dm1312+34b	N028	-11.8	-11.7	-11.6	-11.2	-11.2	-11.2	-11.2	-12.2	-12.6	-12.7	-12.4
dm1314+35	dm1314+35a	I119	-10.7	-10.8	-10.9	-10.6	-10.6	-10.6	-10.7	-12.9	-13.1	-12.9	-12.3
dm1314+35	dm1314+35b	I120	-11.6	-11.7	-11.7	-11.4	-11.4	-11.5	-11.5	-12.8	-13.2	-13.1	-12.6
dm1319+55	dm1319+55a	I061	-	-11.7	-11.7	-11.7	-11.7	-11.6	-11.6	-12.2	-12.4	-12.0	-11.7
dm1319+55	dm1319+55b	I062	-	-	-12.0	-11.8	-11.8	-11.8	-11.9	-12.7	-13.0	-12.6	-12.2
dm1337+18	dm1337+18a	I023	-12.1	-11.8	-12.2	-11.9	-11.9	-11.8	-11.9	-12.6	-13.0	-12.6	-12.4
dm1337+18	dm1337+18b	I024	-12.1	-11.8	-12.2	-11.9	-11.9	-11.9	-12.0	-12.8	-13.1	-12.9	-12.4
dm1338+22	dm1338+22a	I059	-11.8	-11.8	-11.8	-11.7	-11.7	-11.8	-11.7	-12.8	-13.2	-13.3	-12.5
dm1338+22	dm1338+22b	I060	-11.9	-11.7	-11.8	-11.7	-11.7	-11.7	-11.6	-12.9	-13.2	-13.2	-12.6
dm1342+52	dm1342+52a	N011	-	-	-11.2	-11.1	-11.1	-11.2	-11.2	-12.3	-12.6	-12.5	-11.9
dm1342+52	dm1342+52b	N012	-	-	-11.5	-11.3	-11.4	-11.5	-11.5	-12.8	-13.0	-13.0	-12.3
dm1349-02	dm1349-02a	N015	-11.9	-11.9	-11.8	-11.6	-11.6	-11.6	-11.6	-12.7	-13.1	-12.9	-12.6

Table A.3 (cont'd)

Pair Name	ID1	ID2	$\log F_F$	$\log F_N$	$\log F_u$	$\log F_g$	$\log F_r$	$\log F_i$	$\log F_z$	$\log F_{W1}$	$\log F_{W2}$	$\log F_{W3}$	$\log F_{W4}$
			(erg cm <sup>-2</sup> s <sup>-1</sup> Å <sup>-1</sup> )										
dm1349-02	dm1349-02b	N016	-11.8	-11.9	-12.0	-11.9	-11.9	-12.0	-12.0	-12.9	-13.3	-13.0	-12.6
dm1350-02	dm1350-02a	N087	-11.7	-11.7	-11.7	-11.4	-11.4	-11.4	-11.4	-12.5	-12.9	-13.0	-12.6
dm1350-02	dm1350-02b	N088	-11.6	-11.6	-11.5	-11.2	-11.1	-11.1	-11.2	-12.5	-12.8	-12.7	-12.5
dm1352+03	dm1352+03a	N033	-11.7	-11.8	-11.7	-11.5	-11.4	-11.4	-11.5	-12.7	-13.1	-13.3	-12.6
dm1352+03	dm1352+03b	N034	-11.4	-11.5	-11.4	-11.2	-11.2	-11.2	-11.3	-12.8	-13.2	-13.0	-12.6
dm1357+54	dm1357+54a	I089	-11.5	-11.6	-11.6	-11.4	-11.4	-11.4	-11.4	-12.3	-12.7	-12.5	-12.2
dm1357+54	dm1357+54b	I090	-11.5	-11.6	-11.7	-11.5	-11.5	-11.6	-11.6	-12.6	-12.9	-12.9	-12.3
dm1402+50	dm1402+50a	N045	-11.5	-11.4	-11.1	-10.8	-10.8	-10.8	-10.8	-11.7	-12.1	-12.1	-12.2
dm1402+50	dm1402+50b	N046	-12.1	-11.9	-11.7	-11.4	-11.3	-11.3	-11.3	-12.8	-13.2	-13.1	-12.7
dm1403+41	dm1403+41a	I053	-11.6	-11.6	-11.6	-11.3	-11.4	-11.4	-11.5	-12.4	-12.7	-12.7	-12.3
dm1403+41	dm1403+41b	I054	-11.7	-11.8	-11.9	-11.7	-11.7	-11.7	-11.8	-12.0	-12.4	-13.3	-12.6
dm1406+55	dm1406+55a	N025	-13.0	-12.3	-11.3	-10.8	-10.6	-10.5	-10.5	-11.5	-12.0	-12.8	-12.6
dm1406+55	dm1406+55b	N026	-11.4	-11.4	-11.5	-11.1	-11.1	-11.1	-11.1	-12.6	-13.0	-13.2	-12.6
dm1418+21	dm1418+21a	I063	-	-	-12.1	-11.9	-11.9	-11.9	-12.0	-13.1	-13.5	-13.2	-12.7
dm1418+21	dm1418+21b	I064	-	-	-11.9	-11.7	-11.9	-12.2	-12.2	-13.2	-13.3	-12.4	-12.0
dm1419+39	dm1419+39a	N049	-11.0	-11.0	-11.0	-10.8	-10.8	-10.8	-10.8	-12.0	-12.4	-12.3	-11.8
dm1419+39	dm1419+39b	N050	-11.9	-12.0	-12.0	-11.7	-11.7	-11.7	-11.7	-13.4	-13.8	-13.1	-12.7
dm1422+18	dm1422+18a	N013	-11.7	-11.8	-11.8	-11.5	-11.5	-11.5	-11.6	-12.6	-12.9	-13.0	-12.6
dm1422+18	dm1422+18b	N014	-12.4	-12.3	-12.0	-11.6	-11.5	-11.4	-11.4	-12.1	-12.4	-12.2	-12.4
dm1422+22	dm1422+22a	I013	-11.0	-11.1	-11.3	-11.0	-11.0	-11.1	-11.4	-12.3	-12.6	-12.5	-12.3
dm1422+22	dm1422+22b	I014	-11.0	-11.1	-11.6	-11.0	-11.0	-11.1	-11.5	-12.3	-12.6	-12.5	-12.3

Table A.3 (cont'd)

Pair Name	ID1	ID2	$\log F_F$	$\log F_N$	$\log F_u$	$\log F_g$	$\log F_r$	$\log F_i$	$\log F_z$	$\log F_{W1}$	$\log F_{W2}$	$\log F_{W3}$	$\log F_{W4}$
dm1427+56	dm1427+56a	N051	-12.7	-12.5	-12.1	-11.7	-11.6	-11.6	-11.6	-12.7	-13.1	-13.3	-12.7
dm1427+56	dm1427+56b	N052	-12.1	-12.1	-11.7	-11.3	-11.2	-11.1	-11.2	-12.3	-12.7	-13.0	-12.4
dm1429+40	dm1429+40a	N043	-11.2	-11.2	-11.3	-11.1	-11.1	-11.1	-11.1	-12.5	-12.9	-13.1	-12.4
dm1429+40	dm1429+40b	N044	-12.0	-12.0	-11.9	-11.5	-11.5	-11.6	-11.6	-12.6	-13.0	-13.2	-12.5
dm1440+14	dm1440+14a	I101	-11.9	-11.9	-11.9	-11.7	-11.7	-11.7	-11.7	-12.8	-13.1	-13.0	-12.4
dm1440+14	dm1440+14b	I102	-11.6	-11.6	-11.6	-11.3	-11.2	-11.2	-11.2	-12.4	-12.7	-12.8	-12.5
dm1447+17	dm1447+17a	I111	-12.0	-12.0	-12.0	-11.7	-11.7	-11.7	-11.7	-12.6	-13.0	-12.9	-12.4
dm1447+17	dm1447+17b	I112	-12.3	-11.8	-11.7	-11.5	-11.4	-11.4	-11.4	-12.5	-12.9	-12.8	-12.3
dm1449+36	dm1449+36a	N007	-11.1	-11.3	-11.3	-11.2	-11.3	-11.3	-11.4	-12.7	-13.0	-13.3	-12.5
dm1449+36	dm1449+36b	N008	-11.2	-11.3	-11.4	-11.3	-11.3	-11.4	-11.5	-12.8	-13.1	-13.1	-12.4
dm1503+00	dm1503+00a	N001	-11.0	-11.1	-11.4	-11.4	-11.4	-11.6	-11.6	-12.6	-12.8	-12.9	-12.3
dm1503+00	dm1503+00b	N002	-11.0	-11.1	-11.8	-11.6	-11.6	-11.7	-11.7	-12.6	-12.8	-12.9	-12.3
dm1505+01	dm1505+01a	N029	-13.2	-12.6	-12.0	-11.6	-11.4	-11.4	-11.4	-12.5	-12.9	-13.3	-12.7
dm1505+01	dm1505+01b	N030	-11.8	-11.8	-11.8	-11.6	-11.5	-11.5	-11.5	-12.8	-13.2	-13.1	-12.5
dm1520+01	dm1520+01a	I069	-11.8	-11.7	-11.8	-11.6	-11.5	-11.6	-11.6	-12.5	-12.9	-12.7	-12.5
dm1520+01	dm1520+01b	I070	-11.7	-11.7	-11.5	-11.2	-11.2	-11.2	-11.2	-12.0	-12.4	-12.2	-12.2
dm1523+36	dm1523+36a	I077	-12.2	-12.0	-12.1	-11.8	-11.7	-11.8	-11.8	-12.2	-12.6	-13.3	-12.6
dm1523+36	dm1523+36b	I078	-11.5	-11.7	-11.7	-11.5	-11.5	-11.5	-11.5	-12.4	-12.7	-12.9	-12.7
dm1526+24	dm1526+24a	I083	-11.6	-11.7	-11.6	-11.4	-11.4	-11.4	-11.5	-12.5	-12.8	-12.4	-12.2
dm1526+24	dm1526+24b	I084	-12.3	-12.2	-12.2	-11.9	-11.8	-11.8	-11.9	-12.8	-13.1	-13.2	-12.5
dm1526+41	dm1526+41a	I033	-12.2	-12.3	-12.3	-12.0	-12.0	-11.9	-12.0	-12.8	-13.1	-12.8	-12.5

(erg cm<sup>-2</sup> s<sup>-1</sup> Å<sup>-1</sup>)

Table A.3 (cont'd)

Pair Name	ID1	ID2	$\log F_F$	$\log F_N$	$\log F_u$	$\log F_g$	$\log F_r$	$\log F_i$	$\log F_z$	$\log F_{W1}$	$\log F_{W2}$	$\log F_{W3}$	$\log F_{W4}$
								(erg cm <sup>-2</sup> s <sup>-1</sup> Å <sup>-1</sup> )					
dm1526+41	dm1526+41b	I034	-12.3	-12.2	-12.1	-11.8	-11.7	-11.7	-11.7	-12.3	-12.6	-12.0	-12.0
dm1529+26	dm1529+26a	I011	-	-	-10.9	-10.8	-10.9	-10.9	-10.9	-12.4	-12.7	-12.8	-12.2
dm1529+26	dm1529+26b	I012	-	-	-11.5	-11.3	-11.4	-11.4	-11.4	-12.6	-13.0	-13.2	-12.6
dm1539+34	dm1539+34a	N037	-11.5	-11.5	-11.4	-11.2	-11.1	-11.1	-11.2	-12.0	-12.4	-12.2	-12.3
dm1539+34	dm1539+34b	N038	-11.7	-11.8	-11.7	-11.5	-11.5	-11.5	-11.5	-12.6	-12.9	-12.8	-12.5
dm1616+34	dm1616+34a	I075	-12.1	-12.0	-12.0	-11.7	-11.7	-11.7	-11.7	-12.7	-13.1	-13.3	-12.6
dm1616+34	dm1616+34b	I076	-11.6	-11.7	-11.8	-11.6	-11.7	-11.7	-11.8	-13.1	-13.3	-13.1	-12.4
dm1620+25	dm1620+25a	I091	-11.9	-	-11.8	-11.5	-11.5	-11.6	-11.6	-12.3	-12.6	-12.2	-11.9
dm1620+25	dm1620+25b	I092	-12.5	-12.5	-12.3	-12.0	-11.9	-11.9	-12.0	-12.7	-13.0	-13.0	-12.5
dm1623+15	dm1623+15a	I087	-11.9	-12.0	-11.9	-11.6	-11.6	-11.6	-11.7	-12.6	-13.0	-12.8	-12.3
dm1623+15	dm1623+15b	I088	-11.8	-11.9	-11.9	-11.7	-11.7	-11.7	-11.8	-12.8	-13.1	-13.0	-12.3
dm1647+21	dm1647+21a	I007	-	-11.2	-11.2	-10.9	-11.0	-11.1	-11.2	-12.7	-13.1	-13.2	-12.4
dm1647+21	dm1647+21b	I008	-	-11.4	-11.6	-10.9	-11.0	-11.1	-11.8	-13.0	-13.2	-13.0	-12.1
dm1718+30	dm1718+30a	I065	-11.3	-11.1	-11.1	-10.9	-10.8	-10.9	-10.9	-11.6	-11.9	-11.1	-10.7
dm1718+30	dm1718+30b	I066	-12.3	-12.1	-11.8	-11.4	-11.4	-11.4	-11.4	-12.3	-12.7	-12.7	-12.4
dm2227-09	dm2227-09a	I071	-10.9	-11.0	-10.9	-10.7	-10.7	-10.8	-10.8	-12.6	-12.9	-13.0	-12.3
dm2227-09	dm2227-09b	I072	-11.0	-11.1	-11.2	-11.0	-11.1	-11.1	-11.1	-12.6	-12.9	-12.9	-12.3
dm2358+14	dm2358+14a	I081	-11.5	-11.6	-11.6	-11.5	-11.5	-11.6	-11.6	-12.5	-12.9	-12.7	-12.3
dm2358+14	dm2358+14b	I082	-11.7	-11.8	-11.8	-11.6	-11.6	-11.6	-11.6	-12.6	-12.8	-13.0	-12.3

Note. —  $F_F$  is the GALEX FUV filter.  $F_N$  is the GALEX NUV filter. Not all of the TNT dwarf galaxies were observed with GALEX and are marked accordingly.

# Appendix B

## *Spitzer* Infrared Imaging of Isolated TNT Dwarf Galaxies

### B.1 Motivation

Low mass dwarf galaxies constitute the most numerous extragalactic population in the local universe (Karachentsev et al., 2004). Interactions between these galaxies are thought to be the building blocks of more massive galaxies. Their typically low metallicities suggest the processes governing their star formation may reflect those at work at higher redshifts when gas in galaxies was relatively unenriched. Dwarfs thus provide a rich source of information for our understanding of galaxy evolution.

Studies of massive interacting galaxies at low redshift reveal strong indications of interactions in close galaxy pairs, which produce diluted metals, enhanced star formation, bluer colors, and higher AGN fractions (e.g., Patton et al. (2011), Ellison et al. (2011)). These effects are consistent with predictions from simulations, including gas inflows, triggered star formation, and the activation of central supermassive black holes after close passages (e.g., Scudder et al. (2012), Torrey et al. (2012)). After interactions which end in mergers, the end products tend to be quenched systems, so close galaxy pairs provide insight into both starbursts and quenching mechanisms. Many of these side effects of interactions observed in more massive galaxies should also be present in low mass dwarf-dwarf pairs in the field. However, we do not observe quenched dwarf systems that are isolated from massive galaxies (Geha et al. (2012)), thus suggesting that mergers may proceed differently at lower masses.

Dwarf galaxies are observed to have redder  $[3.6 \mu\text{m}]-[4.5 \mu\text{m}]$  colors than more massive spiral galaxies (Smith & Hancock (2009)). This mid-infrared color also shows significant scatter in the low metallicity regime. The cause of the reddening and the variations in the flux in these infrared bands is unknown. They could be due to a number of factors related to both stellar populations and the properties of the interstellar medium (ISM). Starbursting dwarf galaxies may have a larger population of hot young stars than star-forming spiral galaxies, and these stars have redder infrared colors than the cooler population of stars in more massive galaxies (Pahre et al., 2004). Br $\alpha$  emission from a young population of hot ionizing stars can also contribute significantly to the  $4.5 \mu\text{m}$  flux (Povich et al., 2007). In highly obscured systems, the observed light can be reddened in these bands due to dust extinction. Nebular continuum emission can also dominate the infrared fluxes of low metallicity, starbursting systems (e.g., Krueger et al. (1995), Hunt et al. (2001)). Finally, emission from dust heated to high temperatures by intense UV radiation from young stars may contribute significantly to the  $4.5 \mu\text{m}$  flux (e.g., Hunter et al. (2006), Engelbracht et al. (2005)).

Smith & Hancock (2009) noted that the reddest dwarf galaxies systems (and those that exhibit largest IR color scatter) were the ones that showed evidence of recent interactions and/or mergers with other galaxies. Reasonably high resolution and sensitive infrared imaging of a systematically selected sample of isolated interacting dwarf galaxies are critical to determine what physical processes are contributing to the observed scatter in IR color. Detecting the infrared stellar and small grain dust emission out as far as at least the optical extent of each interacting dwarf would be extremely time consuming from the ground. The sky brightness in the near infrared is highly variable (typical  $\mu_K \sim 13.4 \text{ mag arcsec}^{-2}$ ) which is at least 11 magnitudes above the limit to detect these processes.

All of the TiNy Titans (TNT; Stierwalt et al. (2015)) dwarf galaxies have been observed in the infrared in the Wide-field Infrared Survey Explorer (WISE; see Chapter 2). However, although the WISE All-Sky Survey reaches sensitivities that offer a vast improvement on ground-based observations, they are still not sensitive enough to detect the full extent of our dwarf galaxies, which is critical for determining the distribution of any IR color variations throughout these systems. Furthermore, Figure B.1 demonstrates why the  $6''$  resolution of WISE is insufficient for this work. Many of the TNT dwarf galaxies are only marginally resolved in the WISE imaging, and thus investigations of the nuclear versus extended dust emission are not possible<sup>1</sup>. Additionally, 7 pairs are too close to be

---

<sup>1</sup>Walker et al. (2013) found that the optical and infrared colors of interacting galaxy groups evolve on different timescales, thus the optical data we have is not sufficient to understand the dust evolution.

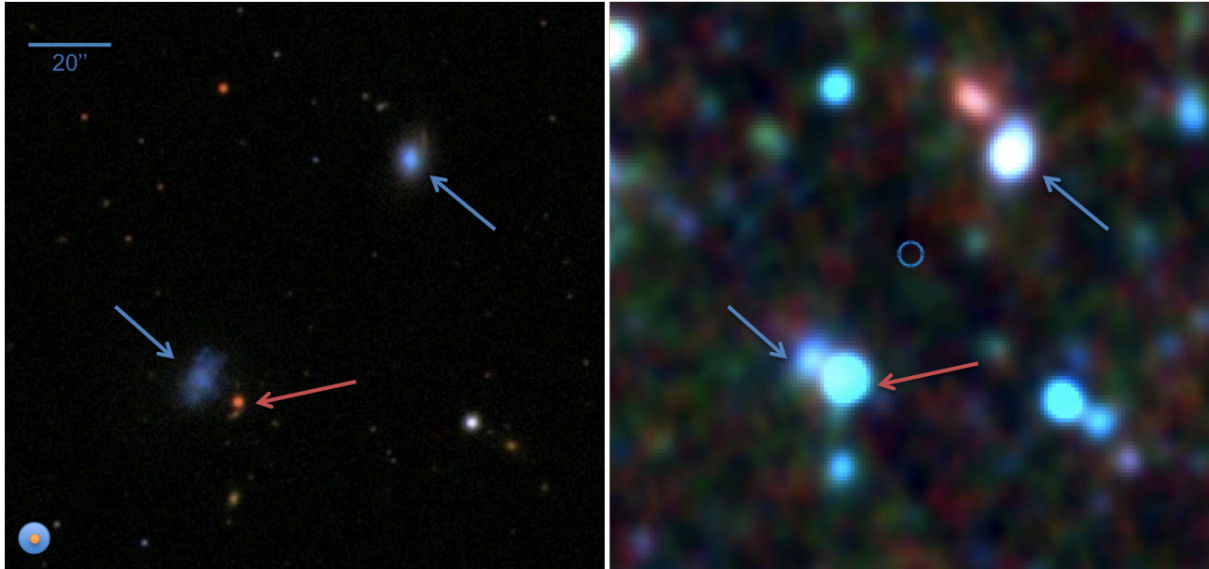


Figure B.1 Example of the resolution of SDSS optical image of a TNT pair (left) vs. WISE infrared image of the same pair (right). The blue arrows are pointing to the dwarf galaxies in both panels, and the red arrow to a nearby star. The WISE infrared emission of this star overlaps the southern galaxy in the pair, thus contaminating the measured flux in these bands.

resolved at all with WISE ( $r_{\text{sep}} < 6''$ ), thus prohibiting any exploration of trends with pair separation to separations below  $\sim 10$  kpc. Finally, in a small number of cases ( $\sim 5$ ), contamination from a bright foreground star or a red background galaxy as revealed by the optical SDSS imaging are clearly blended in the WISE photometry.

In order to address these issues, we have obtained Spitzer Warm Mission IRAC Channel 1 & 2 imaging for a sample of 60 of our isolated ( $D_{\text{host}} > 1.5$  Mpc) TNT dwarf galaxy pairs. The IRAC angular resolution of  $2''$  is well-matched to the spatial extents of our dwarfs ( $2''$  is  $\sim 300$  pc at 35 Mpc, our median distance). Thus the IRAC imaging will enable us to differentiate between nuclear and extended emission. Furthermore, this increased resolution will help to eliminate the foreground stellar and/or background galactic contamination found in the WISE data. This imaging will first allow us to determine the extent to which the  $3.6$  and  $4.5 \mu\text{m}$  bands are dominated by stellar light and investigate a) the extent to which interacting pairs show IR excess and b) whether the excess is related to the pair separation, mass ratio, star formation rate, and/or gas fraction. We will also look at how the IR color varies within each galaxy – is it fairly consistent throughout, or is there a color gradient? Is the emission from hot dust centrally concentrated, or is it extended? We will further use this IR photometry in conjunction with our complementary multiwavelength data to constrain the processes contributing to the observed color excess and scatter in each system. Our optical and ultraviolet data

will allow us to disentangle the direct stellar light contribution, and our H $\alpha$  data will allow us to estimate the contributions from Br $\alpha$  and nebular continuum emission, leaving the dust contribution as the outstanding variable.

## B.2 Progress and Future Plans

We have begun our analysis of the Spitzer data by performing custom-aperture photometry with Surphot (Reines et al., 2008) on each dwarf in order to derive their [3.6  $\mu\text{m}$ ]-[4.5  $\mu\text{m}$ ] colors. The TNT dwarfs occupy a similar color space that Smith & Hancock (2009) observe the interacting dwarfs (uncorrected colors) in their sample and span a larger range of metallicities (see Figure B.2). All of the TNT dwarfs have a larger IR color excess than predicted by unextincted starlight, suggesting that there are other processes contributing to the IR colors of these systems. We have further explored trends between the observed IR colors and the TNT pair parameters (see Figure B.3). We observe no obvious trends with respect to projected radial separation, projected velocity separation, pair mass ratio, or redshift.

We will expand our investigation of how the IR color varies with pair parameters. While no individual parameter appears to have a significant effect, we will look for co-variance between these variables as potential dependencies. We will further investigate other environmental factors, such as the local gravitational environment as generated by both a dwarf's pair member and nearby massive galaxies.

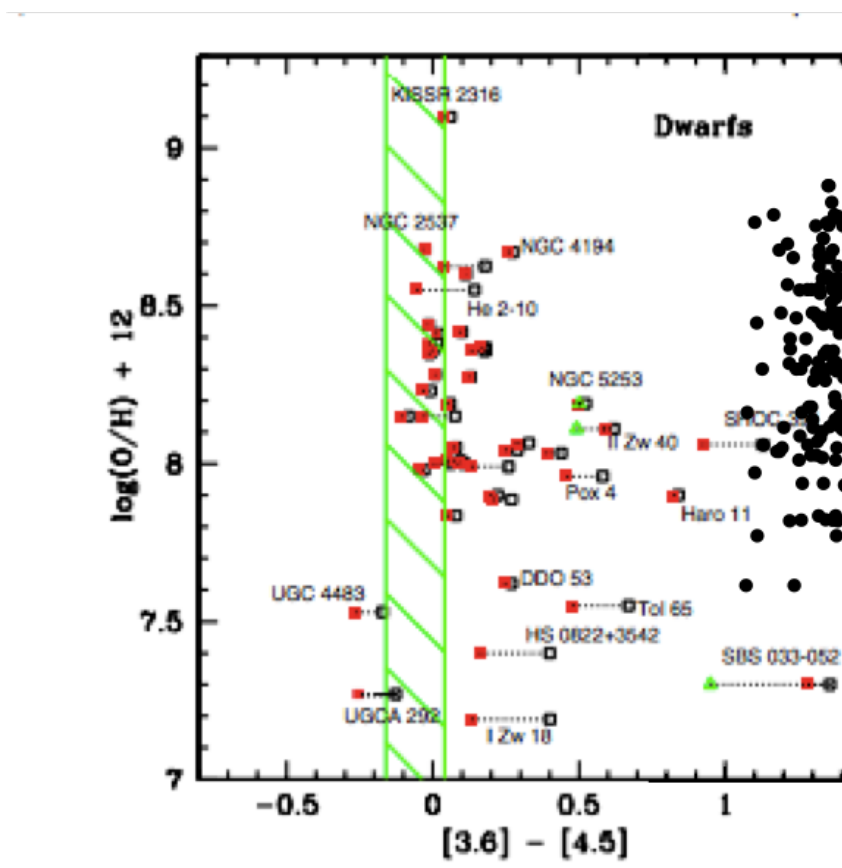


Figure B.2 TNT infrared colors in context: Modified figure from Smith and Hancock (2009) showing the metallicity of a sample of dwarf galaxies as a function of infrared color with the TNT interacting dwarf galaxies shown as solid black circles. The green hatched region indicates the range of expected colors if all IR emission was due to contributions from unextinguished starlight. The TNT dwarfs occupy a similar color space that Smith & Hancock (2009) observe the interacting dwarfs in their sample and span a larger range of metallicities.

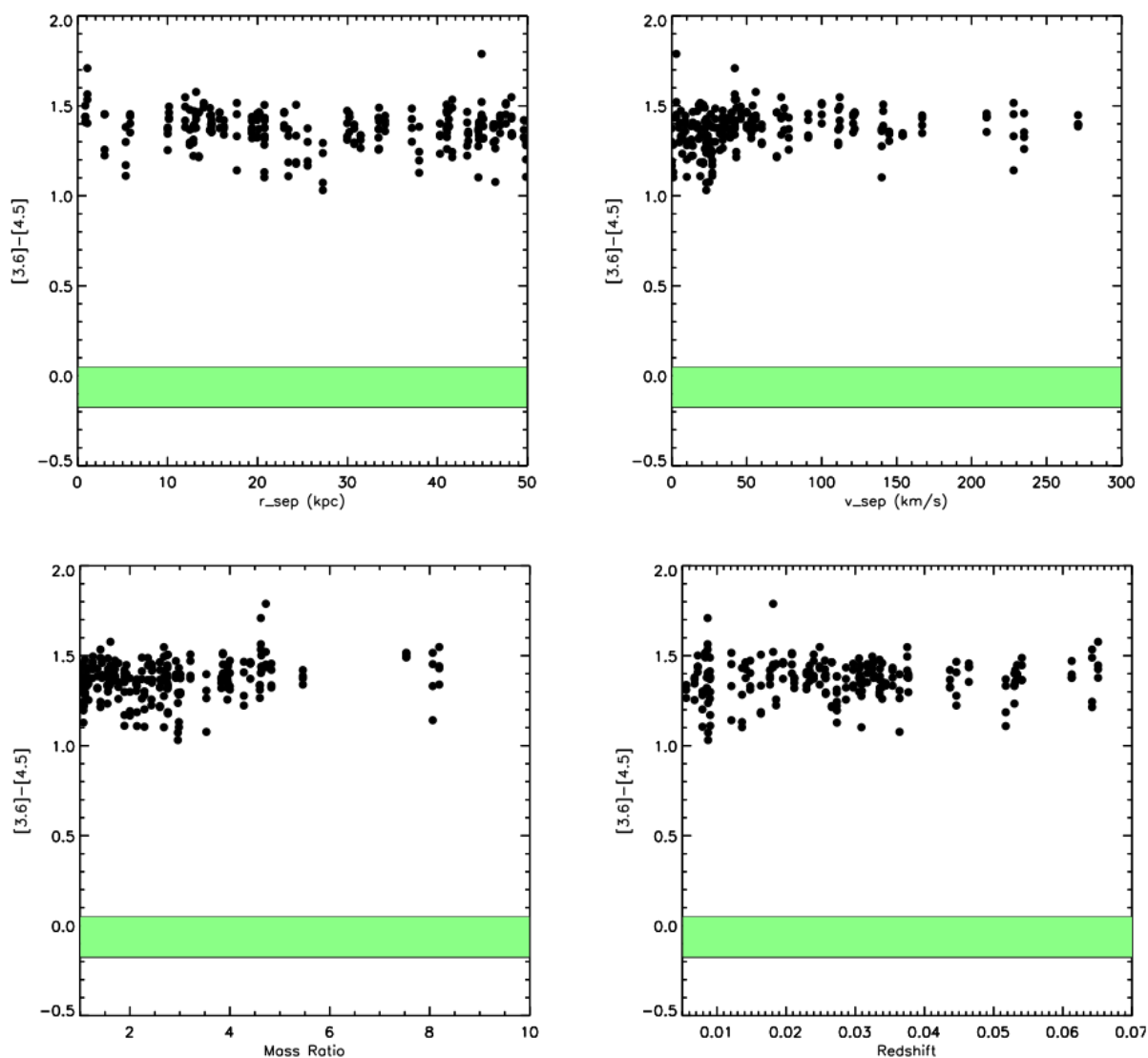


Figure B.3 TNT infrared colors dependence on pair properties. The filled green region indicates the range of expected colors if all IR emission was due to contributions from unextincted starlight. Top left: IR color as a function of projected pair separation. Top right: IR color as a function of projected velocity separation. Bottom left: IR color as a function of mass ratio. Bottom right: IR color as a function of pair redshift.

# Appendix C

## Dark Skies, Bright Kids! and the Value of Repeated Interactions with Elementary School Students

Since I began studying science, my interest in the field of astronomy has grown into a fascination with understanding the evolution of our universe and a dedication to sharing that passion with others. Throughout my academic career I have actively sought opportunities to incorporate teaching and outreach into my scientific pursuits. Specifically, as a graduate student at the University of Virginia, I have been an active and leading member of the Dark Skies, Bright Kids! outreach program run out of the Department of Astronomy. We seek to make the excitement of scientific discovery accessible to others, with a focus on upper elementary school students from underserved backgrounds. In this appendix, I share a white paper I authored for the American Astronomical Society's Educational Task Force in 2016 that summarizes the DSBK program, its impact on our community, and the keys to its success.

---

Dark Skies, Bright Kids! (DSBK) is a volunteer-run outreach program that targets underserved elementary school students in central Virginia<sup>1</sup>. The core mission of DSBK is to build positive attitudes about science through long term, one-on-one interactions with scientists in a non-traditional educational setting. The heart of the program is an eight-to ten- week after school “astronomy club” that covers a set of major astronomical topics.

---

<sup>1</sup>For more information, go to our website at <http://faculty.virginia.edu/DSBK/> or find us on Facebook at <https://www.facebook.com/DarkSkiesBrightKids>.

We present content to the students through a combination of demos and hands-on activities that build curiosity and excitement as they demonstrate those scientific concepts. This program is operated entirely by volunteers drawn from the students, staff, and faculty affiliated with the Department of Astronomy at the University of Virginia. Since our founding in 2009, these DSBK volunteers have contributed over 15,000 volunteer contact hours toward the education of students in central Virginia. DSBK is funded from education components of research grants, gifts from the community, outreach support funds at the University, and external grants. In recognition of its accomplishments, DSBK was honored as a 2012 “Program that Works” by the Virginia Mathematics and Science Coalition, the highest award for informal education programs in Virginia. In 2015, DSBK was awarded a grant from the David and Lucile Packard Foundation to facilitate a series of summer astronomy camps at rural locations in Virginia.

There are several unique aspects to the program that we believe are paramount to its success:

- **Our outreach model is built around developing meaningful relationships between students and scientists through repeated and prolonged interactions.** It has been noted that “random acts of EPO” have little lasting impact on the public<sup>2</sup>. AAS programs like the Astronomy Ambassadors promote the development of “ongoing, sustainable partnerships with schools or other organizations”<sup>2</sup>, which is precisely what DSBK does. In our experience, while one time events (such as public observing nights) may expose students to science in an exciting way, repeated interactions are what lead them to become invested in it. By taking a mentorship approach in our astronomy clubs, DSBK volunteers are able to build relationships with students on an interpersonal level to demonstrate that we (scientists) are not so different from them (students).
- **Our primary goal is to improve students’ attitudes toward science.** While we do strive to teach our students basic astronomy concepts, our main focus is to encourage them to develop a positive connection to the scientific community. Many elementary school students have already become disillusioned with the scientific endeavor, not having been shown any clear connection between science and their everyday lives<sup>3</sup>. We seek to break down any negative stereotypes they may hold

---

<sup>2</sup><https://aas.org/outreach/aas-astronomy-ambassadors-program>

<sup>3</sup>Barman, Charles R, Karen L. Ostlund, Cindy C. Gatto, and Mimi Halferty. *Fifth Grade Students’ Perceptions About Scientists and How They Study and Use Science*. AETS Conference Proceedings, p. 688-699, 1997.

by interacting with them as ‘real live scientists.’ Each DSBK activity is designed for the students to engage with science in much the same way we do as scientists, and care is given to emphasize that the students’ own curiosity and enjoyment are important aspects of the scientific process.

- **DSBK itself is organized like a research group and depends on ideas from each volunteer.** Our volunteers collaborate to contribute to the overall mission of DSBK in much the same way that diverse scientists pool their individual expertise to solve a scientific problem. Furthermore, we grow and evolve according to the interests and input of the volunteers, which has resulted in our longevity (we are in our 8<sup>th</sup> consecutive year and 14<sup>th</sup> astronomy club). Though the vast majority of our volunteers have no formal instructional training, this model has allowed us to develop and implement novel outreach activities. As a result, our members themselves gain valuable experience in curriculum development, teaching, grant writing, and leadership, which has led to great success in other EPO endeavors; we have had five volunteers selected as AAS Astronomy Ambassadors; two who received NSF Postdoctoral Fellowships; one who held a postdoctoral fellowship at Southern Illinois University Edwardsville STEM Center for Research, Education, and Outreach; one alum who manages the Astronomy Education Program at the Smithsonian National Air and Space Museum; and another former DSBK volunteer who is now the Assistant Director for Education and Physical Sciences at White House Office of Science and Technology Policy.
- **We have built an assessment program into our outreach efforts.** We recognize the importance of being able to quantitatively demonstrate the effectiveness of our program<sup>4</sup>. This is complicated by the fact that many standard classroom evaluation metrics do not work within our non-traditional framework. We work to develop specific content goals along with each week’s activities. We then create journal pages that are aligned with these learning goals, and analyze them each week to track how effective our activities are at conveying astronomy content. We also administer the Draw-A-Scientist test<sup>5</sup> to each student twice (once before the first day of their astronomy club and once on the last day) in order measure changes in student perceptions of scientists. These worksheets, in combination with volunteer observations and photo-documentation, allow us to pinpoint what is working and

---

<sup>4</sup>Beaton, Rachael L., Sokal, Kimberly R., Liss, Sandra E., Johnson, Kelsey E. *Getting the Most Bang from Your Volunteer Hour: Easy Assessments in the Dark Skies, Bright Kids Program*. Astronomical Society of the Pacific Conference Series, 500, 67, 2015.

<sup>5</sup>Chambers, David W. *Stereotypic Images of the Scientist: The Draw-A-Scientist Test*. Science Education, 67(2) 255-265, 1983.

what needs to be improved. This crucial aspect of our program is still under development, and we hope that the larger astronomical and educational communities can assist us in improving it.

We believe DSBK fills a highly desirable niche for informal science education. The program was founded to bring science to students who have limited access to science content from other informal outreach providers in our central Virginia community. We have been extremely successful in accomplishing our goals, demonstrated not only through our assessments efforts but also through feedback from students, parents, and teachers. For example, this quote from one of our students shows the positive influence our astronomy club can have in shifting their attitudes regarding science:

*“I was gonna think it was boring but it was actually really fun! I was surprised.”*

Furthermore, we have found that our model of using scientist educators in a research group style organization that provides one-on-one interactions benefits not only our students, but also our volunteers. Volunteers gain valuable teaching experience, leadership skills, communication skills, grant writing experience, and networks within the community. The core components of DSBK can be easily translated to other institutions and communities and adapted to meet their specific outreach goals. We believe that the DSBK framework could be useful as a model for developing similar programs and, as an organization, are interested in supporting future efforts to do so<sup>6</sup>.

---

<sup>6</sup>Kimberly Sokal & Sandra Liss *Making Science Fun: The “Dark Skies, Bright Kids” Program*. Mercury Magazine, 43, 3, 2014.

# Bibliography

- Abazajian, K. N., Adelman-McCarthy, J. K., Agüeros, M. A., et al. 2009, *ApJS*, 182, 543
- Alatalo, K., Appleton, P. N., Lisenfeld, U., et al. 2015, *ApJ*, 812, 117
- Armus, L., Mazzarella, J. M., Evans, A. S., et al. 2009, *PASP*, 121, 559
- Bekki, K. 2008, *MNRAS*, 388, L10
- Besla, G., Kallivayalil, N., Hernquist, L., et al. 2007, *ApJ*, 668, 949
- . 2012, *MNRAS*, 421, 2109
- Besla, G., Martínez-Delgado, D., van der Marel, R. P., et al. 2016, *ApJ*, 825, 20
- Bianchi, L., Conti, A., & Shiao, B. 2014, *Advances in Space Research*, 53, 900
- Brown, M. J. I., Moustakas, J., Smith, J.-D. T., et al. 2014, *ApJS*, 212, 18
- Coziol, R., & Plauchu-Frayn, I. 2007, *AJ*, 133, 2630
- Davis, M., Efstathiou, G., Frenk, C. S., & White, S. D. M. 1985, *ApJ*, 292, 371
- Dressler, A., Bigelow, B., Hare, T., et al. 2011, *PASP*, 123, 288
- Ellison, S. L., Patton, D. R., Mendel, J. T., & Scudder, J. M. 2011, *MNRAS*, 418, 2043
- Engelbracht, C. W., Gordon, K. D., Rieke, G. H., et al. 2005, *ApJ*, 628, L29
- Gallagher, J. S., & Grebel, E. K. 2002, in *IAU Symposium, Vol. 207, Extragalactic Star Clusters*, ed. D. P. Geisler, E. K. Grebel, & D. Minniti, 745
- Gallagher, S. C., Durrell, P. R., Elmegreen, D. M., et al. 2010, *AJ*, 139, 545
- Geha, M., Blanton, M. R., Masjedi, M., & West, A. A. 2006, *ApJ*, 653, 240
- Geha, M., Blanton, M. R., Yan, R., & Tinker, J. L. 2012, *ApJ*, 757, 85

- Grebel, E. K., Kolatt, T., & Brandner, W. 1999, in IAU Symposium, Vol. 192, The Stellar Content of Local Group Galaxies, ed. P. Whitelock & R. Cannon, 447
- Hickson, P. 1982, *ApJ*, 255, 382
- Hook, I. M., Jørgensen, I., Allington-Smith, J. R., et al. 2004, *PASP*, 116, 425
- Hopkins, P. F., Kereš, D., Oñorbe, J., et al. 2014, *MNRAS*, 445, 581
- Hubble, E. P. 1925, *Popular Astronomy*, 33
- . 1926, *ApJ*, 64, doi:10.1086/143018
- . 1936, *Realm of the Nebulae*
- Hunt, L. K., Vanzani, L., & Thuan, T. X. 2001, *A&A*, 377, 66
- Hunter, D. A., Elmegreen, B. G., & Martin, E. 2006, *AJ*, 132, 801
- Indebetouw, R., de Messières, G. E., Madden, S., et al. 2009, *ApJ*, 694, 84
- Johnson, K. E., Hibbard, J. E., Gallagher, S. C., et al. 2007, *AJ*, 134, 1522
- Johnson, K. E., Hunt, L. K., & Reines, A. E. 2009, *AJ*, 137, 3788
- Kalari, V. M. 2017, in *Revista Mexicana de Astronomía y Astrofísica*, vol. 27, Vol. 49, *Revista Mexicana de Astronomía y Astrofísica Conference Series*, 89–89
- Kant, I., & L. Jaki, S. 1981, 1
- Kapteyn, J. C., & van Rhijn, P. J. 1920, *ApJ*, 52, 23
- Karachentsev, I. D., Karachentseva, V. E., Huchtmeier, W. K., & Makarov, D. I. 2004, *AJ*, 127, 2031
- Karachentsev, I. D., Makarov, D. I., & Kaisina, E. I. 2013, *AJ*, 145, 101
- Kennicutt, Jr., R. C. 1998, *ARA&A*, 36, 189
- Kirby, E. N., Cohen, J. G., Guhathakurta, P., et al. 2013, *ApJ*, 779, 102
- Krueger, H., Fritze-v. Alvensleben, U., & Loose, H.-H. 1995, *A&A*, 303, 41
- Landolt, A. U. 1992, *AJ*, 104, 340
- Lelli, F., Fraternali, F., & Verheijen, M. 2014, *A&A*, 563, A27

- Madau, P., Weisz, D. R., & Conroy, C. 2014, *ApJ*, 790, L17
- Malhotra, S., Rhoads, J. E., Pirzkal, N., et al. 2005, *ApJ*, 626, 666
- Mancuso, C., Lapi, A., Shi, J., et al. 2016, *ApJ*, 833, 152
- McConnachie, A. W., Ellison, S. L., & Patton, D. R. 2008, *MNRAS*, 387, 1281
- Meurer, G. R., Hanish, D. J., Ferguson, H. C., et al. 2006, *ApJS*, 165, 307
- Mokiem, M. R., Martín-Hernández, N. L., Lenorzer, A., de Koter, A., & Tielens, A. G. G. M. 2004, *A&A*, 419, 319
- Moreno, J., Torrey, P., Ellison, S. L., et al. 2015, *MNRAS*, 448, 1107
- Murray, N. 2011, *ApJ*, 729, 133
- O'Connell, R. W., Gallagher, III, J. S., & Hunter, D. A. 1994, *ApJ*, 433, 65
- Oey, M. S., Meurer, G. R., Yelda, S., et al. 2007, *ApJ*, 661, 801
- Oke, J. B. 1990, *AJ*, 99, 1621
- Pahre, M. A., Ashby, M. L. N., Fazio, G. G., & Willner, S. P. 2004, *ApJS*, 154, 235
- Patton, D. R., Ellison, S. L., Simard, L., McConnachie, A. W., & Mendel, J. T. 2011, *MNRAS*, 412, 591
- Patton, D. R., Torrey, P., Ellison, S. L., Mendel, J. T., & Scudder, J. M. 2013, *MNRAS*, 433, L59
- Pearson, S., Besla, G., Putman, M. E., et al. 2016, *MNRAS*, 459, 1827
- Povich, M. S., Stone, J. M., Churchwell, E., et al. 2007, *ApJ*, 660, 346
- Ramos, B. H. F., Pellegrini, P. S., Benoist, C., et al. 2011, *AJ*, 142, 41
- Reines, A. E., Johnson, K. E., & Goss, W. M. 2008, *AJ*, 135, 2222
- Rémy-Ruyer, A., Madden, S. C., Galliano, F., et al. 2013, *A&A*, 557, A95
- Sales, L. V., Wang, W., White, S. D. M., & Navarro, J. F. 2013, *MNRAS*, 428, 573
- Sanders, D. B., Soifer, B. T., Elias, J. H., et al. 1988, *ApJ*, 325, 74
- Scudder, J. M., Ellison, S. L., Torrey, P., Patton, D. R., & Mendel, J. T. 2012, *MNRAS*, 426, 549

- Shapley, H. 1919, *ApJ*, 49, doi:10.1086/142469
- Smith, B. J., Giroux, M. L., Struck, C., & Hancock, M. 2010, *AJ*, 139, 1212
- Smith, B. J., & Hancock, M. 2009, *AJ*, 138, 130
- Spekkens, K., Urbancic, N., Mason, B. S., Willman, B., & Aguirre, J. E. 2014, *ApJ*, 795, L5
- Springel, V., White, S. D. M., Jenkins, A., et al. 2005, *Nature*, 435, 629
- Stierwalt, S., Besla, G., Patton, D., et al. 2015, *ApJ*, 805, 2
- Stierwalt, S., Liss, S. E., Johnson, K. E., et al. 2017, *Nature Astronomy*, 1, 0025
- Thilker, D. A., Braun, R., & Walterbos, R. A. M. 2000, *AJ*, 120, 3070
- Toomre, A. 1977, in *Evolution of Galaxies and Stellar Populations*, ed. B. M. Tinsley & R. B. G. Larson, D. Campbell, 401
- Torrey, P., Cox, T. J., Kewley, L., & Hernquist, L. 2012, *ApJ*, 746, 108
- Trumpler, R. J. 1930, *PASP*, 42, 214
- Tully, R. B., Rizzi, L., Dolphin, A. E., et al. 2006, *AJ*, 132, 729
- Veilleux, S., Weiner, B. J., Rupke, D. S. N., et al. 2010, *AJ*, 139, 145
- Vogelsberger, M., Genel, S., Springel, V., et al. 2014, *MNRAS*, 444, 1518
- Walborn, N. R., Drissen, L., Parker, J. W., et al. 1999, *AJ*, 118, 1684
- Walker, L. M., Johnson, K. E., Gallagher, S. C., et al. 2010, *AJ*, 140, 1254
- Walker, L. M., Butterfield, N., Johnson, K., et al. 2013, *ApJ*, 775, 129
- Wheeler, C., Oñorbe, J., Bullock, J. S., et al. 2015, *MNRAS*, 453, 1305
- Whitmore, B. C., Chandar, R., Bowers, A. S., et al. 2014, *AJ*, 147, 78
- Wright, E. L., Eisenhardt, P. R. M., Mainzer, A. K., et al. 2010, *AJ*, 140, 1868
- Zaragoza-Cardiel, J., Smith, B. J., Rosado, M., et al. 2018, *ApJS*, 234, 35
- Zucker, C., Walker, L. M., Johnson, K., et al. 2016, *ApJ*, 821, 113